Title
Interplay of symmetry breaking and topological order

Author
Wang, Yanqi

Publication Date
2023

Peer reviewed|Thesis/dissertation

Interplay of symmetry breaking and topological order

by

Yanqi Wang

A dissertation submitted in partial satisfaction of the

requirements for the degree of

Doctor of Philosophy

in

Physics

in the

Graduate Division

of the

University of California, Berkeley

Committee in charge:

Professor Joel E. Moore, Chair
Professor Michael P. Zaletel
Professor Lin Lin

Summer 2023

Interplay of symmetry breaking and topological order

Abstract

Interplay of symmetry breaking and topological order

by

Yanqi Wang

Doctor of Philosophy in Physics

University of California, Berkeley

Professor Joel E. Moore, Chair

The two most prevalent classes of ordered states in quantum materials are those arising from spontaneous symmetry breaking (SSB) and from topological order. However, a systematic study for their coexistence in interacting systems is still lacking. In this thesis, we will investigate how the topological configuration in order parameter spaces from SSB interplays with the symmetry protected/enriched topological orders in two spatial dimensions. We start from a phenomenological model of the domain wall structure in chiral spin liquids with domains of opposite chiralities. Based on a standard model, we obtain a spatially varying, self-consistent mean-field solution for the spinons that describes both the gapless edge modes and the change of chirality at the domain wall. We derive the non-universal properties, such as the velocity of the topologically protected domain wall edge states and its modification to domain wall tension. Then we discuss the interplay between topological orders from a more formal point of view. We consider two-dimensional topologically ordered systems with coexisting long-range orders, where the only gapless excitations in the spectrum are Goldstone modes of spontaneously broken continuous symmetries. We show that the universal properties of point defects and textures are determined by the remnant symmetry enriched topological order in the symmetry-breaking ground state with non-fluctuating order parameters, and provide a classification for their properties using algebraic topology. We further investigate the quantum dynamics that can happen at the domain wall of topological orders, where particle-hole scattering leads to linear-in-temperature resistivity of edge modes. Finally, we introduce an effective edge network theory to characterize the boundary topology of coupled edge states generated from various types of topological insulators.

To my parents

Contents

List of Figures

List of Tables

Acknowledgments

First and foremost, I want to thank my advisor, Professor Joel E. Moore. It's been my greatest honor working with him as a graduate student researcher. He is extremely supportive and patient, and he always reserves time to discuss with us in an incredibly punctual way. I have been admiring his depth and breadth of knowledge in physics since I was an undergrad. He's always able to explain things to me with a clear physical picture and via the most fundamental concepts. I have benefited a lot from his insightful research ideas. Joel has brought me many opportunities to collaborate with the experimental groups, introducing me to realistic solid state physics. It's very kind of him to support me with the all-time RAship, encourage me to attend summer schools and research conferences, as well as provide detailed guidance in seeking for postdoc positions. Besides, Joel is perhaps the most virtuous gentleman that I ever run into in the real world. Patient, responsible, professional..., there are so many good characteristics that one can learn from him.

I would like to thank Professor Dung-Hai Lee, whose fantastic lectures introduced me to two of the most important concepts in modern condensed matter theory, "classification of topological phases of matter" and "renormalization group". I am also indebted for his generous and timely help during my application for postdocs. Many thanks to Professor Yuan-Ming Lu from Ohio State University, who kindly introduced me to the field of topological order in a formal way. Yuan-Ming provided me a completely different viewpoint and mathematical toolbox at my hardest time. I shall always remember his encouragement in our collaboration, as well as his critical help and advice during application season. I am very grateful to Professor Michael Crommie for making my first experience of collaboration with experimental group turn into a nice clean story, and always willing to discuss with us on either theoretical proposals or experimental outcomes.

Besides, I have also learned a lot from the discussions or the lectures of other Berkeley professors: Michael Zaletel, Feng Wang, Ehud Altman, Joseph Orenstein, Steven Louie, Norman Yao, Hitoshi Murayama, Petr Horava and many others. It's my great pleasure as well to have the opportunity to discuss with the professors outside Berkeley: Xiao-Gang Wen, Ashvin Vishwanath, Meng Cheng, Leonid Glazman, Alexey Gorshkov, Victor Galitski, Jason Alicea, Christoph Karrasch, Trithep Devakul, Andrei Bernevig, Päivi Törmä, Michael Levin and Luca Delacrétaz. I am particularly grateful to my undergraduate advisor, Professor Xiong-Jun Liu, who introduced me to condensed matter and AMO physics. Finally, many thanks to Professor Michael Zaletel and Professor Lin Lin for serving on my committee.

I am glad to express my utmost appreciation to Dr. Chunxiao Liu. It's my great fortune to meet him during the last stage of my PhD career. Despite being a postdoctoral mentor, Chunxiao is more like a three years older brother to me. Chunxiao is a fantastic teacher, he's always ready to provide detailed instructions for the fields that he's specialized in (which is already remarkably wide for a postdoc), and willing to lead the exploration of the unknown areas with me. I thank him for the numerous discussions we had, sometimes till midnight. I really appreciate his valuable advice in research directions and conducting research collab-

orations. He is always there for me no matter what problems I run into, from academia to daily life. Chunxiao provides a role model for me on how to be a good mentor and postdoc.

It's my great pleasure to address my sincere thanks to Dr. Michał Papaj. It's him who supervised me for the first theoretical project in material science. Michał taught me step by step not only in band and transport theory analytically, but also in how to use clusters and KWANT. He's able to answer any of my questions in solids and coding, no matter how technical or how fundamental they are. I am particularly grateful for his help and understanding in wrapping up the paper, when I was in hospital and almost unable to work. I hope I can still have the chance to work on solid state physics, talk about history and exchange hand-made desserts with him in the future.

My sincere thanks should also go to Zhi-Qiang Gao for giving me the precious opportunity to mentor him based on the tutorial skills I learnt from Joel, Chunxiao and Michał. Zhi-Qiang has tremendous enthusiasm in exploring the interdisciplinary areas between high-energy physics and condensed matter theory. He's always happy to actively share his ideas and readings with me. I can see the fire of his sincere love for this field, and I feel lucky to be with him on his journey of bravery. I wish him all the best in his future career.

I am delighted to thank my other friends and colleagues: Aaron Szasz, Vir Bulchandani, Daniel Parker, William Berdanier, Tianrui Xu, Elizabeth Dresselhaus, Alexander Avdoshkin, Tessa Cookmeyer, Nick Sherman, Kai Klocke, Noelle Blose, Meabh Allen, Yi Zhao, Takahiro Morimoto, Johannes Mitscherling, Zhehao Dai, Shubhayu Chatterjee, Yu-Ping Lin, Dan Borgnia, Marc Vila Tusell, Thais Victa Trevisan, Jyong-Hao Chen, Wei Ruan, Tiancong Zhu, Hongyuan Li, Canxun Zhang, Tomohiro Soejima, Sajant Anand, Tianle Wang, Taige Wang, Stefan Divic, Ting Cao, Zhenglu Li, Meng Wu, Jingwei Jiang and many others. I greatly appreciate the hard work of the Berkeley physics department staffs, in particular for the great help from Joelle Miles and Beth McCleary.

I would like to extend my sincere thanks to Emily and Ron Poon who took great care of my stay in Berkeley, in particular during the pandemic. Special thanks to the folks at "paw for mental health" and the doggos there (Jojo and Peter the corgis, Comet the golden retriever and Trouper the great Pyrenees), who have done a fantastic job in relieving feelings of stress, anxiety, and depression of us Cal students.

Finally, I would like to express my deepest appreciation to my parents for their unconditional love and support. Words can not express my gratitude to your patience and courage, and I owe you a debt for almost everything in my life. This thesis is dedicated to you.

Chapter 1

Introduction

Perhaps the two most prevalent classes of ordered states in quantum materials are those arising from spontaneous symmetry breaking and from topological order. The nature of boundaries in these two kinds of ordered states is generally quite different: most, but not all, topological states have protected gapless excitations at their boundaries, while symmetry-breaking states need not. The focus of this thesis is on the nature of the interplayer between symmetry breaking and topological order.

In this chapter, we will give a brief introduction on the fundamental concepts of symmetry breaking physics and topological phases of matter. In Sec. [1.1], we briefly introduce the concept of symmetry breaking, which gives birth to the topological defects and topological textures. We also introduce the natural mathematical language of topological defects and textures, which is the homotopy theory. We introduce the concept of topological order in Sec. [1.2], as well as the symmetry enriched topological (SET) orders and symmetry protected topological (SPT) orders. In Sec. [1.3], we give an example for invertible topological order, the Chern insulator. We further introduce for group cohomology, which is the mathematical tools for SET/SPT in Sec. [1.4]. Finally, in Sec. [1.5] we give the outline for the rest of this thesis.

1.1 Symmetry breaking, topological defects/textures and homotopy theory

One of the most successful theories in condensed matter physics is the Landau's theory of phases and phase transitions [148, 72, 146, 147]: phases are distinguished by their symmetries, and phase transitions are described by symmetry breaking. An ordered phase with broken symmetry is identified through the formation of off-diagonal long-range order and is characterized by a local order parameter.

Topological defects and textures are presented in an ordered phase as a consequence of the nontrivial topology of the order parameter space [178]. We define the *classical topology* to be the topological configuration in order parameter space. Depending on whether the

order parameter has singularity or not, the classical topological configuration can be divided into two classes. The topological defects are configuration which has singularity in order parameter spaces. On the other hand, the topological textures, does not have singularity. This classical topology can lead to very rich physics. For example, the topological defects have their own dynamics and may also lead to phase transitions at finite temperatures [20, 21, 138]. Topological defects and textures also commonly appear in soft matter physics [130, 256] and ultracold atom physics [156, 235].

	$d=1$	$d=2$	$d=3$
π_0	point defect	line defect	surface defect
π_1	texture	point defect	line defect
π_2		texture	point defect
π_3			texture

Table 1.1: Homotopy group for topological defect/texture in $d = 1, 2, 3$ dimension.

In this section, first we briefly review the homotopy theory of topological defects and textures in the order parameters [178, 264]. Mathematically, the long-range order of spontaneous symmetry breaking is described by a local order parameter

$$O(\vec{r}) \in \mathcal{M} = G/H, \tag{1.1}$$

i.e. the order parameter is valued on the (left) coset space of G modulo H, where the full symmetry G of the Hamiltonian is spontaneously broken down to a subgroup H in a ground state with a fixed order parameter configuration. In particular, the remnant symmetry H is the subgroup of G which keeps the order parameter $\{\hat{O}(\vec{r})\}$ invariant:

$$H \equiv \{h \in G | h\hat{O}(\vec{r})h^{-1} = \hat{O}(\hat{h}\vec{r})\}. \tag{1.2}$$

Given the order parameter manifold $\mathcal{M} = G/H$, in d spatial dimensions, one can consider an order parameter configuration with point (line, surface etc.) defects, where the order parameter $O(\vec{r})$ is a smooth function of spatial coordinate $\vec{r}$ except for singularities on isolated points (lines, surfaces etc.). Most generally, a $(d-D-1)$-dimensional defect (i.e. a defect of codimension $D+1$) is described by a continuous map:

$$\vec{r} \in S^D \to O(\vec{r}) \in \mathcal{M} = G/H \tag{1.3}$$

of order parameters on a submanifold enclosing the defect. The inequivalent classes of $(d-D-1)$-dimensional defects in d spatial dimensions is hence classified by the homotopy group $\pi_D(G/H)$ [178] for $d \geq D+1$. Below we list a few defects in low dimensions:

(i) 0-dimensional point defects are classified by $\pi_{d-1}(G/H)$ for $d \geq 1$;

(ii) 1-dimensional line defects are classified by $\pi_{d-2}(G/H)$ for $d \geq 2$;

(iii) 2-dimensional defects are classified by $\pi_{d-3}(G/H)$ for $d \geq 3$.

In addition to defect configurations where the order parameter $O(\vec{r})$ becomes singular somewhere in space, homotopy theory also classifies textures of the order parameter configurations which are smooth everywhere. They are classified by the following continuous map:

$$\vec{r} \in S^d \to O(\vec{r}) \in \mathcal{M} = G/H \tag{1.4}$$

where we compactify the d-dimensional real space to S^d. As a result, topologically inequivalent textures in d dimensions are classified by the homotopy group $\pi_d(G/H)$. Similarly one can also consider spacetime textures, classified by homotopy group $\pi_{d+1}(G/H)$ where the $(d+1)$-dimensional spacetime is compactified to S^{d+1}. Homotopy group for topological defect/texture in $d = 1, 2, 3$ dimension can be found in Table. 1.1.

In this work, we shall restrict ourselves to two spatial dimensions ($d = 2$), where different types of topological defects and textures are classified by the following homotopy groups:

(i) Domain walls with codimension 1, where order parameters are smooth everywhere except for along a line, are classified by $\pi_0(G/H)$;

(ii) Point defects (i.e. vortices) with codimension 2, where order parameters are smooth everywhere except for one point, are classified by $\pi_1(G/H)$;

(iii) Textures where order parameters are smooth everywhere, are classified by $\pi_2(G/H)$. A well-known example is a skyrmion in a $2+1$D O(3) nonlinear sigma model (NLSM), as will be discussed in detail later.

The main goal of this work is to establish a connection between topological defects and textures of the symmetry-breaking order parameters, and the underlying topological ground states. The main mathematical tool that reveals this connection is the long exact sequence of homotopy groups [178]:

$$\cdots \longrightarrow \pi_n(H) \longrightarrow \pi_n(G) \longrightarrow \pi_n(G/H) \longrightarrow \pi_{n-1}(H) \longrightarrow \pi_{n-1}(G) \longrightarrow \cdots . \tag{1.5}$$

Here, "exact" means that for each term G in the sequence $N \xrightarrow{p} G \xrightarrow{q} Q$, the kernel of the outgoing map q, $\ker(q) = \{m \in G | q(m) = 0\}$ is equal to the image of the incoming map p, $\mathrm{im}(p) = f(N)$: $\mathrm{im}(p) = \ker(q)$. We noticed that the general idea of mapping topological defects and textures to symmetry defects through "connecting homomorphism" $\pi_k(G/H) \to \pi_{k-1}(H)$ have been pointed out in Refs. [198, 58].

1.2 Topological order

Since the discover of the quantum Hall effects in the 1980s [132, 255, 151], the notion of phases of matter have been extended beyond Landau's theory. Let us focus on gapped phases of matter, which, by definition, are phases with gapped excitations that are robust against local perturbations without closing the gap. In absence of symmetry, these different phases are determined by the long-range entanglement structure of the ground state wave functions [275], with the trivial one being an "atomic insulator" whose ground state shares the same phase as a collection of isolated atoms. A topological order, on the other hand,

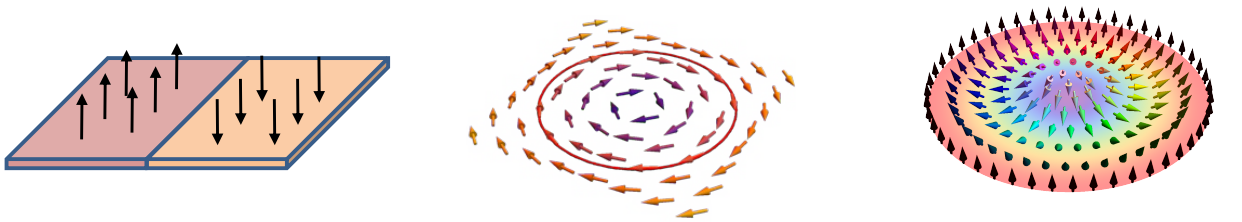

Domain wall **(line defect)** $\pi_0(Z_2)$ **Vortex** **(point defect)** $\pi_1(U(1))$ **Skyrmion** **(texture)** $\pi_2(S^2)$

Figure 1.1: Illustration for examples of topological defects (domain wall and vortex) and topological textures (skyrmion).

has a nontrivial entanglement structure in their wave function, which manifest itself, e.g. through ground state degeneracy when placed on a topologically nontrivial manifold [270]. Here, while the word "topological" in topological order still refers to the robustness of the low energy excitations against local perturbations without closing the gap, this feature is a direct consequence of the long-range entanglement of the wave function [275]. In presence of symmetry, either a topologically trivial state or a topologically ordered state may be further separated into different phases. The result is either a symmetry protected topological (SPT) phase [83, 41, 39, 40, 42, 45, 44, 43, 197, 170, 274, 154, 277] or a symmetry enriched topological (SET) phase [59, 179, 169, 245, 14], and in both cases different gapped ground states are characterized by certain topological invariants. As the quantum state counterpart of the order parameter in a broken phase in Landau's theory, the topological invariants reflect the robustness of the state under small perturbations and are a manifestation of the *quantum topology* that arises from many-body quantum entanglement in the wave function.

1.3 Chern insulator

The Hall effect is the production of a voltage difference (Hall voltage) across an electric conductor, transverse to an electric current in the conductor and to an applied magnetic field to the current. The integer quantum Hall effect is a quantum mechanical version of the Hall effect, observed in 2d electron system subjected to low temperature and strong magnetic field, in which the Hall conductance σ_{xy} undergoes quantum Hall transitions to take on the quantized values [5].

A Chern insulator, also called quantum anomalous Hall effect (QAHE), can be viewed as integer quantum Hall effect without external magnetic field. A Chern insulator is normally regarded as an invertible topological order[1]. One central feature for the topological phases of matter is the topological invariants, which reflect the robustness of the state under small

[1]Topological orders with no topological excitations are called invertible topological orders. The Chern insulator and the quantum anomalous Hall state are just different names for the same fermionic invertible topological order with integer chiral central charge c. For every invertible topological order $\mathcal{C}$, there exists

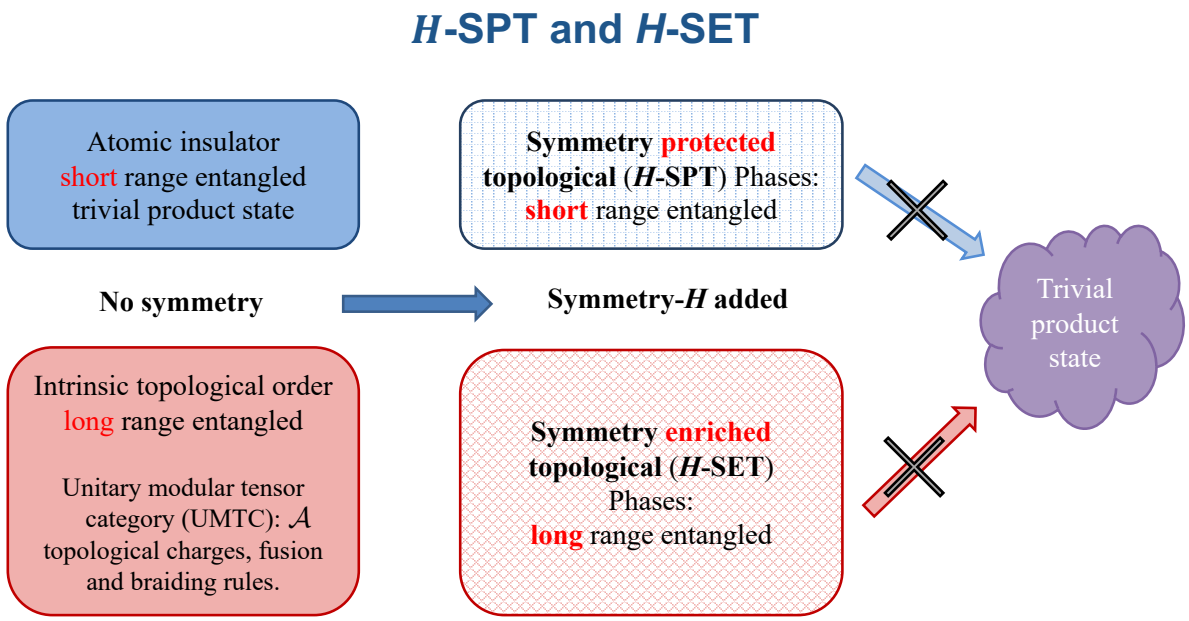

Figure 1.2: Relation between intrinsic topological order, symmetry-H protected topological order, and symmetry-H enriched topological order.

perturbation. For Chern insulator, the topological invariant is called Chern number, which is directly associated with the quantization of Hall conductance σ_{xy} and the number of gapless edge modes of the system.

In this section, following Ref. [81, 105, 37], we give a brief introduction on Chern insulators. We first give a definition of Chern number of a two spatial dimensional two level system with periodic boundary condition in Sec. [1.3.1]. Then we consider the Chern number for a continuous 2D massive Dirac fermion in Sec. [1.3.2]. We briefly introduce the symmetries analysis for Chern insualtor in Sec. [1.3.4]. We discuss the edge states and bulk edge correspondence in Sec. [1.3.5].

1.3.1 Chern number for a two bands model in 2D periodic system

Consider a two bands model captured by the following Hamiltonian,

$$\mathcal{H}(\boldsymbol{k}) = \boldsymbol{h}(\boldsymbol{k}) \cdot \boldsymbol{\sigma}. \tag{1.6}$$

Here $\boldsymbol{\sigma} = (\sigma_x, \sigma_y, \sigma_z)$ are Pauli matrices, and $\boldsymbol{h}(\boldsymbol{k})$ is a three component vector defined as $\boldsymbol{h}(\boldsymbol{k}) \equiv (h_x(\boldsymbol{k}), h_y(\boldsymbol{k}), h_z(\boldsymbol{k}))$ which is a function of momentum in two spatial dimension

another topological order $\mathcal{D}$ as its inverse, such that stacking $\mathcal{C}$ and $\mathcal{D}$ on top of each other gives us a gpped state that has no topological order, i.e., belongs to the phase of product states [275].

$\boldsymbol{k} = (k_x, k_y)$. In the presence of periodic boundary condition, the momentum $\boldsymbol{k}$ lives on the 2D Brillouin Zone. The two-level system Eq. [1.6] has two eigenstates. The eigenstates and eigenvalues are given by:

$$\mathcal{H}\left|u_+\right\rangle = h_0\left|u_+\right\rangle, \quad \mathcal{H}\left|u_-\right\rangle = h_0\left|u_-\right\rangle, \tag{1.7}$$

where h_0 is defined as:

$$h_0(\boldsymbol{k}) = \sqrt{h_x^2(\boldsymbol{k}) + h_y^2(\boldsymbol{k}) + h_z^2(\boldsymbol{k})}. \tag{1.8}$$

One can define the Berry connection in momentum space as:

$$\mathcal{A}_l^{\pm}(\boldsymbol{k}) = i\left\langle u_\pm\right|\partial_{k_l}\left|u_\pm\right\rangle, \tag{1.9}$$

and so as the Berry curvature:

$$\mathcal{F}^{\pm}(\boldsymbol{k}) = \vec{\nabla}\times\vec{\mathcal{A}}^{\pm}(\boldsymbol{k}). \tag{1.10}$$

Below we provide an elegant way to write out Berry curvature Eq. [1.10] explicitly [37]. First, we note that the Berry connections in momentum space can be written in terms of the derivative of h_α, where $\alpha = x, y, z$:

$$\mathcal{A}_l^{\pm}(\boldsymbol{k}) = i\left\langle u_\pm\right|\partial_{k_l}\left|u_\pm\right\rangle = \frac{\partial h_\alpha}{\partial k_l}[i\left\langle u_\pm\right|\partial_{h_\alpha}\left|u_\pm\right\rangle], \tag{1.11}$$

where we have used the Einstein notation that repeated greek indices stands for summation. We can further define the Berry connection in h_α space as: $\tilde{\mathcal{A}}_\alpha^{\pm}(\boldsymbol{h}) = i\left\langle u_\pm\right|\partial_{h_\alpha}\left|u_\pm\right\rangle$, such that $\mathcal{A}_l^{\pm}(\boldsymbol{k}) = (\partial h_\alpha/\partial k_l)\tilde{\mathcal{A}}_\alpha^{\pm}(\boldsymbol{h})$. We further have the z-component of Berry curvature given by:

$$\begin{aligned}\mathcal{F}_z^{\pm}(\boldsymbol{k}) &= \frac{\partial \mathcal{A}_y^{\pm}}{\partial k_x} - \frac{\partial \mathcal{A}_x^{\pm}}{\partial k_y} = \frac{\partial}{\partial k_x}\left(\frac{\partial h_\beta}{\partial k_y}\tilde{\mathcal{A}}_\beta^{\pm}\right) - \frac{\partial}{\partial k_y}\left(\frac{\partial h_\alpha}{\partial k_x}\tilde{\mathcal{A}}_\alpha^{\pm}\right) \\ &= \frac{\partial h_\alpha}{\partial k_x}\frac{\partial h_\beta}{\partial k_y}\left(\frac{\partial \tilde{\mathcal{A}}_\beta^{\pm}}{\partial h_\alpha} - \frac{\partial \tilde{\mathcal{A}}_\alpha^{\pm}}{\partial h_\beta}\right) = \frac{\partial h_\alpha}{\partial k_x}\frac{\partial h_\beta}{\partial k_y}\epsilon_{\alpha\beta\gamma}f_\gamma^{\pm},\end{aligned} \tag{1.12}$$

where $f_\pm^\gamma = \mp h_\gamma/2h_0^3$. Then we have the simpler form of the z-component of Berry curvature reads:

$$\mathcal{F}_z^{\pm}(\boldsymbol{k}) = \mp\frac{1}{2h_0^3(\boldsymbol{k})}\boldsymbol{h}(\boldsymbol{k})\cdot\left(\frac{\partial \boldsymbol{h}(\boldsymbol{k})}{\partial k_x}\times\frac{\partial \boldsymbol{h}(\boldsymbol{k})}{\partial k_y}\right). \tag{1.13}$$

The Chern number for the upper and lower subband is defined as:

$$\mathcal{C}^{\pm} = \frac{1}{2\pi}\int[d^2\boldsymbol{k}]\mathcal{F}_z^{\pm}(\boldsymbol{k}). \tag{1.14}$$

One can rewrite Eq. [1.14] in the following way:

$$\mathcal{C}^{\pm} = \mp\frac{1}{4\pi}\int\frac{1}{h_0^2(\boldsymbol{k})}\underbrace{\frac{\boldsymbol{h}(\boldsymbol{k})}{h_0(\boldsymbol{k})}}_{\hat{\boldsymbol{h}}(\boldsymbol{k})}\cdot\underbrace{\left[\left(\frac{\partial \boldsymbol{h}(\boldsymbol{k})}{\partial k_x}dk_x\right)\times\left(\frac{\partial \boldsymbol{h}(\boldsymbol{k})}{\partial k_y}dk_y\right)\right]}_{d^2\boldsymbol{S}}. \tag{1.15}$$

In the integrand, the term $\hat{\boldsymbol{h}}(\boldsymbol{k})$ denotes the unit vector along the radius direction, and the $\hat{\boldsymbol{h}}(\boldsymbol{k}) \cdot d^2\boldsymbol{S}$ is the area on the $\boldsymbol{h}$- surface. After being divided by $h_0^2(\boldsymbol{k})$, it becomes the solid angle $d\Omega$ extended by the area. This solid angle $d\Omega$ is equal to the area of $\hat{\boldsymbol{h}}(\boldsymbol{k}) \cdot d^2\boldsymbol{S}$ projected on a two sphere S^2 with unit radius. The $\boldsymbol{k}$- vector lives on the torus of 2D Brillouin zone, $\boldsymbol{k} \in T^2$. The function $\boldsymbol{h}(\boldsymbol{k})$ defines a continuous map from a torus T^2 of Brillouin Zone to a closed surface in $\boldsymbol{h}$-space, the later of which can be further mapped to a two sphere S^2 mentioned before. The Chern number actually compute how much solid angle is sweeped by $\boldsymbol{h}(\boldsymbol{k})$ when $\boldsymbol{k}$ run through the torus of Brillouin Zone. This mapping from the torus T^2 to the two-sphere S^2 is captued by the second homotopy group $\pi_2(T^2) = \mathbb{Z}$. Thus when the integral of Eq. [1.15] is performed through the whole Brillouin Zone, the Chern number must be a quantized integer. Furthermore, from linear response or semi-classical equation [81, 24], the conductivity σ_{xy} is associated with the Chern number of the filled band. If Eq. [1.6] is gapped, then the σ_{xy} reads:

$$\sigma_{xy} = \frac{e^2}{h}\mathcal{C}^-. \tag{1.16}$$

1.3.2 Chern number for massive Dirac fermion in 2D continuous system

A massive Dirac fermion in two spatial dimension is given by taking $h_x(\boldsymbol{k}) = k_x$, $h_y(\boldsymbol{k}) = k_y$, and $h_z(\boldsymbol{k}) = m$ in Eq. [1.6]. Substitute this into Eq. [1.13], we have the Berry curvature for the lower subband of massive Dirac fermion reads [105]:

$$\mathcal{F}_z^-(\boldsymbol{k}) = \frac{m}{2(k_x^2 + k_y^2 + m^2)^{3/2}}. \tag{1.17}$$

By pulgging this into the Eq. [1.14], one can have:

$$\mathcal{C}^- = \int [d^2\boldsymbol{k}]\mathcal{F}_z^-(\boldsymbol{k}) = \int_0^\infty dk k \frac{1}{2}\frac{m}{(k^2 + m^2)^{3/2}} = \frac{\text{sign}(m)}{2}. \tag{1.18}$$

The Chern number calculated here is non-quantized. This is because the Dirac fermion we discussed here is a continuum model where the integral over all momenta extends over the whole $\mathbb{R}^2$ instead of a torus T^2 in Sec. [1.3.1], and therefore no reason to expect the Chern number to be quantized. In fact, as we will see in the next section, the Dirac Hamiltonian can arise from the low-energy expansion around high-symmetry points in the Brillouin Zone of certain lattice model. For the full lattice, the $k \to \infty$ integral would be regularized due to the Brillouin Zone boundary, and the whole system would has a quanzied Hall conductvitiy. However, the region close to the "Dirac-pint" contributes $\pm 1/2$ to the Chern number.

This result from Eq. [1.18] can be further generalized as following [105]:

$$\mathcal{H}(\boldsymbol{k}) = \sum_{i,j}^{2} B_{ij} k_i \sigma_j + m\sigma_z, \tag{1.19}$$

we have the conductvity reads:

$$\mathcal{C}^- = \frac{1}{2}\text{sign}(m)\text{sign}(\det B). \tag{1.20}$$

A gap closure process (i.e. m change sign) will lead to the change of Chern number for the Dirac fermion by 1.

1.3.3 Chern insulator and quantum anomalous Hall effect

The topological future of Chern insulator can be intrinsically imbedded in the Berry curvature of the Bloch band. In this section, we introduce one of the simplest two-dimensional lattice model proposed by Qi, Wu and Zhang (QWZ model) [201, 105]. The Hamiltonian for the QWZ model is given by the following:

$$H_{\text{QWZ}} = \begin{pmatrix} c^\dagger_{k,A} & c^\dagger_{k,B} \end{pmatrix} \mathcal{H}_0(k_x, k_y) \begin{pmatrix} c_{k,A} \\ c_{k,B} \end{pmatrix} \tag{1.21}$$

where the Bloch Hamiltonian is a function of Bloch momentum (k_x, k_y) and $c^\dagger_{k,A(B)}$ stands for the creation operator for a Bloch electron at momentum k at sublattice $A(B)$:

$$\mathcal{H}_0(k_x, k_y) = \sin(k_x)\sigma_x + \sin(k_y)\sigma_y + [2 - m - \cos(k_x) - \cos(k_y)]\sigma_z. \tag{1.22}$$

The Chern number for the lower subband of Eq. [1.22] can be understood by the following [37, 81, 105]:

- $-\infty < m < 0$: Eq. [1.13] reaches to the atomic insulator limit that all the eigenstates are localized on single site. The system should have no Hall conductance such that $\sigma_{xy} = 0$ and $\mathcal{C}^- = 0$. This can be verified by direct substitute this into Eq. [1.14].

- $0 < m < 2$: there is a gap closure process happend at $\boldsymbol{k} = 0$ at $m = 0$ when m goes from $-\infty$. One can expand the Hamiltonian around $k_x = k_y = 0$ as $\mathcal{H}_0 = k_x\sigma_x + k_y\sigma_y - m\sigma_z$. Therefore, the change of Chern number as $\Delta\mathcal{C}^- = \frac{1}{2}\text{sign}(-m)|_{m>0} - \frac{1}{2}\text{sign}(-m)|_{m<0} = -1$. As the Chern number for $m < 0$ is 0, we conclude that the Chern number for $0 < m < 2$ as $\mathcal{C}^- = -1$.

- $2 < m < 4$: at $m = 2$ the gap close at $(\pi, 0)$ and $(0, \pi)$, and we can expand the Hamiltonian around these points: $\mathcal{H}_{(\pi,0)} = k_x\sigma_x - k_y\sigma_y + (2 - m)\sigma_z$ and $\mathcal{H}_{(0,\pi)} = -k_x\sigma_x + k_y\sigma_y + (2 - m)\sigma_z$. From this we can get the change in Chern number: $\mathcal{C}^- = -2\times[\frac{1}{2}\text{sign}(2-m)|_{m>2} - \frac{1}{2}\text{sign}(2-m)|_{m<2}] = 2$. Since the Chern number for $0 < m < 2$ is -1, we conclude the Chern number for $2 < m < 4$ as $\mathcal{C}^- = +1$.

- $4 < m < +\infty$: at $m = 4$, the gap-closing happens at (π, π), around which we have: $\mathcal{H}_{(\pi,\pi)} = -k_x\sigma_x - k_y\sigma_y + (4 - m)\sigma_z$. We have the change of Chern number as $\Delta\mathcal{C}^- = \frac{1}{2}\text{sign}(4-m)|_{m>4} - \frac{1}{2}(4-m)|_{m<4} = -1$. Since the Chern number for $2 < m < 4$ is $+1$, we conclude the Chern number at $m > 4$ is 0. This is in accordance with the fact that when $m \to +\infty$ the system goes to the trvial atomic insulator limit.

Phase diagram for Chern number of Chern insulator as a parameter of m is shown in Fig. [1.3].

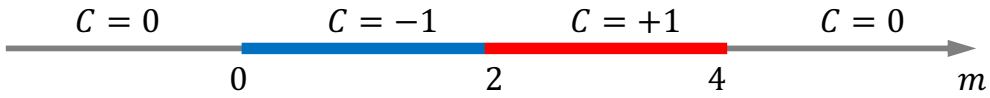

Figure 1.3: Phase diagram for Chern number of Chern insulator as a parameter of m.

1.3.4 Symmetries and classification, ten fold way

Below we listed three non-spaital symmetries: time-reversal, particle-hole and chiral symmetries, as well as how they act in momentum space of the single particle Bloch Hamiltonian $\mathcal{H}(\boldsymbol{k})$ [49, 81]:

1. Time reversal symmetry T is an anti-unitary symmetry which commutes with Bloch Hamiltonian:
$$T\mathcal{H}(\boldsymbol{k})T^{-1} = \mathcal{H}(-\boldsymbol{k}), \quad T = U_T\mathcal{K}, \quad T^2 = \pm 1, \tag{1.23}$$
where $\mathcal{K}$ is the operator for complex conjugation and U_T is a unitary matrix.

2. Particle-hole symmetry C is an anti-unitary symmetry which anti-commutes with Bloch Hamiltonian:
$$C\mathcal{H}(\boldsymbol{k})C^{-1} = -\mathcal{H}(-\boldsymbol{k}), \quad C = U_C\mathcal{K}, \quad C^2 = \pm 1, \tag{1.24}$$
where $\mathcal{K}$ is the operator for complex conjugation and U_C is a unitary matrix.

3. Chiral symmetry S is a unitary symmetry which anti-commutes with Bloch Hamiltonian:
$$S\mathcal{H}(\boldsymbol{k})S^{-1} = -\mathcal{H}(\boldsymbol{k}), \quad S = U_S, \quad S^2 = 1, \tag{1.25}$$
where U_S is a unitary matrix.

All of the different possible combinations of the presence or absence of these symmetries leads us to 10 different possibilities, as given in Table. [1.2]. Each row in Table. [1.2] tells how different insulators with the same symmetry are classified by topological invariants. Gapped phases that can be smoothly connected to each other via tunning the parameter are in the same topological phase. One can check the Chern insulator given by QWZ model Eq. [1.21] does not have any of aforementioned three symmetries, thus it falls into A-class. In 2-spatial dimension, the A class has a $\mathbb{Z}$ classification, in accordance to the integer value of Chern number in Chern insulators.

Symmetry				Dimension								
AZ	T^2	C^2	S^2	0	1	2	3	4	5	6	7	8
A	0	0	0	$\mathbb{Z}$	0	$\mathbb{Z}$	0	$\mathbb{Z}$	0	$\mathbb{Z}$	0	$\mathbb{Z}$
AIII	0	0	1	0	$\mathbb{Z}$	0	$\mathbb{Z}$	0	$\mathbb{Z}$	0	$\mathbb{Z}$	0
AI	1	0	0	$\mathbb{Z}$	0	0	0	$\mathbb{Z}$	0	$\mathbb{Z}_2$	$\mathbb{Z}_2$	$\mathbb{Z}$
BDI	1	1	1	$\mathbb{Z}_2$	$\mathbb{Z}$	0	0	0	$\mathbb{Z}$	0	$\mathbb{Z}_2$	$\mathbb{Z}_2$
D	0	1	0	$\mathbb{Z}_2$	$\mathbb{Z}_2$	$\mathbb{Z}$	0	0	0	$\mathbb{Z}$	0	$\mathbb{Z}_2$
DIII	-1	1	1	0	$\mathbb{Z}_2$	$\mathbb{Z}_2$	$\mathbb{Z}$	0	0	0	$\mathbb{Z}$	0
AII	-1	0	0	$\mathbb{Z}$	0	$\mathbb{Z}_2$	$\mathbb{Z}_2$	$\mathbb{Z}$	0	0	0	$\mathbb{Z}$
CII	-1	-1	1	0	$\mathbb{Z}$	0	$\mathbb{Z}_2$	$\mathbb{Z}_2$	$\mathbb{Z}$	0	0	0
C	0	-1	0	0	0	$\mathbb{Z}$	0	$\mathbb{Z}_2$	$\mathbb{Z}_2$	$\mathbb{Z}$	0	0
CI	1	-1	1	0	0	0	$\mathbb{Z}$	0	$\mathbb{Z}_2$	$\mathbb{Z}_2$	$\mathbb{Z}$	0

Table 1.2: Periodic table of topological insulators and superconductors. The leftmost column (A,AIII,...,CI) denotes the ten symmetry classes of fermionic Hamiltonian, which are characterized by the presence or absence of time reversal (T), particle-hole (C), and chiral (S) symmetries of different types denoted by ± 1. This table is taken from Ref. [49, 174].

1.3.5 Bulk edge correspondence and edge states

A central feature of topological insulators (TI) is the bulk-edge correspondence: a d-dimensional TI with given symmetries has a bulk energy gap but symmetry protected gapless $d-1$ dimensional boundary excitations. Heuristically, to go from the phase with one topological index to another phase with different topological index, the spatially dependent energy gap needs to close near the interface in otder to make the topology to change.

Let's take the QWZ model as an simple example [37, 201]. For simplicity, expanding the Hamiltonian around $(0,0)$ gives the following low energy Hamiltonian for a spatial varying massive Dirac fermion:

$$\mathcal{H}_D = \hbar v_F k_x \sigma_x + \hbar v_F k_y \sigma_y + m(x)\sigma_z. \tag{1.26}$$

Note that we have restore the dimension in the above Hamiltonian. The term v_F is the fermi velocity, and $\hbar$ is the Planckian constant. The mass term $m(x)$ now has the dimension of energy. We further assume that mass term $m(x)$ take the following profile x goes from $-\infty$ to $+\infty$:

$$m(x) \begin{cases} > 0 \text{ for } x > 0, \\ < 0 \text{ for } x < 0, \end{cases} \tag{1.27}$$

The exact profile of $m(x)$ does not matter, as long as it is monotonic and smooth compared to the electron wavelength. Further, we keep translational invariant along y-direction. This describes a 1D boundary along the y-axis. This set up is shown in Fig. [1.4].

Transforming Hamiltonian Eq. [1.26] into real space:

$$\mathcal{H}_D(x,y) = -i\hbar v_F \partial_x \sigma_x - i\hbar v_F \partial_y \sigma_y + m(x)\sigma_z, \tag{1.28}$$

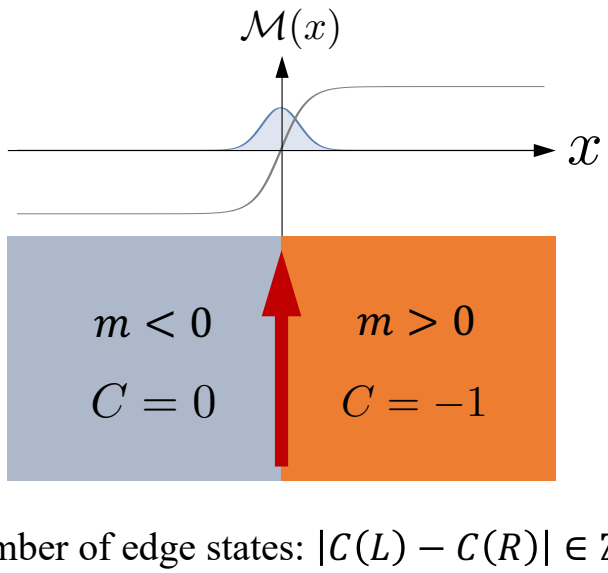

Figure 1.4: Boundary of a Chern insulator and the corresponding edge state.

we now would like to solve the differential equation:

$$\mathcal{H}(x,y)\phi(x,y) = \mathcal{E}\phi(x,y). \tag{1.29}$$

To do so, we first factorize the ansatz of wave function as:

$$\phi(x,y) = \phi_1(x)\phi_2(y). \tag{1.30}$$

Since the y-direction is translationally invariant, we can take the ansatz as a plane wave $\phi_2(y) = e^{ik_y y}$. Therefore, the equation for $\phi_1(x) = (f(x), g(x))^T$ reads:

$$\begin{pmatrix} m(x) & -i\hbar v_F\left(\frac{\partial}{\partial x} + k_y\right) \\ -i\hbar v_F\left(\frac{\partial}{\partial x} - k_y\right) & -m(x) \end{pmatrix} \begin{pmatrix} f(x) \\ g(x) \end{pmatrix} = \mathcal{E}(k_y) \begin{pmatrix} f(x) \\ g(x) \end{pmatrix}. \tag{1.31}$$

Eliminating $g(x)$ from the coupled equations, one can get:

$$-(\hbar v_F)^2\left(\frac{\partial^2}{\partial x^2} - k_y^2\right) f(x) = (\mathcal{E}^2 - m^2) f(x). \tag{1.32}$$

We have assumed that $m(x)$ varies slowly so that $\partial m(x)/\partial x$ can be neglected. One can find that the Eq. [1.32] has the following normalizable solution:

$$f(x) = e^{-\frac{1}{\hbar v_F}\int_0^x dx' m(x')}, \quad \mathcal{E}(k_y) = \hbar v_F k_y. \tag{1.33}$$

Thus we find a solution of the system with the wave function

$$\phi_1(x) = e^{-\frac{1}{\hbar v_F}\int_0^x dx' m(x')} \begin{pmatrix} 1 \\ i \end{pmatrix}, \tag{1.34}$$

which is localized near the $x = 0$. One can show that the localization length is inversely propotional to the bulk gap of the Chern isnualtor. This is the so called edge states, whose dispersion is $\mathcal{E}(k_y) = \hbar v_F k_y$. This edge mode travels ballistically upwards on $x = 0$ in Fig. [1.4] at the group velocity v_F. It provides the non-zero Hall conductivity of the system.

On the other hand, if

$$m(x) \begin{cases} > 0 \text{ for } x < 0, \\ < 0 \text{ for } x > 0, \end{cases} \tag{1.35}$$

then we have the normalizable solution for:

$$\phi_1(x) = e^{\frac{1}{\hbar v_F}\int_0^x dx' m(x')} \begin{pmatrix} 1 \\ -i \end{pmatrix}, \tag{1.36}$$

is a localized eigenstate with $\mathcal{E}(k_y) = -\hbar v_F k_y$. Physically, this means that if the mass profile changes from positive to negative when x goes from $-\infty$ to ∞, the edge mode at $x = 0$ will move in the opposite direction (downward in Fig. [1.4]).

1.4 Introduction to group cohomology

In this section, we give a short introduction to group cohomology [179], which will be frequently used in the part for SPT and SET.

1.4.1 Cochain, cocycle and coboundary

The input data for group cohomology is a group G (Abelian or non-Abelian) and an Abelian group $\mathcal{A}$ equipped with an action of G: $G \times \mathcal{A} \to \mathcal{A}$, $g \times \mathsf{a} \mapsto g.\mathsf{a}$. Equivalently, the G action on $\mathcal{A}$ defines a map ρ: $G \to \mathrm{Aut}(\mathcal{A})$ from G to the automorphism group of $\mathcal{A}$. Consider n-argument functions $\omega(g_1, g_2, \cdots, g_n) \in \mathcal{A}$ that maps an n tuple of group elements in G to the Abelian group $\mathcal{A}$

$$\omega : \underbrace{G \times G \times \cdots \times G}_{n \text{ times}} \to \mathcal{A}. \tag{1.37}$$

Such a group function is called an n-cochain. The set of all n-cochains, which we denote by $C^n(G, \mathcal{A})$, forms an Abelian group under group multiplication in $\mathcal{A}$

$$(\omega_1 \cdot \omega_2)(g_1, \cdots, g_n) = \omega_1(g_1, \cdots, g_n) \cdot \omega_2(g_1, \cdots, g_n). \tag{1.38}$$

here we define the identity n-cochain to be the trivial group function whose value is always the identity in $\mathcal{A}$. One can define a map ∂: $C^n(G, \mathcal{A}) \to C^{n+1}(G, \mathcal{A})$, $\omega \mapsto \partial\omega$ by

$$\begin{aligned} &\partial\omega(g_1, \cdots, g_{n+1}) = \\ &\quad [g_1 \,.\, \omega(g_2, \cdots, g_{n+1})] \cdot \omega^{(-1)^{n+1}}(g_1, \cdots, g_n) \\ &\quad \times \prod \omega^{(-1)^i}(g_1, \cdots, g_{i-1}, g_i \cdot g_{i+1}, g_{i+2}, \cdots, g_{n+1}), \end{aligned} \tag{1.39}$$

where the symbol $g_1 \,.\, \omega(g_2, \cdots, g_{n+1})$ denotes the action of the group element g_1 on the function ω, inherited from the action of G on $\mathcal{A}$.

One can check that (1) $\partial^2\omega := \partial(\partial\omega) = I$, where I denotes the identity $(n+2)$-cochain, (2) for two n-cochains, ω_1, ω_2, $\partial(\omega_1 \cdot \omega_2) = (\partial\omega_1) \cdot (\partial\omega_2)$.

An n-cochain $\omega(g_1, \cdots, g_n)$ is called an n-cocycle if and only if it is mapped to the trivial elemenet under the map ∂, i.e. $\partial\omega = I$. The set of all n-cocycles, denoted by $Z^n(G, \mathcal{A})$ is a subgroup of $C^n(G, \mathcal{A})$.

Since ∂^2 maps every cochain to the trivial one, any $(n-1)$-cochain $c(g_1, \cdots, g_{n-1})$, defines an n-cocycle ∂c. If an n-cocycle b can be represented as $b = \partial c$ for some $c \in C^{n-1}(G, \mathcal{A})$, b is called an n-coboundary. The set of all n-coboundaries is a subgroup of $Z^n(G, \mathcal{A})$, which we denote by $B^n(G, \mathcal{A})$. Two n-cocycles ω_1, ω_2 are equivalent (denoted by $\omega_1 \sim \omega_2$) if and only if they differ by an n-coboundary: $\omega_1 = \omega_2 \cdot b$, where $b \in B^n(G, \mathcal{A})$.

The nth cohomology group of a group G with coefficients in $\mathcal{A}$, $\mathcal{H}^n(G, \mathcal{A})$, is formed by the equivalence classes in $Z^n(G, \mathcal{A})$ (i.e. up to $B^n(G, \mathcal{A})$). More precisely, we have:

$$\mathcal{H}^n_\rho(G, \mathcal{A}) = \frac{Z^n(G, \mathcal{A})}{B^n(G, \mathcal{A})}. \tag{1.40}$$

Here the subscript ρ in the cohomology group is a reminder of the group action $\rho\colon G \to \mathrm{Aut}(\mathcal{A})$.

For concreteness, we give the expression for the first and second group cohomology:

$$\mathcal{H}^1_\rho(G, \mathcal{A}) = \frac{Z^1(G, \mathcal{A})}{B^1(G, \mathcal{A})} = \frac{\{d\colon G \to \mathcal{A} | d(\mathrm{id}) = \mathsf{0}, d(gh) = g.d(h) + d(g)\ \forall g, h \in G\}}{\{d_0\colon G \to \mathcal{A} | d_0(g) = g.\mathsf{a} - \mathsf{a} \text{ for some } \mathsf{a} \in \mathcal{A}\}}. \tag{1.41}$$

$$\begin{aligned}\mathcal{H}^2_\rho(G, \mathcal{A}) &= \frac{Z^2(G, \mathcal{A})}{B^2(G, \mathcal{A})} \\ &= \frac{\{\omega\colon G\times G \to \mathcal{A} | \omega(1, g_1) = \omega(g_1, 1) = 0, \omega(g_1, g_2) + \omega(g_1 g_2, g_3) = g_1.\omega(g_2, g_3) + \omega(g_1, g_2 g_3), \forall g_1, g_2, g_3 \in G\}}{\{\omega\colon G\times G \to \mathcal{A} | \omega(g_1, g_2) = g_1.d(g_2) - d(g_1 g_2) + d(g_1) \text{ for some } d\colon G \to \mathcal{A} \text{ with } d(1) = 0\}}.\end{aligned} \tag{1.42}$$

We note that the Abelian group $\mathcal{A}$ can be either finite (such as $\mathbb{Z}_2$), discrete infinite (such as $\mathbb{Z}$) or continuous (such as $U(1)$). The group G can also in principle be finite, discrete or continuous (the continuous case may be treated with additional caution), and in this work we will mostly work with a discrete group G.

Finially, note that one can directly search for all the solutions to Eqs. (1.41) and (1.42) by implementing them in a computer program, and this is the method we used for computing the cohomology of dihedral and quaternion groups. This method is quite elementary, brutal force in nature, but works well for any finite group G with small order and finite Abelian group $\mathcal{A}$, and can provides the most complete data.

1.4.2 Künneth Formula

When the group G acts trivially on the coefficient $\mathcal{A}$, a useful decomposition formula for $\mathcal{H}^n(G,\mathcal{A})$ exists for those G that have a direct product form $G = G_1 \times G_2$, namely the Künneth formula:

$$\mathcal{H}^n(G,\mathcal{A}) = \sum_{k=0}^{n} \mathcal{H}^n(G_1, \mathcal{H}^{n-k}(G_2,\mathcal{A})), \tag{1.43}$$

this says that the nth cohomology group of G can be obtained from the cohomology groups of G_1 and G_2 in lower degree, but in a "nested" fashion. Note that here we allow the coefficient $\mathcal{A}$ to be either $U(1)$, which appears in the classification of bosonic SPT (in $d = n-1$ spatial dimensions), or a finite Abelian group, which appears in symmetry fractionalization of SET ($n = 2$).

In the case of SPT phases with a $U(1)$ coefficient, this formula implies that SPT phases with G symmetry in d spatial dimension can be constructed from SPT phases with G_1 symmetry and G_2 symmetry in lower dimensions. Specifically, the $k = 0$ term in the formula reads:

$$\mathcal{H}^0(G_1, \mathcal{H}^{d+1}(G_2, U(1))) = \mathcal{H}^{d+1}(G_2, U(1)), \tag{1.44}$$

physically, this means that some SPT phases with symmetry G in d dimension are identified with SPT phases with a subgroup symmetry G_2 in d dimension. The $k = n$ term admits a similar meaning for the subgroup G_1.

In the special case of $\mathcal{A} = \mathbb{Z}_2$, the summands in the Künneth formula can be further decomposed into tensor product of groups, and we have [207]:

$$\mathcal{H}^n_{\text{id}}(G_1 \times G_2, \mathbb{Z}_2) = \bigoplus_{p+q=n} \Big(\mathcal{H}^p_{\text{id}}(G_1,\mathbb{Z}_2) \otimes \mathcal{H}^q_{\text{id}}(G_2,\mathbb{Z}_2) \Big). \tag{1.45}$$

1.5 Outline of the thesis and previous publications

Portion of the content presented in this thesis is adapted from previously published works by the author of this dissertation. The rest of this thesis is organized as following:

- In Chapter 2, we start from a phenomenological model of interplay between topology orders and symmetry breaking. We study the domain wall structure in chiral spin liquids with domains of opposite chiralities. Based on a standard model, we obtain a spatially varying, self-consistent mean-field solution for the spinons that describes both the gapless edge modes and the change of chirality at the domain wall. We further derive the non-universal properties, such as the velocity of the topologically protected domain wall edge states and its modification to domain wall tension. Our approach provides the first systematic study of the interplay between topological order and symmetry-breaking physics, and can be applied to many other systems. This part is based on arXiv:2208.14056 (Ref. [265]), and is done in collaboration with Chunxiao Liu and Joel E. Moore.

- In Chapter 3, we make the attempt to study the interplay between topological orders from a more formal point of view. We consider two-dimensional topologically ordered systems with coexisting long-range orders, where the only gapless excitations in the spectrum are Goldstone modes of spontaneously broken continuous symmetries. We show that the universal properties of point defects and textures are determined by the remnant symmetry enriched topological order in the symmetry-breaking ground state with non-fluctuating order parameters, and provide a classification for their properties using algebraic topology. Our work serves as a first step towards a complete classification and characterization of quantum phases with both long-range classical orders and topological orders. This part is based on arXiv:2211.13207 (Ref. [264]), and is done in collaboration with Chunxiao Liu and Yuan-Ming Lu.

- In Chapter 4, we propose a mechanism and an explicit model to realize the linear-in-temperature resistivity that is the hallmark of bad metals, then verify the behavior with advanced DMRG-type simulations. Our work gives a means to test the existence of limits on how rapidly currents can be dissipated. What is more, this type of quantum dynamics can happen at the domain wall of topological orders, where particle-hole scattering leads to linear-in-temperature resistivity of edge modes. This part is based on Phys. Rev. B 107, L100301 (Ref. [267]), and is done in collaboration with Roman Rausch, Christoph Karrasch, and Joel E. Moore.

- In Chapter 5, we introduce an effective edge network theory to characterize the boundary topology of coupled edge states generated from various types of topological insulators. Two examples studied are a two-dimensional second-order topological insulator and three-dimensional topological fullerenes, which involve multi-leg junctions. As a consequence of bulk-edge correspondence, these edge networks can faithfully predict properties such as the energy and fractional charge related to the bound states (edge solitons) in the aforementioned systems, including several aspects that were previously complicated or obscure. This part is based on Phys. Rev. B 99, 155102 (Ref. [266]), and is done in collaboration with Joel E. Moore.

Chapter 2

Structure of domain walls in chiral spin liquids

A chiral spin liquid (CSL) is a long-range-entangled spin liquid ground state, which, despite the absence of conventional magnetic order, spontaneously breaks time-reversal symmetry and develops a chiral order [273, 64, 271, 115, 116, 9, 16, 170, 94, 93, 76, 92, 28, 282, 77, 99, 98, 189, 46, 219]. The prototypical example is the Kalmeyer–Laughlin (KL) CSL [115, 116]: as a spin system analog of the $\nu = 1/2$ bosonic fractional quantum Hall state [270], it hosts both spin-1/2 anyonic quasiparticles (spinons) in the bulk [86] and chiral gapless modes on the edge [268]. The universal bulk physics of the KL CSL is captured by the Chern–Simons (CS) effective theory. Many model systems are found to support such a state [250, 191, 73, 79]; some of them are explicitly time-reversal invariant [241, 296, 302, 50, 38, 250, 191, 73, 79] and host degenerate chiral ground states and possibly domains of either chiralities; variation in domain size between samples could explain the variable thermal conductivities reported in some spin liquid candidates [241].

While the CS theory contains the full topological data of the bulk, it does not capture the symmetry-breaking properties of a CSL, nor some of the non-universal but experimentally important features of the system. For one thing, the CS theory provides little information about the details of the quasiparticle energetic structure. It is well known that the CS term is not gauge invariant in a system with boundary, and a gapless edge mode must exist at the boundary to restore the gauge invariance [34, 36, 176]. The velocity of such an edge mode enters the CS term as an effective parameter [278, 164, 163, 152, 118], which, in a quantum Hall fluid, would be determined externally by the electric and magnetic fields at the edge. In a CSL, however, there is no established way to determine the edge current velocity in terms of the fundamental data of the CSL.

A more interesting, yet less explored, scenario occurs when a CSL contains multiple domains. In this case, an interface of two domains with opposite chiralities hosts gapless mode with a total chiral current carrying spin $S = 2$ [271, 273, 64]. The chiral order parameter across the interface is determined *self-consistently* to minimize the total energy of the multiple domain system, and its spatial profile reveals many system-dependent properties of

CSLs. Previously, the self-consistent mean-field theory has been widely applied to the study of homogeneous quantum spin liquid systems [271, 269]. The solution, called a mean-field ansatz, provides a convenient description for the bulk spinons in a quantum spin liquid state. It is thus desirable to develop a microscopic theory to capture both bulk and domain wall physics of CSLs, and the self-consistent mean-field theory, building on its previous successes, can be adapted to provide valuable insight into this problem.

In this chpater, we study the domain wall structure in CSLs with domains of opposite chiralities. Based on a standard model [271], we obtain a spatially varying, self-consistent mean-field solution for the spinons that describes both the gapless edge modes and the change of chirality at the domain wall. We complement the numerics by an effective field theory analysis for the mean-field bond amplitude fluctuations, and analytically solve the domain wall profile within the conventional Ising domain wall theory. By modeling the low energy theory for spinons as Dirac fermions with spatially varying mass term, the velocity of the topologically protected domain wall edge states can be accessed through the Jackiw-Rebbi mechanism. We further find that, while the conventional Ising (i.e., ϕ^4) theory shows approximate agreement with the numerics in terms of the domain wall profile, the gapless modes at the edge should in principle contribute an extra, non-analytic, $|\phi^3|$ term to the theory, and indeed such a term appears in derivatives of the bulk energy.

2.1 Chiral spin liquid and parton construction

Consider a spin-1/2 model defined on a square lattice, as shown in Fig. [2.1]:

$$H = \sum_{\boldsymbol{ij}} J_{\boldsymbol{ij}} \boldsymbol{S_i} \cdot \boldsymbol{S_j}, \tag{2.1}$$

with antiferromagnetic nearest-neighbor and next-nearest-neighbor coupling $J_1 > J_2 > 0$ [271, 273, 64]. This is one of the canonical models for CSLs and we review the parton self-consistent mean-field treatment here, although naturally a mean-field theory will not predict the energetics of the ground state reliably.

We will use the mean-field approximation to understand its physical properties: let $\boldsymbol{S_i} = \langle \boldsymbol{S_i} \rangle + \delta \boldsymbol{S_i}$, and we obtain the following mean-field Hamiltonian:

$$H_{\text{mean}} = \sum_{\langle \boldsymbol{ij} \rangle} J_{\boldsymbol{ij}} (\langle \boldsymbol{S}_i \rangle \cdot \boldsymbol{S}_j + \boldsymbol{S}_i \cdot \langle \boldsymbol{S_j} \rangle - \langle \boldsymbol{S_i} \rangle \langle \boldsymbol{S}_j \rangle). \tag{2.2}$$

We introduce the fermionic parton operators $f_{\boldsymbol{i}\alpha}$, $\alpha = 1, 2$, defined by

$$\boldsymbol{S_i} = f^\dagger_{\boldsymbol{i}\alpha} \boldsymbol{\sigma}_{\alpha\beta} f_{\boldsymbol{i}\beta}/2, \tag{2.3}$$

with $\boldsymbol{\sigma}$ denotes the three-component vector of Pauli matrices. Physically, these operators describe the spin-1/2 charge-neutral spinon excitations in the CSL phase. Substitute $\boldsymbol{S_i} =$

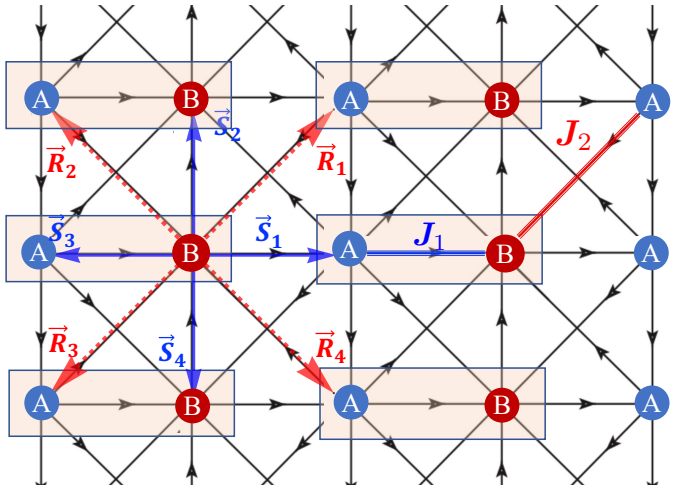

Figure 2.1: Gauge-field conventions for a chiral spin state on a frustrated square lattice $J_1 - J_2$ model [273, 64]. The nearest neighbors are labeled by $\boldsymbol{S}_1 = -\boldsymbol{S}_3 = (a_0, 0)$, $\boldsymbol{S}_2 = -\boldsymbol{S}_4 = (0, a_0)$, and the nearest neighbors are labeled by $\boldsymbol{R}_1 = -\boldsymbol{R}_3 = (a_0, a_0)$, $\boldsymbol{R}_2 = -\boldsymbol{R}_4 = (-a_0, a_0)$, with a_0 the distance between two nearest sites. The black arrows on the links represent a phase of $\pi/2$. Since charge for each electron is $-e$ with $e > 0$, the Pieles substitution reads: $t_{ij} \to t_{ij} e^{+i\frac{q}{\hbar}\int_i^j \boldsymbol{A}\cdot d\boldsymbol{l}} = t_{ij} e^{-i\frac{e}{\hbar}\int_i^j \boldsymbol{A}\cdot d\boldsymbol{l}}$. Thus along the black arrows we get an additional factor $-i$ compared with the hopping in the absence of flux. Introduction of flux breaks the time reversal symmetry for ground state effectively. For each unit cell, there are two sites: A, B.

$f^\dagger_{i\alpha}\boldsymbol{\sigma}_{\alpha\beta} f_{i\beta}/2$ into Eq. (2.1), we arrive at:

$$\begin{aligned} H &= \sum_{\langle ij\rangle} J_{ij}\boldsymbol{S}_i \cdot \boldsymbol{S}_j = \sum_{\langle ij\rangle} \frac{J_{ij}}{4} f^\dagger_{i\alpha}\boldsymbol{\sigma}_{\alpha\beta} f_{i\beta} f^\dagger_{j\alpha'}\boldsymbol{\sigma}_{\alpha'\beta'} f_{j\beta'} \\ &= \sum_{\langle ij\rangle} -\frac{J_{ij}}{2} f^\dagger_{i\alpha} f_{j\alpha} f^\dagger_{j\beta} f_{i\beta} + \sum_{\langle ij\rangle} J_{ij}\left(\frac{1}{2}n_i - \frac{1}{4}n_i n_j\right). \end{aligned} \tag{2.4}$$

Here, we have used $\boldsymbol{\sigma}_{\alpha\beta}\cdot\boldsymbol{\sigma}_{\alpha'\beta'} = 2\delta_{\alpha\beta'}\delta_{\alpha'\beta} - \delta_{\alpha\beta}\delta_{\alpha'\beta'}$ and n_i is the number of fermions at site i. The second term in the second line of Eq. (2.4) is a constant and will be dropped in the following discussions. Notice that the Hilbert space of Eq. (2.4) with four states per site is larger than Eq. (2.1), which has two states per site. The equivalence between Eq. (2.4) and Eq. (2.1) is valid only in the subspace where there is exactly one fermion per site. Therefore, to use Eq. (2.4) to describe the spin state, we need to impose the constraint:

$$f^\dagger_{i\alpha} f_{i\alpha} = f^\dagger_{i1} f_{i1} + f^\dagger_{i2} f_{i2} = 1, \quad f_{i\alpha} f_{i\beta}\epsilon_{\alpha\beta} = f_{i1} f_{i2} + f_{i2} f_{i1} = 0. \tag{2.5}$$

A mean-field ground state at zeroth-order is obtained by making the following two approximations, we first replace Eq. (2.5) by its ground-state average:

$$\langle f^\dagger_{i\alpha} f_{i\alpha}\rangle = 1. \tag{2.6}$$

such a constraint can be enforced by including a site-dependent and time independent Lagrangian multiplier $a_0(\boldsymbol{i})(f^\dagger_{\boldsymbol{i}\alpha}f_{\boldsymbol{i}\alpha}-1)$ in the Hamiltonian. Second, we replace the operator $f^\dagger_{\boldsymbol{i}\alpha}f_{\boldsymbol{j}\alpha}$ by its ground state expectation value $\eta_{\boldsymbol{ij}}$, again ignoring their fluctuations. In this way, we obtain the zeroth-order mean-field Hamiltonian:

$$H_{\text{mean}}=\sum_{\langle \boldsymbol{ij}\rangle}-\frac{1}{2}J_{\boldsymbol{ij}}\left[(f^\dagger_{\boldsymbol{i}\alpha}f_{\boldsymbol{j}\alpha}\eta_{\boldsymbol{ji}}+\text{h.c.})-|\eta_{\boldsymbol{ij}}|^2\right]+\sum_i a_0(\boldsymbol{i})(f^\dagger_{\boldsymbol{i}\alpha}f_{\boldsymbol{i}\alpha}-1). \tag{2.7}$$

The $\eta_{\boldsymbol{ij}}$ in Eq. (2.7) must satisfy the self-consistency condition:

$$\eta_{\boldsymbol{ij}}=\langle f^\dagger_{\boldsymbol{i}\alpha}f_{\boldsymbol{j}\alpha}\rangle, \tag{2.8}$$

and the site-dependent chemical potential $a_0(\boldsymbol{i})$ is chosen such that the Eq. (2.6) is satisfied by the mean-field ground state. We call the pattern of η_{ij} the mean-field ansatz. Then we conduct the iterative process shown in Fig. [2.2].

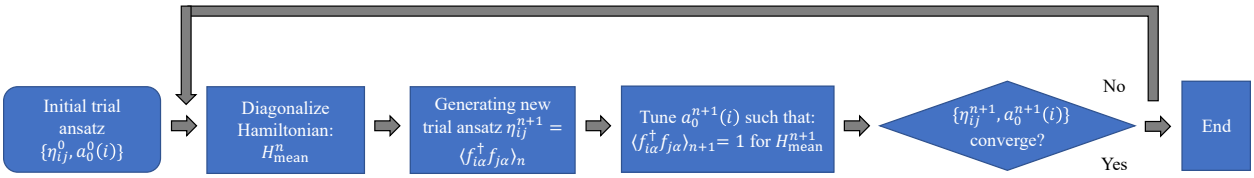

Figure 2.2: The iterative self-consistent procedure. The convergence condition in the last step is set to $\sum_{ij}|\eta^{n+1}_{\boldsymbol{ij}}-\eta^n_{\boldsymbol{ij}}|<\delta$ and $\sum_i|a^{n+1}_0(i)-a^n_0(i)|<\delta$, while δ is a positive number which decides the accuracy.

2.2 Homogeneous self-consistent ansatz for chiral spin liquid

2.2.1 Mean field Hamiltonian in momentum space

From Sec. [2.1], we know that for the spin-1/2 J_1-J_2 model defined on the square lattice (see in Fig. [2.1]), the mean-field Hamiltonian based on Eq. (2.7) is given by [273, 64]:

$$H=H_1+H_2, \tag{2.9}$$

with the nearest neighbor terms,

$$\begin{aligned}H_1 =& -\sum_{i,\sigma}\{[J_1^x\eta^1_{ba}(\boldsymbol{r}_i^a)\hat{C}^\dagger_{a,\sigma}(\boldsymbol{r}_i^a)\hat{C}_{b,\sigma}(\boldsymbol{r}_i^a+\boldsymbol{S}_1)+J_1^y\eta^2_{aa}(\boldsymbol{r}_i^a)\hat{C}^\dagger_{a,\sigma}(\boldsymbol{r}_i^a)\hat{C}_{a,\sigma}(\boldsymbol{r}_i^a+\boldsymbol{S}_2)+\text{H.c.}]\\ &+\frac{J_1^x}{2}|\eta^1_{ba}(\boldsymbol{r}_i^a)|^2+\frac{J_1^y}{2}|\eta^2_{aa}(\boldsymbol{r}_i^a)|^2\}\\ &-\sum_{i,\sigma}\{[J_1^x\eta^1_{ab}(\boldsymbol{r}_i^b)\hat{C}^\dagger_{b,\sigma}(\boldsymbol{r}_i^b)\hat{C}_{a,\sigma}(\boldsymbol{r}_i^b+\boldsymbol{S}_1)+J_1^y\eta^2_{bb}(\boldsymbol{r}_i^b)\hat{C}^\dagger_{b,\sigma}(\boldsymbol{r}_i^b)\hat{C}_{b,\sigma}(\boldsymbol{r}_i^b+\boldsymbol{S}_2)+\text{H.c.}]\\ &+\frac{J_1^x}{2}|\eta^1_{ab}(\boldsymbol{r}_i^b)|^2+\frac{J_1^y}{2}|\eta^2_{bb}(\boldsymbol{r}_i^b)|^2\},\end{aligned} \tag{2.10}$$

and the second nearest neighbor terms,

$$\begin{aligned}H_2 =& -\sum_{i,\sigma}\{[J_2^+\eta^3_{ba}(\boldsymbol{r}_i^a)\hat{C}^\dagger_{a,\sigma}(\boldsymbol{r}_i^a)\hat{C}_{b,\sigma}(\boldsymbol{r}_i^a+\boldsymbol{R}_1)+J_2^-\eta^4_{ba}(\boldsymbol{r}_i^a)\hat{C}^\dagger_{a,\sigma}(\boldsymbol{r}_i^a)\hat{C}_{b,\sigma}(\boldsymbol{r}_i^a+\boldsymbol{R}_4)+\text{H.c.}]\\ &+\frac{J_2^+}{2}|\eta^3_{ba}(\boldsymbol{r}_i^a)|^2+\frac{J_2^-}{2}|\eta^4_{ba}(\boldsymbol{r}_i^a)|^2\}\\ &-\sum_{i,\sigma}\{[J_2^+\eta^3_{ab}(\boldsymbol{r}_i^b)\hat{C}^\dagger_{b,\sigma}(\boldsymbol{r}_i^b)\hat{C}_{a,\sigma}(\boldsymbol{r}_i^b+\boldsymbol{R}_1)+J_2^-\eta^4_{ab}(\boldsymbol{r}_i^b)\hat{C}^\dagger_{b,\sigma}(\boldsymbol{r}_i^b)\hat{C}_{a,\sigma}(\boldsymbol{r}_i^b+\boldsymbol{R}_4)+\text{H.c.}]\\ &+\frac{J_2^+}{2}|\eta^3_{ab}(\boldsymbol{r}_i^b)|^2+\frac{J_2^-}{2}|\eta^4_{ab}(\boldsymbol{r}_i^b)|^2\}.\end{aligned} \tag{2.11}$$

For simplicity, we will drop the constant terms temporarily and only add them back in the free energy Eq. (2.28). In the homogeneous limit, the following ansatz represents a chiral spin liquid phase:

$$\begin{aligned}&\eta^1_{ba}(\boldsymbol{r}_i^a)\equiv\eta^1_{ba}=+i\bar{\rho}^a_x,\quad \eta^1_{ab}(\boldsymbol{r}_i^b)\equiv\eta^1_{ab}=+i\bar{\rho}^b_x,\quad \eta^2_{aa}(\boldsymbol{r}_i^a)\equiv\eta^2_{aa}=-i\bar{\rho}^a_y,\quad \eta^2_{bb}(\boldsymbol{r}_i^a)\equiv\eta^2_{bb}=+i\bar{\rho}^b_y,\\ &\eta^3_{ba}(\boldsymbol{r}_i^a)\equiv\eta^3_{ba}=+i\bar{\lambda}^a_+,\quad \eta^3_{ab}(\boldsymbol{r}_i^b)\equiv\eta^3_{ab}=-i\bar{\lambda}^b_+,\quad \eta^4_{ba}(\boldsymbol{r}_i^a)\equiv\eta^4_{ba}=+i\bar{\lambda}^a_-,\quad \eta^4_{ab}(\boldsymbol{r}_i^b)\equiv\eta^4_{ab}=-i\bar{\lambda}^b_-.\end{aligned} \tag{2.12}$$

We introduce the the Fourier transformation,

$$\hat{C}_a(\boldsymbol{r}_j)=\frac{1}{\sqrt{N}}\sum_{\boldsymbol{k}}e^{+i\boldsymbol{k}\cdot\boldsymbol{r}_j}\hat{C}_a(\boldsymbol{k}),\quad \hat{C}_b(\boldsymbol{r}_j)=\frac{1}{\sqrt{N}}\sum_{\boldsymbol{k}}e^{+i\boldsymbol{k}\cdot\boldsymbol{r}_j}\hat{C}_b(\boldsymbol{k}), \tag{2.13}$$

upon dropping the constant terms, we shall have Eq. (2.9) transformed into momentum space:

$$H=\sum_{\sigma,\boldsymbol{k}}\begin{pmatrix}\hat{C}^\dagger_{a,\sigma}(\boldsymbol{k}) & \hat{C}^\dagger_{b,\sigma}(\boldsymbol{k})\end{pmatrix}(h_1+h_2)\begin{pmatrix}\hat{C}_{a,\sigma}(\boldsymbol{k})\\ \hat{C}_{b,\sigma}(\boldsymbol{k})\end{pmatrix} \tag{2.14}$$

with the kernel:

$$\begin{aligned} h_1 =& - J_1^x(-\bar{\rho}_x^a + \bar{\rho}_x^b)\cos(\boldsymbol{k}\cdot\boldsymbol{S}_1)\sigma_y + J_1^x(\bar{\rho}_x^a + \bar{\rho}_x^b)\sin(\boldsymbol{k}\cdot\boldsymbol{S}_1)\sigma_x \\ & - J_1^y(+\bar{\rho}_y^a - \bar{\rho}_y^b)\sin(\boldsymbol{k}\cdot\boldsymbol{S}_2)\sigma_0 - J_1^y(\bar{\rho}_y^a + \bar{\rho}_y^b)\sin(\boldsymbol{k}\cdot\boldsymbol{S}_2)\sigma_z \\ h_2 =& + [J_2^+(\bar{\lambda}_+^a + \bar{\lambda}_+^b)\cos(\boldsymbol{k}\cdot\boldsymbol{R}_1) + J_2^-(\bar{\lambda}_-^a + \bar{\lambda}_-^b)\cos(\boldsymbol{k}\cdot\boldsymbol{R}_4)]\sigma_y \\ & + [J_2^+(\bar{\lambda}_+^a - \bar{\lambda}_+^b)\sin(\boldsymbol{k}\cdot\boldsymbol{R}_1) + J_2^-(\bar{\lambda}_-^a - \bar{\lambda}_-^b)\sin(\boldsymbol{k}\cdot\boldsymbol{R}_4)]\sigma_x. \end{aligned} \tag{2.15}$$

We can further take the limit for each unit cell the parameters take the same value or a and b:

$$\bar{\rho}_x^a = \bar{\rho}_x^b = \bar{\rho}_x^0, \quad \bar{\rho}_y^a = \bar{\rho}_y^b = \bar{\rho}_y^0, \quad J_2^+ = J_2^- \quad \bar{\lambda}_+^a = \bar{\lambda}_+^b = \bar{\lambda}_+^0, \quad \bar{\lambda}_-^a = \bar{\lambda}_-^b = \bar{\lambda}_-^0. \tag{2.16}$$

The Bloch Hamiltonian can be further simplified as:

$$\begin{aligned} h_0 =& 2J_1^x\bar{\rho}_x^0\sin(\boldsymbol{k}\cdot\boldsymbol{S}_1)\sigma_x + [2J_2^+\bar{\lambda}_+^0\cos(\boldsymbol{k}\cdot\boldsymbol{R}_1) + 2J_2^-\bar{\lambda}_-^0\cos(\boldsymbol{k}\cdot\boldsymbol{R}_4)]\sigma_y - 2J_1^y\bar{\rho}_y^0\sin(\boldsymbol{k}\cdot\boldsymbol{S}_2)\sigma_z \\ =& 2J_1^x\bar{\rho}_x^0\sin(k_x a_0)\sigma_x + 2[J_2^+\bar{\lambda}_+^0 + J_2^-\bar{\lambda}_-^0]\cos k_x a_0\cos k_y a_0\sigma_y \\ & - 2[J_2^+\bar{\lambda}_+^0 - J_2^-\bar{\lambda}_-^0]\sin k_x a_0\sin k_y a_0\sigma_y - 2J_1^y\bar{\rho}_y^0\sin(k_y a_0)\sigma_z. \end{aligned} \tag{2.17}$$

In the limit $J_2^+ = J_2^- = J_2$ such that $\lambda_+^0 = \lambda_-^0 = \lambda^0$, with the constants added back, we arrive at:

$$h_0(k_x,k_y) = J_1|\bar{\rho}_x|^2 + J_1|\bar{\rho}_y|^2 + 2J_2|\bar{\lambda}|^2 + h_x(k_x,k_y)\sigma_x + h_y(k_x,k_y)\sigma_y + h_z(k_x,k_y)\sigma_z, \tag{2.18}$$

with:

$$\begin{aligned} h_x(k_x,k_y) &= +2J_1\rho_x\sin(k_x a_0) \\ h_y(k_x,k_y) &= +4J_2\lambda\cos(k_x a_0)\cos(k_y a_0) \\ h_z(k_x,k_y) &= -2J_1\rho_y\sin(k_y a_0), \end{aligned} \tag{2.19}$$

which gives the gap at $(k_x,k_y) = (0,0)$:

$$\Delta = 2\times 4J_2\bar{\lambda}^0 = 8J_2\bar{\lambda}^0. \tag{2.20}$$

2.2.2 Self-consistent solution via iterative procedure

For a two level system (whose energy is normalized to 1):

$$\mathcal{H}_A = \sin\theta\cos\phi\sigma_x + \sin\theta\sin\phi\sigma_y + \cos\theta\sigma_z, \tag{2.21}$$

we shall have the eigenstates:

$$\epsilon = -1, \quad \psi_- = \begin{pmatrix} \sin\left(\frac{\theta}{2}\right)e^{-i\phi} \\ -\cos\left(\frac{\theta}{2}\right), \end{pmatrix}, \quad \epsilon = +1, \quad \psi_+ = \begin{pmatrix} \cos\left(\frac{\theta}{2}\right)e^{-i\phi}, \\ \sin\left(\frac{\theta}{2}\right) \end{pmatrix}. \tag{2.22}$$

Compared with Eq. (2.18), we can define

$$\begin{aligned}
\hat{d}_x(k_x,k_y) &= \sin\theta\cos\phi = \frac{h_x(k_x,k_y)}{\sqrt{h_x^2(k_x,k_y)+h_y^2(k_x,k_y)+h_z^2(k_x,k_y)}} \\
&= +\frac{2J_1^x\bar{\rho}_x^0\sin(k_xa_0)}{\sqrt{[2J_1^x\bar{\rho}_x^0\sin(k_xa_0)]^2+[4J_2\lambda^0\cos(k_xa_0)\cos(k_ya_0)]^2+[2J_1^y\bar{\rho}_y^0\sin(k_ya_0)]^2}}, \\
\hat{d}_y(k_x,k_y) &= \sin\theta\sin\phi = \frac{h_y(k_x,k_y)}{\sqrt{h_x^2(k_x,k_y)+h_y^2(k_x,k_y)+h_z^2(k_x,k_y)}} \\
&= +\frac{4J_2\lambda^0\cos(k_xa_0)\cos(k_ya_0)}{\sqrt{[2J_1^x\bar{\rho}_x^0\sin(k_xa_0)]^2+[4J_2\lambda^0\cos(k_xa_0)\cos(k_ya_0)]^2+[2J_1^y\bar{\rho}_y^0\sin(k_ya_0)]^2}}, \\
\hat{d}_z(k_x,k_y) &= \cos\theta = \frac{h_z(k_x,k_y)}{\sqrt{h_x^2(k_x,k_y)+h_y^2(k_x,k_y)+h_z^2(k_x,k_y)}} \\
&= -\frac{2J_1^y\bar{\rho}_y^0\sin(k_ya_0)}{\sqrt{[2J_1^x\bar{\rho}_x^0\sin(k_xa_0)]^2+[4J_2\lambda^0\cos(k_xa_0)\cos(k_ya_0)]^2+[2J_1^y\bar{\rho}_y^0\sin(k_ya_0)]^2}}.
\end{aligned} \tag{2.23}$$

Then we shall have the self consistency equations for the lower subband,

$$\begin{aligned}
i\bar{\rho}_x^a = i\bar{\rho}_x^0 \equiv \eta_{ba}^1 &= \sum_\sigma \iint [d\boldsymbol{k}] e^{-ik_xa_0}\left[-\cos\left(\frac{\theta}{2}\right)\right]^*\left[\sin\left(\frac{\theta}{2}\right)e^{-i\phi}\right] \\
&= \iint [d\boldsymbol{k}]\frac{i2J_1^x\bar{\rho}_x^0\sin^2(k_xa_0)}{\sqrt{h_x^2(k_x,k_y)+h_y^2(k_x,k_y)+h_z^2(k_x,k_y)}},
\end{aligned} \tag{2.24}$$

where we define:

$$\iint [d\boldsymbol{k}] = \int_{-\pi}^{+\pi}\frac{dk_y}{2\pi}\int_{-\pi/2}^{+\pi/2}\frac{dk_x}{\pi}. \tag{2.25}$$

Similarly, for the η_{aa}^2 and η_{ba}^3, we arrive at the self-consistency equations:

$$\begin{aligned}
-i\bar{\rho}_y^a \equiv \eta_{aa}^2 &= \iint [d\boldsymbol{k}]\frac{-i2J_1^y\bar{\rho}_y^0\sin^2(k_ya_0)}{\sqrt{h_x^2(k_x,k_y)+h_y^2(k_x,k_y)+h_z^2(k_x,k_y)}}, \\
+i\bar{\lambda}^0 \equiv \eta_{ba}^3 &= \iint [d\boldsymbol{k}]\frac{i4J_2\lambda^0\cos^2(k_xa_0)\cos^2(k_ya_0)}{\sqrt{h_x^2(k_x,k_y)+h_y^2(k_x,k_y)+h_z^2(k_x,k_y)}}.
\end{aligned} \tag{2.26}$$

To solve above self-consistency equation, we use the following recursion relations:

$$\begin{aligned}
\bar{\rho}^0_{x,n+1} &= \iint [d\boldsymbol{k}] \frac{J_1^x \bar{\rho}^0_{x,n} \sin^2(k_x a_0)}{\sqrt{[J_1^x \bar{\rho}^0_{x,n} \sin(k_x a_0)]^2 + [2J_2 \lambda^0_n \cos(k_x a_0)\cos(k_y a_0)]^2 + [J_1^y \bar{\rho}^0_{y,n} \sin(k_y a_0)]^2}}, \\
\bar{\rho}^0_{y,n+1} &= \iint [d\boldsymbol{k}] \frac{2J_1^y \bar{\rho}^0_{y,n} \sin^2(k_y a_0)}{\sqrt{[2J_1^x \bar{\rho}^0_{x,n} \sin(k_x a_0)]^2 + [4J_2 \lambda^0_n \cos(k_x a_0)\cos(k_y a_0)]^2 + [2J_1^y \bar{\rho}^0_{y,n} \sin(k_y a_0)]^2}}, \\
\bar{\lambda}^0_{n+1} &= \iint [d\boldsymbol{k}] \frac{4J_2 \lambda^0_n \cos^2(k_x a_0)\cos^2(k_y a_0)}{\sqrt{[2J_1^x \bar{\rho}^0_{x,n} \sin(k_x a_0)]^2 + [4J_2 \lambda^0_n \cos(k_x a_0)\cos(k_y a_0)]^2 + [2J_1^y \bar{\rho}^0_{y,n} \sin(k_y a_0)]^2}},
\end{aligned} \tag{2.27}$$

and one can run the iterations for a number of times until reaching convergence as $n \to \infty$ based on the procedure shown in Fig. [2.2].

2.2.3 Self-consistent solution via minimizing mean-field energy

The free energy per unit cell per spin reads:

$$\begin{aligned}
&F_\sigma(\rho^0_x, \rho^0_y, \lambda^0) = J_1^x |\rho^0_x|^2 + J_1^y |\rho^0_y|^2 + 2J_2 |\lambda^0|^2 \\
&- \iint [d\boldsymbol{k}] \sqrt{[2J_1^x \bar{\rho}^0_x \sin(k_x a_0)]^2 + [4J_2 \lambda^0 \cos(k_x a_0)\cos(k_y a_0)]^2 + [2J_1^y \bar{\rho}^0_y \sin(k_y a_0)]^2},
\end{aligned} \tag{2.28}$$

variational equations:

$$\frac{\delta F}{\delta \rho^0_x} = 0, \quad \frac{\delta F}{\delta \rho^0_y} = 0, \quad \frac{\delta F}{\delta \lambda^0} = 0, \tag{2.29}$$

will give the same relation as given in the self-consistency equations Eq. (2.24) and Eq. (2.26). The energy profile and the solutions are illustrated in Fig. 2.3(b).

2.2.4 Chern number and chirality

We first look for a self-consistent homogeneous solution $\{\rho_x(\boldsymbol{i}), \rho_y(\boldsymbol{i}), \lambda(\boldsymbol{i})\} \equiv (\rho_x, \rho_y, \lambda)$ by solving the self-consistency condition Eq. (2.27) in an iterative manner [94]. When $J_2 > 0.46 J_1$, we find eight solutions $(\pm\bar{\rho}_x, \pm\bar{\rho}_y, \pm\bar{\lambda})$ with $\bar{\rho}_x = \bar{\rho}_y$ and $\bar{\lambda} > 0$, ensuring the Hamiltonian is gapped. The solutions can be grouped by their chirality $\chi = \pm\chi_0$, where $\chi_0 = |\bar{\rho}_x \bar{\rho}_y \bar{\lambda}|$. The corresponding Bloch Hamiltonian reads (we set lattice constant $a_0 = 1$)

$$\begin{aligned}
h_0(\boldsymbol{k}) &= J_1 |\rho_x|^2 + J_1 |\rho_y|^2 + 2J_2 |\lambda|^2 + \boldsymbol{d}(\boldsymbol{k}) \cdot \boldsymbol{\sigma}, \\
\boldsymbol{d}(\boldsymbol{k}) &= 2(J_1 \rho_x \sin k_x, 2J_2 \lambda \cos k_x \cos k_y, -J_1 \rho_y \sin k_y).
\end{aligned} \tag{2.30}$$

The order parameter for time-reversal symmetry breaking is the spin chirality operator, defined as

$$\chi(\boldsymbol{i}) \equiv 2\boldsymbol{S}(\boldsymbol{r}^a_{\boldsymbol{i}}) \cdot (\boldsymbol{S}(\boldsymbol{r}^b_{\boldsymbol{i}}) \times \boldsymbol{S}(\boldsymbol{r}^a_{\boldsymbol{i}} + \hat{e}_y)) = \rho_x(\boldsymbol{i}) \rho_y(\boldsymbol{i}) \lambda(\boldsymbol{i}). \tag{2.31}$$

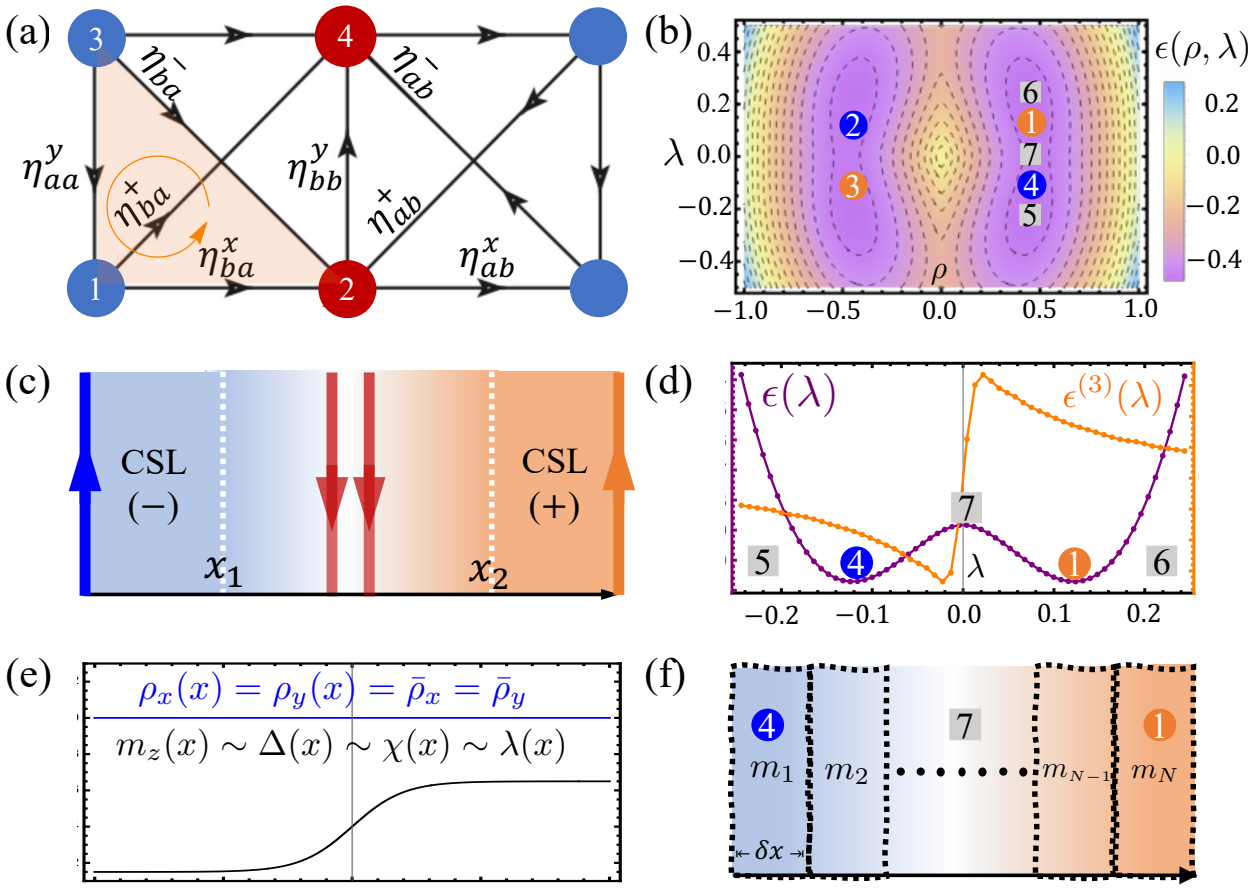

Figure 2.3: (a) Parton mean-field hoppings ($+i$ along the arrow), with blue (red) circle stands for the a (b) sublattice. (b) Density-contour plot for the Eq. (2.28) in the parameter space, where $\epsilon(\rho,\lambda) = F(\rho,\rho,\lambda)/J_1$. The orange (blue) dots stand for the solution with positive (negative) chirality. (c) The two-domain setup. The system is finite along x direction but periodic along y direction, which can be viewed as a quasi-1D ribbon. The blue (orange) part to the left (right) of x_1 (x_2) are the chiral spin states with negative (positive) chirality, held fixed during the numerical iteration, while the region between x_1 and x_2 are subjected to the iteration. (d) The energy $\epsilon(\lambda)$ and its third derivative $\epsilon^{(3)}(\lambda)$ along $5 \to 4 \to 7 \to 1 \to 6$ in (b). (e) A converged solution for the domain wall structure. Note that the local mass $m_z(x)$, gap $\Delta(x)$, and chirality $\chi(x)$ are all proportional to $\lambda(x)$. (f) Partition for the ribbon mentioned in (c).

The Chern number of the lower band $C = -\mathrm{sgn}(\rho_x\rho_y\lambda)$ is associated with $\chi(\boldsymbol{i})$ of the original spin model [24], which we shows as following.

For a two-band system, the Chern number associated with the lower subband of Eq. (2.21)

is defined as [24]

$$C = \frac{1}{2\pi}\int [dk_x dk_y]\mathcal{F}_{xy}, \quad \mathcal{F}_{\mu\nu} = \frac{1}{2}\epsilon^{\alpha\beta\gamma}\hat{d}_\alpha(\boldsymbol{k})\partial_{k_\mu}\hat{d}_\beta(\boldsymbol{k})\partial_{k_\nu}\hat{d}_\gamma(\boldsymbol{k}), \tag{2.32}$$

from which we have

$$\mathcal{F}_{xy} = -\frac{8J_1^2 J_2\lambda\rho_x\rho_y[\cos^2(k_y)\sin^2(k_x)+\cos^2(k_x)\cos^2(k_y)+\cos^2(k_x)\sin^2(k_y)]}{\{[2J_1^x\bar{\rho}_x\sin(k_x a_0)]^2+[4J_2\lambda\cos(k_x a_0)\cos(k_y a_0)]^2+[2J_1^y\bar{\rho}_y\sin(k_y a_0)]^2\}^{3/2}}. \tag{2.33}$$

After some calculations, we further arrive at the Chern number:

$$C = -\mathrm{Sign}(\rho_x\rho_y\lambda), \tag{2.34}$$

where Sign denotes for sign function. This can be associated to the form of chirality operator in terms of mean field ansatz, as given in Eq. (2.31).

2.3 Self-consistent solution for an inhomogeneous chiral spin liquid with domain wall

One central approach in this work is a self-consistent mean-field ansatz for a CSL system with both positive and negative chirality domains. For such a spatially inhomogeneous ansatz, the iteration method is particularly efficient compared to the energy minimization approach and hence will be our main tool in the analysis below. For simplicity, we consider a two-domain setup as illustrated in Fig. 2.3(c): the system is finite along x direction and periodic along y direction, with a negative (positive) chirality $-\chi_0$ ($+\chi_0$) CSL domain existing on the left (right). While the chirality is nearly uniform far away from the interface, a profile develops near the interface, leading to a finite domain wall whose width will be determined self-consistently and interatively.

2.3.1 Self consistent calculations for a 1D ribbon

If we apply the open boundary condition along x direction but keep infinite boundary condition along y direction for Eq. (2.9), we shall get a configuration of ribbon, which is the setup for Fig. 1c of the main text. We define the following partial Fourier transformation:

$$\hat{C}_{\alpha,\sigma}(x_i^\alpha, y_j^\alpha) = \frac{1}{\sqrt{N_y}}\sum_{k_y} e^{+ik_y y_j^\alpha}\hat{C}_{\alpha,\sigma}(x_i, k_y). \tag{2.35}$$

Plugging back to Eq. (2.9), we arrive at the partial Fourier transformation for H_1:

$$\begin{aligned}
H_1 =& -\sum_{n,k_y,\sigma} J_1^x[\eta_{ba}^1(2n-1)\,|\Psi_{a,\sigma}(2n-1,k_y)\rangle\,\langle\Psi_{b,\sigma}(2n,k_y)| \\
&+\eta_{ab}^1(2n)\,|\Psi_{b,\sigma}(2n,k_y)\rangle\,\langle\Psi_{a,\sigma}(2n+1,k_y)|+\text{H.c.}] \\
&-\sum_{n,k_y,\sigma} J_1^y[\eta_{aa}^2(2n-1)e^{+ik_y a_0}\,|\Psi_{a,\sigma}(2n-1,k_y)\rangle\,\langle\Psi_{a,\sigma}(2n-1,k_y)| \\
&+\eta_{bb}^2(2n)e^{+ik_y a_0}\,|\Psi_{b,\sigma}(2n,k_y)\rangle\,\langle\Psi_{b,\sigma}(2n,k_y)|+\text{H.c.}].
\end{aligned} \tag{2.36}$$

Thus the self-consistency equation for the ribbon reads (the occ means the summation runs through all the occupied bands)

$$\begin{aligned}
\eta_{ba}^1(\boldsymbol{r}_i^a) =& \eta_{ba}^1(x_i^a) = \eta_{ba}^1(2n-1) = \langle \hat{C}_{b,\sigma}^\dagger(\boldsymbol{r}_i^a + \boldsymbol{S}_1)\hat{C}_{a,\sigma}(\boldsymbol{r}_i^a)\rangle \\
=& \frac{1}{N_y}\sum_{k_y^1,k_y^2,j,\sigma} \langle \hat{C}_{b,\sigma}^\dagger(x_i^a + a_0, k_y^1)e^{-ik_y^1 y_j^a}\hat{C}_{a,\sigma}(x_i^a,k_y^2)e^{+ik_y^2 y_j^a}\rangle \\
=& \frac{1}{N_y}\sum_{k_y}\sum_{\sigma}\langle \hat{C}_{b,\sigma}^\dagger(x_i^a + a_0,k_y)\hat{C}_{a,\sigma}(x_i^a,k_y)\rangle \\
=& \frac{1}{N_y}\sum_{\sigma,k_y\in[-\pi,+\pi)}\sum_{\zeta\in\text{occ}} \Psi_{b,\sigma}^{*,\zeta}(2n,k_y)\Psi_{a,\sigma}^{\zeta}(2n-1,k_y) \\
\eta_{ab}^1(\boldsymbol{r}_i^b) =& \frac{1}{N_y}\sum_{k_y}\sum_{\sigma}\langle \hat{C}_{a,\sigma}^\dagger(x_i^b + a_0,k_y)\hat{C}_{b,\sigma}(x_i^b,k_y)\rangle \\
=& \frac{1}{N_y}\sum_{\sigma,k_y\in[-\pi,+\pi)}\sum_{\zeta\in\text{occ}} \Psi_{a,\sigma}^{*,\zeta}(2n+1,k_y)\Psi_{b,\sigma}^{\zeta}(2n,k_y) \\
\eta_{aa}^2(\boldsymbol{r}_i^a) =& \frac{1}{N_y}\sum_{k_y}\sum_{\sigma}\langle e^{-ik_y a_0}\hat{C}_{a,\sigma}^\dagger(x_i^a,k_y)\hat{C}_{a,\sigma}(x_i^a,k_y)\rangle \\
=& \frac{1}{N_y}\sum_{\sigma,k_y\in[-\pi,+\pi)}\sum_{\zeta\in\text{occ}} e^{-ik_y a_0}\Psi_{a,\sigma}^{*,\zeta}(2n-1,k_y)\Psi_{a,\sigma}^{\zeta}(2n-1,k_y) \\
\eta_{bb}^2(\boldsymbol{r}_i^b) =& \frac{1}{N_y}\sum_{k_y}\sum_{\sigma}\langle e^{-ik_y a_0}\hat{C}_{b,\sigma}^\dagger(x_i^b,k_y)\hat{C}_{b,\sigma}(x_i^b,k_y)\rangle \\
=& \frac{1}{N_y}\sum_{\zeta\in\text{occ}}\sum_{\sigma,k_y\in[-\pi,+\pi)} e^{-ik_y a_0}\Psi_{b,\sigma}^{*,\zeta}(2n,k_y)\hat{\Psi}_{b,\sigma}^{\zeta}(2n,k_y).
\end{aligned} \tag{2.37}$$

Similarly, the next-nearest neighbor coupling can also be partially transformed into Fourier space

$$\begin{aligned}
H_2 = &- \sum_{i,k_y,\sigma} [J_2^+ \eta^3_{ba}(x_i^a) e^{+ik_y a_0} \left|\Psi_{a,\sigma}(2n-1,k_y)\right\rangle \left\langle\Psi_{b,\sigma}(2n,k_y)\right| + \text{H.c.}] \\
&- \sum_{i,k_y,\sigma} [J_2^+ \eta^3_{ab}(x_i^b) e^{+ik_y a_0} \left|\Psi_{b,\sigma}(2n,k_y)\right\rangle \left\langle\Psi_{a,\sigma}(2n+1,k_y)\right| + \text{H.c.}] \\
&- \sum_{i,k_y,\sigma} [J_2^- \eta^4_{ba}(x_i^a) e^{-ik_y a_0} \left|\Psi_{a,\sigma}\right\rangle (2n-1,k_y) \left\langle\Psi_{b,\sigma}(2n,k_y)\right| + \text{H.c.}] \\
&- \sum_{i,k_y,\sigma} [J_2^- \eta^4_{ab}(x_i^b) e^{-ik_y a_0} \left|\Psi_{b,\sigma}(2n,k_y)\right\rangle \left\langle\Psi_{a,\sigma}(2n+1,k_y)\right| + \text{H.c.}],
\end{aligned} \tag{2.38}$$

and we have the following self-consistent equations:

$$\begin{aligned}
\eta^3_{ba}(\boldsymbol{r}_i^a) &= \eta^3_{ba}(x_i^a) = \eta^3_{ba}(2n-1) = \langle \hat{C}^\dagger_{b,\sigma}(\boldsymbol{r}_i^a + \boldsymbol{R}_1)\hat{C}_{a,\sigma}(\boldsymbol{r}_i^a)\rangle \\
&= \frac{1}{N_y} \sum_{k_y^1,k_y^2,j,\sigma} \langle \hat{C}^\dagger_{b,\sigma}(x_i^a + a_0, k_y^1) e^{-ik_y^1(y_j^a + a_0)} \hat{C}_{a,\sigma}(x_i^a, k_y^2) e^{+ik_y^2 y_j^a}\rangle \\
&= \frac{1}{N_y} \sum_{k_y} \sum_{\sigma} \langle e^{-ik_y a_0} \hat{C}^\dagger_{b,\sigma}(x_i^a + a_0, k_y) \hat{C}_{a,\sigma}(x_i^a, k_y)\rangle \\
&= \frac{1}{N_y} \sum_{\sigma, k_y \in [-\pi,+\pi)} \sum_{\zeta \in \text{occ}} e^{-ik_y a_0} \Psi^{*,\zeta}_{b,\sigma}(2n,k_y) \Psi^{\zeta}_{a,\sigma}(2n-1,k_y) \\
\eta^3_{ab}(\boldsymbol{r}_i^b) &= \frac{1}{N_y} \sum_{k_y} \sum_{\sigma} \langle e^{-ik_y a_0} \hat{C}^\dagger_{a,\sigma}(x_i^b + a_0, k_y) \hat{C}_{b,\sigma}(x_i^b, k_y)\rangle \\
&= \frac{1}{N_y} \sum_{\sigma, k_y \in [-\pi,\pi)} \sum_{\zeta \in \text{occ}} e^{-ik_y a_0} \Psi^{*,\zeta}_{a,\sigma}(2n+1,k_y) \Psi^{\zeta}_{b,\sigma}(2n,k_y) \\
\eta^4_{ba}(\boldsymbol{r}_i^a) &= \frac{1}{N_y} \sum_{k_y} \sum_{\sigma} \langle e^{+ik_y a_0} \hat{C}^\dagger_{b,\sigma}(x_i^a + a_0, k_y) \hat{C}_{a,\sigma}(x_i^a, k_y)\rangle \\
&= \frac{1}{N_y} \sum_{k_y} \sum_{\sigma, k_y \in [-\pi,\pi)} \sum_{\zeta \in \text{occ}} e^{+ik_y a_0} \Psi^{*,\zeta}_{b,\sigma}(2n,k_y) \Psi^{\zeta}_{a,\sigma}(2n-1,k_y) \\
\eta^4_{ab}(\boldsymbol{r}_i^b) &= \frac{1}{N_y} \sum_{k_y} \sum_{\sigma} \langle e^{+ik_y a_0} \hat{C}^\dagger_{a,\sigma}(x_i^b + a_0, k_y) \hat{C}_{b,\sigma}(x_i^b, k_y)\rangle \\
&= \frac{1}{N_y} \sum_{k_y} \sum_{\sigma, k_y \in [-\pi,\pi)} \sum_{\zeta \in \text{occ}} e^{+ik_y a_0} \Psi^{*,\zeta}_{a,\sigma}(2n+1,k_y) \Psi^{\zeta}_{b,\sigma}(2n,k_y).
\end{aligned} \tag{2.39}$$

The central approach in this work is a self-consistent mean-field ansatz for a CSL system with both positive and negative chirality domains. For such a spatially inhomogeneous

ansatz, the iteration method is particularly efficient compared to the energy minimization approach and hence will be our main tool in the analysis below. We attempt a self-consistent mean-field description of a multi-domain CSL. For simplicity, we consider a two-domain setup as illustrated in Fig. 2.3(c): the system is finite along x direction and periodic along y direction, with a negative (positive) chirality $-\chi_0$ ($+\chi_0$) CSL domain existing on the left (right). While the chirality is nearly uniform far away from the interface, a profile develops near the interface, leading to a finite domain wall whose width will be determined self-consistently in the following procedure: (1) choose one of the ansatze of the homogeneous system with negative (positive) chirality obtained above, $\eta_{\boldsymbol{ij}}^{-,a}$ ($\eta_{\boldsymbol{ij}}^{+,b}$), and assign it to the region $x < x_1$ on the far left ($x > x_2$ on the far right) in Fig. 2.3(c); (2) choose a set of mean-field bonds arbitrarily and assign it to the middle region $x_1 < x < x_2$; (3) repeat the iteration process only for the bonds between x_1 and x_2, with the far left $x < x_1$ and far right $x_2 < x$ bonds held fixed; (4) a solution is obtained when the bonds converge. If multiple solutions exist, then the one with the lowest energy at half-filling will be chosen.

2.3.2 Numerical results

Given a set of (J_1, J_2), we perform the self-consistent calculation for a system with 50 unit cells ($L = 100$ sites) along the x-direction with sufficiently dense k_y points to conduct the numerical k_y integral. For $J_2 \geq 0.46J_1$, we find a converging solution of the following form: $\bar{\rho}_x$ and $\bar{\rho}_y$ remain constant in the entire system, while $\lambda(x)$ in the domain wall region extends between $-\bar{\lambda}$ (the value on the far left) and $\bar{\lambda}$ (the value on the far right). This solution is shown in Fig. 2.4. One can fit the $\lambda(x)$ profile and hence the chirality profile very well with a tanh function

$$\chi(x) = \chi_0 \tanh[(x - x_0)/(\sqrt{2}\xi)], \tag{2.40}$$

here x_0 defines the domain wall location. Changing the domain wall location does not affect the shape of the domain wall or the total energy of the system, hence we will manually set $x_0 = L/2$.

It is interesting to study the domain wall width ξ as a function of the exchange parameters (J_1, J_2). We find that ξ is directly proportional to the inverse of the bulk gap (far away from the domain wall), which in turn is a function of J_2/J_1. In the limit where the bulk gap $\Delta = 8J_2\bar{\lambda}$ vanishes (corresponding to $J_2 \approx 0.46J_1$), the domain wall width diverges, as shown in Fig. 2.4(d).

2.4 Amplitude fluctuation

The bulk of a CSL contains both spinon excitations and gauge fluctuations – both are gapped, due to finite spinon mass and a nonzero spinon Chern number. A third type, the amplitude fluctuations of the spinon hoppings, are often not discussed, as they are irrelevant to the description of a homogeneous CSL and are suppressed in the usual large-N treatment.

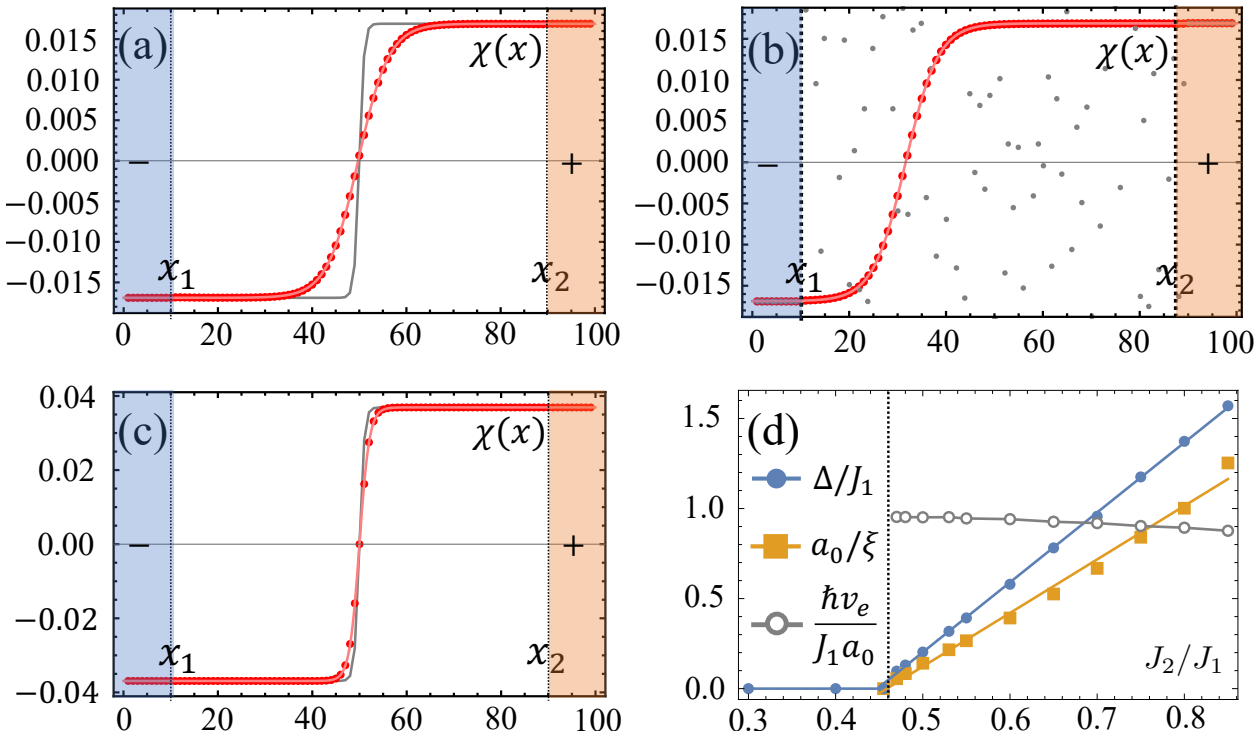

Figure 2.4: (a-c) Domain wall configurations, with the gray line standing for the initially proposed chirality profile and the red dots the final chirality profile of the converged solution. The left blue (right orange) part are the chiral spin states fixed to the ground state value $(\bar{\rho}_x, \bar{\rho}_y, -\bar{\lambda})$ $((\bar{\rho}_x, \bar{\rho}_y, +\bar{\lambda}))$ during the iteration. (a) $J_2/J_1 = 0.53$, with the symmetric sharp initial condition for chirality. (b) $J_2/J_1 = 0.53$ with the random initial condition for chirality. (c) $J_2/J_1 = 0.70$, with symmetric sharp initial condition for chirality. (d) The bulk gap Δ for homogeneous limit and the inverse correlation length ξ^{-1} with respect to J_2/J_1, from which we obtain $J_1 a_0/\xi = 0.77\Delta$. The values J_2/J_1, Δ/J_1, a_0/ξ and $\hbar v_{\text{edge}}/J_1 a_0$ have a one-to-one correspondence with each other.

Nevertheless, the amplitude fluctuations can provide important information for a spatially varying CSL state.

To understand the amplitude fluctuation, we want to introduce the dynamical field:

$$H_0 \sim \sum_{\boldsymbol{k}} \psi^\dagger_{\boldsymbol{k}} [(u^0_x + \hat{u}_x) k_x a_0 \sigma_x + (u^0_y + \hat{u}_y) k_y a_0 \sigma_y + (u^0_z + \hat{m}_z)\sigma_z] \psi_{\boldsymbol{k}}, \tag{2.41}$$

which means we assume that the flux pattern in the chiral spin liquid phase we considered is fixed (i.e. no phase fluctuation for the gauge fields), while the amplitude for the mean-field bonds (i.e., the value of $\rho_x, \rho_y, \lambda_\pm$) can fluctuate. The fluctuations of the mean-field bonds are captured by the newly introduced classical field $\hat{u}_x$, $\hat{u}_y$ and $\hat{u}_z$, which are related to the

fluctuations of the original bond amplitude by:

$$\hat{u}_x = 2J_1^x\hat{\rho}_x, \quad \hat{u}_y = -2J_1^y\hat{\rho}_y, \quad \hat{m}_z = 2(J_2^+\hat{\lambda}_+ + J_2^-\hat{\lambda}_-). \tag{2.42}$$

The total action then reads (with ∂_τ the derivative with respect to imaginary time):

$$S_s = \int d\tau d^2x\bar{\psi}_s\big(\partial_\tau + u_x^0\tau^x k_x a_0 + u_y^0\tau^y k_y a_0 + u_z^0\tau^z + \hat{u}_x k_x a_0\tau^x + \hat{u}_y k_y a_0\tau^y + \hat{m}_z\tau^z\big)\psi_s. \tag{2.43}$$

Upon doing the transformation,

$$\psi_s \to e^{-i\frac{\pi}{4}\tau^z}\psi, \quad \bar{\psi}_s \to i\bar{\psi}e^{-i\frac{\pi}{4}\tau^z}. \tag{2.44}$$

We shall then arrive at:

$$S_s = \int d\tau d^2x\bar{\psi}(\tau^z\partial_\tau + u_x^0 a_0\partial_x\tau^x + u_y^0 a_0\partial_y\tau^y + u_z^0\tau_0 + \underbrace{\hat{u}_x k_x a_0 i\tau^x + \hat{u}_y k_y a_0 i\tau^y + \hat{m}_z\tau_0}_{\text{perturbation}})\psi \tag{2.45}$$

We can treat the last part as a perturbation. Then we shall have the form:

$$\begin{aligned} S_{\text{eff}} &= -\ln\det[\tau^z\partial_\tau + u_x^0 a_0\partial_x\tau^x + u_y^0 a_0\partial_y\tau^y + u_z^0\tau_0 + \hat{u}_x k_x a_0 i\tau^x + \hat{u}_y k_y a_0 i\tau^y + \hat{m}_z\tau_0] \\ &= -\mathrm{Tr}\ln[\tau^z\partial_\tau + u_x^0 a_0\partial_x\tau^x + u_y^0 a_0\partial_y\tau^y + u_z^0\tau_0 + \hat{u}_x k_x a_0 i\tau^x + \hat{u}_y k_y a_0 i\tau^y + \hat{m}_z\tau_0] \\ &= -\mathrm{Tr}\ln[G^{-1} + \mathcal{V}] = -\mathrm{Tr}\ln G^{-1} - \mathrm{Tr}\ln[1 + G\mathcal{V}] \\ &= \text{const} - \mathrm{Tr}[G\mathcal{V}] + \frac{1}{2}\mathrm{Tr}[G\mathcal{V}G\mathcal{V})] + \cdots \end{aligned} \tag{2.46}$$

$(u_x^0, u_y^0, u_z^0) = (2J_1\bar{\rho}_x, 2J_1\bar{\rho}_y, 4J_2\bar{\lambda})$. As we have set $\bar{\rho}_x = \bar{\rho}_y$, from which we shall have $u_x^0 = u_y^0$, and can further define: $m_z^0 = u_z^0/u_x^0 = 2J_1\bar{\lambda}/J_1\bar{\rho}_x$, $k_0 = \hbar\omega/u_x^0 a_0$. Thus the propagator is defined as:

$$G(k) = \frac{iu_x^0 k_x a_0\tau_x + iu_y^0 k_y a_0\tau_y + i\hbar\omega\tau_z + u_z^0\tau_0}{(\hbar\omega)^2 + (u_x^0 k_x a_0)^2 + (u_y^0 k_y a_0)^2 + (u_z^0)^2} = \frac{1}{u_x^0}\frac{i\tilde{k}_x\tau_x + i\tilde{k}_y\tau_y + i\tilde{k}_0\tau_z + m_z^0\tau_0}{\tilde{k}_x^2 + \tilde{k}_y^2 + \tilde{k}_0^2 + (m_z^0)^2}, \tag{2.47}$$

where the dimensionless momentum are defined as $(\tilde{k}_x, \tilde{k}_y, \tilde{k}_0) = (k_x a_0, k_y a_0, k_0 a_0)$. Similarly, the vertex is defined as:

$$\mathcal{V} = \mathcal{V}_x + \mathcal{V}_y + \mathcal{V}_z = \hat{u}_x\tilde{k}_x i\tau^x + \hat{u}_y\tilde{k}_y i\tau^y + \hat{m}_z\tau_0, \quad \mathcal{V}_x = \hat{u}_x\tilde{k}_x i\tau^x,\ \mathcal{V}_y = \hat{u}_y\tilde{k}_y i\tau^y,\ \mathcal{V}_z = \hat{m}_z\tau_0. \tag{2.48}$$

The leading order term vanishes, and we would love to see the dynamical field from:

$$\begin{aligned} &\frac{1}{2}\mathrm{Tr}[G\mathcal{V}G\mathcal{V}] \\ =&\frac{1}{2}\mathrm{Tr}\ln[G(\tilde{p}_x, \tilde{p}_y, m_z^0)(\hat{u}_x\tilde{p}_x i\tau^x + \hat{u}_y\tilde{p}_y i\tau^y + \hat{m}_z\tau_0)G(\tilde{k}_x, \tilde{k}_y, m_z^0)(\hat{u}_x\tilde{k}_x i\tau^x + \hat{u}_y\tilde{k}_y i\tau^y + \hat{m}_z\tau_0)]. \end{aligned} \tag{2.49}$$

Below we will use the dimensionless momentum and drop the tilde on momentum.

2.5 The effective action

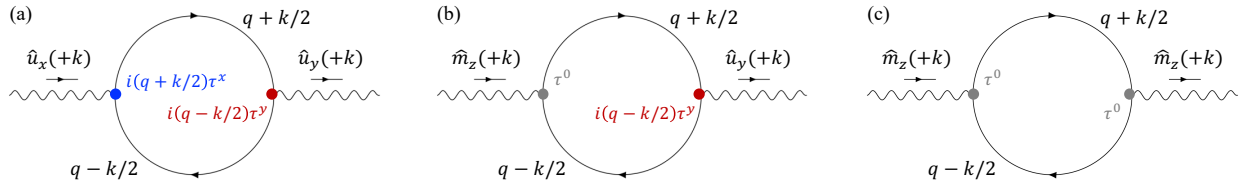

Figure 2.5: Feynman diagrams for evaluation of S_{eff} given in Eq. (2.50), with (a) for a term in S^A_{eff}, (b) for a term in S^B_{eff}, and (c) for a term in S^C_{eff}.

One can integrate out the fermions to get the effective field theory for $\hat{u}_x$, $\hat{u}_y$, and $\hat{m}_z$ (or equivalently, the $\hat{\rho}_x$, $\hat{\rho}_y$ and $\hat{\lambda}$). After the lengthy calculation in Section [2.10], we arrive at the following effective action:

$$S_{\text{eff}} = S^A_{\text{eff}} + S^B_{\text{eff}} + S^C_{\text{eff}} \tag{2.50}$$

with the term associated with two velocity vertices:

$$S^A_{\text{eff}} \equiv \sum_{\mu,\nu=x,y} \frac{1}{2} \int \frac{d^3k}{(2\pi)^3} \Pi^A_{\mu\nu}(k) \hat{u}_\mu(+k) \hat{u}_{-\nu}(k), \tag{2.51}$$

and two mass vertices:

$$S^B_{\text{eff}} \equiv \frac{1}{2} \int \frac{d^3k}{(2\pi)^3} \Pi^B_{zz}(k) \hat{m}_z(+k) \hat{m}_z(-k), \tag{2.52}$$

and one velocity vertex and one mass vertex:

$$S^C_{\text{eff}} \equiv \sum_{\mu,\nu=x,y} \frac{1}{2} \int \frac{d^3k}{(2\pi^3)} [\Pi^C_{z\nu}(k) \hat{m}_z(+k) \hat{u}_\nu(-k) + \Pi^C_{\mu z}(k) \hat{u}_\mu(+k) \hat{m}_z(-k)]. \tag{2.53}$$

We could write the effective action in a simpler way:

$$S_{\text{eff}} \simeq \frac{\hbar}{2(u^0_x)^2} \int \frac{d^3k}{(2\pi)^3} \begin{pmatrix} \hat{u}_x(+k) & \hat{u}_y(+k) & \hat{m}_z(+k) \end{pmatrix} \mathcal{S} \begin{pmatrix} \hat{u}_x(-k) \\ \hat{u}_y(-k) \\ \hat{m}_z(-k) \end{pmatrix} \tag{2.54}$$

The matrix element of $\mathcal{S}$ reads (note that we have defined $m = |m^0_z|$):

$$\begin{aligned}
&\mathcal{S}_{xx} = \frac{2m^3}{3\pi} + \frac{m}{12\pi}(k^2 - k_x^2), \quad \mathcal{S}_{xy} = \frac{m^3}{6\pi} + \frac{m}{24\pi}(k^2 - k_x^2 - k_y^2), \quad \mathcal{S}_{xz} = \frac{m^3}{2\pi} + \frac{m}{24\pi}(k^2 - k_x^2), \\
&\mathcal{S}_{yx} = \frac{m^3}{6\pi} + \frac{m}{24\pi}(k^2 - k_x^2 - k_y^2), \quad \mathcal{S}_{yy} = \frac{2m^3}{3\pi} + \frac{m}{12\pi}(k^2 - k_y^2), \quad \mathcal{S}_{yz} = \frac{m^2}{2\pi} + \frac{m}{24\pi}(k^2 - k_y^2), \\
&\mathcal{S}_{zx} = \frac{m^3}{2\pi} + \frac{m}{24\pi}(k^2 - k_x^2), \quad \mathcal{S}_{zy} = \frac{m^3}{2\pi} + \frac{m}{24\pi}(k^2 - k_y^2), \quad \mathcal{S}_{zz} = \frac{7m^3}{8\pi} + \frac{3k^2 m}{32\pi}.
\end{aligned} \tag{2.55}$$

such that we have:

$$\mathcal{S} = \mathcal{M}_0(m_z^0) + \mathcal{T}_k(m_z^0), \tag{2.56}$$

with mass $\mathcal{M}_0(m_z^0)$ and stiffness $\mathcal{T}_k(m_z^0)$ reads:

$$\begin{aligned}
\mathcal{M}_0(m_z^0) &= \frac{m^3}{24\pi}\begin{pmatrix} 16 & 4 & 12 \\ 4 & 16 & 12 \\ 12 & 12 & 21 \end{pmatrix}, \\
\mathcal{T}_k(m_z^0) &= \frac{m}{24\pi}\begin{pmatrix} 2(k^2-k_x^2) & (k^2-k_x^2-k_y^2) & (k^2-k_x^2) \\ (k^2-k_x^2-k_y^2) & 2(k^2-k_y^2) & (k^2-k_y^2) \\ (k^2-k_x^2) & (k^2-k_y^2) & \frac{9}{4}k^2 \end{pmatrix}.
\end{aligned} \tag{2.57}$$

From the effective action, we can get the free energy for one valley $(0,0)$:

$$F(m_z^0) = \frac{1}{2u_x^0}\int \frac{d^2k}{(2\pi)^2}\begin{pmatrix}\hat{u}_x(+k) & \hat{u}_y(+k) & \hat{m}_z(+k)\end{pmatrix}\mathcal{F}(m_z^0)\begin{pmatrix}\hat{u}_x(-k) \\ \hat{u}_y(-k) \\ \hat{m}_z(-k)\end{pmatrix}. \tag{2.58}$$

where:

$$\mathcal{F}(m_z^0) = \mathcal{M}_0(m_z^0) + \mathcal{T}_k(m_z^0). \tag{2.59}$$

This gives a Ginzburg–Landau theory for the three-component vector field. By using the fact that $k^2 = k_x^2 + k_y^2$, we have:

$$\mathcal{T}_k(m_z^0) = \frac{m}{24\pi}\begin{pmatrix} 2k_y^2 & 0 & k_y^2 \\ 0 & 2k_x^2 & k_x^2 \\ k_y^2 & k_x^2 & \frac{9}{4}(k_x^2+k_y^2) \end{pmatrix} \tag{2.60}$$

Another valley $(0,\pi)$ corresponds to $\mathcal{F}(-m_z^0)$, such that we have:

$$\begin{aligned}
\tilde{\mathcal{F}}(m_z^0) &= \mathcal{F}(m_z^0) + \mathcal{F}(-m_z^0) \\
&= \mathcal{M}_0(m_z^0) + \mathcal{T}_k(m_z^0) + \mathcal{M}(-m_z^0) + \mathcal{T}_k(-m_z^0) = 2\mathcal{M}_0(m) + 2\mathcal{T}_k(m) = 2\mathcal{F}(m_z^0).
\end{aligned} \tag{2.61}$$

2.5.1 Domain wall structure

As we have discussed above, the deviation $(\hat{u}_x, \hat{u}_y, \hat{m}_z)$ from the self-consistent ansatz in the homogeneous limit $(u_x^0, u_y^0, u_z^0) = (2J_1\bar{\rho}_x, -2J_1\bar{\rho}_y, 4J_2\bar{\lambda})$ captures the amplitude fluctuations around the energy minima. Treating the deviation as a three-component field $\Psi = (\hat{u}_x, \hat{u}_y, \hat{m}_z)^{\mathrm{T}}$, and assuming $\bar{\rho}_0 = \bar{\rho}_x = \bar{\rho}_y$, we arrive at:

$$S_{\text{eff}} \simeq \frac{\hbar}{2(u_x^0)^2}\int [d^3\tilde{k}]\Psi^\dagger[\mathcal{M}_0 + \mathcal{T}_{\tilde{k}}]\Psi, \tag{2.62}$$

with the mass matrix $\mathcal{M}_0$ and the stiffness matrix $\mathcal{T}_{\tilde{k}}$. We define the dimensionless parameter $m = |u_z^0/u_x^0| = |2J_2\bar{\lambda}/J_1\bar{\rho}_0|$. The energy at zero temperature of the field is derived by dropping

the frequency dependence. Assuming translation symmetry along the y direction as shown in Fig. 4.1(c), we set $k_y=0$ in order to minimize the energy. This leads to,

$$\mathcal{T}_k = \frac{m}{24\pi}\begin{pmatrix} 0 & 0 & 0 \\ 0 & 2k_x^2 & k_x^2 \\ 0 & k_x^2 & \frac{9}{4}k_x^2 \end{pmatrix} \tag{2.63}$$

We further integrate over y direction, and then we shall have the total free energy:

$$\begin{aligned} F_T &= F(m_z^0) + F(-m_z^0) \\ &\simeq \frac{m}{u_x^0}\int\frac{dk}{2\pi}[2u_y(+k)u_y(-k) + u_y(+k)m_z(-k) + m_z(+k)u_y(-k) + \frac{9}{4}m_z(+k)m_z(-k)] \\ &+ \frac{m}{u_x^0}\int\frac{dk}{2\pi}m^2[16u_x(+k)u_x(-k) + 4u_x(+k)u_y(-k) + 12u_x(+k)m_z(-k)] \\ &+ \frac{m}{u_x^0}\int\frac{dk}{2\pi}m^2[4u_y(+k)u_x(-k) + 16u_y(+k)u_y(-k) + 12u_y(+k)m_z(-k)] \\ &+ \frac{m}{u_x^0}\int\frac{dk}{2\pi}m^2[12m_z(+k)u_x(-k) + 12m_z(+k)u_y(-k) + 21m_z(+k)m_z(-k)], \end{aligned} \tag{2.64}$$

from which, we shall further have in the real space:

$$\begin{aligned} F_T = \int[d^2x]\mathcal{F}_T &\simeq \frac{m}{u_x^0 a_0}\int[dx][2(\partial_x u_y)^2 + (\partial_x u_y)(\partial_x m_z) + (\partial_x m_z)(\partial_x u_y) + \frac{9}{4}(\partial_x m_z)^2] \\ &+ \frac{m}{u_x^0 a_0}\int[dx]m^2[16u_y^2 + 12u_y m_z + 12m_z u_y + 21m_z^2] \\ &+ \frac{m}{u_x^0 a_0}\int[dx]m^2[16u_x^2 + 4u_x u_y + 12u_x m_z + 4u_y u_x + 12m_z u_x]. \end{aligned} \tag{2.65}$$

Since $\mathcal{M}_0$ and $\mathcal{T}_{\vec{k}}$ are positive definite, any non-zero fluctuations would increase the energy.

Recall that our inhomogenous ansatz for the two-domain CSL system has constant nearest-neighbor hopping $\bar{\rho}_{x,y}$, and the change of chirality is entirely due to the spatial variation of the next-nearest neighbor λ. Motivated by this fact, we focus our attention on the fluctuation of $\hat{m}_z$, keeping $\hat{u}_x = \hat{u}_y = 0$. This reduces our effective theory to that of a single scalar field $\hat{m}_z$. To restore the energy for a domain wall configuration in the full order parameter space, we plug back $(u_x, u_y, m_z) = (u_x^0, u_y^0, u_z^0 + \hat{m}_z)$, with each (u_x, u_y, m_z) a parameter point $(\rho_x, \rho_y, \lambda) = (u_x/2J_1, -u_y/2J_1, m_z/4J_2)$ in Fig. 4.1(b). In the following, we go beyond the quadratic theory of Eq. (2.62) and examine higher order fluctuations of $\hat{m}_z$. We hope that these higher order fluctuations can provide information for not only fluctuations around local minima, but also tunneling between different minima.

2.6 Conventional Ginzburg Landau theory for domain wall

2.6.1 Free energy for fluctuations and full Ginzburg Landau theory

Consider the following free energy functional in d-dimensions, where the $\phi(\boldsymbol{x})$ is the full field for certain order parameter:

$$F[\phi] = \int [d^d x] \left[K[\nabla\phi(\boldsymbol{x})]^2 + \frac{\mathcal{M}}{2}\phi^2(\boldsymbol{x}) + \frac{U}{4}\phi^4(\boldsymbol{x}) \right], \tag{2.66}$$

we shall then get the equation of motion which reads:

$$0 = \frac{\delta F}{\delta \phi} = -K\nabla^2\phi + \mathcal{M}\phi + U\phi^3, \tag{2.67}$$

which gives a solution for $\mathcal{M} < 0$ and $U > 0$,

$$\phi_0(\boldsymbol{x}) \equiv \pm\sqrt{-\frac{\mathcal{M}}{U}} = \pm\phi_0, \tag{2.68}$$

as the local minimal for effective potential:

$$V_{\text{eff}} = \frac{\mathcal{M}}{2}\phi^2(\boldsymbol{x}) + \frac{U}{4}\phi^4(\boldsymbol{x}). \tag{2.69}$$

Note that, if we already know the position, we could also uniquely determine the interaction strength:

$$U = -\frac{\mathcal{M}}{\phi_0^2}. \tag{2.70}$$

Now we introduce the fluctuations $\delta\phi$ close to $\pm\phi_0$

$$\phi(\boldsymbol{x}) = \pm\phi_0 + \delta\phi, \tag{2.71}$$

then we can write down

$$\begin{aligned}
F[\phi] =& \int [d^d x] \left[K[\nabla\delta\phi(\boldsymbol{x})]^2 + \frac{\mathcal{M}}{2}[\pm\phi_0 + \delta\phi(\boldsymbol{x})]^2 + \frac{U}{4}[\pm\phi_0 + \delta\phi(\boldsymbol{x})]^4 \right] \\
\approx& \int [d^d x] \left[K[\nabla\delta\phi(\boldsymbol{x})]^2 + \frac{\mathcal{M}}{2}[\phi_0^2 \pm 2\phi_0\delta\phi(\boldsymbol{x}) + (\delta\phi(\boldsymbol{x}))^2] \right. \\
&\left. + \frac{U}{4}[\phi_0^4 \pm 4\phi_0^3\delta\phi(\boldsymbol{x}) + 6\phi_0^2(\delta\phi(\boldsymbol{x}))^2 \pm 4\phi_0(\delta\phi_0(\boldsymbol{x}))^3 + (\delta\phi(\boldsymbol{x}))^4] \right] \\
=& \int [d^d x] \left\{ K[\nabla\delta\phi(\boldsymbol{x})]^2 + \frac{\mathcal{M}}{2}\phi_0^2 + \frac{U}{4}\phi_0^4 \right. \\
&\left. + \left[\frac{\mathcal{M}}{2} + \frac{6U}{4}\phi_0^2 \right] (\delta\phi(\boldsymbol{x}))^2 \pm U\phi_0(\delta\phi_0(\boldsymbol{x}))^3 + \frac{U}{4}(\delta\phi(\boldsymbol{x}))^4 \right\},
\end{aligned} \tag{2.72}$$

by dropping the constant term and the odd term, and introducing

$$\mathcal{M}_{\text{eff}} = \frac{\mathcal{M}}{2} + \frac{6U}{4}\phi_0^2 = \frac{\mathcal{M}}{2} - \frac{3U}{2}\frac{\mathcal{M}}{u} = -\mathcal{M}, \tag{2.73}$$

we have the effective field theory for fluctuations solely:

$$F[\delta\phi] = \int [d^d x]\left[K[\nabla\delta\phi(\boldsymbol{x})]^2 + \mathcal{M}_{\text{eff}}[\delta\phi(\boldsymbol{x})]^2 + \frac{U}{4}[\delta\phi(\boldsymbol{x})]^4\right], \quad \mathcal{M}_{\text{eff}} = -\mathcal{M}, \quad U = -\frac{\mathcal{M}}{\phi_0^2}. \tag{2.74}$$

this is the energy for fluctuations just like the one we derived from Eq. (2.65), and we can also get the full field theory from the coefficient we derived from the effective field theory.

2.6.2 Generic domain wall

Consider the following free energy functional:

$$F[\phi] = \int [d^d x][K(\nabla\phi(\boldsymbol{x}))^2 + \frac{\mathcal{M}}{2}\phi^2(\boldsymbol{x}) + \frac{U}{4}\phi^4(\boldsymbol{x})]. \tag{2.75}$$

We shall then get the equation of motion which reads:

$$0 = \frac{\delta F}{\delta\phi} = -K\nabla^2\phi + \mathcal{M}\phi + U\phi^3. \tag{2.76}$$

Here K is the stiffness with respect to the spatial variation of ϕ, and one can define a length scale $\xi = \sqrt{K/|\mathcal{M}|}$ as the coherence length. Rescaling the free energy with respect to $\phi(\boldsymbol{x}) \equiv \sqrt{|\mathcal{M}|/U}\Phi$, and one can obtain:

$$\begin{aligned} F[\Phi] &= \int [d^d x]\left[K\frac{|\mathcal{M}|}{U}(\nabla\Phi)^2 + \frac{\mathcal{M}}{2}\frac{|\mathcal{M}|}{U}\Phi^2 + \frac{U}{4}\frac{\mathcal{M}^2}{U^2}\Phi^4\right] \\ &= \int [d^d x]\frac{\mathcal{M}^2}{U}\left[\frac{K}{|\mathcal{M}|}(\nabla\Phi)^2 + \frac{\text{sgn}(\mathcal{M})}{2}\Phi^2 + \frac{1}{4}\Phi^4\right]. \end{aligned} \tag{2.77}$$

Then we get the new EOM:

$$-\xi^2\nabla^2\Phi + \text{sgn}(\mathcal{M})\Phi + \Phi^3 = 0. \tag{2.78}$$

Consider the case of a domain $\mathcal{M} < 0$, we assume that all spatial variation occurs in the x-direction, and we set $\Phi(x = x_0) = 0$ and $\Phi(x = \infty) = 1$, we then arrive at:

$$-\xi^2\Phi''(x) - \Phi + \Phi^3 = 0, \tag{2.79}$$

which may be written as:

$$\xi^2\frac{d^2\Phi}{dx^2} = \frac{\partial}{\partial\Phi}\left[\frac{1}{4}(1-\Phi^2)^2\right]. \tag{2.80}$$

Multiplying the above equation by $\Phi'(x)$ and integrating once, we have:

$$\xi^2\left(\frac{d\Phi}{dx}\right)^2 = \frac{1}{2}(1-\Phi^2)^2 + C, \tag{2.81}$$

where C is a constant, which is fixed by setting $\Phi(x \to \infty) = +1$, which says $\Phi'(\infty) = 0$, hence $C = 0$. Integrating once more, we shall have:

$$\Phi(x) = \tanh\left(\frac{x - x_0}{\sqrt{2}\xi}\right), \tag{2.82}$$

and x_0 is determined by the zero points of the system. The width of the domain wall is ξ. In terms of the original field, that is:

$$\phi(\boldsymbol{x}) = \sqrt{\frac{|\mathcal{M}|}{K}}\Phi = \sqrt{-\frac{\mathcal{M}}{K}}\tanh\left(\frac{x - x_0}{\sqrt{2}\xi}\right), \quad \xi = \sqrt{\frac{K}{|\mathcal{M}|}} = \sqrt{-\frac{K}{\mathcal{M}}}. \tag{2.83}$$

The term $K = 0$ corresponds to the sharp domain wall.

2.6.3 Analysis of the domain wall

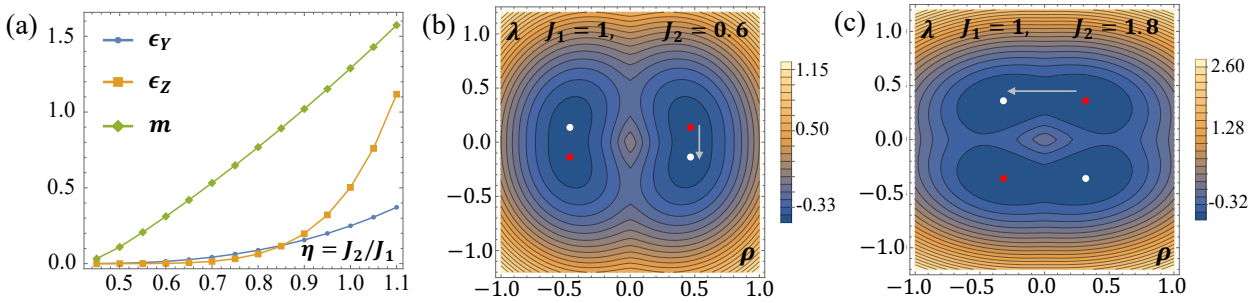

Figure 2.6: (a) The relations for $\mathcal{E}_Y(\eta)$ (blue), $\mathcal{E}_Z(\eta)$ (yellow), and $m(\eta)$, with $\eta = J_2/J_1$ tell the ratio between the nearest neighbor and second nearest neighbor coupling. The domain wall energy is calculated with respect to homogenous limit (without domain wall) (b) Contour plot of free energy $F(\rho_x^0 = \rho_y^0, \lambda^0)$ for small $\eta = J_2/J_1 = 0.6$, in which we can see the domain wall has the tendency to go from the red point with positive chirality to the white point with opposite λ along the arrow. (c) Contour plot of free energy $F(\rho_x^0 = \rho_y^0, \lambda^0)$ for large $\eta = J_2/J_1 = 1.8$ (which may not be realistic), which it tends to form the velocity domain wall.

The $F_T[u_x, u_y, m_z]$ is positive definite, means all kinds for the fluctuations should increase the energy compared with the homogeneous solution. For a given value of J_1, J_2, the mean-field ansatz corresponds to eight points in Hilbert space, each four belonging to one chirality, and we would like to pick the path that connecting two points with opposite chirality with minimal energy cost.

As these are all fluctuations, we can have by forcing via the boundary condition

1. u_x cannot change sign by these dynamics

2. u_y can change sign via nonzero $(\partial_x u_y)^2$, we can force $m_z = u_x = 0$, this leads to effective energy for fluctuation fields, i.e., Eq. (2.74):

$$F_T \simeq \frac{m}{24\pi u_x^0 a_0}\int [dx]\mathcal{F}_Y(x) = \frac{m}{24\pi u_x^0 a_0}\int [dx][2a_0^2(\partial_x u_y)^2 - 16m^2 u_y^2 + \frac{U_y}{4}u_y^4], \tag{2.84}$$

by using the relation mentioned in Sec. [2.6.1], and defining the full field $\tilde{u}_y = u_y^0 + u_y$, we arrive at the full Ginzburg–Landau theory, i.e., Eq. (2.66)

$$F_T \simeq \frac{m}{24\pi u_x^0 a_0}\int [dx]\mathcal{F}_Y(x) = \frac{m}{24\pi u_x^0 a_0}\int [dx][2a_0^2(\partial_x \tilde{u}_y)^2 - 16m^2 \tilde{u}_y^2 + \frac{U_y}{4}\tilde{u}_y^4], \tag{2.85}$$

comparing with Eq. (2.66), one can read off the coefficients as:

$$K = 2a_0^2, \quad \frac{\mathcal{M}}{2} = -16m^2, \quad U_y = -\frac{\mathcal{M}}{\phi_0^2} = \frac{32m^2}{(u_y^0)^2}. \tag{2.86}$$

From Sec. [2.6.2], we know that such a theory can hold a domain wall if one can impose the twisted boundary condition for $\tilde{u}_y$, with the correlation length ξ

$$\xi_b = \sqrt{-\frac{K}{\mathcal{M}}} = \sqrt{\frac{a_0^2}{16m^2}} = \frac{a_0}{4|m|}. \tag{2.87}$$

This leads to the configuration:

$$\tilde{u}_y = u_y^0 \tanh[(x - x_0)/\sqrt{2}\xi_b], \quad u_y^0 = 1. \tag{2.88}$$

With the domain wall energy reads:

$$\begin{aligned}\mathcal{E}_Y &\simeq \frac{m}{24\pi u_x^0 a_0}\int [dx][2[\partial_x \tilde{u}_y(x)]^2 - 16m^2[\tilde{u}_y(x)]^2 + \frac{2}{4}\tilde{u}_y(x)^4 - \mathcal{F}_Y(\infty)] \\ &\propto \frac{1}{\pi}\int [dx]\{m^3 \mathrm{sech}^4[2\sqrt{2}mx]\}\end{aligned} \tag{2.89}$$

As the fluctuations $u_x = m_z = 0$, such that the full field $\tilde{u}_x$ and $\tilde{m}_z$ is spatial independent, we can further derive the configuration for chirality $\chi(x)$:

$$\chi(x) = \tilde{u}_x(x)\tilde{u}_y(x)\tilde{m}_z(x) = u_x^0 u_y^0 m_z^0 \tanh[(x - x_0)/\sqrt{2}\xi_b] = \chi_0 \tanh[(x - x_0)/\sqrt{2}\xi_b], \tag{2.90}$$

where χ_0 is the chirality for homogeneous case. By slightly modifying Sec. [2.8.2] (expanding Bloch Hamiltonian around $(0, \pi/2)$), we have the edge dispersion reads:

$$E_{\text{edge}}(k_y) = \pm v_{\text{edge}} k_y, \quad v_{\text{edge}} = 4J_2\lambda a_0/\hbar. \tag{2.91}$$

3. m_z can change sign via the dynamic of non-zero $(\partial_x m_z)^2$, we can force $u_x = u_y = 0$, this leads to the effective energy for fluctuation fields, i.e., Eq. (2.74)

$$F_T \simeq \frac{m}{24\pi u_x^0 a_0}\int [dx]\mathcal{F}_Z(x) = \frac{m}{24\pi u_x^0 a_0}\int [dx][\frac{9}{4}a_0^2(\partial_x m_z)^2 - 21m^2 m_z^2 + \frac{U_z}{4}m_z^4], \tag{2.92}$$

by using the relation mentioned in Sec. [2.6.1], and defining the full field $\tilde{m}_z = m_z^0 + m_z$, we arrive at the full Ginzburg Landau theory, i.e. Eq. (2.66):

$$F_T \simeq \frac{m}{24\pi u_x^0 a_0}\int [d^2x]\mathcal{F}_Z(x) = \frac{m}{24\pi u_x^0 a_0}\int [dx][\frac{9}{4}a_0^2(\partial_x \tilde{m}_z)^2 - 21m^2 \tilde{m}_z^2 + \frac{U_z}{4}\tilde{m}_z^4], \tag{2.93}$$

comparing with Eq. (2.66), one can read the coefficient as:

$$K = \frac{9}{4}a_0^2,\ \frac{\mathcal{M}}{2} = -21m^2,\ U_z = -\frac{\mathcal{M}}{\phi_0^2} = \frac{42m^2}{(m_z^0)^2}, \tag{2.94}$$

From Sec. [2.6.2], we know that such a theory can hold a domain wall if one can impose the twisted boundary condition for $\tilde{m}_z$, with the correlation length ξ_z

$$\xi_z = \sqrt{-\frac{K}{\mathcal{M}}} = \frac{3a_0}{2|m|\sqrt{42}}, \quad \tilde{m}_z = m_z^0 \tanh[(x - x_0)/\sqrt{2}\xi_z], \quad m_z^0 = \pm m. \tag{2.95}$$

With the domain wall energy reads:

$$\begin{aligned}\mathcal{E}_Z &\simeq \frac{m}{24\pi u_x^0 a_0}\int [dx][\frac{9}{4}a_0^2(\partial_x \tilde{m}_z)^2 - 21m^2\tilde{m}_z^2 + \frac{U_z}{4}\tilde{m}_z^4 - \mathcal{F}_Z(\infty)] \\ &\propto \frac{1}{\pi u_x^0 a_0}\int [dx]\left[\frac{21m^5}{16}\mathrm{sech}^4\left(2\sqrt{\frac{7}{3}}mx\right)\right],\end{aligned} \tag{2.96}$$

and the chirality also have the profile

$$\chi(x) = \tilde{u}_x(x)\tilde{u}_y(x)\tilde{m}_z(x) = u_x^0 u_y^0 m_z^0 \tanh[(x - x_0)/\sqrt{2}\xi_z] = \chi_0 \tanh[(x - x_0)/\sqrt{2}\xi_z]. \tag{2.97}$$

According to Jackiw's theory Eq. (2.122), we have the edge dispersion for this type of domain wall as:

$$E_{\text{edge}}(k_y) = \pm v_{\text{edge}} k_y, \quad v_{\text{edge}} = 2J_1\bar{\rho}_y a_0/\hbar. \tag{2.98}$$

Now we would like to compare the free energy for velocity domain wall Eq. (2.89) and lambda domain wall Eq. [2.101], as shown in Fig.[2.6.(a)]. For small $\eta = J_2/J_1$ (which is the physical case as the next-nearest neighbor coupling is weaker than the nearest neighbor coupling), the system will favor the lambda domain wall. This is consistent with the energy plot of Fig. 2.6.(b,c), where the transition will happen along the smoother approach, though the phase transition point may be different based on numerics.

2.6.4 Domain wall tension for the Ginzburg Landau ϕ^4 theory

The domain wall energy can be written in terms of dimensionless local gap $\tilde{m}(x) = m(x)/J_1$ as

$$F = \int [dx]\mathcal{F}[x] \sim \frac{m_0 J_1}{24\pi a_0}\int [dx]\bigg[K(\partial_x m)^2 - \frac{r}{2}m^2 + \frac{U}{4}m^4\bigg], \tag{2.99}$$

where $m_0 = 2J_2\bar{\lambda}/J_1\bar{\rho}_0$ is the dimensionless mass deep in the bulk, which is proportional to the bulk gap in the homogeneous limit. For $J_2 < J_1$, in general $0 < m_0 < 1$.

According to the effective field theory mentioned in our previous note, $K = \tilde{K}_0 l_0^2$, with $\tilde{K}_0$ is a pure number, while $r \propto m_0^2$, and $Um_0^2 = r$. We have the following solution for equation of motions for the boundary condition mentioned in Fig. [2.3.(b)]:

$$\tilde{m}(x) = m_0 \tanh[(x - x_0)/(\sqrt{2}\xi)], \quad \xi = \sqrt{\frac{K}{r}} = \frac{l_0}{m_0}, \tag{2.100}$$

where l_0 is a length scale close to the lattice constant.

The domain wall tension (domain wall energy measured from the homogenous results) reads:

$$\begin{aligned}\mathcal{E} &= \frac{m_0 J_1}{24\pi}\int [dx][K(\partial_x m)^2 - \frac{r}{2}m + \frac{U}{4}m^4 - \mathcal{F}(\infty)] \\ &= \frac{m_0^5 J_1 \tilde{K}_0}{96\pi}\int [dx]\bigg[\mathrm{sech}^4\bigg(\frac{x - x_0}{\sqrt{2}\xi}\bigg)\bigg] \propto m_0^5 J_1 \ll J_1 \sim J_2,\end{aligned} \tag{2.101}$$

where we have used fact $0 < m_0 < 1$ such that $m_0^5 \ll 1$, while J_1 and J_2 are to the same order.

2.7 Singular Ginzburg-Landau $|\phi|^3$ theory

We point out that the gapless edge modes on the domain wall can introduce additional terms to the Ginzburg–Landau free energy. Specifically, in our case a $|m_z^3|$ term appears. To see this, let's consider the most generic Ginzburg-Landau theory:

$$F \simeq \frac{m}{u_x^0 a_0}\int [dx]\bigg[K(\partial_x m)^2 + V(m)\bigg], \tag{2.102}$$

where $V(m)$ is w-shaped with two local minimal, and does not have to be a traditional ϕ^4 theory.

2.7.1 Energy for a homogenous slab and approximation based on Dirac-fermion's spectrum

Since we know the domain wall solution is $\rho(x) = \bar{\rho}_x$, $\rho(y) = \bar{\rho}_y$ and $\lambda(x) = \bar{\lambda}\tanh x/(\sqrt{2}\xi)$, we could take the approximation that the spectrum is that of a massive Dirac fermion, such

that we can formulate the energy in terms of the local mass m as (we would like to see the scaling so we drop all the coefficient with dimension such as v_F):

$$V(m) \sim m^2 - \int_{\mathrm{BZ}} [d^2k]\sqrt{k^2+m^2} \sim m^2 - \int_0^{k_0} dkk\sqrt{k^2+m^2} \sim m^2 + \frac{1}{3}|m|^3 - \frac{1}{3}(k_0^2+m^2)^{3/2}, \tag{2.103}$$

where k_0 is the cutoff from the BZ. Note the presence of a $|m|^3$ term, which is the unique signature from the spectrum of Dirac fermions in 2D, and would be singular at the gapless point $m = 0$.

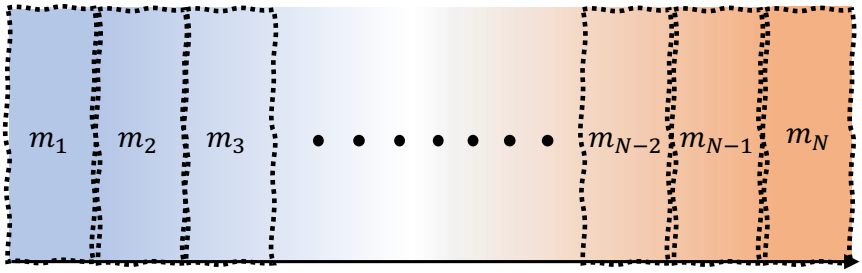

Figure 2.7: Partition of chiral spin liquid with spatial varying mass. We assume that the mass is uniform in each block m_i, with $m_1 \equiv -m_0 = -4J_2\bar{\lambda}$ and $m_N = +m_0 = +4J_2\bar{\lambda}$.

2.7.2 Singular Ginzburg-Landau theory for domain walls

We know the domain wall can be captured by the chirality profile $\chi(x) = \rho_x(x)\rho_y(x)\lambda(x) = \bar{\rho}_x\bar{\rho}_y\lambda(x)$. The local mass $m(x)$ is proportional to $\lambda(x)$ as $m(x) = 4J_2\lambda(x)$. So long as the domain varies slow enough, we can divide it into individual slabs, as shown in Fig. [2.7]. One can view the mass as homogenous for i-th slab as m_i, and the energy for i-th slab can be captured by Eq. (2.103). Thus the potential energy for the domain wall is:

$$V(m) = \sum_i V(m_i) \sim \sum_i \left[m_i^2 + \frac{1}{3}|m_i|^3 - \frac{1}{3}(k_0^2+m_i^2)^{3/2}\right] \sim \int [dx]\left[-\frac{r}{2}m^2 + \frac{S}{3}|m|^3\right], \tag{2.104}$$

add back the stiffness term, we have the singular Ginzburg Landau theory:

$$F \simeq \frac{m}{u_x^0 a_0}\int dx\left[K(\partial_x m)^2 + V(m)\right] = \frac{m}{u_x^0 a_0}\int dx\left[K(\partial_x m)^2 - \frac{r}{2}m^2 + \frac{S}{3}|m|^3\right]. \tag{2.105}$$

One can plot Eq. (5.30) with ρ_x and ρ_y fixed to the homogenous mean field value $\bar{\rho}_x$ and ρ_y, as the $V(\lambda)$ shown in Fig. [2.8.(a)]. There are two local minimals in $V(\lambda)$, and the domain wall captures the tunneling from one local minimal to the other minimal with opposite chirality. The $V(\lambda)$ here may be viewed as the potential function $V(m)$ in the Ginzburg-Landau theory for m in Eq. (2.102). The discontinuity of the third order derivative for $V(m)$ shows the existence of $|\lambda|^3$ ($|m|^3$) in the expansion of $V(\lambda)$ ($V(m)$).

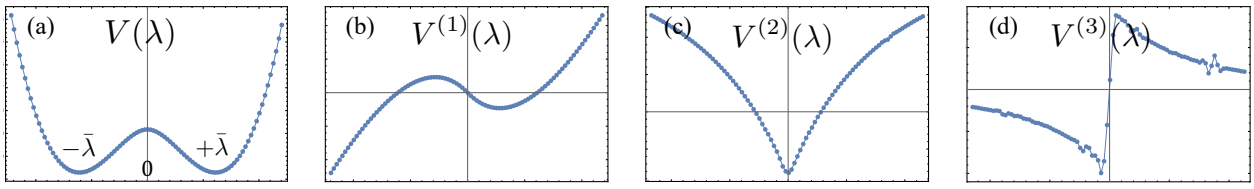

Figure 2.8: (a) $V(\lambda) = V(\bar{\rho}_x, \bar{\rho}_y, \lambda)$ of Eq. (5.30) with ρ_x and ρ_y fixed to their homogenous value $\bar{\rho}_x$ and $\bar{\rho}_y$ respectively, while λ is varying. The horizontal axis is λ for (a-d). Figure (b-d) are the first, second, and third order differentiate of $V(\lambda)$. Clearly, the discontinuity in (d) for the $\frac{d^3V(\lambda)}{d\lambda^3}$ at $\lambda = 0$ implies the existence of $|\lambda^3|$.

2.7.3 Modification to domain wall profile

Consider the following generic Ginzburg-Landau theory for order parameter ϕ:

$$F[\phi] \simeq \frac{m}{u_x^0 a_0} \int dx \Big[K(\partial_x \phi)^2 + V(\phi) \Big], \tag{2.106}$$

where $V(\phi)$ is an even function with two local minima with a shape of w like Fig. [2.8.(a)] (but not necessary to be a ϕ^4 theory). The equation of motion then reads:

$$-K\partial_x^2 \phi + \frac{dV(\phi)}{d\phi} = 0. \tag{2.107}$$

Since:

$$\phi'' = \frac{d\phi'}{dx} = \frac{d\phi'}{d\phi}\frac{d\phi}{dx} = \frac{d\phi'}{d\phi}\phi' = \frac{1}{2}\frac{d[(\phi')^2]}{d\phi}, \tag{2.108}$$

then we shall have:

$$\frac{K}{2}\frac{d(\phi')^2}{d\phi} = \frac{dV(\phi)}{d\phi} \tag{2.109}$$

integrating from both sides we have:

$$\frac{K}{2}(\phi')^2 = V[\phi] + \text{Const.} \tag{2.110}$$

We assume that when $x \to \infty$, $\phi(x) \to \phi_m$ (the local minimal for $V(\phi)$ deep in the bulk) and $\phi'(x) = 0$, thus we have

$$\frac{d\phi}{dx} = \pm\sqrt{\frac{2}{K}[V(\phi) - V(\phi_m)]} \tag{2.111}$$

from which we can solve:

$$x - x_0 = \pm \int_0^{\Phi} \frac{d\phi}{\sqrt{\frac{2}{K}[V(\phi) - V(\phi_m)]}} \tag{2.112}$$

the right hand side counts for the time of a classical particle moving in some strange potential field. The profile may no longer have a closed-form analytic solution like tanh as in the ϕ^4 theory, and we have the decay half-width:

$$d = \int_0^{\phi_m/2} \frac{d\phi}{\sqrt{\frac{2}{K}[V(\phi) - V(\phi_m)]}} = \sqrt{\frac{K}{r}} \int_0^{\phi_m/2} \frac{d\phi}{\sqrt{2[V(\phi) - V(\phi_m)]/r}} = \eta\xi, \tag{2.113}$$

where ϕ_m is the value of order parameter that deep in the bulk (i.e., $x \to \pm\infty$). Then we shall have $d_1 = \eta_1\xi$ and $d_2 = \eta_2\xi$ denotes the width of the domain wall. They have the same order ξ (inverse proportional to bulk gap), but the exact value of η_1 and η_2 may be different, as we will find in the following case.

Consider two different way to formulate the potential $V(\phi)$, where mass r for them are from integrate out the spinons in our old note which should be identical:

$$\begin{aligned} V_1(\phi) &= -\frac{r}{2}\phi^2 + \frac{S}{3}|\phi|^3 + \frac{U_1\phi^4}{4}, \\ V_2(\phi) &= -\frac{r}{2}\phi^2 + \frac{U_2}{4}\phi^4. \end{aligned} \tag{2.114}$$

The local minimal for $V_1(\phi)$ and $V_2(\phi)$ are set at same value ϕ_m, such that:

$$\left.\frac{\partial V_1(\phi)}{\partial\phi}\right|_{\phi_m} = \left.\frac{\partial V_2(\phi)}{\partial\phi}\right|_{\phi_m} = 0, \quad \left.\frac{\partial^2 V_1(\phi)}{\partial\phi^2}\right|_{\phi_m} > 0, \quad \left.\frac{\partial^2 V_2(\phi)}{\partial\phi^2}\right|_{\phi_m} > 0, \tag{2.115}$$

solving above leads to the following requirement S, U_1, U_2:

$$U_2 = \frac{S^2 + 2rU_1 + S\sqrt{S^2 + 4rU_1}}{2r}. \tag{2.116}$$

With Eq. [2.116], we will have $V_1(\phi)$ and $V_2(\phi)$ has the same value of local minimal. Now we substitute Eq. (2.114) into Eq. (2.112), and conduct the integral numerically, as shown in Fig. (2.9). From which we find that a positive $|\phi^3|$ will make the domain wall wider than the ϕ^4 theory.

2.8 Edge states for chiral spin liquids

2.8.1 Low energy theory for the bulk

We can expand the Hamiltonian around the point $(k_x, k_y) \sim (0, 0)$, then we shall have:

$$H_0 \sim \sum_{\boldsymbol{k}} \tilde{\psi}^\dagger_{\boldsymbol{k}}[2J_1^x\bar{\rho}_x^0 a_0 k_x\sigma_x + 2(J_2^+\bar{\lambda}_+^0 + J_2^-\bar{\lambda}_-^0)\sigma_y - 2J_1^y\bar{\rho}_y^0 a_0 k_y\sigma_z]\tilde{\psi}_{\boldsymbol{k}} \tag{2.117}$$

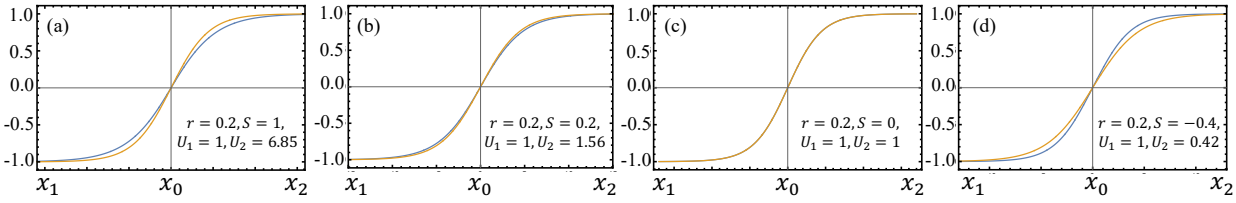

Figure 2.9: Profile of ϕ from integrating Eq. [2.112] for two potentials given in Eq. [2.114]. With the data listed in the bottom right of each plot, $V_1(\phi)$ and $V_2(\phi)$ would have same value of local minimal ϕ_m as long as the constraint Eq. [2.116] is satisfied. The blue curve is the solution from integraing $V_1(\phi)$, and the orange curve is from integrating $V_2(\phi)$. For $S = 0$, $U_1 = U_2$, we have two profile coincides with each other, as shown in (c). For $S > 0$, we have wider domain wall as the $|\phi^3|$ is introduced, see in (b). In general, the large $|S|$ is, the greater the modification to the domain wall width will be. When $S < 0$, we have the domain wall with $|\phi^3|$ become sharper compared with the ϕ^4 theory, as shown in (d).

one can further set $\tilde{\psi}_{\boldsymbol{k}} = \sigma_x \psi_{\boldsymbol{k}}$ to rotate the above to a more convenient way

$$H_0 \sim \sum_{\boldsymbol{k}} \psi^\dagger_{\boldsymbol{k}} [\hbar v_x k_x \sigma_x + \hbar v_y k_y \sigma_y + \tilde{m}\sigma_z] \psi_{\boldsymbol{k}}, \tag{2.118}$$

with:

$$\hbar v_x = 2J_1^x \bar{\rho}_x^0 a_0, \quad \hbar v_y = -2J_1^y \bar{\rho}_y^0 a_0, \quad \tilde{m} = 2(J_2^+ \bar{\lambda}_+^0 + J_2^- \bar{\lambda}_-^0). \tag{2.119}$$

2.8.2 Edge velocity from Jackiw-Rebbi mechanism and QAHE

The Jackiw-Rebbi mechanism [110, 24] for QAHE tells that, for a low energy effective theory:

$$H = \int dx dk_y \{\psi^\dagger_{k_y}(x)[\hbar v_x k_x \sigma_x + \hbar v_y k_y \sigma_y + \tilde{m}(x)\sigma_z]\psi_{k_y}(x)\}, \tag{2.120}$$

where $\tilde{m}(x)$ change sign at $x = 0$, say $\tilde{m}(x) = \tilde{m}_0 \tanh[(x - x_0)/(\sqrt{2}\xi)]$ for instance, then the edge states on $x = x_0$ will have the following dispersion:

$$E_{\text{edge}}(k_y) = -v_{\text{edge}} k_y, \quad v_{\text{edge}} = |v_y|, \tag{2.121}$$

for the low energy theory of chiral spin liquid Eq. (2.117), we shall have:

$$v_{\text{edge}} = |2J_1^y \bar{\rho}_y^0 a_0|. \tag{2.122}$$

Note that the domain wall hosts four $S = 1/2$ spinon edge modes, and the full edge theory is described by four copies of Eq. (2.120), as shown in Fig. 2.10(b). By applying the non-double occupancy condition one recovers the physical $S=1$ excitation from the two $S=1/2$ spinon edge modes from each domain [167, 143], and the edge excitation has total spin $S = 2$.

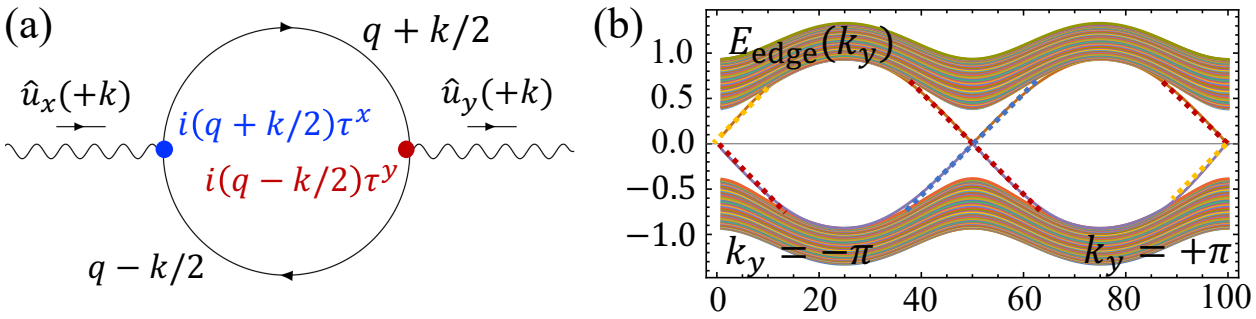

Figure 2.10: (a) Feynman diagram for spinon-amplitude fluctuation at one-loop level. (b) Spinon energy spectrum corresponding to Fig. 2.4(a). Note that there are in total four linear dispersions in the plot. The two linear dispersions marked by red (each has double degeneracy) correspond to the four spinon edge modes right at the domain wall. The blue (orange) dotted lines correspond to the edge modes on the boundary on the far left (far right).

2.8.3 Edge spinon confinement

We follow Refs. [167, 143] to get the effective field theory from our mean field chiral spin liquids. The two flavors of fermions, $\{f_\pm\}$, fill the lowest bands with Chern number $C_\pm = 1$. Conserved fermion currents J^μ_m can be expressed in terms of dynamical U(1) gauge field a^m_μ as $J^\mu_m = \epsilon^{\mu\nu\lambda}\partial_\nu a^m_\lambda/(2\pi)$, where the summation over repeated μ, ν, λ is assumed. The fermion band structure in this CSL is described by the following two copies of U(1) Chern Simons theory:

$$\begin{aligned}\mathcal{L}_f &= \frac{\epsilon^{\mu\nu\lambda}}{4\pi}\left(\sum_{m=\pm} C_m a^m_\mu \partial_\nu a^m_\lambda\right) + \frac{\epsilon^{\mu\nu\lambda}}{2\pi} A^{S^z}_\mu \partial_\nu \left[\frac{1}{2}(a^+_\lambda - a^-_\lambda)\right] \\ &= \frac{\epsilon^{\mu\nu\lambda}}{4\pi} C_{IJ} a_{I\mu}\partial_\nu a_{J\lambda} + \frac{\epsilon^{\mu\nu\lambda}}{2\pi} t_I A^{S^z}_\mu \partial_\nu a_{I\lambda},\end{aligned} \tag{2.123}$$

where $A^{S^z}_\mu$ is the gauge potential that couples to the S^z spin density and current, $I, J = 1, 2$ and:

$$C = \begin{pmatrix} 1 & 0 \\ 0 & 1 \end{pmatrix}, \quad t = \begin{pmatrix} +1/2 \\ -1/2 \end{pmatrix}. \tag{2.124}$$

The local no-double occupancy constraint:

$$\langle f^\dagger_{i\alpha} f_{i\alpha}\rangle = 1, \tag{2.125}$$

can be written in a covariant form:

$$\frac{\epsilon^{\mu\nu\lambda}}{2\pi}\sum_m \partial a^m_\lambda = \sum_{m=\pm} J^\mu_m = \bar{J}^\mu \equiv \frac{\epsilon^{\mu\nu\lambda}}{2\pi}\partial_\nu \bar{a}_\lambda, \tag{2.126}$$

where $\bar{a}_\mu$ is a nondynamical (constant) background field, whose density $\bar{J}^0 = (\partial_x \bar{a}_y - \partial_y \bar{a}_x)/2\pi$ is the right hand side of Eq. (2.125). The constriant can be implemented by introducing an extra U(1) gauge field b_μ as a Lagrangian multiplier:

$$\mathcal{L}_{\rm con} = \frac{\epsilon^{\mu\nu\lambda}}{2\pi} b_\mu \partial_\nu \big(a^+_\lambda + a^-_\lambda - \bar{a}_\lambda\big) = \frac{\epsilon^{\mu\nu\lambda}}{2\pi} b_\mu \partial_\nu \big(\sum_I a_{I\lambda} - \bar{a}_\lambda\big). \tag{2.127}$$

After integrating out the gauge field b^μ and $a_{2\mu}$ (or a^-_μ in the original language), we can obtain the low-energy theory of the CSL:

$$\mathcal{L}_{\rm CS} = \mathcal{L}_f + \mathcal{L}_{\rm con} = \frac{\epsilon^{\mu\nu\lambda}}{4\pi} K a_\mu \partial_\nu a_\lambda + \frac{\epsilon^{\mu\nu\lambda}}{2\pi} q A^{S^z}_\mu \partial_\nu a_\lambda, \tag{2.128}$$

with a_μ for a^+_μ or $a_{1\mu}$. The 1×1 K matrix and q-vector are:

$$K = 2, q = 1. \tag{2.129}$$

The CSL has spin quantum Hall conductance in unit of $1/2\pi$:

$$\sigma^S_{xy} = q^T K^{-1} q = 1/2, \tag{2.130}$$

in accordance with the bulk spinon transport.

The corresponding edge theory can be derived from bulk-edge correspondence. The effective edge theory can be written as:

$$\mathcal{L}_{\rm edge} = \frac{1}{4\pi} K \partial_t \phi \partial_x \phi - V(\partial_x \phi)^2 + \frac{1}{2\pi} q A^{S^z}_0 (\partial_x \phi - \partial_t \phi). \tag{2.131}$$

The K-matrix and q vector are defined in Eq. (2.129). The V is the edge velocity, as K is positive, the edge state is chiral and stable. The S^z density on the edge is given by the defined bosons as:

$$S^z(x) \simeq q \frac{\partial_x \phi(x)}{2\pi}, \tag{2.132}$$

as $q = 1$ it indeed carries S^z quantum number $+1$. The edge boson fields satisfy the Kac-Moody algebra:

$$[\phi(x), \partial_x \phi(y)] = i2\pi (K^{-1}) \delta(x - y) = i\pi \delta(x - y), \tag{2.133}$$

or $[\phi(x), \phi(y)] = i(\pi/2)\text{sign}(x - y)$, which is indeed a $\text{U}(1)_2$ theory.

2.9 Discussion and outlook

We studied the domain wall for $\nu = 1/2$ Kalmeyer-Laughlin chrial spin liquid with opposite chiralities. Starting from a spatially varying, self-consistent mean-field ansatz for spinons, we mapped out the spatial profile of the domain wall in terms of the spin chirality. We further

proposed an effective Ginzburg–Landau field theory for mean-field bond amplitude fluctuations which qualitatively produces the change of chirality across the domains, from which we derived the non-topological properties of the multi-domain system, such as the domain wall tension and edge velocity. We argue that the gapless modes at the edge contribute an extra, non-analytic, $|\phi^3|$ term to the domain wall theory. As shown in Fig. 2.4(d), in our toy model, the non-universal features, such as the bulk spinon gap Δ, domain wall width ξ and edge spinon velocity v_{edge}, are all determined by the fundamental exchange parameters J_1 and J_2. While there is no direct way of measuring the exchange strength, other quantities, such as the spinon gap, can be directly read out from e.g. neutron scattering experiments. The experimental determination of any quantities above would provide information about the others.

Note that, although our work focused on a simple $J_1 - J_2$ model for CSL on a square lattice, the self-consistent mean-field numerics and Ginzburg–Landau analysis can be carried out in many other contexts, such as other lattices. It is also possible to extend the Ginzburg–Landau analysis to a larger space of magnetic order parameters, as was recently considered in [103]. Our approach could be applied to the features of other multi-domain systems with coexisting conventional order and topological order, such as Pfaffian–anti-Pfaffian-domains in the $\nu = 5/2$ fractional quantum Hall system [295, 300, 51, 52] and spontaneous time-reversal symmetry breaking domains in fractional topological insulators [190, 139, 225, 251]. Another example would be the excitonic condensed phase of quantum Hall insulators [112], where the order parameter for exciton condensation may have a similar profile as that of the spin chirality in chiral spin liquids.

2.10 Appendix: Detailed field theory calculations

2.10.1 Useful Dictionary

Before conducting the calculations for the loop diagram, we acknowledge the following useful formulas for traces of Pauli matrices [257, 203]:

$$\mathrm{Tr}\tau^a\tau^b = 2\delta^{ab}, \quad \mathrm{Tr}\tau^a\tau^b\tau^c = 2i\epsilon^{abc}, \quad \mathrm{Tr}(\tau^a\tau^b\tau^c\tau^d) = 2(\delta^{ab}\delta^{cd} + \delta^{ad}\delta^{bc} - \delta^{ac}\delta^{bd}). \quad (2.134)$$

and for Feynman integrals:

$$\int \frac{d^{2\omega}l}{(2\pi)^{2\omega}} \frac{1}{(l^2+M^2+2l\cdot p)^A} = \frac{\Gamma(A-\omega)}{(4\pi)^\omega \Gamma(A)} \frac{1}{(M^2-p^2)^{A-\omega}},$$
$$\int \frac{d^{2\omega}l}{(2\pi)^{2\omega}} \frac{l_\mu}{(l^2+M^2+2l\cdot p)^A} = -\frac{\Gamma(A-\omega)}{(4\pi)^\omega \Gamma(A)} \frac{p_\mu}{(M^2-p^2)^{A-\omega}},$$
$$\int \frac{d^{2\omega}l}{(2\pi)^{2\omega}} \frac{l_\mu l_\nu}{(l^2+M^2+2l\cdot p)^A} = \frac{1}{(4\pi)^\omega \Gamma(A)} \times \left[p_\mu p_\nu \frac{\Gamma(A-\omega)}{(M^2-p^2)^{A-\omega}} + \frac{1}{2}\delta_{\mu\nu} \frac{\Gamma(A-1-\omega)}{(M^2-p^2)^{A-1-\omega}} \right],$$
$$\int \frac{d^{2\omega}l}{(2\pi)^{2\omega}} \frac{l_\mu l_\nu l_\rho l_\sigma}{(l^2+M^2+2l\cdot p)^A} = \frac{1}{(4\pi)^\omega \Gamma[A]} \Bigg[p_\mu p_\nu p_\rho p_\sigma \frac{\Gamma(A-\omega)}{(M^2-p^2)^{A-\omega}}$$
$$+ \frac{1}{2}[\delta_{\mu\nu}p_\rho p_\sigma + \delta_{\nu\sigma}p_\mu p_\rho + \delta_{\rho\sigma}p_\mu p_\nu + \delta_{\mu\rho}p_\nu p_\sigma + \delta_{\nu\rho}p_\mu p_\sigma + \delta_{\mu\sigma}p_\rho p_\nu] \frac{\Gamma(A-1-\omega)}{(M^2-p^2)^{A-1-\omega}}$$
$$+ \frac{1}{4}[\delta_{\mu\nu}\delta_{\rho\sigma} + \delta_{\nu\rho}\delta_{\mu\sigma} = \delta_{\mu\rho}\delta_{\nu\sigma}] \frac{\Gamma(A-2-\omega)}{(M^2-p^2)^{A-2-\omega}} \Bigg]. \tag{2.135}$$

2.10.2 Two $\hat{u}$ vertices (Diagrams like Fig. [2.5.(a)])

The effective action reads:

$$S^A_{\text{eff}} \equiv \frac{1}{2} \int \frac{d^3k}{(2\pi)^3} \Pi^A_{\mu\nu}(k) \hat{u}_\mu(+k) \hat{u}_{-\nu}(k). \tag{2.136}$$

With the corresponding polarization function $\Pi^1_{\mu\nu}(k)$, and two $\hat{u}$ vertices reads: $(q_\mu + k_\mu/2)\tau^\mu$, and $(q_\nu - k_\nu/2)\tau^\nu$ (note that the repeated indices μ, ν does not stands for summation, it's just means that the Pauli matrix is bond to the corresponding momentum, say $k_x\tau_x$ and

$k_y\tau_y)$

$$
\begin{aligned}
\Pi^A_{\mu\nu}(k) =& -\int \frac{d^3q}{(2\pi)^3}\mathrm{Tr}\left[\frac{m_z^0+i(q_a+k_a/2)\tau^a}{(m_z^0)^2+(q+k/2)^2}\tau^\mu\frac{m_z^0+i(q_b-k_b/2)\tau^b}{(m_z^0)^2+(q-k/2)^2}\tau^\nu\right](q_\mu+k_\mu/2)(q_\nu-k_\nu/2)\\
=& -\int \frac{d^3q}{(2\pi)^3}\mathrm{Tr}\left[\frac{[m_z^0+i(q_a+k_a/2)\tau^a]\tau^\mu[m_z^0+i(q_b-k_b/2)\tau^b]\tau^\nu}{[(m_z^0)^2+(q+k/2)^2][(m_z^0)^2+(q-k/2)^2]}\right](q_\mu+k_\mu/2)(q_\nu-k_\nu/2)\\
=& -\int \frac{d^3q}{(2\pi)^3}\int_0^1[dx]\frac{\Gamma(1+1)}{\Gamma(1)\Gamma(1)}\mathrm{Tr}\left[\frac{[m_z^0+i(q_a+k_a/2)\tau^a]\tau^\mu[m_z^0+i(q_b-k_b/2)\tau^b]\tau^\nu}{\{[(q+k/2)^2+(m_z^0)^2](1-x)+[(q-k/2)^2+(m_z^0)^2]x\}^2}\right]\\
&\times(q_\mu+k_\mu/2)(q_\nu-k_\nu/2)\\
=& -\int \frac{d^3q}{(2\pi)^3}\int_0^1[dx]\mathrm{Tr}\left[\frac{[m_z^0+i(q_a+k_a/2)\tau^a]\tau^\mu[m_z^0+i(q_b-k_b/2)\tau^b]\tau^\nu}{\{q^2+2q\cdot[1/2-x]k+(m_z^0)^2+k^2/4\}^2}\right]\\
&\times(q_\mu+k_\mu/2)(q_\nu-k_\nu/2)\\
=& -\int \frac{d^3q}{(2\pi)^3}\int_0^1[dx]\mathrm{Tr}\left[\frac{[m_z^0+i(q_a+k_a/2)\tau^a]\tau^\mu[m_z^0+i(q_b-k_b/2)\tau^b]\tau^\nu}{[(q+(1/2-x)k)^2+x(1-x)k^2+(m_z^0)^2]^2}\right]\\
&\times(q_\mu+k_\mu/2)(q_\nu-k_\nu/2)
\end{aligned}
\tag{2.137}
$$

We can further define:

$$
\tilde{q}=q+(1/2-x)k,\quad \tilde{q}+xk=q+k/2,\quad \tilde{q}-k+xk=q-k/2. \tag{2.138}
$$

Then we arrive at:

$$
\begin{aligned}
\Pi^A_{\mu\nu}(k) =& -\int_0^1[dx]\int\frac{d^3\tilde{q}}{(2\pi)^3}\mathrm{Tr}\left[\frac{[m_z^0+i(\tilde{q}_a+xk_a)\tau^a]\tau^\mu[m_z^0+i(\tilde{q}_b-k_b+xk_b)\tau^b]\tau^\nu}{[\tilde{q}^2+x(1-x)k^2+(m_z^0)^2]^2}\right]\\
&\times(\tilde{q}_\mu+xk_\mu)(\tilde{q}_\nu-k_\nu+xk_\nu)\\
=& -\int_0^1[dx]\int\frac{d^3q}{(2\pi)^3}\mathrm{Tr}\left[\frac{[m_z^0+i(q_a+xk_a)\tau^a]\tau^\mu[m_z^0+i(q_b-k_b+xk_b)\tau^b]\tau^\nu}{[q^2+x(1-x)k^2+(m_z^0)^2]^2}\right]\\
&\times(q_\mu+xk_\mu)(q_\nu-k_\nu+xk_\nu)
\end{aligned}
\tag{2.139}
$$

Note that

$$
\begin{aligned}
&\mathrm{Tr}\{[m_z^0+i(q_a+xk_a)\tau^a]\tau^\mu[m_z^0+i(q_b-k_b+xk_b)\tau^b]\tau^\nu\}\\
=&2[(m_z^0)^2+q^2+x(1-x)k^2]\delta^{\mu\nu}+4[k^\mu k^\nu-k^2\delta^{\mu\nu}](x-x^2)\\
&-4q^\mu q^\nu+(2-4x)(k^\mu q^\nu+k^\nu q^\mu)-2m_z^0\epsilon^{\mu\nu\lambda}k_\lambda,
\end{aligned}
\tag{2.140}
$$

with these, we shall have the response function divided into the following parts:

$$\begin{aligned}
\Pi^{A}_{\mu\nu}(k) &= \Pi^{A,1}_{\mu\nu}(k) + \Pi^{A,2}_{\mu\nu}(k) + \Pi^{A,3}_{\mu\nu}(k) + \Pi^{A,4}_{\mu\nu}(k) + \Pi^{A,5}_{\mu\nu}(k) \\
\Pi^{A,1}_{\mu\nu}(k) &= -\int_0^1 [dx] \int \frac{d^3q}{(2\pi)^3} \frac{2\delta^{\mu\nu}(q_\mu + xk_\mu)(q_\nu - k_\nu + xk_\nu)}{[(m_z^0)^2 + q^2 + x(1-x)k^2]} \\
\Pi^{A,2}_{\mu\nu}(k) &= -\int_0^1 [dx] \int \frac{d^3q}{(2\pi)^3} \frac{-4q^\mu q^\nu(q_\mu + xk_\mu)(q_\nu - k_\nu + xk_\nu)}{[(m_z^0)^2 + q^2 + x(1-x)k^2]^2} \\
\Pi^{A,3}_{\mu\nu}(k) &= -\int_0^1 [dx] \int \frac{d^3q}{(2\pi)^3} \frac{4[k^\mu k^\nu - k^2\delta^{\mu\nu}](q_\mu + xk_\mu)(q_\nu - k_\nu + xk_\nu)(x - x^2)}{[(m_z^0)^2 + q^2 + x(1-x)k^2]^2} \\
\Pi^{A,4}_{\mu\nu}(k) &= -\int_0^1 [dx] \int \frac{d^3q}{(2\pi)^3} \frac{(2-4x)(k^\mu q^\nu + k^\nu q^\mu)(q_\mu + xk_\mu)(q_\nu - k_\nu + xk_\nu)}{[(m_z^0)^2 + q^2 + x(1-x)k^2]^2} \\
\Pi^{A,5}_{\mu\nu}(k) &= -\int_0^1 [dx] \int \frac{d^3q}{(2\pi)^3} \frac{-2m\epsilon^{\mu\nu\lambda}k_\lambda(q_\mu + xk_\mu)(q_\nu - k_\nu + xk_\nu)}{[(m_z^0)^2 + q^2 + x(1-x)k^2]^2}
\end{aligned} \tag{2.141}$$

The numerators that are odd in q will vanish. So let us look into the numerator term by term: (again, the repeat indices for μ and ν does not stands for summation)

$$\begin{aligned}
N[\Pi^{A,1}_{\mu\nu}(k)] &= -2\delta^{\mu\nu}(q_\mu + xk_\mu)(q_\nu + xk_\nu - k_\nu) \\
&= -2\delta^{\mu\nu}(q_\mu q_\nu + xk_\mu q_\nu + xq_\mu k_\nu + x^2 k_\mu k_\nu - q_\mu k_\nu - xk_\mu k_\nu) \\
N[\Pi^{A,2}_{\mu\nu}(k)] &= 4q^\mu q^\nu(q_\mu + xk_\mu)(q_\nu + xk_\nu - k_\nu) \\
&= 4q^\mu q^\nu(q_\mu q_\nu + xk_\mu q_\nu + xq_\mu k_\nu + x^2 k_\mu k_\nu - q_\mu k_\nu - xk_\mu k_\nu) \\
N[\Pi^{A,3}_{\mu\nu}(k)] &= -4[k^\mu k^\nu - k^2\delta^{\mu\nu}](x - x^2)(q_\mu + xk_\mu)(q_\nu + xk_\nu - k_\nu) \\
&= -4(x - x^2)[k^\mu k^\nu - k^2\delta^{\mu\nu}](q_\mu q_\nu + xk_\mu q_\nu + xq_\mu k_\nu + x^2 k_\mu k_\nu - q_\mu k_\nu - xk_\mu k_\nu),
\end{aligned} \tag{2.142}$$

and so as the other two terms:

$$\begin{aligned}
N[\Pi^{A,4}_{\mu\nu}(k)] &= -(2-4x)[k^\mu q^\nu + k^\nu q^\mu](q_\mu q_\nu + xk_\mu q_\nu + xq_\mu k_\nu + x^2 k_\mu k_\nu - q_\mu k_\nu - xk_\mu k_\nu) \\
&= -(2-4x)[k^\mu q^\nu q_\mu q_\nu + xk^\mu q^\nu k_\mu q_\nu + xk^\mu q^\nu q_\mu k_\nu + x^2 k^\mu q^\nu k_\mu k_\nu - k^\mu q^\nu q_\mu k_\nu - xk^\mu q^\nu k_\mu k_\nu] \\
&+ -(2-4x)[k^\nu q^\mu q_\mu q_\nu + xk^\nu q^\mu k_\mu q_\nu + xk^\nu q^\mu q_\mu k_\nu + x^2 k^\nu q^\mu k_\mu k_\nu - k^\nu q^\mu q_\mu k_\nu - xk^\nu q^\mu k_\mu k_\nu] \\
N[\Pi^{A,5}_{\mu\nu}(k)] &= 2m_0^z\epsilon^{\mu\nu\lambda}k_\lambda(q_\mu + xk_\mu)(q_\nu + xk_\nu - k_\nu) \\
&= 2m_0^z\epsilon^{\mu\nu\lambda}k_\lambda(q_\mu q_\nu + xk_\mu q_\nu + xq_\mu k_\nu + x^2 k_\mu k_\nu - q_\mu k_\nu - xk_\mu k_\nu)
\end{aligned} \tag{2.143}$$

They can be further simplified as:

$$\begin{aligned}
N_e[\Pi^{A,1}_{\mu\nu}(k)] &= -2\delta^{\mu\nu}[(x^2 - x)k_\mu k_\nu + q_\mu q_\nu] \\
N_e[\Pi^{A,2}_{\mu\nu}(k)] &= 4[q^\mu q_\mu q^\nu q_\nu + (x^2 - x)q^\mu q^\nu k_\mu k_\nu] \\
N_e[\Pi^{A,3}_{\mu\nu}(k)] &= -4(x - x^2)[k^\mu k^\nu - k^2\delta^{\mu\nu}][q_\mu q_\nu + (x^2 - x)k_\mu k_\nu] \\
N_e[\Pi^{A,4}_{\mu\nu}(k)] &= -(2-4x)[xq^\nu q_\nu k^\mu k_\mu + (x-1)q^\nu q_\mu k^\mu k_\nu + xq^\mu q_\nu k^\nu k_\mu + (x-1)q^\mu q_\mu k^\nu k_\nu] \\
N_e[\Pi^{A,5}_{\mu\nu}(k)] &= 2m_0^z\epsilon^{\mu\nu\lambda}k_\lambda[q_\mu q_\nu + (x^2 - x)k_\mu k_\nu]
\end{aligned} \tag{2.144}$$

With the above, we shall have by defining $m = |m_0^z|$:

$$\begin{aligned}
\Pi_{\mu\nu}^{A,1}(k) &= \int_0^1 [dx] \int \frac{d^3q}{(2\pi)^3} \frac{-2\delta^{\mu\nu}[(x^2-x)k_\mu k_\nu + q_\mu q_\nu]}{[q^2 + (m_z^0)^2 + x(1-x)k^2]} \\
&= \int_0^1 [dx] \frac{\Gamma(1-3/2)}{(4\pi)^{3/2}\Gamma(1)} \frac{-2\delta^{\mu\nu}(x^2-x)k_\mu k_\nu}{[(m_z^0)^2 + x(1-x)k^2]^{1-3/2}} \\
&+ \int_0^1 [dx] \frac{-2\delta^{\mu\nu}}{(4\pi)^{3/2}\Gamma(1)} \frac{\delta_{\mu\nu}}{2} \frac{\Gamma(1-1-3/2)}{[(m_z^0)^2 + x(1-x)k^2]^{-3/2}} \\
&= \frac{\delta^{\mu\nu}}{2\pi} \int_0^1 [dx] \frac{(x^2-x)k_\mu k_\nu}{[(m_z^0)^2 + x(1-x)k^2]^{-1/2}} + \frac{(\delta^{\mu\nu})^2}{6\pi} \int_0^1 [dx] \frac{1}{[(m_z^0)^2 + x(1-x)k^2]^{-3/2}} \\
&= -\frac{\delta^{\mu\nu}k_\mu k_\nu}{2\pi} \left[\frac{(-6k^3m - 8km^3 + (-3k^4 - 8k^2m^2 + 16m^4)\mathrm{arccot}[2m/k])}{64k^3} \right] \\
&+ \frac{(\delta^{\mu\nu})^2}{6\pi} \left[\frac{(6k^3m + 40km^3 + 3(k^2+4m^2)^2\mathrm{arccot}[2m/k])}{64k} \right] \\
&\approx -\frac{\delta^{\mu\nu}k_\mu k_\nu}{2\pi} \left[-\frac{m}{6} - \frac{k^2}{60m} + \frac{k^4}{1120m^3} + \mathcal{O}(k^6) \right] \\
&+ \frac{(\delta^{\mu\nu})^2}{6\pi} \left[m^3 + \frac{mk^2}{4} + \frac{k^4}{80m} + \mathcal{O}(k^6) \right]
\end{aligned} \tag{2.145}$$

and:

$$\begin{aligned}
\Pi^{A,2}_{\mu\nu}(k) &= \int_0^1 [dx] \int \frac{d^3q}{(2\pi)^3} \frac{4[q^\mu q_\mu q^\nu q_\nu + (x^2-x)q^\mu q^\nu k_\mu k_\nu]}{[q^2 + (m_z^0)^2 + x(1-x)k^2]^2} \\
&= \int_0^1 [dx] \frac{4}{(4\pi)^{3/2}\Gamma(2)} \frac{1}{4} [\delta_{\mu\mu}\delta_{\nu\nu} + \delta_{\mu\nu}\delta_{\nu\mu} + \delta_{\mu\nu}\delta_{\mu\nu}] \frac{\Gamma(2-2-3/2)}{[(m_z^0)^2 + x(1-x)k^2]^{2-2-3/2}} \\
&+ \int_0^1 \frac{4(x^2-x)k_\mu k_\nu}{(4\pi)^{3/2}\Gamma(2)} \frac{\delta_{\mu\nu}}{2} \frac{\Gamma(2-1-3/2)}{[(m_z^0)^2 + x(1-x)k^2]^{2-1-3/2}} \\
&= \frac{1}{6\pi}[1 + 2(\delta_{\mu\nu})^2] \int_0^1 [dx] \frac{1}{[(m_z^0)^2 + x(1-x)k^2]^{-3/2}} \\
&- \frac{k_\mu k_\nu \delta_{\mu\nu}}{2\pi} \int_0^1 [dx] \frac{(x^2-x)}{[(m_z^0)^2 + x(1-x)k^2]^{-1/2}} \\
&= \frac{1}{6\pi}[1 + 2(\delta_{\mu\nu})^2] \left[\frac{(6k^3m + 40km^3 + 3(k^2+4m^2)^2 \mathrm{arccot}[2m/k])}{64k} \right] \\
&+ \frac{k_\mu k_\nu \delta_{\mu\nu}}{2\pi} \left[\frac{(-6k^3m - 8km^3 + (-3k^4 - 8k^2m^2 + 16m^4)\mathrm{arccot}[2m/k])}{64k^3} \right] \\
&\approx \frac{[1 + 2(\delta_{\mu\nu})^2]}{6\pi} \left[m^3 + \frac{mk^2}{4} + \frac{k^4}{80m} + \mathcal{O}(k^6) \right] \\
&+ \frac{k_\mu k_\nu \delta_{\mu\nu}}{2\pi} \left[-\frac{m}{6} - \frac{k^2}{60m} + \frac{k^4}{1120m^3} + \mathcal{O}(k^6) \right]
\end{aligned} \tag{2.146}$$

and:

$$
\begin{aligned}
\Pi^{A,3}_{\mu\nu}(k) &= \int_0^1 [dx] \int \frac{d^3q}{(2\pi)^3} \frac{-4(x-x^2)[k^\mu k^\nu - k^2\delta^{\mu\nu}][q_\mu q_\nu + (x^2-x)k_\mu k_\nu]}{[q^2+(m_z^0)^2+x(1-x)k^2]^2} \\
&= -\int_0^1 [dx] 4(x-x^2)[k^\mu k^\nu - k^2\delta^{\mu\nu}] \frac{1}{(4\pi)^{3/2}\Gamma(2)} \frac{1}{2}\delta_{\mu\nu} \frac{\Gamma(2-1-3/2)}{[(m_z^0)^2+x(1-x)k^2]^{2-1-3/2}} \\
&+ \int_0^1 [dx] 4(x^2-x)^2[k^\mu k^\nu - k^2\delta^{\mu\nu}] \frac{\Gamma(2-3/2)}{(4\pi)^{3/2}\Gamma(2)} \frac{k_\mu k_\nu}{[(m_z^0)^2+x(1-x)k^2]^{2-3/2}} \\
&= -\frac{\delta_{\mu\nu}[k^\mu k^\nu - k^2\delta^{\mu\nu}]}{2\pi} \int_0^1 [dx] \frac{(x^2-x)}{[(m_z^0)^2+x(1-x)k^2]^{-1/2}} \\
&+ \frac{[k^\mu k^\nu - k^2\delta^{\mu\nu}]}{2\pi} \int_0^1 [dx] \frac{(x^2-x)^2}{[(m_z^0)^2+x(1-x)k^2]^{1/2}} \\
&= -\frac{\delta_{\mu\nu}[k^\mu k^\nu - k^2\delta^{\mu\nu}]}{2\pi} \left[\frac{-6k^3m - 8k^2m^3 + (-3k^4 - 8k^2m^2 + 16m^4)\mathrm{arccot}[2m/k]}{64k^3} \right] \\
&+ \frac{[k^\mu k^\nu - k^2\delta^{\mu\nu}]}{2\pi} k_\mu k_\nu \left[\frac{6km(k^2-4m^2) + (4k^4 - 8k^2m^2 + 48m^4)\mathrm{acrcot}[2m/k]}{64k^5} \right] \\
&= -\frac{\delta_{\mu\nu}(k^\mu k^\nu - k^2\delta^{\mu\nu})}{2\pi} \left[-\frac{m}{6} - \frac{k^2}{60m} + \frac{k^4}{1120m^3} + \mathcal{O}(k^6) \right] \\
&+ \frac{[k^\mu k^\nu - k^2\delta_{\mu\nu}]k_\mu k_\nu}{2\pi} \left[\frac{1}{30m} - \frac{k^2}{280m^3} + \frac{k^4}{1680m^5} + \mathcal{O}[k^6] \right]
\end{aligned}
\tag{2.147}
$$

and:

$$
\begin{aligned}
\Pi^{A,4}_{\mu\nu}(k) =& \int_0^1 [dx] \int \frac{d^3q}{(2\pi)^3} \times \\
& \times \frac{-(2-4x)[xq^\nu q_\nu k^\mu k_\mu + (x-1)q^\nu q_\mu k^\mu k_\nu + xq^\mu q_\nu k^\nu k_\mu + (x-1)q^\mu q_\mu k^\nu k_\nu]}{[q^2 + (m_z^0)^2 + x(1-x)k^2]^2} \\
=& \int_0^1 [dx] \frac{(4x-2)xk^\mu k_\mu}{(4\pi)^{3/2}\Gamma(2)} \frac{\delta^{\nu\nu}}{2} \frac{\Gamma(2-1-3/2)}{[(m_z^0)^2 + x(1-x)k^2]^{2-1-3/2}} \\
& + \int_0^1 [dx] \frac{(4x-2)(x-1)k^\mu k_\nu}{(4\pi)^{3/2}\Gamma(2)} \frac{1}{2}\delta^{\mu\nu} \frac{\Gamma(2-1-3/2)}{[(m_z^0)^2 + x(1-x)k^2]^{2-1-3/2}} \\
+ & \int_0^1 [dx] \frac{(4x-2)xk^\nu k_\nu}{(4\pi)^{3/2}\Gamma(2)} \frac{\delta^{\mu\mu}}{2} \frac{\Gamma(2-1-3/2)}{[(m_z^0)^2 + x(1-x)k^2]^{2-1-3/2}} \\
& + \int_0^1 [dx] \frac{(4x-2)(x-1)k^\nu k_\mu}{(4\pi)^{3/2}\Gamma(2)} \frac{1}{2}\delta^{\nu\mu} \frac{\Gamma(2-1-3/2)}{[(m_z^0)^2 + x(1-x)k^2]^{2-1-3/2}} \\
=& -\int_0^1 [dx] \frac{(2x-1)x}{4\pi} \frac{k^\mu k_\mu \delta^{\nu\nu} + k^\nu k_\nu \delta^{\mu\mu}}{[(m_z^0)^2 + x(1-x)k^2]^{-1/2}} \\
& - \int_0^1 [dx] \frac{(2x-1)(x-1)}{4\pi} \frac{k^\mu k_\nu \delta^{\nu\mu} + k^\nu k_\mu \delta^{\mu\nu}}{[(m_z^0)^2 + x(1-x)k^2]^{-1/2}} \\
=& -\frac{k^\mu k_\mu \delta^{\nu\nu} + k^\nu k_\nu \delta^{\mu\mu}}{4\pi} \int_0^1 [dx] \frac{(2x-1)x}{[(m_z^0)^2 + x(1-x)k^2]^{-1/2}} \\
& - \frac{k^\mu k_\nu \delta^{\nu\mu} + k^\nu k_\mu \delta^{\mu\nu}}{4\pi} \int_0^1 [dx] \frac{(2x-1)(x-1)}{[(m_z^0)^2 + x(1-x)k^2]^{-1/2}} \\
=& -\left[\frac{k^\mu k_\mu \delta^{\nu\nu} + k^\nu k_\nu \delta^{\mu\mu}}{4\pi} + \frac{k^\mu k_\nu \delta^{\nu\mu} + k^\nu k_\mu \delta^{\mu\nu}}{4\pi}\right] \left[\frac{(2k^3 m - 8km^3 + (k^2+4m^2)^2 \mathrm{arccot}(2m/k))}{32k^3}\right] \\
=& -\left[\frac{k^\mu k_\mu \delta^{\nu\nu} + k^\nu k_\nu \delta^{\mu\mu}}{4\pi} + \frac{k^\mu k_\nu \delta^{\nu\mu} + k^\nu k_\mu \delta^{\mu\nu}}{4\pi}\right] \left[\frac{m}{6} + \frac{k^2}{120m} - \frac{k^4}{3360m^3} + \mathcal{O}[k^6]\right]
\end{aligned}
\tag{2.148}
$$

and:

$$\begin{aligned}
\Pi^{A,5}_{\mu\nu}(k) &= \int_0^1 [dx] \int \frac{d^3q}{(2\pi)^2} \frac{2m_z^0 \epsilon^{\mu\nu\lambda} k_\lambda [q_\mu q_\nu + (x^2-x)k_\mu k_\nu]}{[q^2 + (m_z^0)^2 + x(1-x)k^2]^2} \\
&= \int_0^1 [dx] \frac{2m_z^0 \epsilon^{\mu\nu\lambda} k_\lambda}{(4\pi)^{3/2}\Gamma(2)} \frac{1}{2} \delta_{\mu\nu} \frac{\Gamma(2-1-3/2)}{[(m_z^0)^2 + x(1-x)k^2]^{2-1-3/2}} \\
&+ \frac{\Gamma(2-3/2)}{(4\pi)^{3/2}\Gamma(2)} \int_0^1 [dx] \frac{(x^2-x) 2m_z^0 \epsilon^{\mu\nu\lambda} k_\mu k_\nu k_\lambda}{[(m_z^0)^2 + x(1-x)k^2]^{2-3/2}} \\
&= -\frac{\delta_{\mu\nu} m_z^0 \epsilon^{\mu\nu\lambda} k_\lambda}{4\pi} \int_0^1 [dx] \frac{1}{[(m_z^0)^2 + x(1-x)k^2]^{-1/2}} \\
&+ \frac{m_z^0 \epsilon^{\mu\nu\lambda} k_\mu k_\nu k_\lambda}{4\pi} \int_0^1 [dx] \frac{(x^2-x)}{[(m_z^0)^2 + x(1-x)k^2]^{1/2}} \\
&= -\frac{\delta_{\mu\nu} m_0^z \epsilon^{\mu\nu\lambda} k_\lambda}{4\pi} \left[\frac{m}{2} + \frac{i(k^2+4m^2)(\ln(-ik+2m) - \ln(ik+2m))}{8k} \right] \\
&+ \frac{m_z^0 \epsilon^{\mu\nu\lambda} k_\mu k_\nu k_\lambda}{4\pi} \left[-\frac{2km + (k^2-4m^2)\arctan[k/2m]}{4k^3} \right] \\
&\approx -\frac{\delta_{\mu\nu} m_z^0 \epsilon^{\mu\nu\lambda} k_\lambda}{4\pi} \left[m + \frac{k^2}{12m} - \frac{k^4}{240m^3} + \mathcal{O}[k^6] \right] \\
&+ \frac{m_z^0 \epsilon^{\mu\nu\lambda} k_\mu k_\nu k_\lambda}{4\pi} \left[-\frac{1}{6m} + \frac{k^2}{10m^3} - \frac{3k^4}{1120m^5} + \mathcal{O}[k^6] \right]
\end{aligned} \tag{2.149}$$

2.10.2.1 Second order to k

Up to second order of k, we shall have

$$\begin{aligned}
\Pi^{A,1}_{\mu\nu}(k) &\approx \frac{m^3}{6\pi}(\delta^{\mu\nu})^2 + \frac{m}{12\pi}\delta^{\mu\nu}k_\mu k_\nu + \frac{m}{24\pi}(\delta^{\mu\nu})^2 k^2 \\
\Pi^{A,2}_{\mu\nu}(k) &\approx \frac{m^3}{6\pi}[1 + 2(\delta_{\mu\nu})^2] + \frac{m}{24\pi}[1 + 2(\delta_{\mu\nu})^2]k^2 - \frac{m}{12\pi}\delta_{\mu\nu}k_\mu k_\nu \\
\Pi^{A,3}_{\mu\nu}(k) &\approx \frac{m}{12\pi}\delta_{\mu\nu}(k^\mu k^\nu - k^2\delta^{\mu\nu}) \\
\Pi^{A,4}_{\mu\nu}(k) &\approx -\frac{m}{24\pi}[k_\mu^2 + k_\nu^2 + 2k_\mu k_\nu \delta^{\mu\nu}] \\
\Pi^{A,5}_{\mu\nu}(k) &\approx 0
\end{aligned} \tag{2.150}$$

which gives:

$$\Pi^{A}_{\mu\nu}(k) = \sum_i \Pi^{A,i}_{\mu\nu}(k) = \frac{m^3}{6\pi}[1 + 3(\delta_{\mu\nu})^2] + \frac{m}{24\pi}[1 + (\delta_{\mu\nu})^2]k^2 - \frac{m}{24\pi}(k_\mu^2 + k_\nu^2) \tag{2.151}$$

and:

$$\begin{aligned}\Pi^A_{xx}(k) &= \frac{2m^3}{3\pi} + \frac{m}{12\pi}(k^2 - k_x^2)\\ \Pi^A_{xy}(k) &= \frac{m^3}{6\pi} + \frac{m}{24\pi}(k^2 - k_x^2 - k_y^2)\\ \Pi^A_{yx}(k) &= \frac{m^3}{6\pi} + \frac{m}{24\pi}(k^2 - k_y^2 - k_x^2)\\ \Pi^A_{yy}(k) &= \frac{2m^3}{3\pi} + \frac{m}{12\pi}(k^2 - k_x^2)\end{aligned} \tag{2.152}$$

2.10.3 Two $\hat{m}_z$ vertices (Diagrams like Fig. [2.5].(b))

The effective action reads:

$$S^B_{\text{eff}} \equiv \frac{1}{2}\int \frac{d^3k}{(2\pi)^3}\Pi^B_{zz}(k)\hat{m}_z(+k)\hat{m}_z(-k), \tag{2.153}$$

with the term:

$$\begin{aligned}\Pi^B_{zz}(k) &= \int \frac{d^3q}{(2\pi)^3}\text{Tr}\left[\frac{m_z^0 + i(q_a + k_a/2)\tau^a}{(m_z^0)^2 + (q + k/2)^2} m_z^0\tau_0 \frac{m_z^0 + i(q_b - k_b/2)\tau^b}{(m_z^0)^2 + (q - k/2)^2} m_z^0\tau_0\right]\\ &= (m_z^0)^2\int_0^1 [dx]\int \frac{d^3q}{(2\pi)^3}\frac{\Gamma(1+1)}{\Gamma(1)\Gamma(1)}\text{Tr}\left[\frac{[m_z^0 + i(q_a + k_a/2)\tau^a][m_z^0 + i(q_b - k_b/2)\tau^b)]}{\{[(m_z^0)^2 + (q + k/2)^2](1-x) + [(m_z^0)^2 + (q - k/2)^2]x\}^2}\right]\\ &= (m_z^0)^2\int_0^1 [dx]\int \frac{d^3q}{(2\pi)^3}\text{Tr}\left[\frac{[m_z^0 + i(q_a + k_a/2)\tau^a][m_z^0 + i(q_b - k_b/2)\tau^b)]}{\{q^2 + 2q\cdot[1/2 - x]k + (m_z^0)^2 + k^2/4\}^2}\right]\end{aligned} \tag{2.154}$$

We can further define:

$$\tilde{q} = q + (1/2 - x)k, \quad \tilde{q} + xk = q + k/2, \quad \tilde{q} - k + xk = q - k/2 \tag{2.155}$$

Then we arrive at:

$$\begin{aligned}
\Pi^B_{zz}(k) &= (m_z^0)^2 \int_0^1 [dx] \int \frac{d^3\tilde{q}}{(2\pi)^3} \mathrm{Tr}\left[\frac{[m_z^0 + i(\tilde{q}_a + xk_a)\tau^a][m_z^0 + i(\tilde{q}_b - k_b + xk_b)\tau^b]}{[\tilde{q}^2 + x(1-x)k^2 + (m_z^0)^2]^2}\right] \\
&= (m_z^0)^2 \int_0^1 [dx] \int \frac{d^3q}{(2\pi)^3} \frac{(m_z^0)^2 - 2(q_a + xk_a)(q_b + xk_b - k_b)\delta^{ab}}{[q^2 + x(1-x)k^2 + (m_z^0)^2]^2} \\
&= (m_z^0)^2 \int_0^1 [dx] \int \frac{d^3q}{(2\pi)^3} \frac{(m_z^0)^2 - 2(q + xk)(q + xk - k)}{[q^2 + x(1-x)k^2 + (m_z^0)^2]^2} \\
&= (m_z^0)^2 \int_0^1 [dx] \int \frac{d^3q}{(2\pi)^3} \frac{(m_z^0)^2 - 2q^2 - 2(xk)^2 - 4qxk + 2(q + xk)k}{[q^2 + x(1-x)k^2 + (m_z^0)^2]^2} \\
&= (m_z^0)^2 \int_0^1 [dx] \int \frac{d^3q}{(2\pi)^3} \frac{(m_z^0)^2 - 2q^2 + 2(x - x^2)k^2}{[q^2 + x(1-x)k^2 + (m_z^0)^2]^2} \\
&= (m_z^0)^2 \int_0^1 [dx] \int \frac{d^3q}{(2\pi)^3} \frac{3(m_z^0)^2 + 4(x - x^2)k^2 - 2(q^2 + x(1-x)k^2 + (m_z^0)^2)}{[q^2 + x(1-x)k^2 + (m_z^0)^2]^2} \\
&= (m_z^0)^2 \int_0^1 [dx] \int \frac{d^3q}{(2\pi)^3} \left[\frac{3(m_z^0)^2 + 4(x - x^2)k^2}{[q^2 + x(1-x)k^2 + (m_z^0)^2]^2} - \frac{2}{[q^2 + x(1-x)k^2 + (m_z^0)^2]}\right]
\end{aligned} \tag{2.156}$$

With each term reads:

$$\begin{aligned}
\Pi^{B,1}_{zz}(k) &= (m_z^0)^2 \int_0^1 [dx] \int \frac{d^3q}{(2\pi)^3} \frac{3(m_z^0)^2 + 4(x - x^2)k^2}{[q^2 + x(1-x)k^2 + (m_z^0)^2]^2} \\
&= (m_z^0)^2 \int_0^1 [dx] \frac{\Gamma(2 - 3/2)}{(4\pi)^{3/2}\Gamma(2)} \frac{3(m_z^0)^2 + 4(x - x^2)k^2}{[(m_z^0)^2 + x(1-x)k^2]^{2-3/2}} \\
&= \frac{(m_z^0)^2}{8\pi} \int_0^1 [dx] \frac{3(m_z^0)^2 + 4(x - x^2)k^2}{[(m_z^0)^2 + x(1-x)k^2]^{1/2}} \\
&= \frac{(m_z^0)^2}{8\pi} \int_0^1 [dx] \left[2m + \left(k + \frac{2m^2}{k}\mathrm{arctan}[k/2m]\right)\right] \\
&\approx \frac{m^2}{8\pi}\left[3m + \frac{5k^2}{12m} - \frac{7k^4}{240m^3} + \mathcal{O}[k^6]\right]
\end{aligned} \tag{2.157}$$

and:

$$\begin{aligned}\Pi^{B,2}_{zz}(k) &= (m^0_z)^2\int_0^1\int\frac{d^3q}{(2\pi)^3}\frac{-2}{[q^2+x(1-x)k^2+(m^0_z)^2]}\\ &= (m^0_z)^2\int_0^1[dx]\frac{(-2)\Gamma(1-3/2)}{(4\pi)^{3/2}\Gamma(1)}\frac{1}{[(m^0_z)^2+x(1-x)k^2]^{1-3/2}}\\ &= \frac{(m^0_z)^2}{2\pi}\int_0^1[dx]\frac{1}{[(m^0_z)^2+x(1-x)k^2]^{-1/2}}\\ &= \frac{(m^0_z)^2}{2\pi}\left[\frac{m}{2}+\frac{i(k^2+4m^2)}{8k}\ln\left(\frac{-ik+2m}{+ik+2m}\right)\right]\\ &= \frac{m^2}{2\pi}\left[m+\frac{k^2}{12m}-\frac{k^4}{240m^3}+\mathcal{O}[k^6]\right]\end{aligned} \tag{2.158}$$

With above, we have:

$$\Pi^B_{zz}(k)\approx\frac{m^2}{8\pi}\left[3m+\frac{5k^2}{12m}-\frac{7k^4}{240m^3}+\mathcal{O}[k^6]\right]+\frac{m^2}{2\pi}\left[m+\frac{k^2}{12m}-\frac{k^4}{240m^3}+\mathcal{O}[k^6]\right] \tag{2.159}$$

to the second order of k, would be:

$$\Pi^B_{zz}(k)\approx\frac{7m^3}{8\pi}+\frac{3m}{32\pi}k^2 \tag{2.160}$$

2.10.4 One $\hat{u}$ vertex and one $\hat{m}_z$ vertex (Diagrams like Fig. [2.5].(c))

$$S^C_{\text{eff}}\equiv\frac{1}{2}\int\frac{d^3k}{(2\pi^3)}[\Pi^C_{z\nu}(k)\hat{m}_z(+k)\hat{u}_\nu(-k)+\Pi^C_{\mu z}(k)\hat{u}_\mu(+k)\hat{m}_z(-k)] \tag{2.161}$$

with the function:

$$\begin{aligned}\Pi^C_{z\nu}(k) &= \int\frac{d^3q}{(2\pi)^3}\text{Tr}\left[\frac{m^0_z+i(q_a+k_a/2)\tau^a}{(m^0_z)^2+(q+k/2)^2}m^0_z\tau_0\frac{m^0_z+i(q_b-k_b/2)\tau^b}{(m^0_z)^2+(q-k/2)^2}\tau^\nu\right]i(q_\nu-k_\nu/2)\\ \Pi^C_{\mu z}(k) &= \int\frac{d^3q}{(2\pi)^3}\text{Tr}\left[\frac{m^0_z+i(q_a+k_a/2)\tau^a}{(m^0_z)^2+(q+k/2)^2}\tau^\mu\frac{m^0_z+i(q_b-k_b/2)\tau^b}{(m^0_z)^2+(q-k/2)^2}m^0_z\tau_0\right]i(q_\mu+k_\mu/2)\end{aligned} \tag{2.162}$$

We shall get them one by one:

$$\begin{aligned}\Pi^C_{z\nu}(k) &= m^0_z\int_0^1[dx]\int\frac{d^3q}{(2\pi)^3}\frac{\Gamma(1+1)}{\Gamma(1)\Gamma(1)}\text{Tr}\left[\frac{[m^0_z+i(q_a+k_a/2)\tau^a][m^0_z+i(q_b-k_b/2)\tau^b]\tau^\nu}{\{[(m^0_z)^2+(q+k/2)^2](1-x)+[(m^0_z)^2+(q-k/2)^2]x\}^2}\right]\\ &\quad\times i(q_\nu-k_\nu/2)\\ &= m^0_z\int_0^1[dx]\int\frac{d^3q}{(2\pi)^3}\text{Tr}\left[\frac{[m^0_z+i(q_a+k_a/2)\tau^a][m^0_z+i(q_b-k_b/2)\tau^b]\tau^\nu}{[(q+(1/2-x)k)^2+x(1-x)k^2+(m^0_z)^2]^2}\right]i(q_\nu-k_\nu/2)\\ &= m^0_z\int_0^1[dx]\int\frac{d^3\tilde{q}}{(2\pi)^3}\text{Tr}\left[\frac{[m^0_z+i(\tilde{q}_a+xk_a)\tau^a][m^0_z+i(\tilde{q}_b-k_b+xk_b)\tau^b]\tau^\nu}{[\tilde{q}^2+x(1-x)k^2+(m^0_z)^2]^2}\right]i(\tilde{q}_\nu-k_\nu+xk_\nu)\end{aligned} \tag{2.163}$$

The trace in the numerator reads:

$$\begin{aligned}
&\mathrm{Tr}\{[m_z^0+i(q_a+xk_a)\tau^a][m_z^0+i(q_b+xk_b-k_b)\tau^b]\tau^\nu\}\\
=&\mathrm{Tr}\{[(m_z^0)^2+im_z^0(q_a+xk_a)\tau^a+im_z^0(q_b+xk_b-k_b)\tau^b-(q_a+xk_a)(q_b+xk_b-k_b)\tau^a\tau^b]\tau^\nu\}\\
=&im_z^0(q_a+xk_a)(2\delta^{a\nu})+im_z^0(q_b+xk_b-k_b)(2\delta^{b\nu})-(q_a+xk_a)(q_b+xk_b-k_b)(2i\epsilon^{ab\nu})\\
=&im_z^0(2)(2q_\nu+2xk_\nu-k_\nu)+q_ak_b(2i\epsilon^{ab\nu})
\end{aligned} \tag{2.164}$$

and the total numerator reads:

$$\begin{aligned}
N[\Pi^C_{z\nu}(k)]&=-(m_z^0)^2(2)(2q_\nu+2xk_\nu-k_\nu)(q_\nu+xk_\nu-k_\nu)-m_z^0q_ak_b(q_\nu+xk_\nu-k_\nu)(2\epsilon^{ab\nu})\\
N_e[\Pi^C_{z\nu}(k)]&=-2(m_z^0)^2[2q_\nu^2+(2x-1)(x-1)k_\nu^2]-2m_z^0q_aq_\nu k_b\epsilon^{ab\nu}
\end{aligned} \tag{2.165}$$

Such that, we shall see (the term we dropped in the second line is q_xq_y will vanish as it's odd to q_x or q_y separately)

$$\begin{aligned}
\Pi^C_{z\nu}(k)&=m_z^0\int_0^1[dx]\int\frac{d^3q}{(2\pi)^3}\frac{-2m_z^0[2q_\nu^2+(2x-1)(x-1)k_\nu^2]-2q_aq_\nu k_b\epsilon^{ab\nu}}{[q^2+x(1-x)k^2+(m_z^0)^2]^2}\\
&=m_z^0\int_0^1[dx]\int\frac{d^3q}{(2\pi)^3}\frac{-2m_z^0[2q_\nu^2+(2x-1)(x-1)k_\nu^2]}{[q^2+x(1-x)k^2+(m_z^0)^2]^2}
\end{aligned} \tag{2.166}$$

We shall have:

$$\begin{aligned}
\Pi^{C,1}_{z\nu}(k)&=m_z^0\int_0^1[dx]\int\frac{d^3q}{(2\pi)^3}\frac{-4m_z^0q_\nu^2}{[q^2+x(1-x)k^2+(m_z^0)^2]^2}\\
&=m_z^0\int_0^1[dx](-4m_z^0)\frac{1}{(4\pi)^{3/2}\Gamma(2)}\frac{1}{2}\delta_{\nu\nu}\frac{\Gamma(2-1-3/2)}{[(m_z^0)^2+x(1-x)k^2]^{2-1-3/2}}\\
&=\frac{(m_z^0)^2\delta_{\nu\nu}}{2\pi}\int_0^1[dx]\frac{1}{[(m_z^0)^2+x(1-x)k^2]^{-1/2}}\\
&=\frac{(m_z^0)^2\delta_{\nu\nu}}{2\pi}\left[\frac{m}{2}+\frac{i(k^2+4m^2)\ln\left(\frac{-ik+2m}{+ik+2m}\right)}{8k}\right]\\
&\approx\frac{m^2\delta_{\nu\nu}}{2\pi}\left[m+\frac{k^2}{12m}-\frac{k^4}{240m^3}+\mathcal{O}(k^6)\right]
\end{aligned} \tag{2.167}$$

and:

$$\begin{aligned}\Pi^{C,2}_{z\nu}(k) &= m_z^0\int_0^1[dx]\int\frac{d^3q}{(2\pi)^3}\frac{-2m_z^0(2x-1)(x-1)k_\nu^2}{[q^2+x(1-x)k^2+(m_z^0)^2]^2}\\ &= (-2m_z^0)m_z^0k_\nu^2\int_0^1[dx](2x-1)(x-1)\frac{\Gamma(2-3/2)}{(4\pi)^{3/2}\Gamma(2)}\frac{1}{[(m_z^0)^2+x(1-x)k^2]^{2-3/2}}\\ &= -\frac{k_\nu^2(m_z^0)^2}{4\pi}\int_0^1[dx]\frac{(2x-1)(x-1)}{[(m_z^0)^2+x(1-x)k^2]^{1/2}}\\ &= -\frac{k_\nu^2(m_z^0)^2}{4\pi}\left[\frac{(-2km+(k^2+4m^2)\mathrm{arccot}[2m/k])}{2k^3}\right]\\ &= -\frac{k_\nu^2m^2}{4\pi}\left[\frac{1}{6m}-\frac{k^2}{120m^4}+\frac{k^4}{1120m^5}+\mathcal{O}[k^6]\right]\end{aligned} \tag{2.168}$$

Thus we have:

$$\Pi^C_{z\nu}(k)=\frac{m^2}{2\pi}\left[m+\frac{k^2}{12m}-\frac{k^4}{240m^3}+\mathcal{O}(k^6)\right]-\frac{k_\nu^2m^2}{4\pi}\left[\frac{1}{6m}-\frac{k^2}{120m^4}+\frac{k^4}{1120m^5}+\mathcal{O}[k^6]\right], \tag{2.169}$$

and to the second order of k:

$$\Pi^C_{z\nu}(k)\approx\frac{m^3}{2\pi}+\frac{m}{24\pi}(k^2-k_\nu^2) \tag{2.170}$$

Similarly, we shall have:

$$\begin{aligned}\Pi^C_{\mu z}(k) &= \int\frac{d^3q}{(2\pi)^3}\mathrm{Tr}\left[\frac{[m_z^0+i(q_a+k_a/2)\tau^a]\tau^\mu[m_z^0+i(q_b-k_b/2)\tau^b]}{[(m_z^0)^2+(q+k/2)^2][(m_z^0)^2+(q-k/2)^2]}m_z^0\tau_0\right]i(q_\mu+k_\mu/2)\\ &= m_z^0\int\frac{d^3q}{(2\pi)^3}\int_0^1[dx]\frac{\Gamma(1+1)}{\Gamma(1)\Gamma(1)}\mathrm{Tr}\left[\frac{[m_z^0+i(q_a+k_a/2)\tau^a]\tau^\mu[m_z^0+i(q_b-k_b/2)\tau^b]}{\{[(m_z^0)^2+(q+k/2)^2](1-x)+[(m_z^0)^2+(q-k/2)^2]x\}^2}\right]\\ &\times i(q_\mu+k_\mu/2)\\ &= m_z^0\int_0^1[dx]\int\frac{d^3q}{(2\pi)^3}\mathrm{Tr}\left[\frac{[m_z^0+i(q_a+k_a/2)\tau^a]\tau^\mu[m_z^0+i(q_b-k_b/2)\tau^b]}{[(q+(1/2-x)k)^2+x(1-x)k^2+(m_z^0)^2]^2}\right]i(q_\mu+k_\mu/2)\\ &= m_z^0\int_0^1[dx]\int\frac{d^3q}{(2\pi)^3}\mathrm{Tr}\left[\frac{[m_z^0+i(\tilde{q}_a+xk_a)\tau^a]\tau^\mu[m_z^0+i(\tilde{q}_b-k_b+xk_b)]}{[\tilde{q}^2+x(1-x)k^2+(m_z^0)^2]^2}\right]i(\tilde{q}_\mu+xk_\mu)\end{aligned} \tag{2.171}$$

The trace in the numerator reads:

$$\begin{aligned}&\mathrm{Tr}\{[m_z^0+i(q_a+xk_a)\tau^a]\tau^\mu[m_z^0+i(q_b+xk_b-k_b)\tau^b]\}\\ =&\mathrm{Tr}\{[m_z^0\tau^\mu+i(q_a+xk_a)\tau^a\tau^\mu][m_z^0+i(q_b+xk_b-k_b)\tau^b]\}\\ =&\mathrm{Tr}[(m_z^0)^2\tau^\mu+im_z^0(q_a+xk_a)\tau^a\tau^\mu+im_z^0(q_b+xk_b-k_b)\tau^\mu\tau^b-(q_a+xk_a)(q_b+xk_b-k_b)\tau^a\tau^\mu\tau^b]\\ =&im_z^0(q_a+xk_a)(2\delta^{a\mu})+im_z^0(q_b+xk_b-k_b)(2\delta^{\mu b})-(q_a+xk_a)(q_b+xk_b-k_b)(2i\epsilon^{a\mu b})\\ =&im_z^0(2)(2q_\mu+2xk_\mu-k_\mu)+q_ak_b(2i\epsilon^{a\mu b}),\end{aligned} \tag{2.172}$$

and the total numerator reads:

$$\begin{aligned} N[\Pi^C_{\mu z}(k)] &= -2(m^0_z)^2(2q_\mu + 2xk_\mu - k_\mu)(q_\mu + xk_\mu) - m^0_z q_a k_b (q_\mu + xk_\mu)(2\epsilon^{a\mu b}) \\ N_e[\Pi^C_{\mu z}(k)] &= -2(m^0_z)^2[2q^2_\mu + (2x-1)xk^2_\mu] - 2m^0_z q_a q_\mu k_b \epsilon^{a\mu b} \end{aligned} \tag{2.173}$$

We obtain:

$$\begin{aligned} \Pi^C_{\mu z}(k) &= m^0_z \int_0^1 [dx] \int \frac{d^3q}{(2\pi)^3} \frac{-2m^0_z[2q^2_\mu + (2x-1)xk^2_\mu] - 2q_a q_\mu k_b \epsilon^{a\mu b}}{[q^2 + x(1-x)k^2 + (m^0_z)^2]^2} \\ &= m^0_z \int_0^1 [dx] \int \frac{d^3q}{(2\pi)^3} \frac{-2m^0_z[2q^2_\mu + (2x-1)xk^2_\mu]}{[q^2 + x(1-x)k^2 + (m^0_z)^2]^2} \end{aligned} \tag{2.174}$$

We then have:

$$\begin{aligned} \Pi^{C,1}_{\mu z}(k) &= m^0_z \int_0^1 [dx] \int \frac{d^3q}{(2\pi)^3} \frac{-4m^0_z q^2_\mu}{[q^2 + x(1-x)k^2 + (m^0_z)^2]^2} \\ &= m^0_z \int_0^1 [dx](-4m^0_z) \frac{1}{(4\pi)^{3/2}\Gamma(2)} \frac{1}{2} \delta_{\mu\mu} \frac{\Gamma(2-1-3/2)}{[(m^0_z)^2 + x(1-x)k^2]^{2-1-3/2}} \\ &= \frac{(m^0_z)^2 \delta_{\mu\mu}}{2\pi} \int_0^1 [dx] \frac{1}{[(m^0_z)^2 + x(1-x)k^2]^{-1/2}} \\ &= \frac{(m^0_z)^2 \delta_{\mu\mu}}{2\pi} \left[\frac{m}{2} + \frac{i(k^2+4m^2)\ln\left(\frac{-ik+2m}{+ik+2m}\right)}{8k} \right] \\ &\approx \frac{m^2 \delta_{\mu\mu}}{2\pi} \left[m + \frac{k^2}{12m} - \frac{k^4}{240m^3} + \mathcal{O}(k^6) \right] \end{aligned} \tag{2.175}$$

and:

$$\begin{aligned} \Pi^{C,2}_{\mu z}(k) &= m^0_z \int_0^1 [dx] \int \frac{d^3q}{(2\pi)^3} \frac{-2m^0_z(2x-1)(x-1)k^2_\mu}{[q^2 + x(1-x)k^2 + (m^0_z)^2]^2} \\ &= m^0_z(-2m^0_z)k^2_\mu \int_0^1 [dx](2x-1)(x-1) \frac{\Gamma(2-3/2)}{(4\pi)^{3/2}\Gamma(2)} \frac{1}{[(m^0_z)^2 + x(1-x)k^2]^{2-3/2}} \\ &= -\frac{k^2_\mu (m^0_z)^2}{4\pi} \int_0^1 [dx] \frac{(2x-1)(x-1)}{[(m^0_z)^2 + x(1-x)k^2]^{1/2}} \\ &= -\frac{k^2_\mu (m^0_z)^2}{4\pi} \left[\frac{(-2km + (k^2+4m^2)\mathrm{arccot}[2m/k])}{2k^3} \right] \\ &\approx -\frac{k^2_\mu m^2}{4\pi} \left[\frac{1}{6m} - \frac{k^2}{120m^4} + \frac{k^4}{1120m^5} + \mathcal{O}[k^6] \right] \end{aligned} \tag{2.176}$$

We shall have:

$$\Pi^C_{\mu z}(k) = \frac{m^2}{2\pi} \left[m + \frac{k^2}{12m} - \frac{k^4}{240m^3} + \mathcal{O}[k^6] \right] - \frac{k^2_\mu m^2}{4\pi} \left[\frac{1}{6m} - \frac{k^2}{120m^4} + \frac{k^4}{1120m^5} + \mathcal{O}[k^6] \right] \tag{2.177}$$

and to the second order of k, that is:

$$\Pi^C_{\mu z}(k) = \frac{m^2}{2\pi} + \frac{m}{24\pi}(k^2 - k_\mu^2) \tag{2.178}$$

Chapter 3

Topological defects and textures in two-dimensional quantum orders

In this chapter, we consider two-dimensional (2d) quantum many-body systems with long-range orders, where the only gapless excitations in the spectrum are Goldstone modes of spontaneously broken continuous symmetries. To understand the interplay between classical long-range order of local order parameters and quantum order of long-range entanglement in the ground states, we study the topological point defects and textures of order parameters in such systems. We show that the universal properties of point defects and textures are determined by the remnant symmetry enriched topological order in the symmetry-breaking ground states with a non-fluctuating order parameter, and provide a classification for their properties based on the inflation-restriction exact sequence. We highlight a few phenomena revealed by our theory framework. First, in the absence of intrinsic topological orders, we show a connection between the symmetry properties of point defects and textures to deconfined quantum criticality. Second, when the symmetry-breaking ground state have intrinsic topological orders, we show that the point defects can permute different anyons when braided around. They can also obey projective fusion rules in the sense that multiple vortices can fuse into an Abelian anyon, a phenomena for which we coin "defect fractionalization". Finally, we provide a formula to compute the fractional statistics and fractional quantum numbers carried by textures (skyrmions) in Abelian topological orders.

3.1 Introduction

One of the most successful theories in condensed matter physics is the Landau's theory of phases and phase transitions [148, 72, 146, 147]: phases are distinguished by their symmetries, and phase transitions are described by symmetry breaking. An ordered phase with broken symmetry is identified through the formation of off-diagonal long-range order and is characterized by a local order parameter. While the spontaneous breaking of a continuous symmetry leads to Goldstone modes [188, 74] which are gapless excitations in the system,

a class of gapped topological excitations – defects and textures – may also be present in an ordered phase as a consequence of the nontrivial topology of the order parameter space [178]. This *classical topology* can lead to very rich physics. For example, the topological defects have their own dynamics and may also lead to phase transitions at finite temperatures [20, 21, 138]. Topological defects and textures also commonly appear in soft matter physics [130, 256] and ultracold atom physics [156, 235].

Since the discover of the quantum Hall effects in the 1980s [132, 255, 151], the notion of phases of matter have been extended beyond Landau's theory. Let us focus on gapped phases of matter, which, by definition, are phases with gapped excitations that are robust against local perturbations without closing the gap. In absence of symmetry, these different phases are determined by the long-range entanglement structure of the ground state wave functions [275], with the trivial one being an "atomic insulator" whose ground state shares the same phase as a collection of isolated atoms. A topological order, on the other hand, has a nontrivial entanglement structure in their wave function, which manifest itself, e.g. through ground state degeneracy when placed on a topologically nontrivial manifold [270]. Here, while the word "topological" in topological order still refers to the robustness of the low energy excitations against local perturbations without closing the gap, this feature is a direct consequence of the long-range entanglement of the wave function [275]. In presence of symmetry, either a topologically trivial state or a topologically ordered state may be further separated into different phases. The result is either a symmetry protected topological (SPT) phase [83, 41, 39, 40, 42, 45, 44, 43, 197, 170, 274, 154, 277] or a symmetry enriched topological (SET) phase [59, 179, 169, 245, 14], and in both cases different gapped ground states are characterized by certain topological invariants. As the quantum state counterpart of the order parameter in a broken phase in Landau's theory, the topological invariants reflect the robustness of the state under small perturbations and are a manifestation of the *quantum topology* that arises from many-body quantum entanglement in the wave function.

So far, most studies on topological phases – SPT and SET – preserve all symmetries of the system, in contrast to the Landau paradigm where spontaneously broken symmetries give rise to long-range orders. In other words, topological (SPT and SET) phases are usually discussed in a context that excludes long-range orders from spontaneous symmetry breaking. In nature, nevertheless, the coexistence of long-range order in a topological phase is not a rare phenomenon: nematic quantum Hall states in higher Landau levels [63], topological superconductors that spontaneously break charge conservation [162], and magnetic fragmentation for spin ice [195], to name a few. On the theoretical side, while most previous works studied examples with an emphasis on non-interacting fermion systems [232, 261, 109, 205, 298, 204, 248, 11, 10, 12, 8, 265], a general theory for interacting topological phases with coexisting long-range orders is still lacking [58].

This motivates us to establish a theoretical framework for topological phases in the presence of long-range orders [58], which is the main focus of the present work. We consider the "gapped" topological phases, where the Goldstone modes that arise from spontaneous breaking of continuous symmetries are the only gapless excitations in the system. Our approach is to study the universal properties of topological defects and textures of the

spontaneously broken symmetries, as a first step towards a classification of topological phases in presence of long-range orders.

One theme of the present work is to establish a concrete connection between classical topology and quantum topology. We will be mainly focusing on topological point defects and smooth textures (i.e. skyrmions) in two-spatial dimensions and their interplay with an SPT or an SET phase. More precisely, when the full symmetry group G spontaneously breaks down to a subgroup H, we consider a symmetry-breaking ground state where the order parameters are not fluctuating and fixed in a classical minimum of the free energy. Since the only gapless excitations in our systems are the Goldstone modes, these symmetry-breaking states must be the ground state of a gapped Hamiltonian that preserves H. In two spatial dimensions, they are either H-SPT phases in the absence of intrinsic topological orders, or more generally H-SET phases. We intend to understand how these H-SPT or H-SET ground states ("quantum topology") affect universal properties of topological defects and textures of the order parameters ("classical topology") in the associated long-range order.

It turns out the crucial connection between classical and quantum topology can be established generally by a map (a "connecting homomorphism" [58]) from topological defects and textures of the order parameters to (extrinsic) symmetry defects [154, 14, 245, 246] in an H-SPT or H-SET phase. We use this map, and the classification of H-SPT and H-SET phases, to obtain a classification and characterization of the universal properties belonging to topological defects and textures in a long-range ordered quantum system.

We first consider the (conceptually simpler) situation in the absence of intrinsic topological orders, where each ground state with fixed non-fluctuating order parameters is an H-SPT phase. We identify two phenomena out of interplay between classical topology and quantum topology: owing to the H-SPT ground state of the long-range order, the point defects of order parameters can carry a projective representation of the remnant symmetry H, while topological textures of the order parameters (i.e. skyrmions) can carry a nontrivial quantum number of the remnant symmetry H. This provides a new angle into a large family of Landau-forbidden quantum phase transitions: i.e. the deconfined quantum critical points (DQCPs) [221, 222, 262, 165].

Next we consider a more general situation, where each ground state with non-fluctuating order parameters is an H-SET phase with bulk anyon excitations [59, 14, 245, 179, 169]. First, we reveal two exotic phenomena associated with point defects: (1) different types of anyons can be permuted after they are braided around a point defect, (2) multiple point defects, when combined together to form a trivial point defect, can instead fuse into an Abelian anyon, a phenomenon for which we coin the term "defect fractionalization". Then, in the case of smooth textures of order parameters, i.e. skyrmions in 2d, we develop a general field theory that couples a topological ordered system to a ferromagnetic order parameter via a topological term in the Lagrangian. Applying this to Abelian topological orders, we obtain the formula for the fractional statistics and fractional quantum numbers of skyrmions in the system.

Another interest of this work comes from the technical side. It has been known for long (and fairly familiar among condensed matter physicists) that classical topological defects

are mathematically described by homotopy groups in algebraic topology [91, 207]. This mathematical object is rather intuitive as it admits a real space picture: it models the topological defects as maps from real space (or spacetime) to the space of parameters (such as the order parameter space which is of interest to this work) and classifies them up to continuous deformation. On the other hand, the theory of symmetry defects and symmetry fractionalization are rather new in condensed matter physics [276, 154, 59, 245, 14], and the main mathematical tool employed are various homology (and cohomology) theories. While homology theory also stems from homotopy theory in algebraic topology, it has developed into an independent subject, whose application in physics is far more rich and profound. Even from this technical point of view, it would be a great pleasure – and would bring great mathematical insight to the physical problem under consideration – to see how these mathematical objects can be united in the treatment of classical topology and quantum topology.

This chapter is organized as follows. In Sec. 3.3, we describe a theoretical framework, which crucially connects the point defects and textures of the order parameters of the broken symmetries to the symmetry defects of the preserved symmetries. This connection allows us to classify and characterize the universal properties of point defects and textures using the topological properties of the ground states. In Sec. 3.4, we continue our theoretical framework by exploring the connection between classical topology and quantum topology, where we provide more mathematical details on group cohomology classification for point defects and textures in SPT and SET phases. The key word there are the so-called "inflation map" that appears in a five-term exact sequence for group cohomology, whose physical meaning will be investigated in great detail. Next we apply this framework to demonstrate universal properties of point defects and textures in 2d quantum orders. In Sec. 3.5, we focus on the simplest cases in the absence of intrinsic topological orders, where all ground states with a fixed order parameter configuration are SPT phases. We show that the exotic phenomena of DQCP can be captured in a concise manner within our framework. Next, we proceed with general cases where the ground states are SET phases with intrinsic topological order. In Sec. 3.6, we classify topological properties of point defects, highlighting two distinct phenomena: non-Abelian point defects that permute anyons when braided around, and a new phenomenon for which we coin "defect fractionalization" where multiple point defects fuse into Abelian anyons. In Sec. 3.7, we study topological textures (i.e. skyrmions) in 2d SET phases, in particular, we compute the fractional statistics and quantum numbers of skyrmions. Finally we summarizes our main results and look into future directions in Sec. 3.8.

3.2 Note on notations

Many Abelian groups are defined in this work. When an Abelian group represents (the fusion of) Abelian anyons we will often denote by blackboard bold symbol, e.g. $\mathbb{Z}_2$. Quite often we use subscript to detail the anyon types, e.g. $\mathbb{Z}_2^{\mathfrak{e}}$ denotes the (fusion) group of the trivial anyon

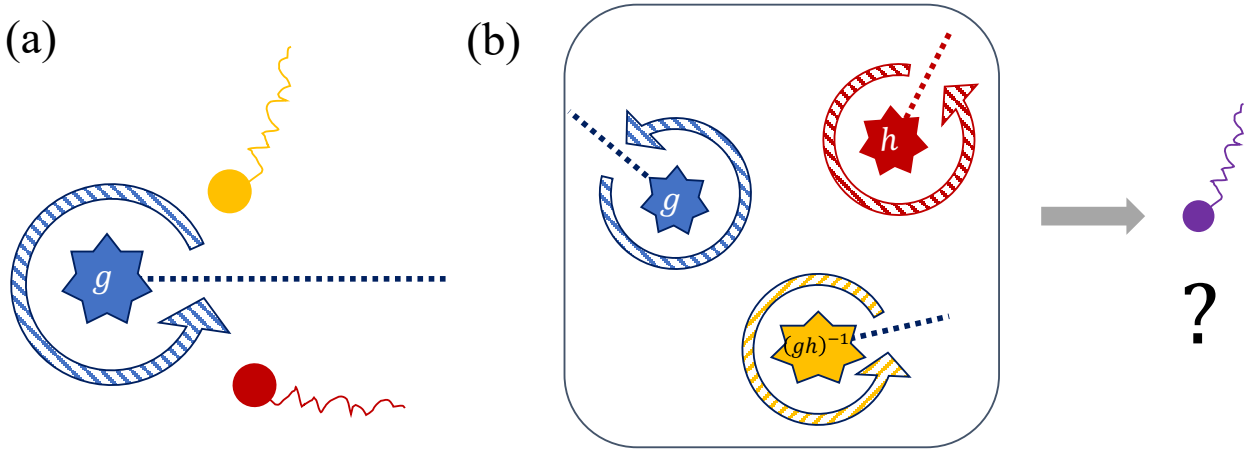

Figure 3.1: (a) Similar to symmetry defects, the topological defects in topological order may also braid the anyons. (b) Defect fractionalization: topological defects in symmetry enriched topological order can fuse to additional anyons.

1 and the "electric" particle e. We also denote the homotopy group and the cohomology group blackboard bold symbol. On the other hand, when an Abelian group appears as a group of symmetry operations we will often denote with the usual symbol, e.g. Z_2 and Z_4. Sometimes a group is indicated by its generators, for example, for the Abelian group generated by the two-fold element h all the following notations are equivalent: $Z_2 = Z_2^h = \{1, h\} = \langle h \rangle$.

Several types of products appear in this work. Since quite often we are dealing with finite Abelian groups, we do not distinguish direct product and direct sum, for example, $\mathbb{Z}_2 \times \mathbb{Z}_2$ and $\mathbb{Z}_2 \oplus \mathbb{Z}_2$, and $\mathbb{Z}_2^2$ all mean the same object. Note these are different from tensor product of groups. As an example, we have $\mathbb{Z}_2 \otimes \mathbb{Z}_2 = \mathbb{Z}_2 \neq \mathbb{Z}_2^2$.

For the group cohomology $\mathcal{H}^*(G, \mathcal{A})$, G can either act trivially or nontrivially on the coefficient $\mathcal{A}$. Quite often when the action is nontrivial it is specified explicitly in some way (either stated in words or using symbols): for example in $\mathcal{H}^2_h(D_2 = Z_2^g \times Z_2^h, \mathcal{A} = \mathbb{Z}_2^{\mathsf{e}} \times \mathbb{Z}_2^{\mathsf{m}}) = \mathbb{Z}_2$ the Abelian group Z_2^h generated by an order-two element h acts nontrivially on the anyons $\mathcal{A}$, and we remind this action by the subscript h in the notation $\mathcal{H}^n_h$. As another example, in the five-term exact sequence, all the cohomology groups with possible nontrivial actions (ρ: $H \to \mathrm{Aut}(\mathcal{A})$), $\widetilde{\rho}$: $\pi_1(G/H) \to \mathrm{Aut}(\mathcal{A})$)) are manifest by the subscripts, whereas the term $\mathcal{H}^1(\pi_1(G), \mathcal{A})$ without subscript (or with the subscript "id") means $\pi_1(G)$ acts trivially on $\mathcal{A}$.

3.3 General framework

We consider the ground state of a 2d quantum many-body system, which exhibits a long-range order associated with spontaneous symmetry breaking. To be precise, the symmetry group G of the Hamiltonian spontaneously breaks down to a subgroup H that is preserved

in an ordered ground state. Moreover, we assume that the possible Goldstone modes, from spontaneously broken continuous symmetries, are the only gapless excitations in the bulk of the system. In other words, the ground state with a fixed nonzero order parameter $O(\vec{r}) = \langle \hat{O}(\vec{r}) \rangle \neq 0$, is a gapped symmetric phase that preserves the remnant symmetry H. In the rest part of the paper, for simplicity, we assume the classical gapless Goldstone modes do not affect the topological data of the remnant gapped quantum phases that we are interested in. In two spatial dimensions, this means the ground state is an H-symmetry enriched topological order. The question we are answering is, what are the universal properties of topological defects and textures in the order parameters therein, when the symmetry-breaking ground state is a topological state enriched by the remnant symmetry H?

To address this question, we need to consider topological defects and textures as excitations in a symmetry-breaking ground state. They turn out to be connected to a special type of excitations known as extrinsic symmetry defects (or twist defects) in symmetry enriched topological (SET) phases. This correspondence allows us classify universal properties of topological defects and textures in ordered media with a nontrivial ground state topology. The key mathematical tool to establish this connection is the long exact sequence of homotopy groups for topological defects and textures. In this section, we outline this connection between classical topology of the order parameters and quantum topology of the entangled ground states, and then utilize this connection to classify point defects and textures in following sections.

3.3.1 Domain walls

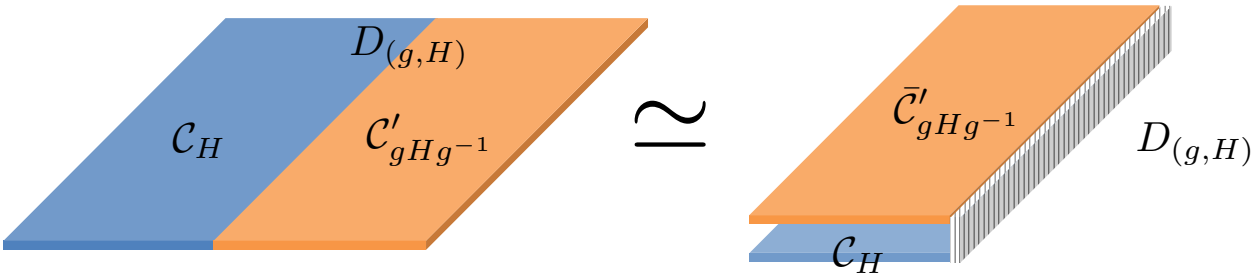

Figure 3.2: The equivalence between a domain wall between two phases $\mathcal{C}_H$ and $\mathcal{C}'_{gHg^{-1}}$, and the boundary of a 2d phase (Eq. (3.2)).

In 2d, a gapped phase that preserves remnant symmetry H is generally an H-SET phase, whose anyon excitations are described by a unitary modular tensor category $\mathcal{C}$ [127, 14, 245]. We use $\mathcal{C}_H$ to label such an H-SET phase. The domain wall in two spatial dimension is a line defect characterized by $\pi_0(G/H)$. In a gapped system whose symmetry group G of the Hamiltonian is spontaneously broken, a generic domain wall $D_{(g,H)}$ is labeled by a remnant subgroup $H < G$ and a group element $g \notin H$, such that it separates a left domain that preserves symmetry subgroup H, and a right domain that preserves subgroup gHg^{-1}, as

shown in Fig. 3.2. We can label the H-SET phase on the left domain as $\mathcal{C}_H$, and the (gHg^{-1})-SET phase on the right domain would be

$$U_g \mathcal{C}_H U_g^{-1} \simeq \mathcal{C}'_{gHg^{-1}} \tag{3.1}$$

where we use U_g to label the action of broken symmetry element g on the H-SET phase on the left domain. Note that the right domain and the left domain may not share the same topological order $\mathcal{C}$, e.g. in the case of a time reversal domain wall with $g = \boldsymbol{T}$, the left and right domains have opposite chiralities and hence $\mathcal{C}' = \bar{\mathcal{C}}$, where $\bar{\mathcal{C}}$ is defined as the time reversal counterpart of topological order $\mathcal{C}$. In this setup, using the folding trick, it is clear that the domain wall $D_{(g,H)}$ between left domain $\mathcal{C}_H$ and right domain $\mathcal{C}'_{gHg^{-1}}$ can be mapped to the boundary of a 2d topological phase:

$$(\mathcal{C} \boxtimes \bar{\mathcal{C}}')_{H_g} \equiv \mathcal{C}_H \boxtimes \bar{\mathcal{C}}'_{gHg^{-1}} \tag{3.2}$$

where we denote the remnant unbroken symmetry of the domain wall configuration as

$$H_g \equiv H \cap (gHg^{-1}) = \{h \in H | g^{-1}hg \in H\} \tag{3.3}$$

Therefore the universal properties of domain walls $D_{(g,H)}$ is captured by boundary excitations of a 2d topological phase described by (3.2), as illustrated in Fig. 3.2.

The physics of boundary excitations in a 2d topological order is in fact a subject extensively studied in the literature [129, 30, 107, 144, 100, 29, 145, 136, 135]. In light of the above physical picture that maps a domain wall to a boundary, we will not attempt to classify topological properties of domain walls in SET phases in this manuscript. From now on we shall discuss only the point defects and textures in two spatial dimensions.

3.3.2 Point defects

In two spatial dimensions, point defects are classified by the fundamental group $\pi_1(G/H)$. Two representative examples of point defects in 2d are the following:

(1) In a system of interacting spinless bosons whose ground state is an m-boson condensate, the boson number conservation symmetry $G = U(1)$ is spontaneously broken down to a $H = Z_n$ subgroup. The vortices of such an m-boson condensate are classified by $\pi_1(G/H) = \pi_1(U(1)) = \mathbb{Z}$. In particular, the fundamental vortex with unit winding number $\nu = 1$ is equivalent to a $2\pi/m$ flux by a gauge transformation.

(2) For interacting ions that form a crystalline lattice in two dimensions, the continuous translation symmetry $G = \mathbb{R}^2$ is spontaneously broken down to a discrete subgroup $H = \mathbb{Z}^2$. The associated point defects, i.e. dislocations, are classified by $\pi_1(G/H) = \mathbb{Z}^2$, characterized by a Burgers vector $\vec{b} = b_1\vec{a}_1 + b_2\vec{a}_2$, where $(b_1, b_2) \in \mathbb{Z}^2$ and $\vec{a}_{1,2}$ are the two primitive lattice vectors. Physically, we can consider a close loop on a translation-invariant lattice. If a particle follows exactly the same path of the loop, which now encloses a dislocation, the particle will not return to the starting point after finishing the path. Instead, the final

position differs from the initial position by the Burgers vector $\vec{b}$ of the dislocation enclosed by the path.

Both examples belong to the general case where a connected topological (continuous) group G is broken down to a discrete subgroup H. We assume H to be a normal subgroup of G (i.e. $H \triangleleft G$), so that the whole point defect configuration of order parameters preserves symmetry H. Applying the long exact sequence Eq. (1.5) to the $n = 1$ case, we obtain the following *short exact sequence*:

$$\cdots \longrightarrow \pi_1(H) = 0 \xrightarrow{f} \pi_1(G) \xrightarrow{i} \pi_1(G/H) \xrightarrow{p} \pi_0(H) = H \xrightarrow{g} \pi_0(G) = 0 \longrightarrow \cdots \quad (3.4)$$

where p is known as the connecting homomorphism between the topological point defects and symmetry defect. The group $\pi_1(G)$ and $\pi_1(G/H)$ are illustrated in Fig. 3.3.

This short exact sequence of groups can be understood as follows: using the exactness of the sequence, it is clear that i is an injective map, hence $\pi_1(G)$ is a normal subgroup of $\pi_1(G/H)$. The connecting homomorphism p is a surjective map so H is isomorphic to the quotient group $\pi_1(G/H)/\pi_1(G)$. Such a short exact sequence defines a group extension problem, and here we say that $\pi_1(G/H)$ is a group extension of the group $\pi_1(G)$ by H.

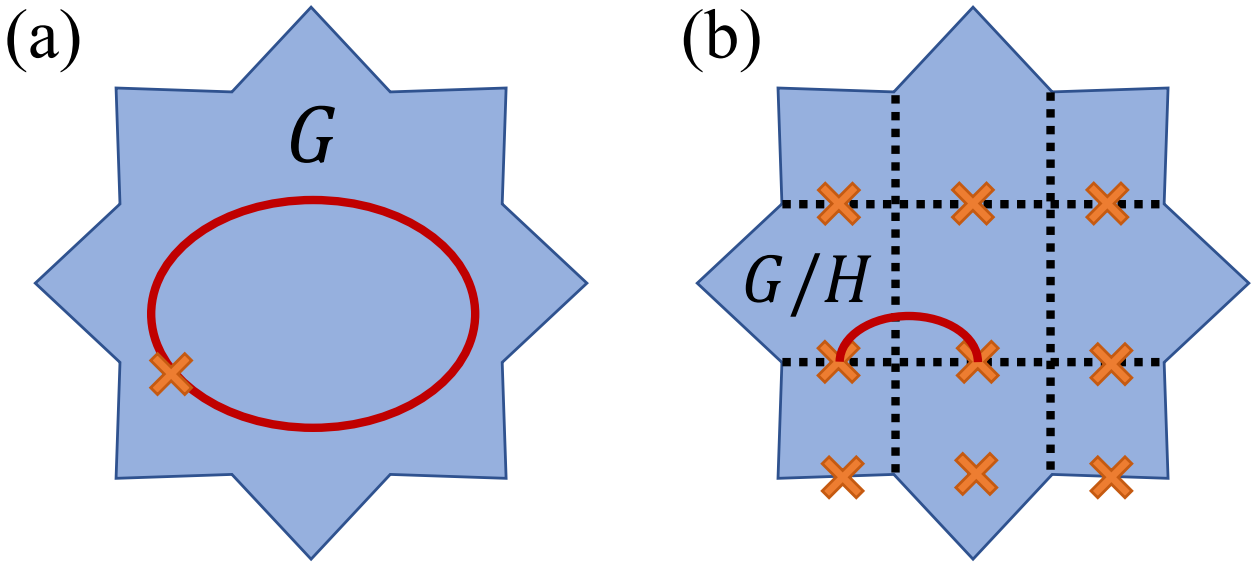

Figure 3.3: Illustration of the fundamental group π_1 of the group manifold. (a) $\pi_1(G)$ captures the winding in G-space. (b) $\pi_1(G/H)$ captures the winding in G/H space. Note that the open line in (a) may be considered as closed loop in (b) as those points are identified in G/H space.

Physically, the surjective map g in the short exact sequence (3.4) connects topological point defects classified by $\pi_1(G/H)$, to symmetry defects associated with elements of the remnant symmetry group H in the symmetry-breaking ground state, which is generally an H-SET phase. Note that the classification and characterization of H-SET phases [14, 245, 246]

is in fact built upon an algebraic theory of h-defects for $h \in H$, which has been extensively studied previously. The above group extension allows us to map each point defect classified by $\pi_1(G/H)$ to an h-defect associated with the group element $h \in H$, therefore allowing us to characterize the topological properties of point defects. In the two examples mentioned above: (1) Since $\pi_1(G = U(1)) \neq 0$, a vorticity-ν vortex in an m-boson condensate is mapped to a $2\pi\nu/m$ flux of the remnant Z_m symmetry, and hence the map p is surjective but not injective. (2) Since $\pi_1(G = \mathbb{R}^d) = 0$, the dislocations are in one to one correspondence with translation symmetry defects, and hence the map p is bijective.

Below we shall apply this idea to two different families of symmetry-breaking phases:

(i) When a symmetry-breaking ground state has no intrinsic topological order, it is described by an H-SPT phase. The point defects can carry linear or projective representations of the remnant symmetry H, a phenomenon closely related to deconfined quantum critical points (DQCP). We discuss point defects of this family in Sec. 3.5.

(ii) When there are intrinsic topological orders in a symmetry-breaking ground state, it is generally an H-SET phase. In this case, the point defects can be non-Abelian defects that permute anyons, or they can exhibit exotic fusion rules. We classify and discuss point defects of this family in Sec. 3.6.

3.3.3 Textures

The most familiar example of a topological texture in two spatial dimension is a skyrmion. When a ferromagnetic order breaks the $G = SO(3)$ spin rotational symmetry to a uniaxial spin rotation subgroup $H = U(1)$, the order parameter manifold is a 2-sphere $\mathcal{M} = G/H = S^2$ with nontrivial textures classified by $\pi_2(S^2) = \mathbb{Z}$. In fact, most familiar realizations of topological textures in 2d are essentially classified by $\pi_2(S^2) = \mathbb{Z}$, and we shall focus on skyrmions as 2d textures in the manuscript.

In the case of skyrmions, the long exact sequence (1.5) reduces to the short exact sequence

$$\begin{aligned} \cdots \longrightarrow \pi_2(SO(3)) = 0 \longrightarrow \pi_2(S^2) = \mathbb{Z} \xrightarrow{i} \pi_1(U(1)) = \mathbb{Z} \\ \longrightarrow \pi_1(SO(3)) = \mathbb{Z}_2 \xrightarrow{p} \pi_1(S^2) = 0 \longrightarrow \cdots \end{aligned} \tag{3.5}$$

This short exact sequence indicates that the connecting homomorphism i is an injective map from skyrmions labeled by $\pi_2(S^2) = \mathbb{Z}$ to fluxes labeled by $\pi_1(U(1)) = \mathbb{Z}$. More precisely, the group of $U(1)$ fluxes $\pi_1(U(1)) = \mathbb{Z}$ is a central extension of the skyrmion group $\pi_2(S^2) = \mathbb{Z}$, with the center being the group of point defects $\pi_1(SO(3)) = \pi_1(SU(2)/Z_2) = \mathbb{Z}_2$ [1].

Physically, it is known that the $\mathbb{Z}_2$ point defect is nothing but a 2π vortex for the $SO(3)$ spins [122, 56]. In other words, the spin of a particle is rotated around one (any) axis by

[1] Note that, here we have used the fact $\pi_1(SU(m)/\mathbb{Z}_m) = \mathbb{Z}_m$ from the following four-term exact sequence

$$\pi_1(SU(m)) = 0 \xrightarrow{f_1} \pi_1(SU(m)/\mathbb{Z}_m) \xrightarrow{f_2} \pi_0(\mathbb{Z}_m) = \mathbb{Z}_m \xrightarrow{f_3} \pi_0(SU(m)) = 0,$$

Using the exactness of the terms, one can show that f_2 is an isomorphism map, therefore $\pi_1(SU(m)/\mathbb{Z}_m) \cong \mathbb{Z}_m$.

2π after circling around the nontrivial point defect in $\pi_1(SO(3)) = \mathbb{Z}_2$. Eq. (3.5) defines a map from the element $a \in \pi_2(S^2)$ to $b \in \pi_1(U(1))$ and then to the trivial element in $\pi_1(SO(3)) = \mathbb{Z}_2$. Since the non-trivial element for that $\mathbb{Z}_2$ point defect is a 2π vortex for spins, the trivial element of $\mathbb{Z}_2$ should correspond to a 4π vortex. Therefore, in Eq. (3.5), a skyrmion with winding number $\nu \in \mathbb{Z}$ is mapped to a $4\pi\nu$ flux of the $U(1)$ spin rotations, i.e., $2\nu \in \pi_1(U(1)) = \mathbb{Z}$ [80, 58].

The map in Eq. (3.5) points to the nature of skyrmions in a ferromagnetic topological order where $SO(3)$ spin rotational symmetry is spontaneously broken down to a $U(1)$ subgroup, as the topological properties of each $\nu = 1$ skyrmion can be extracted from those of $4\pi\nu$ flux/defect of the unbroken $U(1)$ symmetry. We shall follow this approach to identify the fractional stastistics of skyrmions in Sec. 3.7.

3.4 Group cohomology for point defects and textures

3.4.1 Group cohomology for symmetry defects: a brief review

Following Ref. [14, 47, 1, 263], below we give a definition for symmetry defects in both SPT and SET orders. When the physical system has a symmetry H with a given symmetry action ρ on the quasi-particles, one can consider modifying the system by introducing a point-like defect τ_h associated with a group element $h \in H$. When a quasi-particle is braided around an h-symmetry defect τ_h, it is acted upon by the corresponding symmetry action ρ_h. Since H is a global symmetry, the point-like defects τ_h are not finite-energy excitations and must be extrinsically imposed by threading the symmetry flux of h.

As group cohomology is a crucial mathematical object for this work, we have given a self-contained introduction to it from the mathematical side in Chapter. [1]. More detailed characterization and intuition for it from the physics side will be given here and in later sections.

3.4.1.1 Symmetry protected topological (SPT) phases

We start by recalling the definition and classification of bosonic SPT phases. An H-SPT phase is a short-range entangled phase, which, in the presence of symmetry H, cannot be continuously connected to a trivial product state without closing the energy gap. In a system of interacting bosons in d spatial dimensions, different H-SPT phases are classified by the $(d+1)$-th group cohomology $\mathcal{H}^{d+1}(H, U(1))$ [44]. The cohomology group $\mathcal{H}^{d+1}(H, U(1))$ is an Abelian group, whose identity element labels the topologically trivial phase (a featureless product state), and the addition of group elements is implemented by stacking different SPT phases.

When symmetry G is spontaneously broken down to H in a given ground state, a long-range ordered ground state with fixed order parameters is an H-preserving short-range en-

tangled phase[2] which are H-SPT phases classified by the group cohomology $\mathcal{H}^3(H, U(1))$[44].

We consider a 2d SPT phase protected by a symmetry group $H = B \times K$, which is a direct product of two groups B and K. The Künneth formula indicates that the classification of H-SPT phases can be written as a direct product [44]:

$$\mathcal{H}^{d+1}(B\times K, U(1)) = \prod_{i=0}^{d+1} \mathcal{H}^i\big(B, \mathcal{H}^{d+1-i}(K, U(1))\big) \tag{3.6}$$

In the $d = 2$ case which is the interest of this manuscript, we have

$$\begin{aligned}&\mathcal{H}^3(B\times K, U(1)) = \mathcal{H}^3(B, U(1)) \times \mathcal{H}^2(B, \mathcal{H}^1(K, U(1)))\\ &\times \mathcal{H}^1(B, \mathcal{H}^2(K, U(1))) \times \mathcal{H}^3(K, U(1))\end{aligned}$$

where each term has its own physical meaning. Clearly the first term $\mathcal{H}^3(B, U(1))$ classifies the SPT phases protected only by the subgroup B, while the last term $\mathcal{H}^3(K, U(1))$ classifies SPT phases protected only by the subgroup K.

In this work, we are particularly interested in the mixed anomaly of symmetry B and K, which assigns quantum numbers or projective representations of subgroup K to B symmetry defects. The mixed anomaly is captured by the 2nd and 3rd terms in the Künneth expansion (3.7), as suggested by the "decorated domain wall" picture of the SPT phases [43].

(i) The 2nd term $\mathcal{H}^1(B, \mathcal{H}^2(K, U(1)))$ assigns a projective representation $[\omega] \in \mathcal{H}^2(K, U(1))$ to any symmetry defect α_g associated with $g \in B$. As discussed in Sec. 3.3.2, in the exact sequence (3.4), the connecting homomorphism p maps a symmetry breaking point defect (i.e. vortex) of order parameters classified by $\pi_1(G/H)$ to a symmetry defect labeled by elements of $H = B \times K$. If the associated symmetry defect corresponds to an element $g \in B$, this suggests that the point defect of order parameters can carry a projective representation of K. This map will be discussed in detail in Sec. 3.4.3.

(ii) For topological textures of the order parameters in $d = 2$, we shall focus on the case of skyrmions, where the remnant symmetry is $H = U(1) \times K$ with $B = U(1)$. In other words, we consider the full symmetry $G = SO(3) \times K$ is broken down to $H = U(1) \times K$ in the collinear long-range order. In this case, we utilize an important result from the theory of cohomology: for any finite Abelian group M on which $U(1)$ and $\mathbb{Z}$ both act trivially[3],

$$\mathcal{H}^2(U(1), M) \cong M \cong \mathcal{H}^1(\mathbb{Z}, M). \tag{3.7}$$

[2]We use the definition of Ref. [44] for short-range entangled phase, which is different from Kitaev's definition [127]. Therefore we do not consider invertible phases such as topological superconductor in class D [128], and E_8 states of $d = 2$ interacting bosons [127, 170].

[3]Here it is important to specify that by $\mathcal{H}^2(U(1), M)$ we are computing the Borel cohomology, which is the standard cohomology for bosonic SPT [44]. The calculation uses the relation between Borel cohomology and simplicial cohomology $\mathcal{H}^2(U(1), M) = H^2(BU(1), M) = H^2(\mathbb{CP}^\infty, M)$ and the procedure of regarding $H^2(CP^\infty, M)$ as the limiting case of $H^2(CP^n, M) \cong M$ for $n \to \infty$ following Ref. [44]. On the other hand, the part $\mathcal{H}^1(\mathbb{Z}, M) \cong M$ can be obtained in either standard group cohomology or Borel cohomology.

Mathematically, both cohomology groups classify different linear representations $\{R_\nu \in M|\nu \in \mathbb{Z}\}$ of the integer ($\mathbb{Z}$) group formed by the $2\pi\nu,\ \nu \in \mathbb{Z}$ fluxes of the remnant $U(1)$ symmetry with coefficients $R(\nu) \in M$.

As a result, with $B = U(1)$, we can rewrite the 3rd term in Künneth expansion (3.7) as

$$\mathcal{H}^2\big(U(1), \mathcal{H}^1(K, U(1))\big) = \mathcal{H}^1\big(\mathbb{Z}, \mathcal{H}^1(K, U(1))\big) \tag{3.8}$$

Physically, this can be interpreted as assigning quantum numbers (or charges) of symmetry group K, i.e. linear representation $\mathcal{H}^1(K, U(1))$, to the integer fluxes of the unbroken $U(1)$ subgroup.

As discussed in Sec. 3.3.3, the connecting homomorphism i in (3.5) maps the skyrmions labeled by $\nu_s \in \pi_2(G/H) = \mathbb{Z}$ to integer fluxes labeled by $\nu_f \in \pi_1(U(1)) = \mathbb{Z}$. As a result, we can use the SPT classification $\mathcal{H}^2\big(U(1), \mathcal{H}^1(K, U(1))\big)$ for each symmetry-breaking ground state to determine the K symmetry quantum numbers assigned to each skyrmion. This map will be discussed in detail in Sec. 3.4.4.

3.4.1.2 Symmetry enriched topological (SET) order

Consider a topological order described by a unitary modular tensor category $\mathcal{C}$, enriched by symmetry H that is a discrete group. Since the topological order preserves the unbroken symmetry H, an SET phase can arise which in addition to the topological order displays the phenomenon of fractionalization of symmetry [59, 245, 14]. Here we briefly review the physical picture of symmetry fractionalization and the classification of SET.

For each group element $h \in H$, one can associate an extrinsic defect/flux τ_h [245, 14] in the H-symmetry enriched topological order. A symmetry defect can be further *labeled* by an anyon $\mathsf{a} \in \mathcal{C}$ of the topological order, with the identity symmetry defect (i.e. the symmetry defect associated with the identity element of the group) identified with the anyon a itself. The symmetry defects in this sense are generalized anyons and can have nontrivial fusion and braiding rules. In particular, anyons may be permuted when braided around a symmetry defect τ_h. This braiding is one way of detecting the symmetry action $\rho\colon H \to \mathrm{Aut}(\mathcal{C})$, where $\mathrm{Aut}(\mathcal{C})$ denotes the automorphism group of the anyons. The first group cohomology group, $\mathcal{H}^1_\rho(H, \mathcal{A})$, defines a (possibly crossed, when ρ nontrivial) homomorphism $[\omega]$ where $\omega\colon H \to \mathcal{A}$ describes an anyon labeling of symmetry defects that is consistent with the symmetry action on the anyons, ρ. Two anyon-labeling homomorphisms ω', ω'' belong to the same class $[\omega]$ if they differ only by an anyon permutation described by ρ. Physically, $\mathcal{H}^1_\rho(H, \mathcal{A})$ points to the ambiguity that an Abelian anyon $a_h \in \mathcal{A}$ can always be attached to a symmetry defect τ_h to form a new symmetry defect τ'_h corresponding to the same group element $h \in H$.

The additional data to specify an SET phase is symmetry fractionalization (whose physical meaning will now be specified), classified by the second group cohomology $\mathcal{H}^2_\rho(H, \mathcal{A})$. Here ρ denotes the symmetry action on the anyons as introduced above, and $\mathcal{A} \subset \mathcal{C}$ is the

set of Abelian anyons viewed as an Abelian group under fusion [245, 14][4]. The elements $[\omega] \in \mathcal{H}^2_\rho(H, \mathcal{A})$ are cocycle elements ω under the equivalence relation of anyon labeling. The cocycle elements $\omega(g, h) \in \mathcal{A}$ takes as an input two group elements $g, h \in H$ and returns an anyon. Physically, the cocycle, roughly speaking, describes the outcome of fusing three defects τ_g, τ_h, and $\tau_{(gh)^{-1}}$: the result is a trivial defect associated to the identity element of H as required by the "conservation law"of the symmetry H, and the only possible outcome is an Abelian anyon. The symmetry fractionalization data precisely refer to the anyon outcomes after fusion. Crucially, it is inappropriate to think of the outcome anyon as fixed since different anyons may be identified under the equivalence relation; rather symmetry fractionalization refers to the inequivalent ways of assigning defect fusion rules up to anyon relabeling.

To summarize, an H-SET phase is classified by symmetry action ρ on the anyon contents, and the associated (symmetry) defect "fusion rule", which encode symmetry fractionalization data classified by $\mathcal{H}^2_\rho(H, \mathcal{A})$. The defect fusion rule $\mathcal{H}^2_\rho(H, \mathcal{A})$ is defined up to the a relabeling of symmetry defects by Abelian anyons, specified by $\mathcal{H}^1_\rho(H, \mathcal{A})$. As we show below, all these data have correspondence in a phase with coexisting symmetry breaking defect and topological order.

3.4.2 The inflation-restriction exact sequence

In this subsection we introduce the main mathematical tool we will be relying on in the physical interpretation of group cohomology, the *inflation-restriction exact sequence*.

Recall that the input data for group cohomology $\mathcal{H}^n_\rho(G, M)$ is a group G and an Abelian group M equipped with a G-action $\rho\colon G \to \mathrm{Aut}(M)$, $g \mapsto \rho(g)$ (we use $\rho(g)$ and ρ_g interchangeably). For convenience, we denote the G-action on M by the symbol ".", that is, for $g \in G$ and $\mathsf{a} \in M$, we define $\rho(g)(\mathsf{a}) \equiv g.\mathsf{a}$. Suppose N is a normal subgroup of G, and $Q := G/N$ the associated quotient group. Formally, we say that G is an extension of the group Q by N that fits into the short exact sequence

$$\begin{array}{ccccccccc} 0 & \longrightarrow & N & \xrightarrow{i} & G & \xrightarrow{p} & Q = G/N & \longrightarrow & 0 \\ & & & \searrow^{\rho_N} & & \swarrow_{\rho} & \downarrow & & \\ & & & & & & \mathrm{Aut}(M) & & \end{array} \tag{3.9}$$

Note that here the action $\rho_N\colon N \to \mathrm{Aut}(M)$ is inherited from the action ρ. There is also an action $\rho_Q\colon Q \to \mathrm{Aut}(M^N)$, here M^N denotes the subgroup of M that are stabilized under the action of N: $M^N = \{\mathsf{a} \in M | n.\mathsf{a} = \mathsf{a}\ \forall n \in N\}$.

Given these data, a five-term exact sequence exists [207]

$$0 \to \mathcal{H}^1(Q, M^N) \to \mathcal{H}^1(G, M) \xrightarrow{\mathrm{res}} \mathcal{H}^1(N, M)^Q \xrightarrow{d_2} \mathcal{H}^2(Q, M^N) \xrightarrow{\mathrm{inf}} \mathcal{H}^2(G, M), \tag{3.10}$$

[4]Note that in the case of SPT discussed in Sec. 3.4.1.1, the action of the symmetry H on the $U(1)$ coefficient is uniquely determined by the symmetry H itself. Thus here and after we only specify the action of the group cohomology for SET.

this is the inflation-restriction exact sequence. Here $\mathcal{H}^1(N,M)^Q$ denotes the subgroup of $\mathcal{H}^1(N,M)$ that are stabilized under the action of Q in the following sense: for $[\omega]\in\mathcal{H}^1(N,M)$ represented by the cocycle ω,

$$[\omega]\in\mathcal{H}^1(N,\mathcal{A})^Q \iff q.(\omega(q^{-1}nq))=\omega(n), \tag{3.11}$$

for any $q\in Q$ and $n\in N$. The maps "res", "d_2" and "inf" are called the restriction, the transgression (or the differential), and the inflation maps, respectively, and can be defined explicitly.

In the following, we will apply the five-term exact sequence to various short exact sequences of homotopy groups. These homotopy groups describe either point defects or textures in the broken symmetry phase, and the broken symmetry phase is either an SPT or an SET. Below we discuss each cases separately.

3.4.3 Group cohomology for point defects

3.4.3.1 Point defects in SPT

Consider a symmetry breaking from $G=A\times K$ to $H=B\times K$, where A is a continuous group and B a discrete group. A symmetry-breaking ground state with a fixed order parameter is an H-SPT, and we focus on the mixed anomaly described by the $\mathcal{H}^1(B,\mathcal{H}^2(K,U(1)))$ term in the Künneth formula (3.7).

In this case, the topological point defects of the order parameter $\phi(\vec{r})\in G/H$ is classified by the fundamental group $\pi_1(G/H)=\pi_1(A/B)$ which fits into the short exact sequence (3.4). Recall from the Künneth decomposition (3.7) that the term $\mathcal{H}^1(B,\mathcal{H}^2(K,U(1)))$ assigns projective representations in $M:=\mathcal{H}^2(K,U(1))$ to the symmetry defects of B. Note that here we consider the case of B consisting of only unitary symmetry, therefore B acts trivially on M. By (3.9), now the point defects labeled by $\pi_1(A)$ and $\pi_1(A/B)$ all act trivially on M.

Then, applying the five-term exact sequence (3.10) gives

$$\begin{aligned}0\to\mathcal{H}^1(B,\mathcal{H}^2(K,U(1)))&\xrightarrow{d_1}\mathcal{H}^1(\pi_1(A/B),\mathcal{H}^2(K,U(1)))\\&\xrightarrow{\text{res}}\mathcal{H}^1(\pi_1(A),\mathcal{H}^2(K,U(1)))\\&\xrightarrow{d_2}\mathcal{H}^2(B,\mathcal{H}^2(K,U(1)))\xrightarrow{\text{inf}}\mathcal{H}^2(\pi_1(A/B),\mathcal{H}^2(K,U(1))).\end{aligned} \tag{3.12}$$

The term $\mathcal{H}^1(B,\mathcal{H}^2(K,U(1)))$ is exactly the term in the Künneth decomposition (3.7) discussed above, which gives classification for H-SPT phases with the mixed anomaly. The image of injective map d_1 in $\mathcal{H}^1(\pi_1(A/B),\mathcal{H}^2(K,U(1)))$ classifies the K projective representation carried by point defects in $\pi_1(A/B)$.

Since $\mathcal{H}^2(B,\mathcal{H}^2(K,U(1)))$ is one piece out of the Künneth decomposition for $\mathcal{H}^4(B\times K,U(1))$, it physically corresponds to an anomalous symmetry implementation of group $H=B\times K$ on the surface of a three-dimensional H-SPT phase. It can only happen on the

two-dimensional surface of a three-dimensional H-SPT phase, but not in any two-dimensional lattice models with onsite symmetry actions. Therefore the image of the restriction map is the same as the kernel of the transgression map d_2 in the exact sequence (3.12).

More physics of the point defects in H-SPT phases will be discussed in Sec. 3.5.2.

3.4.3.2 Point defects in SET

We consider a continuous symmetry G spontaneously broken down to a discrete subgroup H, where each symmetry-breaking ground state is an H-SET phase, whose intrinsic topological order is specified by the anyons $\mathcal{C}$.

Recall from previous discussions that SET is equipped with a symmetry action on the anyons, $\rho\colon H \to \mathrm{Aut}(\mathcal{C})$ [14, 245]. Suppose that the system started with a larger (continuous) symmetry G that spontaneously broke down to a discrete symmetry group H. The topological point defects of the order parameter is again classified by $\pi_1(G/H)$ that fits into the short exact sequence (3.4). Then, one can pull back the symmetry H-action ρ to obtain actions of the topological point defects on the anyons:

$$\begin{array}{ccccc} \pi_1(G) & \xrightarrow{i} & \pi_1(G/H) & \xrightarrow{p} & H \\ & \searrow^{\tilde{\rho}} & & \swarrow_{\tilde{\rho}} & \downarrow \rho \\ & & & & \mathrm{Aut}(\mathcal{C}). \end{array} \tag{3.13}$$

Applying the five-term exact sequence (3.10) to Eq. (3.13) gives

$$\begin{aligned} 0 \to \mathcal{H}^1_\rho(H,\mathcal{A}) \to \mathcal{H}^1_{\tilde{\rho}}(\pi_1(G/H),\mathcal{A}) \xrightarrow{\text{res}} \mathcal{H}^1(\pi_1(G),\mathcal{A})^H \\ \xrightarrow{d_2} \mathcal{H}^2_\rho(H,\mathcal{A}) \xrightarrow{\text{inf}} \mathcal{H}^2_{\tilde{\rho}}(\pi_1(G/H),\mathcal{A}), \end{aligned} \tag{3.14}$$

where the second group cohomology $\mathcal{H}^2_\rho(H,\mathcal{A})$ classifies the symmetry fractionalization in an H-SET phase [14]. Since the second cohomology group classifies defect fusion rules with anyon as outcome, Eqs. (3.14) is a physical statement that the symmetry fractionalization class of symmetry defects may induce a nontrivial fusion rule of the topological point defects. We coin the term "defect fractionalization" for this phenomenon, in reference to the terminology "symmetry fractionalization" for symmetry defects [59, 14, 245]. While different symmetry fractionalization classes of the H-SET phases are classified by $\mathcal{H}^2_\rho(H,\mathcal{A})$, different defect fractionalization classes are classified by the image of the map $\mathrm{inf}\colon \mathcal{H}^2_\rho(H,\mathcal{A}) \to \mathcal{H}^2_{\tilde{\rho}}(\pi_1(G/H),\mathcal{A})$, as describe by the above sequence (3.14).

We will discuss more about point defects in H-SET phases in Sec. 3.6.

3.4.4 Group cohomology for textures

3.4.4.1 Textures in SPT

Consider the symmetry breaking from $G = SO(3) \times K$ to $H = U(1) \times K$. In the absence of intrinsic topological orders, a symmetry-breaking ground state with fixed order parameters

is an H-SPT phase. Here we focus on those H-SPT phases described by the mixed anomaly $\mathcal{H}^2(B = U(1), \mathcal{H}^1(K, U(1)))$ in the Künneth decompostion (3.7). Due to relation (3.8), the mixed anomaly is also captured by $\mathcal{H}^1(\mathbb{Z}, \mathcal{H}^2(K, U(1)))$.

The topological textures of the order parameter are skyrmions classified by $\pi_2(SO(3)/U(1))$. The point defects associated with $SO(3)$ and $U(1)$ are classified by $\pi_1(SO(3))$ and $\pi_1(U(1))$, respectively. Together they fit into the short exact sequence (3.5). Both defects can carry quantum number of the symmetry K, which is classified by the linear representations in $M := \mathcal{H}^1(K, U(1))$, which we assume to be a finite Abelian group. Note that $\pi_1(U(1)) = \mathbb{Z}$, $\pi_1(SO(3)) = \mathbb{Z}_2$ and $\pi_2(SO(3)/U(1)) = \pi_2(S^2) = \mathbb{Z}$ all act trivially on M. Applying the inflation-restriction exact sequence (3.10) to short exact sequence (3.5) gives

$$\begin{aligned} 0 \to & \mathcal{H}^1(\pi_1(SO(3)), M) = \{m \in M | m \cdot m = 1_M \in M\} \\ & \to \mathcal{H}^1(\pi_1(U(1)), M) = M \\ & \xrightarrow{\text{res}} \mathcal{H}^1(\pi_2(S^2), M) = M \\ & \xrightarrow{d_2} \mathcal{H}^2(\pi_1(SO(3)), M) \xrightarrow{\text{inf=0}} \mathcal{H}^2(\pi_1(U(1)), M) = 0. \end{aligned} \tag{3.15}$$

Physically, as discussed in Sec. 3.3.3, a point defect of an $SO(3)$ breaking noncollinear magnetic order classified by $\pi_1(SO(3)) = \mathbb{Z}$, is equivalent to a 2π flux of any $U(1)$ subgroup of $SO(3)$. A skyrmion with topological charge $\nu \in \pi_1(S^2) = \mathbb{Z}$, is therefore equivalent to a $4\pi\nu$ flux of the remnant $U(1)$ symmetry. Note that a 2π flux is nothing but the symmetry defect of the remnant $U(1)$ symmetry, which can carry a linear representation (i.e. charges) of the unbroken subgroup K due to the mixed anomaly (3.8) in the H-SPT phase. The restriction map ("res") in exact sequence above (3.15) physically states the following: if the K-symmetry charge (or mathematically a linear representation of K) $[R] \in M = \mathcal{H}^1(K, U(1))$ is assigned to each 2π flux, the K-symmetry charge carried by a fundamental ($\nu = 1$) skyrmion is given by that of a 4π flux: $[R \otimes R] \in M$.

The above sequence shows that, if M does not contain an order-2 element, then $\{m \in M | m \cdot m = 1_M \in M\} = \emptyset$ and hence the restriction map ("res") is injective: i.e. the quantum number of the symmetry K carried by the skyrmions is fully determined by that carried by the $U(1)$ vortices. More interestingly, if M contains an order-2 element, then the restriction map is the "multiply by 2" map, while d_2 is the mod 2 map. In this case, skyrmion symmetry quantum number is twice that of the $U(1)$ flux. If we further allow the process of completely breaking the $SO(3)$ symmetry down and then restoring the $U(1)$ subgroup, a skyrmion may carry any quantum numbers allowed on a $U(1)$ flux, due to a possible projective representation carried by the $SO(3)$ defect via the transgression map d_2.

We will discuss in more details the physics of topological textures in H-SPT phases in Sec. 3.5.3.

3.4.4.2 Textures in SET

Here we consider the spontaneous symmetry breaking (SSB) from $G = SO(3)$ to $H = U(1)$, resulting in an H-SET phase in each symmetry-breaking ground state with fixed

order parameters. More generally, we could consider an extra symmetry group K that survives the SSB as in the SPT case discussed above. The K-symmetry charges (i.e. linear representations) carried by skyrmions can be determined in parallel to the H-SPT case. Here we will not discuss this aspect, but focus on the fractional statistics of skyrmions in the $H = U(1)$-SET phase, with $G = SO(3)$ and $H = U(1)$.

Note that due to the relation (3.7) we have

$$\mathcal{H}^2(U(1), \mathcal{A}) = \mathcal{H}^1(\pi_1(U(1)) = \mathbb{Z}, \mathcal{A}) \tag{3.16}$$

where $\mathcal{A}$ is the set of all Abelian anyons, and $\mathbb{Z} = \pi_1(U(1))$ labels the integer flux quanta of the remnant $U(1)$ symmetry. Since distinct $U(1)$-SET phases are classified by $\mathcal{H}^2(U(1), \mathcal{A})$ [14, 245], the above identity (3.16) implies that $U(1)$-SETs are fully characterized by the Abelian anyon $a \in \mathcal{A}$ assigned to each 2π flux (or "fluxon"[168]) in the SET phase. Based on discussions in Sec. 3.3.3, a skyrmion with a topological charge $\nu \in \mathbb{Z} = \pi_2(S^2)$ is equivalent to a $4\pi\nu$ flux of the remnant $H = U(1)$ symmetry, and we can assign Abelian anyon $a^{2\nu}$ to such a skyrmion accordingly.

Mathematically, we apply the five-term exact sequence (3.10) to the short exact sequence (3.5) to obtain

$$0 \to \mathcal{H}^1_\rho(\mathbb{Z}_2, \mathcal{A}) \to \mathcal{H}^1_{\tilde{\rho}}(\mathbb{Z}, \mathcal{A}) \xrightarrow{\text{res}} \mathcal{H}^1(\pi_2(S^2), \mathcal{A}) \xrightarrow{d_2} \mathcal{H}^2_\rho(\pi_1(SO(3)), \mathcal{A}) \xrightarrow{\text{inf}} \mathcal{H}^2_{\tilde{\rho}}(\mathbb{Z}, \mathcal{A}) = 0. \tag{3.17}$$

The fractional statistics carried by a skyrmion of topological charge $\nu \in \mathbb{Z}$ is determined by the image of the restriction map ("res") in the exact sequence above. Physically, since $[R] \in \mathcal{H}^1(\mathbb{Z}, \mathcal{A})$ assigns an Abelian anyon $a \in \mathcal{A}$ to each 2π flux, its image in the restriction map $\tilde{R} \in \mathcal{H}^1(\pi_2(S^2), \mathcal{A})$ implies that Abelian anyon $a^{2\nu}$ is assigned to each skyrmion of topological charge ν. This will determine the fractional statistics of a skyrmion.

We will discuss the physics of topological textures in H-SET phases in more detail in Sec. 3.7.

3.5 Defects and textures in the absence of intrinsic topological orders

3.5.1 From SPT physics of ordered ground states to deconfined quantum critical points

In this section, we first discuss the simpler cases where every long-range ordered ground state with fixed order parameters exhibits no intrinsic topological order. In other words, when symmetry G is spontaneously broken down to H in a given ground state, a long-range ordered ground state with fixed order parameters (not a cat state!) is a H-preserving short-range

entangled phase[5]. In two spatial dimensions, they belong to the H-symmetry protected topological (H-SPT) phases classified by group cohomology $\mathcal{H}^3(H, U(1))$ [44]. What are the physical consequences if each symmetry-breaking ground state is a nontrivial H-SPT? As will become clear soon, this SPT physics is closely related to the physics of deconfined quantum critical points (DQCP) [221, 222, 262].

An H-SPT phase is a short-range entangled phase, which, in the presence of symmetry H, cannot be continuously connected to a trivial product state without closing the energy gap. In a system of interacting bosons in two spatial dimensions, different H-SPT phases are classified by the 3rd group cohomology $\mathcal{H}^3(H, U(1))$ [44]. The cohomology group $\mathcal{H}^3(H, U(1))$ is an Abelian group, whose identity element labels the topologically trivial phase of product states, and the addition of group elements is implemented by stacking different SPT phases.

A deconfined quantum critical point (DQCP) describes the continuous phase transition between two different long-range orders, who are not related to each other by Landau-Ginzburg-Wilson paradigm of spontaneous symmetry breaking [221, 222, 262]. More precisely, the remnant symmetry groups $H_1, H_2 \leq G$ of the two long-range ordered phases do not have a subgroup relation: in other words, H_1 is not a subgroup of H_2 and vice versa. Therefore, a DQCP is clearly beyond the Landau-Ginzburg-Wilson paradigm and provides new mechanism to understand direct quantum phase transitions between different long-range orders.

For example, DQCP is believed to describe the direct transition between a Neel order and a valance bond solid (VBS) on a square lattice [222, 221]. While the Neel order spontaneously breaks the time reversal and spin rotational symmetries, it preserves the 4-fold rotation symmetry C_4 around each lattice site. On the other hand, the columnar VBS phase spontaneously breaks C_4, but preserves both time reversal and spin rotational symmetries. Therefore a direct continuous phase transition between these two long-range orders are incompatible with the Landau-Ginzburg-Wilson paradigm. There are two alternative and complementary physical pictures to understand this DQCP.

(i) The first point of view starts with the following property of the VBS phase: each vortex of the VBS order parameter carries a spin-1/2 [155], which forms a projective representation $[\omega] \in \mathcal{H}^2\big(SO(3) \times Z_2^{\boldsymbol{T}}, U(1)\big)$ of the $SO(3)$ spin rotation and time reversal ($\boldsymbol{T}$) symmetries. Therefore, condensing the VBS vortex will necessarily breaks both time reversal and spin rotational symmetries, while restoring the crystalline C_4 symmetry. This leads to a direct transition from the columnar VBS to the Neel order via a DQCP.

(ii) The other viewpoint starts from the Neel order side, where each fundamental skyrmion (with unit topological charge $\nu = 1 \in \pi_2(S^2) = \mathbb{Z}$) of the Neel order parameter carries a unit C_4 angular momentum [85]. As a result, condensing the skyrmion will necessarily breaks the C_4 crystalline rotation symmetry, while restoring time reversal and spin rotational symmetries. This corresponds to a direct transition from the Neel order to the columnar

[5]We use the definition of Ref. [44] for short-range entangled phase, different from Kitaev's definition [127]. Therefore we do not consider invertible phases such as topological superconductor in class D [128], or E_8 states of $d = 2$ interacting bosons [127, 170].

VBS phase via the DQCP [221, 222].

To unify the above two pictures (i) and (ii), and to treat VBS and Neel order parameters on an equal footing, one can introduce a 5-component order parameter $\vec{n} = (n^1, \cdots, n^5)$, where the first 3 components (n^1, n^2, n^3) represent the Neel vector, while (n^4, n^5) serves as the columnar VBS order parameter [155, 243, 220]. The interplay of the VBS and Neel order parameters, i.e. the spin-1/2 VBS vortex and the C_4 angular momentum of a Neel skyrmion, is captured by a (2+1)-dimensional Wess-Zumino-Witten (WZW) term [280, 284] of the 5-component order parameter $\vec{n}$ [3, 243, 220, 262]:

$$\mathcal{S}_{\text{WZW}} = \frac{2\pi\epsilon_{abcde}}{\text{Area}(S^4)} \int_0^1 \mathrm{d}u \mathrm{d}^3\vec{q}\, n^a \partial_x n^b \partial_y n^c \partial_t n^d \partial_u n^e \tag{3.18}$$

where we use $\vec{q} = (x, y, t) \in S^3$ to parametrize the spacetime manifold S^3, and u is introduced to parametrize a smooth interpolation (extension) between $\vec{n}(\vec{q}, u = 0) = (0, 0, 0, 0, 1)$ and $\vec{n}(\vec{q}, u = 1) = \vec{n}(\vec{q})$. While the physical system only has a microscopic symmetry of $G = C_4 \times SO(3)$, an enlarged $SO(5)$ symmetry that rotates the 5 components of $\vec{n}$ was argued to emerge at the DQCP described by a NLSM with the above WZW term [220, 265].

The aforementioned two pictures for the Neel-VBS transition are both captured by the above WZW term. On the VBS side, a classical vortex configuration for VBS order parameters (n^4, n^5) reduces the topological term (3.18) to an $O(3)$ NLSM with a WZW term, physically corresponding to a spin-1/2 at the vortex core [3]. On the Neel side, a classical skyrmion configuration of Neel order parameters (n^1, n^2, n^3) reduces (3.18) to a $U(1)$ rotor action of VBS order parameters (n^1, n^2), which carries a unit angular momentum of crystalline rotation C_4.

In this work, we want to point out a connection between the two physical pictures of DQCP, and the SPT physics of the symmetry-breaking ground states. More precisely, in a long-range order which spontaneously breaks symmetry G down to a subgroup H, if a symmetry-breaking ground state belongs to certain H-SPT phases, the condensation of topological point defects or textures of the order parameters will lead to a direct transition described by a DQCP. The other side of the direct transition must spontaneously breaks H: it is generally a long-range order with remnant symmetry H', which is neither a subgroup nor a supergroup of H. This observation can be summarized in two classes:

(i) If a symmetry-breaking ground state belongs to certain H-SPT phases, to be elaborated in Sec. 3.5.2, a point defect (i.e. vortex) of the order parameter $\hat{O}(\vec{r}) \in G/H$ can carry a projective representation $[\omega] \in \mathcal{H}^2(H, U(1))$ of the remnant symmetry H. This is a generalization of viewpoint (i) for Neel-VBS transition from the VBS side. Condensing the point defects (vortices) will spontaneously breaks (a part of) symmetry H across the DQCP.

(ii) If a symmetry breaking ground state belongs to certain H-SPT phases, to be elaborated in Sec. 3.5.3, a topological texture (i.e. a skyrmion) of the order parameter can carry a charge (or a linear representation $[\omega] \in \mathcal{H}^1(H, U(1))$) of the remnant symmetry H. This is a generalization of viewpoint (ii) for the Neel-VBS transition from the Neel side. Condensing the skyrmions will spontaneously break the remnant symmetry H across the DQCP.

This general connection allows us to determine whether a given long-range order is in proximity to a DQCP in the phase (parameter) space, and to systematically construct examples of DQCPs based on the H-SPT classification for the symmetry-breaking ground states. For the rest of this section, we shall discuss the two classes in detail: (i) point defects carrying a projective representation of H, in Sec. 3.5.2; (ii) skyrmions carrying a linear representation (i.e. quantum numbers) of H, in Sec. 3.5.3. We will use the mathematical classification based on group cohomology in Sec. 3.4, and its related "decorated domain wall" picture [43], to elucidate the aforementioned connection between SPT phases in symmetry-breaking ground states and the DQCP.

3.5.2 Point defects

Without loss of generality, let's consider the following situation:

$$G = A \times K, \quad H = B \times K, \quad H \triangleleft G. \tag{3.19}$$

where $\times$ is the direct product of two groups, and we assume that H is a discrete normal subgroup of a continuous group G. In other words, the subgroup symmetry A is broken down to $B \triangleleft A$ while the subgroup symmetry K is preserved in the long-range order.

The question we plan to address is the following: does a point defect in $\pi_1(G/H = A/B)$ carry a projective representation of the remnant symmetry H? As discussed in Sec. 3.4.3.1, given the mixed SPT anomaly in $\mathcal{H}^1(B, \mathcal{H}^2(K, U(1)))$ in a symmetry-breaking ground state with fixed order parameters, due to exact sequence (3.12), the projective representation carried by point defects is classified by the image of injective map d_1 in $\mathcal{H}^1(\pi_1(A/B), \mathcal{H}^2(K, U(1)))$. This gives the following criterion for point defect bound states:

(i) When a full symmetry $G = A \times K$ is spontaneously broken down to a subgroup $H = B \times K$, if a symmetry-breaking ground state is an H-SPT with a mixed anomaly described by $[R] \in \mathcal{H}^1(B, \mathcal{H}^2(K, U(1)))$, the projective representation of subgroup K carried by the point defect in $\pi_1(G/H)$ is specified by the image $[\tilde{R}] \in \mathcal{H}^1(\pi_1(G/H), \mathcal{H}^2(K, U(1)))$ of map d_1 in exact sequence (3.12).

Physically, a point defect of the order parameters can be mapped to a symmetry defect by the connecting homomorphism p in exact sequence (3.4). The mixed anomaly $[R] \in \mathcal{H}^1(B, \mathcal{H}^2(K, U(1)))$ assigns a projective representation $\mathcal{H}^2(K, U(1))$ to each symmetry defect $b \in B$. This in turn determines the projective representation assigned to a point defect in $\pi_1(G/H)$. We note that similar physics has been discussed recently in the name of "gapless SPT" phases [215, 252, 157].

Below we discuss one example of such nature, where each fundamental vortex with a unit winding number carries a spin-1/2 in the pair superfluid phase.

3.5.2.1 Symmetry protected pair superfluid with spin-$1/2$ vortices

We consider a bosonic system on a two-dimensional lattice, which consists of hard-core bosons $\{b_i\}$ and a single spin-1/2 d.o.f. $\vec{s}_i$ per unit site. The full symmetry of the Hamiltonian is $G =$

$U(1) \times SO(3)$, which is spontaneously broken down to $H = Z_2 \times SO(3)$ in a pair superfluid phase. In the notation the general discussions above, we have $A = U(1)$, $K = B = Z_2$ and $K = SO(3)$[6]. Each hard-core boson b_i carries a unit charge but no spin (or spin-0), while each $\vec{s}_i$ carries no charge but transforms as a spin-1/2 projective representation of $SO(3)$ symmetry. The filling number for bosons is $\bar{\rho} = 2$ per unit cell.

In the long-range order, we consider a pair superfluid phase where two bosons form a condensate with $\langle (b_i)^2 \rangle \neq 0$ but $\langle b_i \rangle = 0$. To achieve the desired SPT properties, we further require the system to preserve the following magnetic translation symmetry:

$$T_1 T_2 T_1^{-1} T_2^{-1} = (-1)^{\sum_i b_i^\dagger b_i} \tag{3.20}$$

where $T_{1,2}$ are magnetic translations along the two primitive vectors $\vec{a}_{1,2}$. In other words, the bosons experience a π flux in each unit cell when traveling around the lattice. A pair of bosons, carrying charge 2, only experiences 2π flux per unit cell and can condense without breaking the translation symmetry $T_{1,2}$, driving the system into a translation invariant pair superfluid phase. Note that there is a π flux and a single spin-1/2 in each unit cell. Due to the Lieb-Schultz-Mattis theorem for SPT phases [166, 290], in the presence of the magnetic translation symmetry, any short-range entangled ground state preserving the magnetic translation and $H = Z_2 \times SO(3)$ symmetry must be a H-SPT phase, exactly described by a mixed anomaly $[R] \in \mathcal{H}^1(Z_2, \mathcal{H}^2(SO(3), U(1))) < \mathcal{H}^3(H, U(1))$. Physically, in a ground state of the pair superfluid phase, each symmetry defect of the remnant $\mathbb{Z}_2$ (i.e. a π flux) carries a projective representation of the remnant $SO(3)$ symmetry (i.e. a spin-1/2).

On the other hand, the point defect of the order parameter $\langle (b_i)^2 \rangle$ are vortices in the pair superfluid, labeled by an integer-valued vorticity $\nu \in \mathbb{Z}$. In particular, each vorticity-1 vortex corresponds to a π flux, and hence carries a spin-1/2, exactly captured by the mixed anomaly $[\tilde{R}] \in \mathcal{H}^1(\mathbb{Z}, \mathcal{H}^2(SO(3), U(1)))$, the image of map d_1 in exact sequence (3.12). As a result, condensing the elementary ($\nu = \pm 1$) vortices will drive the system into a magnetic order that spontaneously breaks $K = SO(3)$ symmetry, via a DQCP. The Neel vector (n^1, n^2, n^3) and the superfluid order parameters $\langle (b_i)^2 \rangle \sim n^4 + \mathrm{i} n^5$ are described by a NLsM with an $O(5)$ WZW term.

3.5.3 Textures

We consider the symmetry group $G = SO(3) \times K$ to be spontaneously broken down to a subgroup $H = U(1)_{S^z} \times K$, where K is a subgroup of onsite unitary symmetries. In the absence of intrinsic topological orders, the symmetry breaking phase can be an H-SPT phase in two spatial dimensions, classified by $\mathcal{H}^3(H, U(1))$. As discussed in Sec. 3.3.3, a skyrmion of topological charge $\nu \in \mathbb{Z}$ is equivalent to a $4\pi\nu$ flux of the remnant $U(1)$ symmetry.

[6]One can also replace $K = SO(3)$ symmetry by a discrete time reversal symmetry $K = Z_2^{\boldsymbol{T}}$.

To understand the universal properties of skyrmions in the H-SPT phases, again we use the Künneth decomposition in (3.7):

$$\begin{aligned}\mathcal{H}^3(H,U(1)) = \mathcal{H}^3(U(1)_{S^z},U(1)) \times \mathcal{H}^2(U(1)_{S^z},\mathcal{H}^1(K,U(1))) \\ \times \mathcal{H}^1(U(1)_{S^z},\mathcal{H}^2(K,U(1))) \times \mathcal{H}^3(K,U(1)).\end{aligned} \tag{3.21}$$

Note that two of the four terms indicates different topological properties of the flux of the unbroken $U(1)_{S^z}$ symmetry, and hence of the skyrmions. The first term labels the $U(1)_{S^z}$ quantum number $S^z = q \in \mathcal{H}^3(U(1)_{S^z},U(1)) \cong \mathcal{H}^1(U(1)_{S^z},U(1)) = \mathbb{Z}$ carried by each $U(1)_{S^z}$ flux quantum. The third term $\mathcal{H}^1(U(1),\mathcal{H}^2(K,U(1)))$ in (3.21) vanishes when $\mathcal{H}^2(K,U(1))$ is any finite Abelian group. Finally, the fourth term labels the K-SPT phases that do not require the protection of the $U(1)_{S^z}$ symmetry.

Due to the relation (3.8), the 2nd term is equivalent to $\mathcal{H}^1(\mathbb{Z},M)$ with $M \equiv \mathcal{H}^1(K,U(1))$, and hence can be understood as the linear representation (i.e. the charge) of the unbroken subgroup K carried by each flux quantum (or 2π flux) of the $U(1)_{S^z}$ symmetry. Now that each $\nu = 1$ skyrmion can be viewed as a 4π flux, it carries the linear representation $[R\otimes R] \in M$ of unbroken subgroup K. Condensing skyrmions with nontrivial K-symmetry charges will inevitably break the K symmetry while restoring the $SO(3)$ spin rotational symmetry, through a DQCP.

As we are interested in the interplay between the two subgroups $U(1)_{S^z}$ and K of the remnant symmetry $H = U(1) \times K$, we will be focusing on the second term in the Künneth decomposition (3.21). According to the discussions in Sec. 3.4.4.1, the following statement describes the symmetry quantum numbers of topological textures:

(ii) When a full symmetry group $G = SO(3) \times K$ is spontaneously broken down to a subgroup $H = U(1) \times K$, if a symmetry-breaking ground state is an H-SPT described by $[R] \in \mathcal{H}^1(\mathbb{Z},M) \equiv \mathcal{H}^2(U(1),M)$ with $M = \mathcal{H}^1(K,U(1))$, the quantum number (or linear representation) of unbroken subgroup K assigned to each skyrmion is specified by the image $[\tilde{R}] \in \mathcal{H}^1(\pi_2(S^2),M)$ of the restriction map ("res") in the exact sequence (3.15).

Below we discuss two familiar examples of this type in more details.

3.5.3.1 Charge-$2e$ skyrmions in quantum spin Hall insulators

The first example we consider is a fermion system with charge conservation $K = U(1)_c$ and spin rotational symmetry, hence a full symmetry group of $G = SO(3) \times U(1)_c$. A time-reversal-invariant collinear order parameter can spontaneously breaks the symmetry G down to a $H = U(1)_s \times U(1)_c$ subgroup, where $U(1)_s$ is the subgroup of $U(1)$ spin rotational symmetry along e.g. z-axis:

$$f_\uparrow \xrightarrow{e^{\mathrm{i}\theta S^z_{\text{tot}}}} e^{-\mathrm{i}\theta/2} f_\uparrow, \quad f_\downarrow \xrightarrow{e^{\mathrm{i}\theta S^z_{\text{tot}}}} e^{\mathrm{i}\theta/2} f_\downarrow \tag{3.22}$$

We are interested in the case where each symmetry-breaking ground state is a quantum spin Hall (QSH) insulator [117, 22, 137], with a pair of helical edge states protected by the remnant symmetry H.

It is well known that such a QSH insulator exhibits a mixed anomaly between the $U(1)_c$ and $U(1)_s$ subgroups, captured by group cohomology

$$\mathcal{H}^2(U(1)_s, M) = \mathcal{H}^1(\mathbb{Z}, M) \subset \mathcal{H}^3(H, U(1)) \tag{3.23}$$

where $M \equiv \mathcal{H}^1(U(1)_c, U(1))$ labels $U(1)_c$ quantum numbers i.e. electric charges. Specifically, the quantized spin Hall conductance $\sigma_{xy}^{c,s} = e/2\pi$ [23] indicates that each 2π flux of spin symmetry $U(1)_s$ would carry a unit electric charge. As a result, each skyrmion of topological charge $\nu \in \mathbb{Z} = \pi_2(S^2)$, equivalent to a $4\pi\nu$ flux of spin rotational symmetry $U(1)_s$, carries an electron charge of $2\nu e$.

In particular, an elementary $\nu = 1$ skyrmion carries charge $2e$, as pointed out in Ref. [80]. Condensing these elementary skyrmions hence induce a superconducting state that spontaneously breaks the $U(1)_c$ symmetry, which was recently proposed to be one mechanism for superconductivity in magic-angle twisted bilayer graphene [125].

3.5.3.2 Neel order in a spin-1/2 model on the square lattice

Next we discuss a familiar example related to the DQCP, i.e. the Neel order in a spin-1/2 system on the square lattice. Before studying the full space group symmetry, let us first consider a simplified situation where we ignore the translations and mirror reflection: we only take into account the onsite $SO(3)$ spin rotational symmetry and the site-centered 4-fold crystalline rotation symmetry $K = C_4$. In a collinear Neel order, the full symmetry $G = SO(3) \times C_4$ is spontaneously broken down to the remnant symmetry $H = U(1)_{S^z} \times C_4$. In the latter H-preserving Neel ordered phase, there is a quantized topological term of the Wen-Zee type [272, 87], which corresponds to an element in the cohomology class $\mathcal{H}^2(U(1)_{S^z}, \mathcal{H}^1(K, U(1))) \subset \mathcal{H}^3(H, U(1))$ and characterizes the mixed anomaly between C_4 rotation and $U(1)_{S^z}$ spin rotational symmetries. Physically, this cohomology class and associated Wen-Zee term in the continuum field theory implies that each $U(1)_{S^z}$ flux quantum (i.e. 2π flux) carries a C_4 eigenvalue of i (i.e. a unit angular momentum). As a result, each skyrmion (equivalent to 2π flux of $U(1)_{S^z}$ for a spin-1/2 system, see Sec. 3.7.3) also carries a C_4 eigenvalue of i [85], and condensing the skyrmions (which restores the $SO(3)$ spin rotational symmetry) will necessarily break C_4 crystalline rotational symmetry, as is the case of the valence bond solids on the square lattice [85, 222].

Next, we include the translations and consider the full space group symmetry of the square lattice. The full symmetry for the paramagnetic phase is $G = p4m \times SO(3) \times Z_2^{\boldsymbol{T}}$, where $\boldsymbol{T}$ is the time reversal operation and $p4m$ is the wallpaper group that describes the symmetry of the square lattice, generated by translations T_1, T_2, site-centered rotation C_4, and reflection M (with respect to a site-crossing mirror plane). After the transition to Neel order, G is broken down to $H = U(1)_{S^z} \rtimes p_p4m$, where p_p4m is the magnetic space group for the Neel order [160], generated by magnetic translations $\widetilde{T}_{x,y} = \boldsymbol{T} \cdot T_{x,y}$ and point group symmetries C_4 and M. Note that spin rotation $U(1)_{S^z}$ and the magnetic space group do not commute with each other, hence the semidirect product. Due to this semidirect product structure, the Künneth decomposition (3.21) can no longer be used to calcualte

the cohomology. Nevertheless one can show through a spectral sequence calculation that $\mathcal{H}^3(H, U(1))$ contains a summand

$$\mathcal{H}^2(p_p4m, \mathcal{H}^1(U(1)_{S^z}, U(1))) \subset \mathcal{H}^3(H, U(1)). \tag{3.24}$$

One can further show that $\mathcal{H}^2(p_p4m, \mathcal{H}^1(U(1)_{S^z}, U(1))) = \mathcal{H}^1(p_p4m, U(1)) = \mathbb{Z}_2^2$, where the two $\mathbb{Z}_2$ summands label the eigenvalues of C_4 and M, respectively. Compared to the case of $K = C_4$ where the eigenvalues of C_4 are $\{\pm 1, \pm \mathrm{i}\}$, now considering the full magnetic space group p_p4m reduces the eigenvalues of C_4 to $\{1, \mathrm{i}\}$ due to the magnetic translations (the C_4 eigenvalues ± 1 are identified and so are the eigenvalues $\pm \mathrm{i}$). We see that the analysis in the case $K = C_4$ above still holds. This means that, taking into account the full lattice symmetry, condensing the skyrmions (hence restoring the $SO(3)$ internal symmetry) will indeed break the C_4 rotation symmetry spontaneously. Note that a similar analysis has been carried out in Refs. [180, 291].

3.6 Point defects in symmetry enriched topological orders

When the ground state is a SPT phase protected by the unbroken symmetry H, we have shown previously that point defects (or vortices) of the symmetry-breaking order parameters can carry a projective representation of the unbroken symmetry. Below we discuss the more general situation, i.e. two-dimensional intrinsic topological orders with spontaneously broken symmetries, where each symmetry-breaking ground state is a H-symmetry enriched topological (H-SET) phase. As discussed previously in Sec. 3.4.3, due to the short exact sequence (3.4) that maps a topological point defect (an element of $\pi_1(G/H)$) to a symmetry defect (an element of H), one can derive universal properties of point defects from those of symmetry defects, which were extensively studied in the context of SET phases [59, 245, 14]. We found that when topological orders coexist with spontaneous symmetry breaking, due to the presence of anyons which obey fractional statistics, two classes of new phenomena can occur:

(1) Point defects can permute anyons in the topological order when braided around. In other words, after traveling around a point defect, one anyon of a certain type can be transmuted into an anyon of a different type. In these cases, the point defect (vortex) is mapped into a non-Abelian symmetry defect (or twist defect) [13, 11, 10, 14, 245, 249, 246].

(2) Multiple point defects can fuse into Abelian anyons, which we coin "defect fractionalization" for reasons that we describe below in details.

3.6.1 Defect fractionalization phenomenon

Importantly, the topological point defects may obey a nontrivial fusion rule: upon annihilating with each other, these topological defects may leave behind Abelian anyons, similar to the symmetry defects in SET phase.

We have named this phenomenon *d*efect fractionalization in Sec. 3.4.3.2. Here we stress that the understanding of defect fractionalization parallels that of symmetry fractionalization [59, 14]: for SSB $G \to H$, different defect fractionalization classes in the broken symmetry phase should correspond to equivalence classes $[\omega] \in \mathcal{H}^2_{\tilde{\rho}}(\pi_1(G/H), \mathcal{A})$, meaning that for $g, h \in \pi_1(G/H)$, the group element $\omega(g,h)$ in $\mathcal{H}^2_{\tilde{\rho}}(\pi_1(G/H), \mathcal{A})$ denotes the residual anyons after fusing the defects g, h and $(gh)^{-1}$.

In the simplest case of $\pi_1(G) = 0$, we have $\pi_1(G/H) \cong H$ from (3.4), namely there is a one-to-one correspondence between the topological point defects (or vortices) of the order parameter $\phi(\vec{r}) \in \pi_1(G/H)$ and the (extrinsic) symmetry defects $\tau_h, h \in H$. In this case p is an isomorphism, hence $\tilde{\rho} = \rho$. As a result, there is a one-to-one correspondence between defect fractionalization described by $\mathcal{H}^2_{\tilde{\rho}}(\pi_1(G/H), \mathcal{A})$, and symmetry fractionalization described by $\mathcal{H}^2_{\rho}(H, \mathcal{A})$, i.e. $p^* \equiv \inf$ is a bijective map in exact sequence (3.14). One such example is lattice dislocations, where $G = \mathbb{R} \times \mathbb{R}$ and $H = \mathbb{Z}^2$, where dislocations with a Burgers vector $\vec{b} = b_1\vec{a}_1 + b_2\vec{a}_2$ corresponds to symmetry defect of translation operation $T_1^{b_1}T_2^{b_2}$, where $\vec{a}_{1,2}$ are the two primitive translation vectors of the two-dimensional lattice. In Sec. 3.6.4.4, we compute and explicitly demonstrate the nontrivial fusion rules of dislocations in the toric code.

3.6.2 Defect fractionalization vs symmetry fractionalization

It is tempting to conclude that defect fractionalization in the general case of $\pi_1(G) \neq 0$ is classified by $\mathcal{H}^2_{\tilde{\rho}}(\pi_1(G/H), \mathcal{A})$. However, as we shall show in explicit model calculations, $\mathcal{H}^2_{\tilde{\rho}}(\pi_1(G/H), \mathcal{A})$ contains elements that are redundant, and the physical ones are classified by the subgroup which is the image of the inflation map $p^* = \inf$ in the exact sequence (3.14)

$$\mathrm{im}(p^*) \subset \mathcal{H}^2_{\tilde{\rho}}(\pi_1(G/H), \mathcal{A}), \tag{3.25}$$

namely, the classes of symmetry fractionalization that survives the inflation map. When $\pi_1(G) = 0$ is trivial, the inflation map becomes an isomorphism, and correctly reproduces the classification mentioned above.

We claim in the above that in the general case when $\pi_1(G) \neq 0$, the classification for defect fractionalization is fully determined by specifying the inflation map p^*. The inflation map p^* sends the cohomology of the quotient group (in our case, $H = \pi_1(G/H)/\pi_1(G)$) to that of the group extension (in our case, $\pi_1(G/H)$). Physically, it simply sends any symmetry fractionalization class $[\omega]$ – cocycle elements $\omega(h_1, h_2) = \mathsf{a}, \mathsf{a} \in \mathcal{A}, h_1, h_2 \in H$ – to defect fractionalization class $[p^*(\omega)]$ by sending symmetry $h \in H$ to any defect $\phi(\vec{r}) \in \pi_1(G/H)$ that maps to h under p. Here, however, what is nontrivial is that such a class $[\omega]$ may be *trivialized* under the map p^*: the defect fusion rule inherited from ω can be continuously deformed to the one that fuses to no anyons. This happens whenever the the map p^* has a nontrivial kernel – that is, $\ker(p^*) := \{[\omega] | p^*([\omega]) = 0\} \neq \emptyset$.

At this point, the exact sequence (3.14) is introduced as a mathematical computational tool, whose physical meaning is yet to be specified. We now try to understand the physical

meaning of each piece and the exactness among them. To achieve this, recall from Sec. 3.4.1.2 that elements of $\mathcal{H}^1_\rho(H,\mathcal{A})$ describes the "anyon-labeling rule" for the extrinsic symmetry defects $\tau_h, h \in H$. The topological defects $\phi(\vec{r}) \in \pi_1(G/H)$ inherits a similar defect "anyon-labeling rule" consistent with their actions on the anyons, classified by $\mathcal{H}^1_{\tilde{\rho}}(\pi_1(G/H),\mathcal{A})$. Such a heritage is easy to understand since the symmetry H is intact after the SSB $G \to H$. However, one can imagine the alternative, indirect, physical process in which the symmetry G is completely broken down (to $\{1\}$), and then restored to H. We will call this the indirect SSB process $G \to \{1\} \to H$ from now on (note here the arrows are written in a physical sense, not in a mathematical sense). In this scenario, the relevant defect "anyon-labeing rule" is that for the topological defects $\psi(\vec{r}) \in \pi_1(G)$, classified by $\mathcal{H}^1(\pi_1(G),\mathcal{A})$, but when restoring H, only those "anyon-labeling rules" for $\pi_1(G)$ that are *invariant* under the action of H makes sense after H is restored. Here the invariance is defined in the sense of Eq. (3.11). Intuitively, both the defect $g \in \pi_1(G)$ and the anyon $\mathsf{a} \in \mathcal{A}$ may transform nontrivially under H, but the defect–anyon composite must transform *covariantly* under H, implying that the "anyon-labeling rules" for $\pi_1(G)$ is invariant under H.

Together with the physical meaning of $\mathcal{H}^2_\rho(H,\mathcal{A})$ and $\mathcal{H}^2_{\tilde{\rho}}(\pi_1(G/H),\mathcal{A})$ as symmetry fractionalization and defect fractionalization, respectively, that have been introduced before, we are now in a position to understand the exactness of the sequence (3.14). As mentioned before, to know $\mathrm{im}(p^*)$ it suffices to known $\ker(p^*)$. The exactness $\ker(p^*) = \mathrm{im}(d_2)$ states that, after the indirect SSB process $G \to \{1\} \to H$, for any resulting defect (now object in $\pi_1(G/H)$), the only possible "defect fusion rule" compatible with its "anyon-labeling rule" is the trivial one. The exactness at $\mathcal{H}^1(\pi_1(G),\mathcal{A})^H$ states that, if a "defect fusion rule" can be realized in both the direct SSB process $G \to H$ and the indirect process $G \to \{1\} \to H$, the only possible "defect fusion rule" compatible with its "anyon-labeling rule" is the trivial one. The exactness at $\mathcal{H}^1_{\tilde{\rho}}(\pi_1(G/H),\mathcal{A})$ states that, the topological defect "anyon-labeling rule" that originates from a symmetry defect "anyon-labeling rule" cannot be realized at the end of the indirect SSB process $G \to \{1\} \to H$. Finally, the exactness at $\mathcal{H}^1_\rho(H,\mathcal{A})$ states that every symmetry defect "anyon-labeling rule" can be realized in the topological defects of $\pi_1(G/H)$.

We note that the five-term exact sequence (3.14) is a corollary of spectral sequences. We will be using spectral sequences in the calculation of cohomology groups (especially those with nontrivial action on the anyons). We present one quite useful statement about this map:

Theorem 1 *Given Eq.* (3.14). *If $\pi_1(G/H)$ is of a semi-direct product form $\pi_1(G/H) \cong \pi_1(G) \rtimes H$, then $d_2 = 0$, hence $p*$ is injective. Consequently, the symmetry fractionalization classes are in one-to-one correspondence with the defect fractionalization classes.*

This statement is powerful in that it works regardless of the action ρ (trivial or nontrivial alike).

In Table. 3.1 we give examples of the $\mathbb{Z}_2$ topological order (toric code) enriched by two different symmetries: (1) $G = U(1)$, $H = Z_2$, and (2) $G = SO(3)$ and $H = D_2 =$

No.	G	H	H-Action	$\mathcal{H}^1_\rho(H,\mathcal{A})$	$\to$	$\mathcal{H}^1_{\tilde{\rho}}(\pi_1(G/H),\mathcal{A})$	$\to$	$\mathcal{H}^1_{\rm id}(\pi_1(G),\mathcal{A})^H$	$\to$	$\mathcal{H}^2_\rho(H,\mathcal{A})$	$\to$	$\mathcal{H}^2_{\tilde{\rho}}(\pi_1(G/H),\mathcal{A})$
1	$U(1)$	Z_2	Trivial	$\mathbb{Z}_2^{\mathsf{e}}\times\mathbb{Z}_2^{\mathsf{m}}$	$\xrightarrow{\cong}$	$\mathbb{Z}_2^{\mathsf{e}}\times\mathbb{Z}_2^{\mathsf{m}}$	$\xrightarrow{0}$	$\mathbb{Z}_2^{\mathsf{e}}\times\mathbb{Z}_2^{\mathsf{m}}$	$\xrightarrow{\cong}$	$\mathbb{Z}_2^{\mathsf{e}}\times\mathbb{Z}_2^{\mathsf{m}}$	$\to$	0
2	$U(1)$	Z_2	Nontrivial	0	$\to$	$\mathbb{Z}_2^{\mathsf{e}}\times\mathbb{Z}_2^{\mathsf{m}}/\mathbb{Z}_2^{\varepsilon}$	$\xrightarrow{\cong}$	$\mathbb{Z}_2^{\varepsilon}$	$\to$	0	$\to$	0
3	$SO(3)$	D_2	Trivial	$(\mathbb{Z}_2^2)^{\mathsf{e}}\times(\mathbb{Z}_2^2)^{\mathsf{m}}$	$\xrightarrow{\cong}$	$(\mathbb{Z}_2^2)^{\mathsf{e}}\times(\mathbb{Z}_2^2)^{\mathsf{m}}$	$\xrightarrow{0}$	$\mathbb{Z}_2^{\mathsf{e}}\times\mathbb{Z}_2^{\mathsf{m}}$	$\xrightarrow{\text{inj.}}$	$(\mathbb{Z}_2^3)^{\mathsf{e}}\times(\mathbb{Z}_2^3)^{\mathsf{m}}$	$\xrightarrow{\text{surj.}}$	$(\mathbb{Z}_2^2)^{\mathsf{e}}\times(\mathbb{Z}_2^2)^{\mathsf{m}}$
4	$SO(3)$	D_2	Nontrivial	$\mathbb{Z}_2^{\varepsilon}$	$\xrightarrow{\cong}$	$\mathbb{Z}_2^{\varepsilon}$	$\xrightarrow{0}$	$\mathbb{Z}_2^{\varepsilon}$	$\xrightarrow{\cong}$	$\mathbb{Z}_2^{\varepsilon}$	$\xrightarrow{0}$	$\mathbb{Z}_2^{\varepsilon}$

Table 3.1: Defect fractionalization classes from Eq. (3.10), for the toric code with coexisting long-range orders, where the fully symmetry G is spontaneously broken down to a subgroup H. Different H symmetry actions on the anyons are also considered.

$\{1, X, Y, Z\}$, with $\mathcal{A} = \mathbb{Z}_2^{\mathsf{e}} \times \mathbb{Z}_2^{\mathsf{m}}$. For each example we consider the cases of trivial and nontrivial H-actions. All these examples lie outside the application of Theorem 1[7]

3.6.3 Two examples

Below we will use two primary examples to demonstrate the aforementioned properties of point defects in SET phases: i.e. (1) Point defects can permute different anyons when braided around. (2) Point defects can fuse into Abelian anyons, coined defect fractionalization. The two representative examples we consider are

(i) Toric codes with a coexisting pair superfluid order, where the $G = U(1)$ symmetry is spontaneously broken down to a $H = Z_2$ subgroup. In this example, the point defects are vortices classified by fundamental group $\pi_1(G/H) = \mathbb{Z}$, labeled by integer-valued vorticity $\nu \in \mathbb{Z}$. A microscopic model of such will be constructed in Sec. 3.6.4.1.

(ii) Toric codes with a coexisting biaxial nematic order, where the spin rotational symmetry $SO(3)$ is spontaneously broken down to a $H = D_2 \simeq Z_2^2$ subgroup. In this example, the point defects are classified by a non-Abelian fundamental group $\pi_1(G/H) \simeq Q_8$, the quarternion group [178]. Two microscopic models of such will be constructed later: for anyon-permuting vortices in Sec. 3.6.4.2, and for defect fractionalization in Sec. 3.6.4.3.

3.6.3.1 Non-Abelian point defects that permute anyons

The simplest case of such nature is example (1), i.e. toric code with the pair superfluid order, where $G = U(1)$ spin rotational symmetry is broken down to an $H = Z_2$ Ising symmetry. The resulting symmetry enriched topological phases can be obtained by gauging the fermion parity in fermionic non-chiral topological superconductors with an Ising symmetry [199, 82]. In this case, there is an $m \in \mathbb{Z}_8$ classification, where each Ising symmetry defect can permute e and m anyons in the toric code for $m = 1 \mod 2$, while while the Ising symmetry fractionalization happens for $m = 2 \mod 4$. Now that any $\nu =$ odd vortex is mapped into the Ising symmetry defect by (3.4), we conclude that each $\nu =$ odd vortex can permute e

[7] $G = N \rtimes Q$ if and only if the short exact sequence $0 \to N \to G \xrightarrow{p} Q \to 0$ *splits*, i.e. there is a homomorphism $j\colon Q \to G$ s.t. the composed map $p \circ j$ is the identity map on Q. This is not the case for either $0 \to Z \xrightarrow{2} Z \to Z_2 \to 0$ or $0 \to D_2 \to Q_8 \to Z_2$. In fact, Q_8 does not admit a semi-direct product structure.

and m anyons, if the pair superfluid ground state is a Z_2-SET phase with $m = 1 \mod 2$. As shown in Table 3.1.2, in this case with a nontrivial H-action on anyons, both the symmetry fractionalization class and the defect fractionalization class are trivial. A microscopic model of this example is constructed in Sec. 3.6.4.1.

Next we consider example (2), i.e. a biaxial nematic toric code phase with $G = SO(3)$ and $H = D_2 = \{1, X, Y, Z\} \cong Z_2^2$. The associated homotopy groups are $\pi_1(G) \cong Z_2$ and $\pi_1(G/H) \cong Q_8$; the latter is the non-Abelian quarternion group. The H-action can be nontrivial in a H-enriched toric code: e.g. the generator X in $H = Z_2^X \times Z_2^Y$ permutes the e and m particles while Y does not. This is the only nontrivial H-action possible up to isomorphism. This also means that the last group element, $Z = XY$, permutes e and m particles as well. We construct a microscopic lattice model for this phase in Sec. 3.6.4.2.

The five-term exact sequence (3.14) for this case is given in Table. 3.1.4. Interestingly, we find that in this case the defect fractionalization is not inherited from the symmetry defect (see the last map in Table. 3.1.3, which is a zero map). Thus according to our classification, although the symmetry defect fractionalization class is nontrivial, $\mathcal{H}^2_\rho(H, \mathcal{A}) = \mathbb{Z}_2^\epsilon$ in this case, there is no nontrivial fractionalization for the topological point defect.

3.6.3.2 Nontrivial fusion rules of fractionalized defects

Previously we have shown that a nontrivial H-action on anyons leads to a trivial defect fractionalization class in both examples. In fact, in a toric code with a pair superfluid order, when the H-action is trivial, even with a nontrivial symmetry fractionalization class $\mathcal{H}^2_{\mathrm{id}}(H = Z_2, \mathcal{A}) = \mathbb{Z}_2^{\mathsf{e}} \times \mathbb{Z}_2^{\mathsf{m}}$, the defect fractionalization class is still trivial, as shown in Table 3.1.1.

As we show below, example (2), i.e. the toric code with a biaxial nematic order, can realize a nontrivial defect fractionalization class if the H-action is trivial on anyons. Again consider the case $G = SO(3)$ and $H = D_2 \cong Z_2^2$, this time with trivial H-action $\rho = \mathrm{id}$ on the anyons. The five-term exact sequence is given in Table 3.1, where the surjective map on the right allows us to extend the sequence to a six-term exact sequence by appending "$\to 0$" to the right-hand side. We see that defect fractionalizations are *fully determined* by symmetry fractionalizations. This is the only case with a nontrivial topological defect fractionalization among those considered in Eq. (3.1). Only a subgroup $(\mathbb{Z}_2^2)^{\mathsf{e}} \subset H^2(D_2, \mathbb{Z}_2^{\mathsf{e}})$ survives the inflation map p^*. Denote the three nontrivial cocycles of this $(\mathbb{Z}_2^2)^{\mathsf{e}}$ as $\omega_{1,2,3}$. They can be distinguished by the following values

$$\begin{aligned} &\omega_1(X,X) = 1, \quad \omega_1(Y,Y) = 1, \quad \omega_1(XY,XY) = \mathsf{e}, \\ &\omega_2(X,X) = 1, \quad \omega_2(Y,Y) = \mathsf{e}, \quad \omega_2(XY,XY) = 1, \\ &\omega_3(X,X) = \mathsf{e}, \quad \omega_3(Y,Y) = 1, \quad \omega_3(XY,XY) = 1. \end{aligned} \tag{3.26}$$

the cocycle $[\omega_4] \in \mathcal{H}^2(D_2, \mathbb{Z}_2^{\mathsf{e}})$ with $\omega_4(X,X) = \omega_4(Y,Y) = \omega_4(XY,XY) = \mathsf{e}$ does not survive the p^* map and becomes a coboundary in $\mathcal{H}^2(\pi_1(G/H) = Q_8, \mathbb{Z}_2^{\mathsf{e}})$. The other half with the coefficient $\mathbb{Z}_2^{\mathsf{m}}$ can be analyzed in a similar manner.

A microscopic model of this case is constructed in Sec. 3.6.4.3.

3.6.4 Lattice models

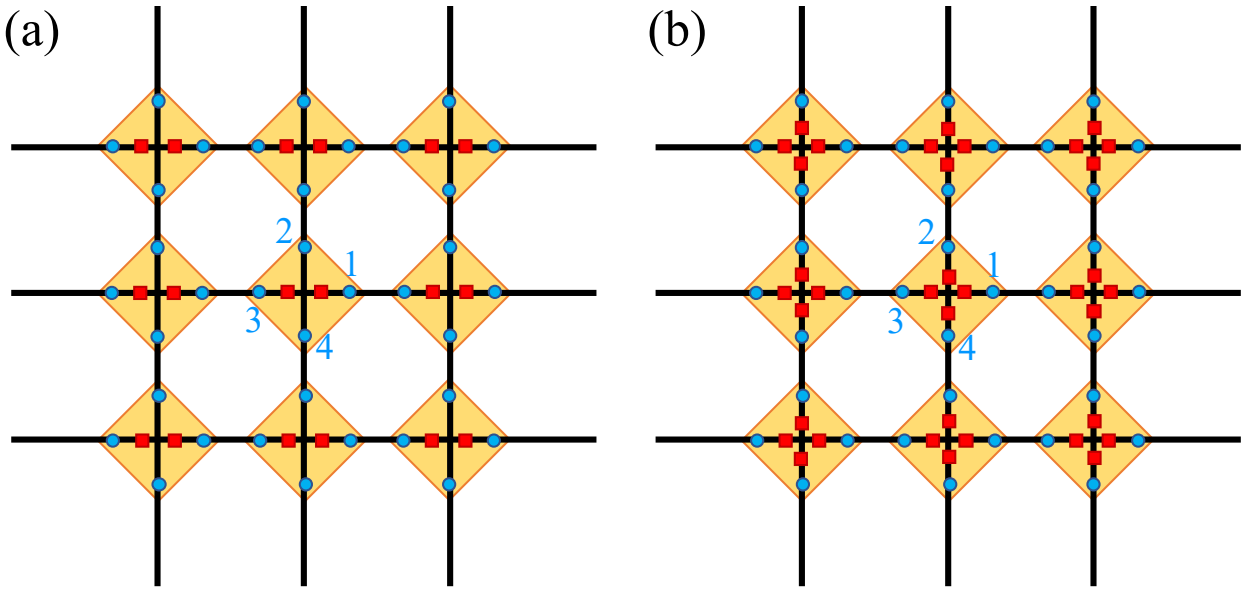

Figure 3.4: Illustration for lattice model on square lattice. Each orange kite stands for a unit cell, the blue circle stands for a Majorana, and the red square stands for a complex fermion. (a) A toric code with pair superfluid order, featuring anyon-permuting vortices. (b) A toric code with biaxial nematic order.

Our general construction of lattice models has the following form:

$$\hat{H} = \hat{H}_{\text{TO}} + \hat{H}_{\text{SSB}} + \hat{H}_{\text{int}}, \tag{3.27}$$

where $\hat{H}_{\text{TO}}$ is a Hamiltonian for the symmetry enriched topological order, $\hat{H}_{\text{SSB}}$ is a Hamiltonian for the (classical) long-range order associated with spontaneous symmetry breaking, and $\hat{H}_{\text{int}}$ describes the coupling between the topological order and the order parameters of the long-range order.

3.6.4.1 Pair superfluids with anyon-permuting vortices

We first construct a model for the toric code enriched by a $H = Z_2$ symmetry, which is spontaneously broken down from a $G = U(1)$ group. The model (3.27) consists of three parts: the $\hat{H}_{\text{TO}}$ is responsible for the Z_2 topological order in the toric code. $\hat{H}_{\text{SSB}}$ is an XY model describing a superfluid that spontaneously breaks $G = U(1)$ symmetry. Meanwhile $\hat{H}_{\text{int}}$ describes the interaction/coupling between the superfluid and the topological order.

Built on the square lattice, the Hilbert space of the model consists of a $2^3 = 8$ dimensional qudit (or 3 qubits) on each site, and an extra spin-1 on each site. The site qudit can be represented by a pair of spin-1/2 complex fermions $f_{\uparrow,\downarrow}$ and four Majorana fermions

$\{\chi_l|1\leq l\leq 4\}$ (see Fig. 3.4(a)), satisfying the following constraint of an even fermion parity on each site i in the lattice Λ (see Fig. 3.4(a)):

$$(-1)^{f_\uparrow^\dagger f_\uparrow+f_\downarrow^\dagger f_\downarrow}\chi_1\chi_2\chi_3\chi_4=1,\quad \forall\ i\in\Lambda. \tag{3.28}$$

Similar to the Kitaev honeycomb model, this can be viewed as a Z_2 gauge constraint (Gauss's law) on each vertex/site. In terms of these fermions, $\hat{H}_{\rm TO}$ writes

$$\hat{H}_{\rm TO}=\sum_{\langle i,j\rangle}\mathrm{i}\chi_{i,l(ij)}\chi_{j,l(ji)}\sum_{\sigma=\uparrow,\downarrow}t_\sigma f_{i,\sigma}^\dagger f_{j,\sigma}-\sum_{i,\sigma}\mu_\sigma f_{i,\sigma}^\dagger f_{i,\sigma}-E_m\sum_{\langle i,j,k,p\rangle}\hat{P}_{\langle i,j,k,p\rangle}. \tag{3.29}$$

We define $\hat{P}_{\langle i,j,k,p\rangle}$ as the Z_2 flux on each square plaquette with vertices i,j,k,p: $\hat{P}_{\langle i,j,k,p\rangle}\equiv\chi_{i,l(ij)}\chi_{j,l(ji)}\chi_{j,l(jk)}\chi_{k,l(kj)}\chi_{k,l(kp)}\chi_{p,l(pk)}\chi_{p,l(pi)}\chi_{i,l(ip)}$, where the Majorana label $l(i,j)$ on NN link $\langle i,j\rangle$ is defined as: $l(i,i+\hat{x})=1,\ l(i,i-\hat{x})=3,\ l(i,i+\hat{y})=2,\ l(i,i-\hat{y})=4$. If $E_m\gg|t_\sigma|,|\mu_\sigma|$, the plaquette term $\hat{P}_{\langle ijkp\rangle}$ favors zero flux in each square plaquette in the ground state, rather than the π flux state favored in the fermion hopping model at half filling [158].

The Hamiltonian for the spin-1's $\vec{S}_i$ takes the form of the Bose Hubbard model [297]:

$$\hat{H}_{\rm SSB}=-\sum_{\langle i,j\rangle}[tS_i^+S_j^-+t_p(S_i^+)^2(S_j^-)^2+\mathrm{h.}c.]-\mu\sum_i S_i^z. \tag{3.30}$$

Quantum Monte Carlo simulations revealed that it favors a pair superfluid ground state with an order parameter $\langle(S_i^+)^2\rangle\neq 0$ in a finite parameter range, e.g. for $t_p/t\geq g_c$ when $\mu=0$ ($g_c\approx 2.5$ on the triangular lattice) [297].

Finally the coupling term between the Z_2 gauge theory and the link spins have the following form:

$$\begin{aligned}\hat{H}_{\rm int}=&-\sum_{\langle i,j\rangle}\mathrm{i}\chi_{i,l(ij)}\chi_{j,l(ji)}\big(S_i^+S_j^+\Delta_\uparrow e^{\mathrm{i}\arg(j-i)}f_{i,\uparrow}f_{j,\uparrow}+\Delta_\downarrow e^{-\mathrm{i}\arg(j-i)}f_{i,\downarrow}f_{j,\downarrow}+h.c.\big)\\&-\Delta_0\sum_i(S_i^-f_{i,\uparrow}^\dagger f_{j,\downarrow}+\mathrm{h.c.}).\end{aligned} \tag{3.31}$$

Clearly the full Hamiltonian (3.27) preserves a $G=U(1)_{S^z}$ spin rotational symmetry: $S_i^+\to e^{\mathrm{i}\theta}S_i^+,\ \ f_{i,\uparrow}\to e^{-\mathrm{i}\theta}f_{i,\uparrow},\ f_{i,\downarrow}\to f_{i,\downarrow},\ \chi_{i,l}\to\chi_{i,l}$. In the pair superfluid phase with $\langle(S_i^+)^2\rangle\neq 0$, the $G=U(1)_{S^z}$ spin rotational symmetry is broken down to a $H=Z_2$ subgroup generated by $S_i^+\to -S_i^+,\ f_{i,\uparrow}\to -f_{i,\uparrow}$. Note that the parity Z_2^F of spin-1/2 fermions is always preserved:

$$(-1)^{\hat{F}}\equiv(-1)^{\sum_i f_{i,\uparrow}^\dagger f_{i,\uparrow}+f_{i,\downarrow}^\dagger f_{i,\downarrow}} \tag{3.32}$$

In the pair superfluid phase with $\langle S_i^+S_j^+\rangle\neq 0$ and $\langle S_i^+\rangle=0$, the $f_\uparrow^\dagger$ fermions enter a $p+\mathrm{i}p$ topological superconducting phase, while the $f_\downarrow$ fermions form a $p-\mathrm{i}p$ topological superconductor. A fundamental $\nu=1$ vortex of the pair superfluid will translate into a vorticity-1 vortex in the $p+\mathrm{i}p$ superconductor of $f_\uparrow$'s, hence trapping a single Majorana zero mode at the vortex core. Therefore an odd-vorticity vortex of the pair superfluid permutes e and m sectors in the Z_2 toric code.

3.6.4.2 Biaxial nematics with anyon-permuting vortices

Another Hamiltonian of the form (3.27) can also give rise to a biaxial nematic phase with Z_2 toric code topological order, which spontaneously breaks the $SO(3)$ spin rotational symmetry down to a $D_2 = (Z_2)^2$ subgroup. Similarly we build our Hilbert space out of fermionic partons: four complex fermions of one s (f_s) and three p ($f_{x,y,z}$) orbitals, and four Majoranas $\{\chi_i | 1 \le i \le 4\}$. The Majoranas and f_s fermions are spinless, while $f_{x,y,z}$ form a vector (spin-1) representation of the $G = SO(3)$ spin rotational symmetry. Again there is a Z_2 gauge constraint for fermion parity on each site of the square lattice (see Fig. 3.4(b)):

$$(-1)^{f_s^\dagger f_s + \sum_{a=x,y,z} f_a^\dagger f_a} \chi_1 \chi_2 \chi_3 \chi_4 = 1, \quad \forall\, i \in \Lambda. \tag{3.33}$$

The topologically ordered Hamiltonian writes

$$\hat{H}_{\rm TO} = -E_m \sum_{\langle i,j,k,p\rangle} \hat{P}_{\langle i,j,k,p\rangle} - \sum_i (\mu_s f_{i,s}^\dagger f_{i,s} + \mu_p \sum_{a=x,y,z} f_{i,a}^\dagger f_{i,a}) + \sum_{\langle i,j\rangle} \mathrm{i}\chi_{i,l(i,j)}\chi_{j,l(j,i)} \big[\Delta_s e^{-\mathrm{i}\arg(j-i)} f_{i,s} f_{j,s} - t_s f_{i,s}^\dagger f_{j,s} + \sum_{a=x,y,z} (\Delta_p e^{\mathrm{i}\arg(j-i)} f_{i,a} f_{j,a} - t_p f_{i,a}^\dagger f_{j,a}) + \text{h.}c.\big] \tag{3.34}$$

It preserves $SO(3)$ symmetry with a ground state with zero flux in each square plaquette, where the f_s fermions form a $p - \mathrm{i}p$ superconductor and each flavor of $f_{x,y,z}$ fermions forms a $p + \mathrm{i}p$ superconductor.

In addition to the $2^5 = 32$-dimensional qudit described by partons, the physical Hilbert space contains another spin-1 $\vec{S}_i$ on each site. The nematic order parameter is given by the following 3×3 matrix

$$Q_{a,b} = \langle S_i^a S_i^b \rangle, \quad a, b = x, y, z. \tag{3.35}$$

The topological order couples with the spin-1's in the following way:

$$\hat{H}_{\rm int} = -J \sum_{i,a,b} f_{i,a}^\dagger f_{i,b} S_i^a S_i^b \tag{3.36}$$

Once the spin-1 Hamiltonian $\hat{H}_{\rm SSB}[\vec{S}_i]$ [55, 25, 233] favors a biaxial nematic ground state with

$$\hat{Q} = \begin{pmatrix} q_2 - q_1/2 & & \\ & -q_2 - q_1/2 & \\ & & q_1 \end{pmatrix} \tag{3.37}$$

the $G = SO(3)$ spin rotational symmetry is spontaneously broken down to a $H = D_2$ group, generated by π rotation along the $\hat{x}$ and $\hat{y}$ axis.

In the limit of $q_1 = 0$ and $J|q_2| \gg |t_p|, |\mu_p|$, the f_x and f_y fermions are driven into a strong-pairing atomic superconductor, giving rise to a Z_2 toric code ground state, with a $p + \mathrm{i}p$ superconductor of f_z's and a $p - \mathrm{i}p$ superconductor of f_s's. Since f_z is odd under a π rotation along either x or y axis, both the $\pm\mathrm{i}\sigma_x$ and $\pm\mathrm{i}\sigma_y$ vortices can trap a single Majorana zero mode of f_z and hence permute e and m anyons.

We note that the $SO(3)$ symmetric phase with $Q_{a,b} \equiv 0$ in this example is an Abelian Z_2 topological order with the following $\mathbf{K}$ matrix [278]: $\mathbf{K} = 4$. It describes the $\nu = 2$ state in Kitaev's 16-fold way [127], where each elementary anyon of statistical angle $\Theta = \mathrm{i}$ carries spin-1/2 (hence a "spinon"), and each fermion $\{f_a | a = s, x, y, z\}$ is a bound state of two such spinons.

3.6.4.3 Biaxial nematics with defect fractionalization

As discussed previously, when the point defects (or vortices) do not permute anyons in a biaxial nematic order with $H = D_2$ symmetry that is broken down from $G = SO(3)$, they can exhibit defect fractionalization phenomenon captured by the group cohomology $\mathcal{H}^2(\pi_1(G/H) = Q_8, \mathcal{A})$. A model for this phenomenon in the Z_2 topological order (toric code) can be constructed in a similar way as the biaxial nematic order with anyon-permuting vortices in the previous section.

Again we consider an s orbital (f_s) and three p orbitals ($f_{x,y,z}$) of complex fermions (see Fig. 3.4(b)), coupled to a Z_2 gauge field implemented by spinless Majorana fermions. The p orbitals $f_{x,y,z}$ transform as a spin-1 representation of the $G = SO(3)$ symmetry. Now we require f_x and f_y fermions to each form a $p + \mathrm{i}p$ superconductor, while f_z and f_s fermions each forms a $p - \mathrm{i}p$ superconductor. In this case, since $f_{x,y}$ fermions are both odd under the $Z \equiv e^{\mathrm{i}\pi S^z}$ spin rotation, the $\pm\mathrm{i}\sigma_z$ vortices will each trap a $e^{\mathrm{i}\pi S^z}$ symmetry defect. In such a D_2 symmetry enriched topological order, the symmetry fractionalization class [82] $[\omega] \in \mathcal{H}^2(D_2, \mathcal{A})$ is characterized by

$$\omega(X, X) = \omega(Y, Y) = 1, \quad \omega(Z, Z) = \epsilon. \tag{3.38}$$

where $X = e^{\mathrm{i}\pi S^x}$, $Y = e^{\mathrm{i}\pi S^y}$, $Z = e^{\mathrm{i}\pi S^z}$ are π rotations along x, y, z axis. As a result, the associated fractionalization class $[\Omega] \in \mathcal{H}^2(Q_8, \mathcal{A})$ for the vortices is characterized by

$$\frac{\Omega(\mathrm{i}\sigma_z, \mathrm{i}\sigma_z)}{\Omega(\mathrm{i}\sigma_x, \mathrm{i}\sigma_x)} = \frac{\omega(Z, Z)}{\omega(X, X)} = 1, \quad \frac{\Omega(\mathrm{i}\sigma_z, \mathrm{i}\sigma_z)}{\Omega(\mathrm{i}\sigma_y, \mathrm{i}\sigma_y)} = \frac{\omega(Z, Z)}{\omega(Y, Y)} = \epsilon. \tag{3.39}$$

Physically this means fusing two $\mathrm{i}\sigma_x$ vortices differ from fusing two $\mathrm{i}\sigma_y$ vortices by a fermion ϵ in the toric code.

One can also arrange $f_{y,z}$ fermions each in a $p + \mathrm{i}p$ superconductor and $f_{x,s}$ fermions each in a $p - \mathrm{i}p$ superconductor, to achieve

$$\omega(Z, Z) = \omega(Y, Y) = 1, \quad \omega(X, X) = \epsilon. \tag{3.40}$$

or arrange $f_{x,z}$ fermions each in a $p + \mathrm{i}p$ superconductor and $f_{y,s}$ fermions each in a $p - \mathrm{i}p$ superconductor, to achieve

$$\omega(Z, Z) = \omega(X, X) = 1, \quad \omega(Y, Y) = \epsilon. \tag{3.41}$$

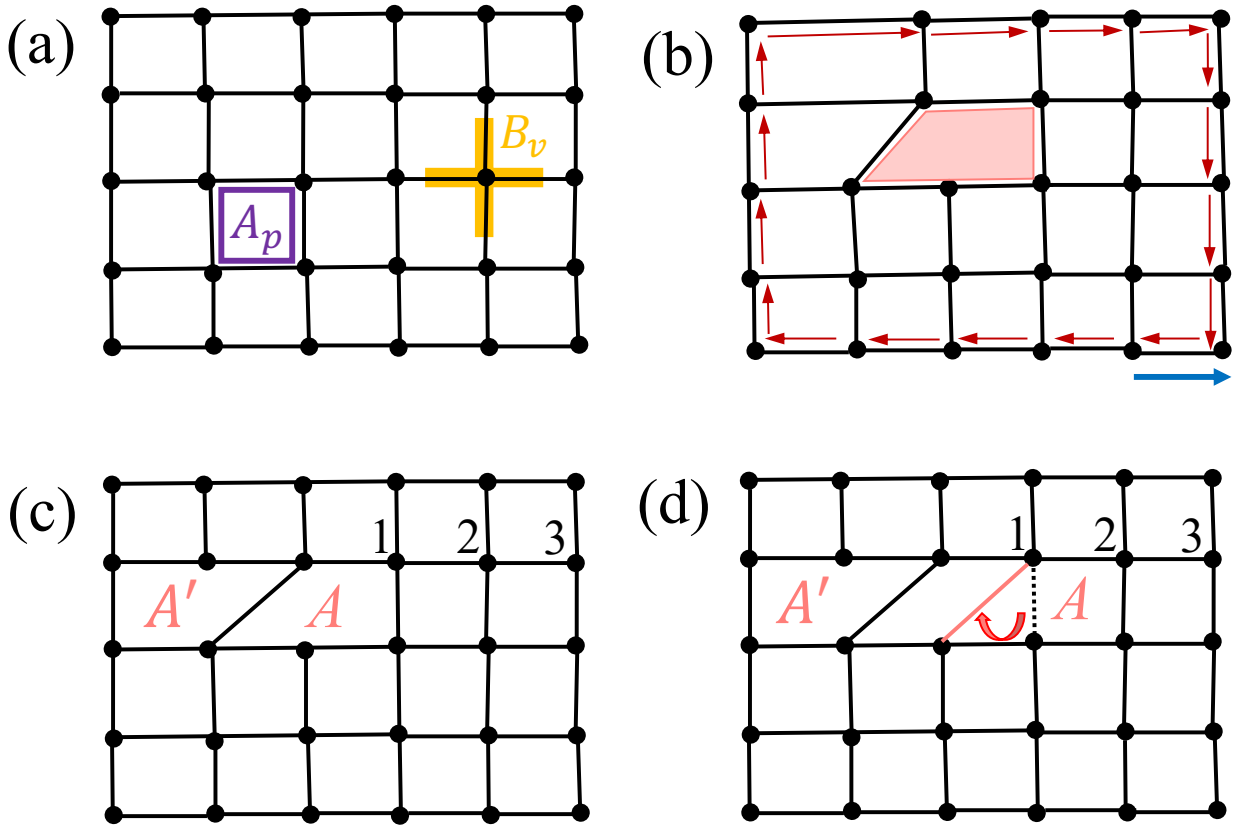

Figure 3.5: (a) Illustration of the model Hamiltonian Eq. (3.42) without any defects. (b) A single dislocation, with the blue arrow denote the Burger vector. (c) A pair of dislocations A and A'. (d) Moving the dislocation A rightward for one unit cell.

3.6.4.4 Fusion rules of dislocations in the toric code

The defect fractionalization is captured by $\mathcal{H}^2(\pi_1(G/H), \mathcal{A})$, as we discussed in Sec. 3.6.1. Consider the fusion of dislocations with trivial action in toric code. Here we choose $G = \mathbb{R} \times \mathbb{R}$ and $H = \mathbb{Z} \times \mathbb{Z}$, such that $\pi_1(G/H) = \mathbb{Z} \times \mathbb{Z}$ captures the dislocation defects in two spatial dimension. The toric code topological order has (Abelian) anyon content $\mathcal{A} = \mathbb{Z}_2^{\mathsf{e}} \times \mathbb{Z}_2^{\mathsf{m}}$. Since the symmetry fractionalization is of a product form $\mathcal{H}^2_{\mathrm{id}}(\pi_1(G/H), \mathbb{Z}_2^{\mathsf{e}} \times \mathbb{Z}_2^{\mathsf{m}}) = \mathcal{H}^2_{\mathrm{id}}(\pi_1(G/H), \mathbb{Z}_2^{\mathsf{e}}) \times \mathcal{H}^2_{\mathrm{id}}(\pi_1(G/H), \mathbb{Z}_2^{\mathsf{m}})$, without loss of generality below we only consider the magnetic anyon sector which has non-trivial defect fractionalization labeled by $\mathcal{H}^2_{\mathrm{id}}(\pi_1(G/H), \mathbb{Z}_2^{\mathsf{m}}) = \mathcal{H}^2_{\mathrm{id}}(\mathbb{Z}^2, \mathbb{Z}_2^{\mathsf{m}}) = \mathbb{Z}_2$. In the following, we will show such a non-trivial defect fractionalization via fusing four dislocations in a lattice model.

The Hamiltonian for toric code on a square lattice is given by:

$$\hat{H}_{\mathrm{TC}} = -\Delta_m \sum_p A_p - \Delta_e \sum_v B_v, \tag{3.42}$$

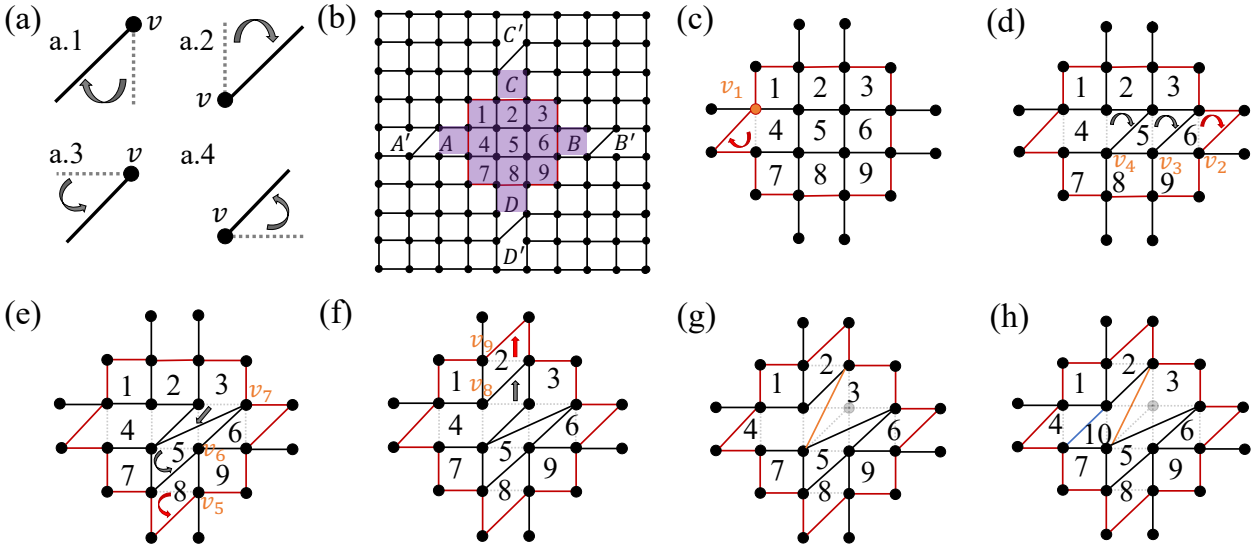

Figure 3.6: Fusion of four dislocation defects. (a) Fundamental operations for defect movements. (b) Toric code with eight dislocation defects. The shaded part is the area that we are interested in. (c) Right move the dislocation A for one lattice constants. (d) Left move dislocation B for three lattice constants. (e) Move dislocation D upwards for three lattice constants. (f) Move dislocation C downward for two lattice constants. (g) Connect two bonds, see Fig. 3.7(b) (h) Add one bond, see Fig. 3.7(c)

where $A_p = \prod_{l\in p} Z_l$ for the product of all bonds associated to plaquette p and $B_v = \prod_{l\in v} X_l$ for the product of all bonds associated to vertex v. Here $X = \sigma_x$, $Z = \sigma_z$ are Pauli matrices. The symmetry operator for translation of one unit cell along x (y) direction is defined as T_x (T_y). The symmetry fractionalization of translation symmetries $H = \mathbb{Z}^{T_x} \times \mathbb{Z}^{T_y}$ can be understood as follows [59]. Consider an eigenstate $|\psi\rangle$ of $\hat{H}_{\text{TC}}$, where a single e particle is created on top of the ground state (assuming the other e particle is at infinity), if it carries the trivial element of the projective representation (i.e., the linear representation) of $\mathcal{H}^2_{\text{id}}(\mathbb{Z}^2, \mathbb{Z}_2^{\mathsf{m}})$, we have $T_x^{-1} \circ T_y^{-1} \circ T_x \circ T_y \,|\psi\rangle = +\,|\psi\rangle$. This is e.g. the case when $\Delta_m > 0$ [59]. On the other hand, if it carries the non-trivial projective representation of the $\mathcal{H}^2_{\text{id}}(\mathbb{Z}^2, \mathbb{Z}_2^{\mathsf{m}})$, we have $T_x^{-1} \circ T_y^{-1} \circ T_x \circ T_y \,|\psi\rangle = -\,|\psi\rangle$. The fact $T_x^{-1} \circ T_y^{-1} \circ T_x \circ T_y \,|\psi\rangle = -\,|\psi\rangle$ means that each plaquette has an m flux, or equivalently traps one m particle. This is the case when $\Delta_m < 0$. Generally, the translation symmetry fractionalization class is given by

$$\frac{\omega(T_x, T_y)}{\omega(T_y, T_x)} = a \in \mathcal{A} \tag{3.43}$$

where $a = 1, m$ in the two scenarios with different sign of Δ_m (both with $\Delta_e > 0$) as discussed above. As discussed in Sec. 3.6.1, if $\pi_1(G) = 0$ as in this case, due to short exact sequence (3.4), there is a one-to-one correspondence between symmetry defects as elements of H and point defects as elements of $\pi_1(G/H) \simeq H$. Therefore, the above cohomology

data of symmetry defects directly translate into cohomology data of point defects of order parameters:

$$\omega(\tau_{\hat{x}}, \tau_{\hat{y}})\omega(\tau_{-\hat{x}}, \tau_{-\hat{y}}) = a \in \mathcal{A} \tag{3.44}$$

where we use $\tau_{\vec{b}}$ to label the dislocation (i.e. the point defect of translation symmetries) with Burgers vector $\vec{b}$. Physically, it means the four dislocations must fuse into an Abelian anyon a:

$$\omega_{\hat{x}} \times \omega_{\hat{y}} \times \omega_{-\hat{x}} \times \omega_{-\hat{y}} = a \in \mathcal{A} \tag{3.45}$$

where a can be considered as the "background anyon" in each unit cell in a translational-invariant topological order[48]. Below, we demonstrate the fusion rule (3.45) for four dislocations, by an explicitly calculation of the anyon a in the toric code on the square lattice.

We consider four pairs of dislocations $(A, A'), (B, B'), (C, C'), (D, D')$, as shown in Fig. 3.6(b). As mentioned earlier, here we focus on distinguishing $a = 1$ vs. $a = m$ (captured by $\mathcal{H}^2(H, Z_2^{\mathsf{m}}) = \mathbb{Z}_2$), which can be detected by a Wilson loop of e type. Such a Wilson loop (red lines) $W_p = \prod \sigma_z$ in Fig. 3.6(b) probes the parity of the number of m particles within it. A similar calculation for the m-type Wilson loop can fully determine the background anyon a in fusion rule (3.45).

Our strategy is to use finite step local unitary operations to move the four inner dislocations A, B, C, D into the Wilson loop, so that the Wilson loop W_p in Fig. 3.6(b) can detect their fusion outcome $a = 1$ vs. $a = m$. To do so, we first define the following unitary operations for Z components:

$$U_{T_x^+}(v) Z_{v,v-\hat{e}_y} U_{T_x^+}^{-1}(v) = Z_{v-\hat{e}_x-\hat{e}_y,v} Z_{v-\hat{e}_y,v-\hat{e}_x-\hat{e}_y}, \tag{3.46a}$$

$$U_{T_x^-}(v) Z_{v,v+\hat{e}_y} U_{T_x^-}^{-1}(v) = Z_{v,v+\hat{e}_x+\hat{e}_y} Z_{v+\hat{e}_y,v+\hat{e}_x+\hat{e}_y}, \tag{3.46b}$$

$$U_{T_y^+}(v) Z_{v,v-\hat{e}_x} U_{T_y^+}^{-1}(v) = Z_{v,v-\hat{e}_x-\hat{e}_y} Z_{v-\hat{e}_x,v-\hat{e}_x-\hat{e}_y}, \tag{3.46c}$$

$$U_{T_y^-}(v) Z_{v,v+\hat{e}_x} U_{T_y^-}^{-1}(v) = Z_{v,v+\hat{e}_x+\hat{e}_y} Z_{v+\hat{e}_x,v+\hat{e}_x+\hat{e}_y}, \tag{3.46d}$$

where v labels the vertex, and $\hat{e}_x$ ($\hat{e}_y$) stands for unit vector along the $\hat{x}$ ($\hat{y}$) direction. The symmetry operations have been shown in Fig. 3.7(a). Note that these operations can be written in terms of two-qubit unitary gates. For example, the $U_{T_x^+}(v)$ operation in Eq. (3.46a) is nothing but the two-qubit swap gate:

$$U_{T_x^+}(v) = U_{T_x^+}^{-1}(v) = \frac{1 + Z_{v,v-\hat{e}_x}}{2} + \frac{1 - Z_{v,v-\hat{e}_x}}{2} X_{v,v+\hat{e}_y}. \tag{3.47}$$

For the vertex $v = 1$, $U_{T_x^+}(v)$ moves the dislocation A in Fig. 3.5(c) rightward by one lattice constant $\hat{x}$, and arrives at the Fig. 3.5(d).

Similarly, for the X components, we have:

$$U_{T_x^+}(v)X_{v,v-\hat{e}_y}U^{-1}_{T_x^+}(v) = X_{v,v-\hat{e}_x-\hat{e}_y}X_{v,v-\hat{e}_y}, \tag{3.48a}$$
$$U_{T_x^-}(v)X_{v,v+\hat{e}_y}U^{-1}_{T_x^-}(v) = X_{v,v+\hat{e}_x+\hat{e}_y}X_{v,v+\hat{e}_y}, \tag{3.48b}$$
$$U_{T_y^+}(v)X_{v,v-\hat{e}_x}U^{-1}_{T_y^+}(v) = X_{v,v-\hat{e}_x-\hat{e}_y}X_{v,v-\hat{e}_x}, \tag{3.48c}$$
$$U_{T_y^-}(v)X_{v,v+\hat{e}_x}U^{-1}_{T_y^-}(v) = X_{v,v+\hat{e}_x+\hat{e}_y}X_{v,v+\hat{e}_x}. \tag{3.48d}$$

Now, let us consider the following symmetry actions for the lattice defined in Fig. 3.6(b): Step 1, move the dislocation A to the right, as shown in Fig. 3.6(c). The corresponding symmetry action reads: $U_1 = U_{T_x^+}(v_1)$. Step 2, move the dislocation B to the left, as shown in Fig. 3.6(d). The corresponding symmetry action will be applying $U_{T_x^-}$ three times: $U_2 = U_{T_x^-}(v_4)U_{T_x^-}(v_3)U_{T_x^-}(v_2)$. Step 3, move the dislocation D upwards, as shown in Fig. 3.6(e). The corresponding symmetry action will be acting $U_{T_y^+}$ for three times: $U_3 = U_{T_y^+}(v_7)U_{T_y^+}(v_6)U_{T_y^+}(v_5)$. Step 4, move the dislocation C downwards, as shown in Fig. 3.6(f). The corresponding symmetry action will be acting $U_{T_y^-}$ twice: $U_4 = U_{T_y^-}(v_9)U_{T_y^-}(v_8)$. The Hamiltonian for Fig. 3.6(b) and Fig. 3.6(f) are actually related by finite step unitary operations $U = U_4U_3U_2U_1$.

We note that not all plaquettes within the Wilson loop in Fig. 3.6(f) are squares. We have shown the part associated with non-square plaquettes and non-cross vertex in Fig. 3.7(a). The Hamiltonian for Fig. 3.7(a) reads:

$$\begin{aligned} H'_a = &- Z_{l_1}Z_{l_2}Z_{l_3}Z_{l_{11}}Z_{l_{12}}Z_{l_9}Z_{l_{10}} - Z_{l_5}Z_{l_6}Z_{l_7}Z_{l_{12}}Z_{l_{11}} \\ &- X_{l_3}X_{l_4}X_{l_5}X_{l_{11}} - \Delta_{11,12}X_{l_{11}}X_{l_{12}} - X_{l_{12}}X_{l_7}X_{l_8}X_{l_9} \\ &- X_{l_2}X_{l_{13}}X_{l_3} - X_{l_9}X_{l_{14}}X_{l_{10}}. \end{aligned} \tag{3.49}$$

To fuse all the defects, we have to introduce two additional local operations. First, we

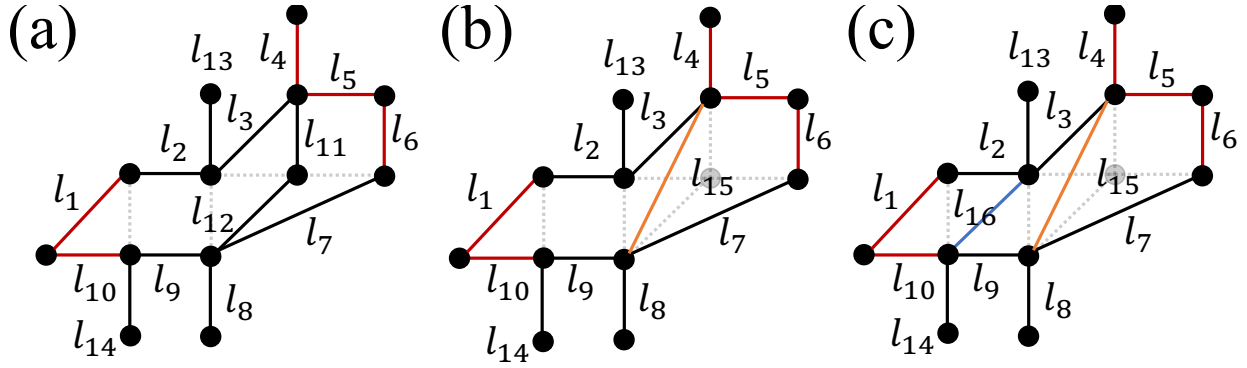

Figure 3.7: Merging line l_{11} and l_{12} in (a) to one line l_{15} (orange) in (b) and adding a line l_{16} (blue) in (c).

need to merge line l_{11} and l_{12} to get the orange line l_{15}, as shown in Fig. 3.7(b). This can

be done by taking the coupling constant $\Delta_{11,12}$ of $X_{ll}X_{12}$ term to infinity, then redefining $X_{15} \equiv X_{11} = X_{12}$ and $Z_{15} = Z_{11}Z_{12}$ in the strong coupling limit. The Hamiltonian for Fig. 3.7(b):

$$\begin{aligned} H'_b = \lim_{\Delta_{11,12}\to\infty} H'_a = &- Z_{l_1}Z_{l_2}Z_{l_3}Z_{l_{15}}Z_{l_9}Z_{l_{10}} - Z_{l_5}Z_{l_6}Z_{l_7}Z_{l_{15}} \\ &- X_{l_3}X_{l_4}X_{l_5}X_{l_{15}} - X_{l_{15}}X_{l_7}X_{l_8}X_{l_9} - X_{l_2}X_{l_{13}}X_{l_3} - X_{l_9}X_{l_{14}}X_{l_{10}}. \end{aligned} \tag{3.50}$$

The second step is to add the blue line l_{16} in Fig. 3.7(c). The Hamiltonian for Fig. 3.7(c) reads:

$$\begin{aligned} H'_c = &- Z_{l_1}Z_{l_2}Z_{l_{16}}Z_{l_{10}} - Z_{l_3}Z_{l_{15}}Z_{l_9}Z_{l_{16}} - Z_{l_5}Z_{l_6}Z_{l_7}Z_{l_{15}} \\ &- X_{l_3}X_{l_4}X_{l_5}X_{l_{15}} - X_{l_{15}}X_{l_7}X_{l_8}X_{l_9} - X_{l_2}X_{l_{13}}X_{l_3}X_{l_{16}} - X_{l_9}X_{l_{14}}X_{l_{10}}X_{l_{16}}. \end{aligned} \tag{3.51}$$

One way to justify adding qubit l_{16} in the last step is to see that in the $h_{16} \to \infty$ limit of a large Zeeman term $-h_{16}X_{16}$, the low-energy effective Hamiltonian of H'_c above reduces back to H'_b.

Note that in all steps discussed above, the gap of the full Hamiltonian never closes. More precisely, we have constructed a smooth path of gapped Hamiltonians which connects the initial Hamiltonian $\hat{H}_0$ in Fig. 3.6(b), and the final Hamiltonian H'_c in Fig. 3.6(h). In other words, the movement of the 4 dislocations into Wilson loop W_p are implemented by a local unitary quantum circuit of finite depth [41].

However, after moving the 4 dislocations into the Wilson loop W_p, one finds that the number of the plaquettes inside the Wilson loop changed from 9 to 10. In the case of a nontrivial translation fractionalization class, with $a = m$ in (3.43) and realized by $\Delta_m < 0$, there is one m particle per unit cell (or plaquette), Therefore after moving the 4 dislocations into the Wilson loop, the Wilson loop now encloses one extra m particle. This means the fusion outcome of the 4 dislocations is nothing but an $a = m$ anyon. On the other hand, if the translation symmetry fractionalization class is trivial with $a = 1$ in (3.43), e.g. realized in the original toric code with $\Delta_{e,m} > 0$, the background anyon per unit cell (or plaquette) is trivial. Therefore moving the 4 dislocations into the Wilson loop does not bring in extra anyons inside the Wilson loop. As a result, the fusion outcome of the 4 dislocations in (3.45) is also trivial, with $a = 1$. Therefore, we have proved in the context of the toric code model that the fusion rule of the dislocations in Eq. (3.45) is determined by the translation fractionalization class (3.43).

3.7 Skyrmions in symmetry enriched topological orders

3.7.1 Field theory of the skyrmions in two-dimensional topological orders

After discussing the point defects in topological orders with coexisting symmetry breaking, in this section we discuss smooth textures of symmetry-breaking order parameters in a topological order. We shall restrict ourselves to skyrmions, e.g. in a ferromagnet where $SO(3)$ spin rotation symmetry is spontaneously broken down to a $U(1)_{S^z}$ subgroup. We shall discuss in detail the universal physical properties of skyrmions following the group cohomology results in Sec. 3.4.4.2.

Consider a skyrmion in ferromagnetic topological orders, where $G = SO(3)$ spin rotational symmetry is spontaneously broken down to a $H = U(1)_{S^z}$ subgroup. As discussed in Sec. 3.4.4.2, due to the short exact sequence (3.17), a skyrmion of topological charge $\nu \in \mathbb{Z} = \pi_2(G/H)$ is equivalent to $4\pi\nu$ flux of the remnant $U(1)_{S^z}$ symmetry. Therefore, we can write down a field theory for the ferromagnetic topological order. Note that the skyrmion 3-current [88, 64, 283] should be treated in the same way as the 4π flux 3-current:

$$J^\mu_{\text{skyrmion}} \equiv \frac{1}{8\pi}\epsilon^{\mu\nu\lambda}\vec{n}\cdot(\partial_\nu\vec{n}\times\partial_\lambda\vec{n}) \simeq \epsilon^{\mu\nu\lambda}\frac{\partial_\nu A_\lambda}{4\pi} \tag{3.52}$$

where unit vector $\vec{n}$ is the ferromagnetic order parameter, and A_μ is the vector potential for the conserved $U(1)_{S^z}$ symmetry. Now that the ferromagnetic topological order has a conserved spin S^z associated with the remnant $U(1)_{S^z}$ symmetry, we can rewrite its conserved S^z current using a dual gauge field a_μ such that

$$j^\mu_{S^z} = \frac{\epsilon^{\mu\nu\lambda}}{2\pi}\partial_\nu a_\lambda \tag{3.53}$$

Since the spin current couples with external vector potential A_μ minimally, the full Lagrangian density of the ferromagnetic topological order can be written as follows:

$$\begin{aligned}\mathcal{L}[\vec{n}, a_\mu] &= \mathcal{L}_{T.O.}[a_\mu] - \frac{\epsilon^{\mu\nu\lambda}}{2\pi}A_\mu\partial_\nu a_\lambda - 2a_\mu J^\mu_{\text{skyrmion}} + \cdots \\ &= \mathcal{L}_{T.O.}[a_\mu] - \frac{\epsilon^{\mu\nu\lambda}}{2\pi}A_\mu\partial_\nu a_\lambda - \frac{\epsilon^{\mu\nu\lambda}}{4\pi}a_\mu\big[\vec{n}\cdot(\partial_\nu\vec{n}\times\partial_\lambda\vec{n})\big] + \cdots\end{aligned}$$

where $\mathcal{L}_{T.O.}[a_\mu]$ describes the intrinsic topological order using the dual gauge field. Integrating out the dual gauge field a_μ can yield an effective action $\mathcal{L}_{rmeff}[\vec{n}]$ for the ferromagnetic order parameter $\vec{n}$. In particular, as we will show below, for a generic topological order, this can induce a Hopf term for the ferromagnetic vector $\vec{n}$, giving rise to fractional statistics of the skyrmions [3, 232].

Finally we point out a universal relation connecting the statistical angle (or topological spin) and $U(1)_{S^z}$ quantum number[8] of a skyrmion. The skyrmion as a spatial texture of order parameter $\vec{n}(x,y,t)$ is classified by the second homotopy group $\pi_2(G/H = S^2) = \mathbb{Z}$. A standard realization of a single skyrmion of topological charge $\nu \in \mathbb{Z}$, of size R and located at the origin, has the following form:

$$\vec{n}(\vec{r},t) = \big(\sin f(r)\cos(\nu\phi), \sin f(r)\sin(\nu\phi), \cos f(r)\big). \tag{3.54}$$

where we introduced the polar coordinate $\vec{r} = (x,y) = r(\cos\phi, \sin\phi)$ and a smooth function $f(r)$ satisfying $f(0) = 0$ and $f(r \geq R) = \pi$. Clearly such a skyrmion texture is invariant under a combined spatial rotation (around origin) by angle θ and spin rotation (along $\hat{z}$ axis) by angle $\nu\theta$. Therefore, the statistical angle $\Theta_\nu \in U(1)$ of a charge-ν skyrmion must be related to its $U(1)_{S^z}$ quantum number Q_ν in the following manner:

$$\Theta_\nu = e^{2\pi\nu \mathrm{i} Q_\nu}. \tag{3.55}$$

3.7.2 Abelian topological orders

To explicitly write down the field theory (3.54) and to obtain universal properties of skyrmions, in this section we focus on the case of an Abelian topological order, which are classified and described by Abelian Chern-Simons theory with a $\mathbf{K}$ matrix[278].

Suppose the underlying system has an Abelian topological order, characterized by the matrix $\mathbf{K}$ and a spin vector $\mathbf{q}$ associated with the remnant $U(1)_{S^z}$ symmetry. In particular, the dual gauge field for the conserved $U(1)_{S^z}$ 3-current is written as

$$a_\mu = \sum_I \mathbf{q}_I a_\mu^I \tag{3.56}$$

From (3.54), the Lagrangian density for the system reads:

$$\mathcal{L} = \frac{1}{4\pi}\epsilon^{\mu\nu\lambda} K_{IJ} a_\mu^I \partial_\nu a_\lambda^J - \mathbf{q}_I a_\mu^I \frac{\epsilon^{\mu\nu\lambda}}{2\pi}\partial_\nu A_\lambda - 2\mathbf{q}_I a_\mu^I J^\mu_{\text{skyrmion}}, \tag{3.57}$$

where the extra 2 in the coefficient of last term denotes the 4π flux carried by each skyrmion instead of ordinary 2π, as we have discussed in Sec. 3.4.4.2.

Integrating out a_μ^I, we obtain the spin Hall conductance associated with A_μ-field [278]:

$$\sigma_{xy}^{S_z} = \mathbf{q}^T \mathbf{K}^{-1} \mathbf{q}. \tag{3.58}$$

[8]Strictly speaking, since the $U(1)_{S^z}$ symmetry is broken by the skyrmion configuration, the $U(1)_{S^z}$ quantum number Q is not well defined. More precisely, different local perturbations can change this quantum number by an integer. However, the fractional part of Q is a universal number, and it shows up in the universal relation (3.55).

Meanwhile, a skyrmion with topological charge $\nu \in \mathbb{Z}$ corresponds to an Abelian anyon labeled by the vector $\mathbf{l}_\nu = 2\nu\mathbf{q}$. The $U(1)_{S^z}$ (spin) quantum number carried by a texture of winding number ν reads:

$$Q_\nu = \mathbf{l}^T\mathbf{K}^{-1}\mathbf{q} = 2\nu\mathbf{q}^T\mathbf{K}^{-1}\mathbf{q} \mod 1, \tag{3.59}$$

and its self-statistics (unit of a^I_μ flux) reads:

$$\Theta_\nu = e^{\mathrm{i}\pi\mathbf{l}^T\mathbf{K}^{-1}\mathbf{l}} = e^{4\pi\mathrm{i}\nu^2\mathbf{q}^T\mathbf{K}^{-1}\mathbf{q}} \tag{3.60}$$

Indeed they obey the universal relation (3.55).

3.7.3 Half-integer spins with $SU(2)$ symmetry

Lastly we clarify one subtle difference between $G = SO(3)$ in systems with integer spins, as discussed previously, and $G = SU(2)$ in systems with half-integer spins.

For a bosonic or fermionic system with half-integer spins, the full symmetry group is $G = SU(2)$ rather than the previously discussed $SO(3)$ case. Since $\pi_1(SU(2)) = 0$, now the skyrmions as elements of $\pi_2(SU(2)/U(1)) = \mathbb{Z}$ and fluxes as elements of $\pi_1(U(1)) = \mathbb{Z}$ have a one-to-one correspondence realized by bijective map f below:

$$\pi_2(SU(2)) = 0 \to \pi_2(S^2) \xrightarrow{f} \pi_1(U(1)) \to \pi_1(SU(2)) = 0. \tag{3.61}$$

More precisely, a skyrmion of winding number ν is now mapped to a $2\pi\nu$ flux (i.e. ν flux quanta) of the unbroken $H = U(1)_{S^z}$ subgroup. The effective theory for an Abelian topological order with an odd $\mathbf{K}$ matrix reads:

$$\mathcal{L} = \frac{1}{4\pi}\epsilon^{\mu\nu\lambda}K_{IJ}a^I_\mu\partial_\nu a^J_\lambda - \mathbf{q}_I a^I_\mu\frac{\epsilon^{\mu\nu\lambda}}{2\pi}\partial_\nu A_\lambda - \mathbf{q}_I a^I_\mu J^\mu_{\text{skyrmion}}. \tag{3.62}$$

Similar to the case for integer spins, a skyrmion of topological charge ν, now labeled by vector $\mathbf{l}_\nu = \nu\mathbf{q}$, carries $U(1)_{S^z}$ quantum number $Q_\nu = \nu\mathbf{q}^T\mathbf{K}^{-1}\mathbf{q} \mod 1$ and self statistical angle $\Theta_\nu = e^{\mathrm{i}\pi\nu^2\mathbf{q}^T\mathbf{K}^{-1}\mathbf{q}}$.

For example, in the quantum Hall ferromagnet in the lowest Landau level [232] with $\mathbf{K} = 1,\ \mathbf{q} = 1$, a $\nu = 1$ skyrmion becomes a fermion with $\Theta_{\nu=1} = -1$ [3]. An alternative way to understand this problem is to gauge the fermion parity symmetry Z_2^F to map it to a bosonic topological order with $G = SO(3),\ H = U(1)$ as discussed previously. In this case, the quantum Hall ferromagnet in the lowest Landau level [232] corresponds to a $U(1)_4$ Chern-Simons theory with $\mathbf{K} = 4,\ \mathbf{q} = 1$ after gauging the fermion parity, where a $\nu = 1$ skyrmion is again a fermion with $\Theta_{\nu=1} = -1$.

3.8 Discussion and outlook

In summary, we described a theoretical framework which classifies point defects and textures in two dimensional quantum phases, where the full symmetry G is spontaneously broken down to a subgroup H of remnant symmetries, so that each symmetry breaking ground state with a fixed (non-fluctuating) order parameter is an H-symmetry enriched topological (H-SET) state. Using the long exact sequence of homotopy groups that maps the point defects and textures of order parameters to symmetry defects in the H-SET phase (see Sec. 3.3), we obtain a group cohomology classification for the point defects and textures (see Sec. 3.4), which is induced from the group cohomology classification of H-SET phases (including the H-SPT phases as a special case).

Using this general framework and the group cohomology classification, we address their physical consequences focusing on three aspects. In Sec. 3.5, we studied point defects and textures of order parameters in H-SPT phases, and reveal their connection to deconfined quantum critical points (DQCPs). In Sec. 3.6, we studied point defects of order parameters in H-SET phases, showing that they can (1) permute anyons when braided around, and (2) fuse into Abelian anyons, a phenomenon we coined "defect fractionalization". In Sec. 3.7 we studied textures of order parameters in H-SET phases, establishing their field theory descriptions and the fractional statistics obeyed by the skyrmions.

This work aims to understand the interplay between classical long-range orders of local order parameters, and quantum orders of long-range entanglement in the ground state [275]. It serves as a first step towards a complete classification and characterization of quantum phases with both classical and quantum orders. While we focused on point defects and textures in two-dimensional bosonic systems in this work, three natural extensions are: (i) to understand domain walls of discrete symmetry breakings; (ii) to study fermionic systems with long-range orders; and (iii) to go beyond two spatial dimensions. For example, in three dimensions, the coexistence of long-range orders and quantum spin liquids (known as "magnetic moment fragmentation") has been proposed in quantum spin ice compounds [214, 31].

In our study of the symmetry breaking in SET phases in Sec. 3.6, we focused on examples of Abelian topological orders, where we used an underlying toric code topological order throughout the analysis. This choice is made for simplicity and for the purpose of explicit lattice model construction in Sec. 3.6.4. We believe the toric code suffices for illustrating the general principle that we laid out using an algebraic means. It is interesting to identify a non-Abelian system which harbors the nontrivial point defects and textures discussed in our formalism.

As discussed in Sec. 3.3.2-3.3.3, in this work, we focused on the case where the long exact sequence (1.5) of homotopy groups cuts off into short exact sequences: (3.4) for point defects and (3.5) for textures (skyrmions) in two spatial dimensions. The consequent short exact sequence allowed us to obtain a compact classification for universal properties of point defects and textures based on group cohomology in Sec. 3.4. While many physical systems fall into this case, in a most generic situation, both nontrivial topological point defects and textures

exist, with possible nontrivial interplay between them [133]. To establish a mathematical classification for the generic case goes beyond the current work, and we leave it for future developments.

Now that we have studied point defects and smooth textures of order parameters associated with SSB from G to H, condensing such point defects (i.e. vortices) or textures (skyrmions) is expected to restore the broken symmetries. However, as we have shown in this work, point defects can carry a projective representation of the remnant symmetry H, and textures can carry fractional statistics and fractional quantum numbers. As a result, the defect/texture condensation transition may spontaneously break other symmetries and/or alter the topological order in the ground state. This will lead to a family of quantum phase transitions beyond the Landau paradigm [222, 134, 29]. For example, condensing a skyrmion obeying bosonic self statistics but nontrivial mutual statistics with other anyons can restore $SO(3)$ symmetry, leading to a paramagnetic ground state with a different topological order than the ferromagnetic phase. We leave these novel phase transitions as future projects.

Finally, note that in two spatial dimensions, point defects of the order parameters in our framework can be mapped to a one-parameter family of gapped H-SET Hamiltonians, while a smooth texture of order parameters in our framework can be mapped to a two-parameter family of gapped H-SET Hamiltonians [127]. Therefore, our classification of point defects and textures in H-SET phases also serves as a first step towards the classification and construction of adiabatic pumping cycles in SET phases [120, 2, 279]. We also leave these developments to future works.

Chapter 4

Minimal one-dimensional model of bad metal behavior from fast particle-hole scattering

A strongly interacting plasma of linearly dispersing electron and hole excitations in two spatial dimensions (2D), also known as a Dirac fluid, can be captured by relativistic hydrodynamics and shares many universal features with other quantum critical systems. We propose a one-dimensional (1D) model to capture key aspects of the 2D Dirac fluid while including lattice effects and being amenable to non-perturbative computation. When interactions are added to the Dirac-like 1D dispersion without opening a gap, we show that this kind of irrelevant interaction is able to preserve Fermi-liquid-like quasi-particle features while relaxing a zero-momentum charge current via collisions between particle-hole excitations, leading to resistivity that is linear in temperature via a mechanism previously discussed for large-diameter metallic carbon nanotubes. We further provide a microscopic lattice model and obtain numerical results via density-matrix renormalization group (DMRG) simulations, which support the above physical picture. The limits on such fast relaxation at strong coupling are of considerable interest because of the ubiquity of bad metals in experiments. What is more, this type of quantum dynamics can happen at the boundary of quantum spin Hall insulator, where particle-hole scattering leads to linear-in-temperature resistivity of edge modes.

4.1 Introduction

A strongly interacting plasma of linearly dispersing electron and hole excitations in two dimension, also known as a Dirac fluid, shares many universal features with other quantum critical systems. With particle-hole symmetry preserved, under external electric field, there exists a "zero momentum mode" in the Dirac fluid which carries a non-vanishing charge current [89, 186, 185]: electrons and holes move symmetrically in opposite directions. Pro-

tected by conservation of momentum, in a continuous translationally invariant system, such a charge current could only be relaxed via scattering within the quasi-particles in the current. The most studied example of this kind of Dirac fluid is the electron-hole plasma in high mobility graphene at the charge neutrality point, which is believed to have Planckian-bounded dissipation [89, 186, 185, 171, 173, 196, 238, 239, 172, 69, 65, 140].

Here Planckian dissipation refers to a relaxation or scattering time $\tau_p \sim \hbar/k_B T$ set only by temperature and the Planck constant [294, 293]. There is considerable experimental evidence for the importance of such relaxation rates as an upper bound in a broad range of "bad metals" [192, 32, 258], most famously in the linear-in-temperature resistivity of some cuprate superconductors at optimal doping, in contrast to the standard form $\rho = \rho_0 + AT^2$ of Fermi liquids. (Note that there can be mechanisms of dissipation that involve the Planckian time scale but do not lead to changes in resistivity, for example in translation-invariant systems where current is conserved by the dissipation process.) The general mechanism of Planckian dissipation remains contested. As nothing in the Dirac fluid picture is manifestly specific to two dimensions, one could ask whether similar features could be obtained in one spatial dimension, where metallic transport is well known to have unique features [26]. Because more non-perturbative calculations are available in one dimension both theoretically and numerically, constructing a one-dimensional Dirac fluid and increasing interactions to strong coupling is a test of one origin of Planckian dissipation.

Conceptually, if one were to take a sheet of graphene and wrap it into a metallic armchair nanotube, one might expect some signs of 2D Dirac fluid transport along the tube axis to be preserved. Indeed, Balents and Fisher argued that interactions in a sufficiently large nanotube, while expected ultimately to open a gap, might show a linear-in-T resistivity over a range of temperatures, based on particle-hole scattering as a perturbation.[7] (Since there are different terminologies appearing in the literature, note that particle-hole scattering can also be viewed as a kind of two-particle Umklapp scattering but with no loss of momentum, as explained below Figure 1.). Our goal here is to find a single-chain model with no observable gap, use a kinetic theory approach to determine its resistivity beyond perturbation theory, and then verify the bad metal regime by taking advantage of the remarkable progress in dynamical matrix product state calculations.

Of course, metals in one dimension are generally more sensitive to electron-electron interactions than in higher dimensions, resulting in a Luttinger liquid rather than the Fermi liquid familiar from higher dimensions. Since the Luttinger liquid also starts from a Fermi surface with isolated points, and its existence is by now well established, the existence of alternative Dirac-fluid physics in one dimension must depend on the details of a microscopic model. The past few years have seen a renaissance in the dynamics of one-dimensional models, including, even without disorder and the possibility of localization, a new kind of hydrodynamics in integrable models resulting from the inhibition of relaxation from extra conservation laws [26]. Planckian dissipation is expected to appear in the opposite limit, where relaxation is happening as rapidly as possible.

The goal of this work is to understand whether one-dimensional Dirac fluids can be engineered in realistic lattice models, how they relate to known physics such as the Luttinger

liquid, and whether they can show the fast relaxation that underlies Planckian behavior. Throughout we use the word "fast" to indicate that the scattering process induces the equilibrium found from kinetic theory before any higher-order interaction effect opens a gap; it is difficult to rule out either analytically or numerically the emergence of a tiny energy gap, which will affect dynamics only at the longest time scales and lowest temperatures.

In the remainder of this introduction, we review when effective hydrodynamic descriptions appear in metallic materials and some existing mechanisms or examples of Planckian dissipation. Real solids have at most discrete translational symmetries, which can be broken down by impurities. Under some conditions, the momentum relaxation processes like Umklapp and impurity scattering possess a characteristic time scale τ_r, which may be much larger in a clean material at low temperature than the Planckian time τ_p. Then a local equilibrium can be reached via collisions between excitations without relaxation of momentum; a well-studied example motivating our study is with particle-hole symmetry [54, 211, 210]. If the conservation laws of the system such as energy, charge and momentum determine the relevant degrees of freedom beyond a certain time scale, one expects approximate phenomenological relativistic hydrodynamic equations to capture the coarse-grained properties [146, 114, 172, 57] up to the momentum relaxation scale, and hydrodynamical effects will influence the measured conductivity.

A major experimental motivation for such models comes from the normal state of cuprate superconductors, and we summarize some of that very briefly. While the origin of linear-in-temperature resistivity in the normal state of high T_c superconductors at optimal doping remains an open question [242, 294, 293, 32, 258], hydrodynamic studies for various kinds of quantum critical fluids suggest one kind of answer[140, 186, 185, 32, 294, 69, 187, 236, 293]: a quantum critical electron fluid with maximal Planckian dissipation is one theoretical route to linear-T resistivity, even if the nature of a quantum critical point near optimal doping is difficult to probe because of the intervening superconductivity. The theoretical study of fast relaxation in higher dimensions was reinvigorated by the introduction of the Sachdev-Ye-Kitaev model, an analytically tractable nonlocal model of randomly interacting fermions [212] with some unusual features such as ground-state entropy and all-to-all interactions that make its connection to materials somewhat opaque.

The Dirac fluid introduced above is a different route to linear-T resistivity that is thought to be relevant to studies of transport in clean graphene samples near half-filling [53]. We can ask which quantum liquids in one dimension, where additional non-perturbative methods are available, can possess similar transport properties to charge-neutral graphene, and what the leading corrections to this behavior are in realistic systems. It is well known that ballistic transport (i.e., free motion of carriers without scattering) in one dimension has quantized conductance at zero temperature. Some special systems in one dimension, the integrable systems mentioned above, possess an extensive set of conservation laws that protect the current from relaxing [159, 95, 244, 71], which often, though not always, leads to ballistic transport up to high temperature [26].

Previous models have been studied to explore whether it is possible to relax the current in an impurity-free, non-integrable 1D system at finite temperature, but these generally have

parametrically slower relaxation than required for linear-in-T resistivity. One example is to sit slightly away from half-filling, with the band curvature considered and three-particle scattering processes introduced, which gives a quasi-particle decay rate scaling with the eighth power of the energy [213, 177]. Another example is to add staggered magnetic field at half-filling, to break the integrability of the 1D XXZ model, which turns out to give a power-law DC conductivity with respect to temperature depending on the Luttinger parameter [104, 33]. These encourage us to look elsewhere for a 1D model which can support Planckian dissipation and linear-T resistivity, in analogy with the Dirac fluid.

Our route is to use a scattering process in 1D, which can be thought of as either particle-hole scattering or fast Umklapp-like scattering (FUS), to approach limits on the relaxation of current in one dimension in an impurity-free system. We start from a one-dimensional Dirac-like continuous model, where the Fermi level lies at the Dirac node (charge neutrality). The scattering will take two electrons from one linearly dispersing chiral branch to the opposite one, with no net momentum transferred. This is different from the conventional Umklapp scattering in an ordinary 1D metal, where the two chiral branches are separated in momentum space at different Fermi points k_L and k_R, such that the scattering process will possess a large momentum transfer $2|k_L - k_R| \sim 2\pi$. From the bosonization of the low energy Hamiltonian, we find that the FUS terms are irrelevant and that the Fermi liquid quasi-particle picture survives. The scattering can thus predominantly contribute to the current relaxation while adding only a small modification to the energy spectrum. Our focus will be on realizing this mechanism while avoiding gap-opening instabilities such as dimerization and also Luttinger liquid behavior from forward scattering.

This scattering is thus an "extrinsic" mechanism [58] in the sense that the fixed point is still a Fermi liquid, but the scattering can still be strong enough to give linear-in-T resistivity. With the quasi-particle picture preserved, combined with conservation of energy, momentum, and charge, we can then use a kinetic theory approach to calculate the DC conductivity. At the perturbative level, the collisionless limit (non-interacting case) gives a quantized conductance identical to that of ballistic transport with two chiral conducting channels. In the presence of collisions, the conservation laws and particle-hole symmetry put a strong constraint on scattering processes. By using a standard variational method, we find that the conductivity is broadened to a Lorentzian by the FUS at finite temperature, and obtain a linear-T resistivity in the DC limit.

In order to check that this physics can be realized in a solid, we then introduce a microscopic lattice model that manifests the aforementioned scattering process and transform it into a spin model via a Jordan-Wigner transformation. We use time-dependent density-matrix renormalization-group (DMRG) simulations [281, 260, 259, 218] to compute the current relaxation at finite temperature. Our results are consistent with the predictions of the field theory. Having a concrete model of linear-T resistivity, in a numerically tractable system with local couplings and interactions, opens the door for future studies of the strong-coupling stability and generality of this kind of transport.

The remainder of this chapter is organized as follows. In Sec. [4.2], we give the low-energy model for a 1D Dirac-like fermionic band structure with the FUS. We show that the particle-

hole scattering/FUS terms are irrelevant and will not modify the band structure to the leading order, thus could preserve the Fermi liquid and the quasi-particle picture. In Sec. [4.3] we use the kinetic equations to study the transport properties for a fermionic model with Dirac-like dispersion, which coincides with the well known results for 1D two-channel ballistic transport. We further calculate the conductivity in the presence of scattering, and show the broadening from collision of quasi-particles in finite temperature. In the low frequency limit, the resistivity linearly dependends on temperature. We provide a lattice realization for aforementioned low energy model in Sec. [4.4]. By using the Jordan-Wigner transformation, we transform the lattice model to a spin model, and confirm the predictions of the field theory numerically via density matrix renormalization-group (DMRG) simulations.

4.2 Low energy model and scattering process

The low-energy theory of a non-interacting 1D metal can be obtained by linearizing the spectrum near the Fermi level. When the Fermi points for the left- and right-moving linear branches coincide with each other, we arrive at a Dirac-like crossing, as shown in Fig. [4.1.(a)]. The linearized free Hamiltonian around the Fermi point, H_0, can be written in a chiral basis as

$$H_0 = v_F \int \frac{dk}{2\pi} k[\psi_R^\dagger(k)\psi_R(k) - \psi_L^\dagger(k)\psi_L(k)] \tag{4.1}$$

where $\psi_R(k)$ and $\psi_L(k)$ stand for the annihilation operators for right- and left-moving chiral fermion modes at one-dimensional momentum k, respectively, and v_F is the Fermi velocity near the Fermi level. Note that, the linear dispersion with an X-type Dirac crossing can be viewed as the edge states of a quantum spin Hall insulator in the absence of interaction [137]. The above chiral basis can be transformed into the energy basis [65, 210], where $\gamma_+(k)$ and $\gamma_-(k)$ annihilate an electron with energy above and below the Dirac node, respectively:

$$\begin{pmatrix}\gamma_+(k)\\ \gamma_-(k)\end{pmatrix} = \frac{1}{2}\begin{pmatrix}1+\vartheta(k) & 1-\vartheta(k)\\ 1-\vartheta(k) & 1+\vartheta(k)\end{pmatrix}\begin{pmatrix}\psi_R(k)\\ \psi_L(k)\end{pmatrix}, \tag{4.2}$$

where $\vartheta(x) = 1$ for $x > 0$ and $\vartheta(x) = -1$ for $x < 0$. Note that the density of states vanishes at the Dirac node, so hereafter we can neglect the singularity at $k = 0$ itself. With this, the free Hamiltonian is transformed into the following form:

$$H_0 = v_F \int \frac{dk}{2\pi} |k|[\gamma_+^\dagger(k)\gamma_+(k) - \gamma_-^\dagger(k)\gamma_-(k)]. \tag{4.3}$$

Both chiral basis and energy basis are plotted in Fig.[4.1.(b)].

Now we study the full Hamiltonian H with an interaction H_{int} turned on:

$$H = H_0 + H_{\text{int}}. \tag{4.4}$$

We would like the interaction to introduce the following fast Umklapp-like scattering (FUS) among the chiral fermions:

$$H_{\rm int} = \int \frac{dk_1}{2\pi}\frac{dk_2}{2\pi}\frac{dq}{2\pi} V(q)[\psi_R^\dagger(k_1+q)\psi_R^\dagger(k_2-q)\psi_L(k_2)\psi_L(k_1) + \psi_L^\dagger(k_1+q)\psi_L^\dagger(k_2-q)\psi_R(k_2)\psi_R(k_1)]. \tag{4.5}$$

This process takes two electrons on the same branch to the opposite branch, as shown in Fig. [4.1.(c)]. Unlike the conventional Umklapp scattering for a 1-component model (see in Fig. [4.1.(d)]), the FUS defined here does not carry large momentum transfer, as the left- and right-moving branches' Fermi points coincide at the Dirac node. One can alternately view one of the processes as the scattering of a hole rather than an electron. Then the basic idea is that, in a particle-hole symmetric system like a Dirac point, a current of oppositely directed particles and holes can have zero total momentum, allowing the current to relax through momentum-conserving collisions. This may also be viewed as a intrinsic current relaxation mechanism for the edge of a clean quantum spin Hall insulator [137].

The interaction Eq. [4.5] can also be written in the energy basis:

$$H_{\rm int} = \sum_{\lambda_1\lambda_2\lambda_3\lambda_4}\int \frac{dk_1}{2\pi}\frac{dk_2}{2\pi}\frac{dq}{2\pi} T_{\lambda_1\lambda_2\lambda_3\lambda_4}(k_1,k_2,q)\gamma^\dagger_{\lambda_4}(k_1+q)\gamma^\dagger_{\lambda_3}(k_2-q)\gamma_{\lambda_2}(k_2)\gamma_{\lambda_1}(k_1), \tag{4.6}$$

where the $\lambda_{1,\dots,4}$ in the summation take the value of $\pm$ and the structure factor

$$T_{\lambda_1\lambda_2\lambda_3\lambda_4}(k_1,k_2,q) = T^2_{\lambda_1\lambda_2\lambda_3\lambda_4} + T^3_{\lambda_1\lambda_2\lambda_3\lambda_4}, \tag{4.7}$$

where: $T^2_{\lambda_1\lambda_2\lambda_3\lambda_4} = V(q)[\lambda_1\vartheta(k_1) - \lambda_4\vartheta(k_1+q)][\lambda_2\vartheta(k_2) - \lambda_3\vartheta(k_2-q)]/16$ and $T^3_{\lambda_1\lambda_2\lambda_3\lambda_4} = V(q)[1-\lambda_1\lambda_3\vartheta(k_1^2+qk_1)][1-\lambda_2\lambda_3\vartheta(k_2^2-qk_2)]/16$ are the matrices which indicate the scattering amplitudes among electrons with positive and negative energy.

The standard bosonized Hamiltonian for Eq. [4.4] reads [71, 288, 285]:

$$H_B = \int [dx]\left\{\frac{v}{2}\left[\frac{(\partial_x\phi)^2}{K} + K(\partial_x\theta)^2\right] - \frac{V\cos[\sqrt{16\pi}\phi(x)]}{2(\pi a_0)^2}\right\}, \tag{4.8}$$

where $\phi(x) = \phi_R(x) + \phi_L(x)$ and $\theta(x) = \phi_R(x) - \phi_L(x)$ are linear combinations of the bosonic fields $\phi_{R,L}(x)$, and a_0 stands for a short-range cut-off, say the lattice constant. As there is no forward scattering in Eq. [4.5], such that the interacting strength for forward scattering $V_{\rm fw} = 0$. Thus for our model Eq. [4.4], we have the renormalized Fermi velocity $v = \sqrt{v_F^2 - V_{\rm fw}^2} = v_F$, and the Luttinger parameter $K = \sqrt{(v_F - V_{\rm fw})/(v_F + V_{\rm fw})} = 1$. The renormalization group analysis [71, 285] shows that the last term in Eq. [4.8] (FUS) is irrelevant when $K > 1/2$, providing our system is still gapless in the weak interacting limit and can be captured by Fermi liquid theory with well-defined quasi particles. One can then use the kinetic theory to describe the 1D transport of the system. Note that, for the particle density $\rho(x) = \psi_R^\dagger(x)\psi_R(x) + \psi_L^\dagger(x)\psi_L(x)$, the continuity equation $\partial_t\rho(x) + \partial_x j(x) = 0$ gives the $U(1)$ current density $j(x) = v_F[\psi_R^\dagger(x)\psi_R(x) - \psi_L^\dagger(x)\psi_L(x)]$. Assume the charge carried

by each particle (hole) is $+Q$ ($-Q$), the total charge current J reads [65, 210]:

$$J = v_F Q \sum_{r=R,L} \int \frac{dk}{2\pi} r \psi_r^\dagger(k) \psi_r(k) \tag{4.9a}$$

$$= v_F Q \sum_{\lambda=\pm} \int \frac{dk}{2\pi} \frac{\lambda k}{|k|} \gamma_\lambda^\dagger(k) \gamma_\lambda(k). \tag{4.9b}$$

Note that in Eq.[4.9a], we have $r = 1$ for right movers (R) and $r = -1$ for left movers (L). Similarly, the total momentum reads:

$$P = \sum_{r=R,L} \int \frac{dk}{2\pi} k \psi_r^\dagger(k) \psi_r(k) = \sum_{\lambda} \int \frac{dk}{2\pi} k \gamma_\lambda^\dagger(k) \gamma_\lambda(k). \tag{4.10}$$

4.3 Transport via kinetic theory

In this section, we evaluate the transport via kinetic theory of the quasiparticles [210, 4, 65]. In Sec. [4.3.1], we first describe the generation of zero momentum mode in a collisionless particle-hole symmetric system in the presence of external electrical field. As a check, we calculate the conductivity for the non-interacting model Eq. [4.1], and show that it is identical to the well-known results of ballistic two-channel 1D transport. In Sec. [4.3.2], we show that the zero momentum mode can be relaxed by the momentum-conserving particle-hole scattering processes. We further calculate the broadening of conductivity due to the FUS, and obtain the Planckian linear-in-temperature resistivity.

4.3.1 Collisionless transport

We can use the standard equation of motion analysis to write down the collisionless transport equations for the excitations. We define the distribution functions under the energy basis $\gamma_\pm$ at time t:

$$f_\lambda(k,t) = \langle \gamma_\lambda^\dagger(k,t) \gamma_\lambda(k,t) \rangle. \tag{4.11}$$

In the equilibrium, without external perturbation, these are related to the Fermi distribution function $f^0(p) = 1/(e^{(p-\mu)/k_B T} + 1)$, with μ the chemical potential, thus

$$f_\pm(k,t) = f^0(\pm\epsilon_k) = \frac{1}{e^{(\pm\epsilon_k - \mu)/k_B T} + 1}. \tag{4.12}$$

In the absence of interactions, we have linear dispersion $\epsilon_\lambda(k) = \lambda \epsilon_k = \lambda v_F |k|$ from Eq. [4.3], with $\lambda = \pm 1$ for the excitations with positive and negative energy, respectively. Here and later, for simplicity we set $\hbar = k_B = 1$, and will only reinsert them back when needed. To the zeroth order, in the presence of an external electric field $E(t)$, in the collisionless limit the dynamics is captured by the following simple kinetic equation:

$$\left[\frac{\partial}{\partial t} + QE(t) \frac{\partial}{\partial k} \right] f_\lambda(k,t) = 0. \tag{4.13}$$

We seek to solve the above kinetic equation within the standard approximation of linear response. First, we parametrize the change in f_λ from its equilibrium value by using the following ansatz [65, 4]:

$$f_\lambda(k,\omega) = 2\pi\delta(\omega)f^0(\lambda\epsilon_k) + Q\frac{kE(\omega)}{|k|}f^0(\lambda\epsilon_k)[1-f^0(\lambda\epsilon_k)]g_\lambda(\epsilon_k,\omega), \tag{4.14}$$

with $g_\lambda(\epsilon_k,\omega)$ a function to be determined. Note that, we have Fourier transformed time t to the frequency domain ω, and replaced $f_\lambda(k,t)$ with $f_\lambda(k,\omega)$. When $\mu = 0$, the system is at particle-hole symmetric point, and an applied electric field $E(\omega)$ generates deviations in the distribution functions for particles and holes with opposite signs. This is due to the fact that the driving term Eq. [4.13] is odd under $\lambda \to -\lambda$, thus the deviation also has to be asymmetric in λ:

$$g_\lambda(\epsilon_k,\omega) = \lambda g(k,\omega). \tag{4.15}$$

In coordinate space, there will be newly generated holes (particles) moving align (anti-align) with the external electric field. This can be viewed as the generation of particle-hole pairs. For the states within the orange and purple square shown in the Fig. [4.2.(a)], at the same k point, the particle and hole has opposite momentum, and each particle-hole pair has zero total momentum defined by Eq. [4.10] in the presence of particle-hole symmetry. On the other hand, since the particles and holes carry opposite charge, if they move in the opposite directions, the total current given by Eq. [4.9] is non-zero.

Substituting Eq. [4.14] into Eq. [4.13], one could derive a solution for g:

$$g_\lambda(\epsilon_k,\omega) = \frac{\lambda v_F/T}{-i\omega+\eta}, \tag{4.16}$$

with η is a positive infinitesimal. One can further insert this into the expression of current operator Eq. [4.9b] to get the conductivity:

$$\begin{aligned}\sigma(\omega) = \frac{\langle J\rangle}{E(\omega)} &= Qv_F\sum_\lambda\int\frac{dk}{2\pi}\frac{\lambda k}{|k|}\left\{Q\frac{k}{|k|}f^0(\lambda\epsilon_k)[1-f^0(\lambda\epsilon_k)]g_\lambda(\epsilon_k,\omega)\right\}\\ &= \frac{2Q^2v_F^2/T}{(-i\omega+\eta)}\int_{-\infty}^{+\infty}\frac{dk}{2\pi}\frac{k^2}{|k|^2}\left[-T\frac{\partial f^0(\epsilon_k)}{\partial(\epsilon_k)}\right] \approx \frac{2Q^2}{h}\frac{\hbar v_F}{-i\hbar\omega+\eta} \to \lim_{\omega\to0}\sigma(\omega) = \frac{2Q^2}{\hbar}v_F\delta(\omega).\end{aligned} \tag{4.17}$$

In the first line, we have used the fact that contribution from the unperturbed distribution function (integral related to the first term in Eq. [4.14]) should vanish. Note that we have restored $\hbar$ and k_B in the last line from dimensional analysis, in the second line. We also have used the relation that $f^0(p)[1-f^0(p)] = -T\partial_p f^0(p)$ is an even function of p, and the extra factor of 2 comes from the summation of particle and hole channels. This is consistent with the bosonization results for clean system in 1D [71]. As the v_F/ω has the unit of length, this in accordance with the fact that the conductivity in 1D is roughly the conductance times the length. In the low frequency limit, the above result is reduced to the Drude peak, which is the signal for ballistic transport [71, 229].

4.3.2 Collision terms in kinetic equation

In this section, we will show the zero momentum mode can be relaxed by the internal collisions among excitations even without disorder and the possibility of localization. With the interaction in Eq. [4.5] or Eq. [4.6], the corresponding collision terms can be derived by a simple application of Fermi's golden rule. From the bosonization results for continuous model showed in Sec. [4.2], one can safely assume that turning on the interaction will neither open a gap, nor have an immediate modification of single-particle spectrum of Eq. [4.3], such that $\epsilon_\lambda(k) = \lambda v_F|k|$, with $\lambda = \pm$ for two flavors of quasiparticles: the positive energy ones with the distribution function $f_+(k,t)$, and the negative energy ones with the distribution function $f_-(k,t)$. However, when it turns to a lattice model, it will be crucial that we take steps to ensure that the interaction does not contain additional terms that might open a gap. We have implicitly assumed that there are no additional conservation laws, as would happen in the special case of integrable models.

From the above, we arrive at the quantum Boltzmann equation with collisions [65, 4, 210]:

$$\left[\frac{\partial}{\partial t} + QE(t)\frac{\partial}{\partial k}\right] f_\lambda(k,t) = -\frac{2\pi}{v_F}\int \frac{dk_1}{2\pi}\frac{dq}{2\pi}\mathcal{R}. \tag{4.18}$$

The integrand $\mathcal{R} = \mathcal{R}_1 + \mathcal{R}_2$, capturing the scattering among excitations, can be divided into two parts. The first part is the scattering among different flavors of excitations (particle-hole to particle-hole) $\mathcal{R}_1 = \delta[(|k| - |k_1|) - (|k+q| - |k_1 - q)]R_1(k,k_1,q)\{f_\lambda(k,t)f_{-\lambda}(k_1,t)[1 - f_\lambda(k+q,t)][1 - f_{-\lambda}(k_1 - q,t)] - [1 - f_\lambda(k,t)][1 - f_{-\lambda}(k_1,t)]f_\lambda(k+q,t)f_{-\lambda}(k_1 - q,t)]\}$, with scattering amplitude $R_1(k,k_1,q) = 4|T_{+--+}(k,k_1,q) - T_{+-+-}(k,k_1,-k-q+k_1)|^2$. The second part captures the scattering among same flavor of excitations (particles to particles or holes to holes), $\mathcal{R}_2 = \delta[(|k| + |k_1|) - (|k+q| + |k_1 - q)|]R_2(k,k_1,q)\{f_\lambda(k,t)f_\lambda(k_1,t)[1 - f_\lambda(k+q,t)][1 - f_\lambda(k_1 - q,t)] - [1 - f_\lambda(k,t)][1 - f_\lambda(k_1,t)]f_\lambda(k+q,t)f_\lambda(k_1 - q,t)]\}$, with $R_2(k,k_1,q) = 2|T_{++++}(k,k_1,q) - T_{++++}(k,k_1,k_1 - k - q)|^2$. Note that we only have two integrals and one delta function on the right hand side of Eq. [4.18], as the conservation of energy and conservation of momentum have the same requirement for linear dispersion in one dimension.

As the interaction is invariant under $\lambda \to -\lambda$, the Eq. [4.15] still holds. With this, we substitute the ansatz Eq. [4.14] into the Eq. [4.18]. As in previous work [65, 4], the solution of $g_\lambda(\epsilon_k,\omega) = \lambda g(k,\omega)$ is the stationary point of the following function $\mathcal{Q}[g]$, (i.e. $\delta Q[g]/\delta[g] = 0$). For simplicity, one can define $\tilde{k} = v_F k/T$. Such that the $\mathcal{Q}[g]$ can be written

as:

$$\begin{aligned}\mathcal{Q}[g] = &\frac{\pi T^2}{4v_F^3}\int \frac{d\tilde{k}}{2\pi}\frac{d\tilde{k}_1}{2\pi}\frac{d\tilde{q}}{2\pi}\frac{\delta(|\tilde{k}|-|\tilde{k}_1|-|\tilde{k}+\tilde{q}|+|\tilde{k}_1-\tilde{q}|)R_1(\tilde{k},\tilde{k}_1,\tilde{q})}{(e^{-|\tilde{k}|}+1)(e^{|\tilde{k}_1|}+1)(e^{|\tilde{k}+\tilde{q}|}+1)(e^{-|\tilde{k}_1-\tilde{q}|}+1)}\\ &\times[\vartheta(\tilde{k})g(\tilde{k},\omega)-\vartheta(\tilde{k}_1)g(\tilde{k}_1,\omega)-\vartheta(\tilde{k}+\tilde{q})g(|\tilde{k}+\tilde{q}|,\omega)+\vartheta(\tilde{k}_1-\tilde{q})g(|\tilde{k}_1-\tilde{q}|,\omega)]^2\\ &+\frac{\pi T^2}{4v_F^3}\int \frac{d\tilde{k}}{2\pi}\frac{d\tilde{k}_1}{2\pi}\frac{d\tilde{q}}{2\pi}\frac{\delta(|\tilde{k}|+|\tilde{k}_1|-|\tilde{k}+\tilde{q}|-|\tilde{k}_1-\tilde{q}|)R_2(\tilde{k},\tilde{k}_1,\tilde{q})}{(e^{-|\tilde{k}|}+1)(e^{-|\tilde{k}_1|}+1)(e^{|\tilde{k}+\tilde{q}|}+1)(e^{+|\tilde{k}_1-\tilde{q}|}+1)}\\ &\times[\vartheta(\tilde{k})g(\tilde{k},\omega)+\vartheta(\tilde{k}_1)g(\tilde{k}_1,\omega)-\vartheta(\tilde{k}+\tilde{q})g(|\tilde{k}+\tilde{q}|,\omega)-\vartheta(\tilde{k}_1-\tilde{q})g(|\tilde{k}_1-\tilde{q}|,\omega)]^2\\ &+\frac{T}{v_F}\int\frac{d\tilde{k}}{2\pi}\frac{g(\tilde{k},\omega)[-i\omega g(\tilde{k},\omega)/2-v_F/T]}{(e^{|\tilde{k}|}+1)(e^{-|\tilde{k}|}+1)}.\end{aligned} \tag{4.19}$$

We seek to understand the integrals in $\mathcal{Q}[g]$. First, in the non-interacting limit $R_1(\tilde{k},\tilde{k}_1,\tilde{q}) = R_2(\tilde{k},\tilde{k}_1,\tilde{q}) = 0$, we note that both the first and the second integral in Eq. [4.19] vanishes. The stationary relation $\delta Q[g]/\delta g = 0$ gives the same solution $g_\lambda(\epsilon_k,\omega)$ as in Eq. [4.16], in accordance with our results for collisionless limit discussed in Sec. [4.3.1]. To relax the current, the collisions (interactions) should be introduced, and the summation of integrals associated with $R_1(\tilde{k},\tilde{k}_1,\tilde{q})$ and $R_2(\tilde{k},\tilde{k}_1,\tilde{q})$ in Eq. [4.19] should be non-zero. By dimension analysis, we have [65] $g(k,\omega) \approx \frac{v_F}{T^2}C(\omega)$ with $C(\omega)$ a dimensionless function. With this, we can pull the $g(k,\omega) \approx v_F C[\omega]/T^2$ functions out from the square brackets, leaving the summation of ϑ functions inside. The conservation of energy (delta function in the integrand) and the structure of the perturbed distribution function (square of the summation of sign functions) put an important constraint on the integral. For the inter-flavor scattering, the integrand $\delta(|\tilde{k}|-|\tilde{k}_1|-|\tilde{k}+\tilde{q}|+|\tilde{k}_1-\tilde{q}|)\times\left[\vartheta(\tilde{k})-\vartheta(\tilde{k}_1)-\vartheta(\tilde{k}+\tilde{q})+\vartheta(\tilde{k}_1-\tilde{q})\right]^2$ only allows a specific type of non-vanishing solution: initial-particle hole pairs moving in the opposite direction ($\tilde{k} = -\tilde{k}_1$) and then bouncing back with respect to each other ($\tilde{k} > 0$, $\tilde{k}_1 < 0$, $\tilde{k}+\tilde{q} < 0$, $\tilde{k}_1-\tilde{q} > 0$, or $\tilde{k} < 0$, $\tilde{k}_1 > 0$, $\tilde{k}+\tilde{q} > 0$, $\tilde{k}_1-\tilde{q} < 0$). Similarly, for the intra-flavor scattering, the integrand $\delta(|\tilde{k}|+|\tilde{k}_1|-|\tilde{k}+\tilde{q}|-|\tilde{k}_1-\tilde{q}|)\times\left[\vartheta(\tilde{k})+\vartheta(\tilde{k}_1)-\vartheta(\tilde{k}+\tilde{q})-\vartheta(\tilde{k}_1-\tilde{q})\right]^2$ does not have a non-vanishing solution; this is in accordance with the fact that the 1D chiral fluid can not be relaxed in the absence of impurities. With everything mentioned above, we can simplify Eq. [4.19] to:

$$\begin{aligned}\mathcal{Q}[C(\omega)] = &\int\frac{d\tilde{k}}{2\pi}\frac{C(\omega)[-i\omega(v_F/T^2)C(\omega)/2-v_F/T]/T}{(e^{|\tilde{k}|}+1)(e^{-|\tilde{k}|}+1)}\\ &+\int\frac{d\tilde{k}}{2\pi}\frac{d\tilde{q}}{2\pi}\frac{2R_1(\tilde{k},-\tilde{k},\tilde{q})C^2(\omega)/(v_F T^2)}{(e^{-|\tilde{k}|}+1)(e^{|\tilde{k}|}+1)(e^{|\tilde{k}+\tilde{q}|}+1)(e^{-|\tilde{k}+\tilde{q}|}+1)}.\end{aligned} \tag{4.20}$$

For a given interaction $V(q)$, one can determine the value of $R_1(\tilde{k},-\tilde{k}_1,\tilde{q})$ based on Eq. [4.6] and Eq. [4.18]. After further performing the integral numerically, the function $\mathcal{Q}[g]$ has the following structure:

$$\mathcal{Q}[C(\omega)] \simeq \frac{v_F}{2T^2}\left[\kappa C^2(\omega) - i\frac{\omega}{T}C^2(\omega) - 2C(\omega)\right], \tag{4.21}$$

where the κ is the numerical result from the the integral associated with $R_1(\tilde{k}, -\tilde{k}_1, \tilde{q})$in Eq. [4.20], depending on the explicit structure of $V(q)$:

$$\kappa = \int \frac{d\tilde{k}}{2\pi}\frac{d\tilde{q}}{2\pi}\frac{4R_1(\tilde{k}, -\tilde{k}, \tilde{q})/v_F^2}{(e^{-|\tilde{k}|}+1)(e^{|\tilde{k}|}+1)(e^{|\tilde{k}+\tilde{q}|}+1)(e^{-|\tilde{k}+\tilde{q}|}+1)}. \tag{4.22}$$

The integrand in Eq. [4.22] is non-negative everywhere. In fact, for usual $V(q)$ and $R_1(\tilde{k}, -\tilde{k}, \tilde{q})$, the integrand is mostly positive on the 2D plane. As a result, the κ, as well as the correction to conductivity due to particle-hole scattering, should be non-zero. From this we can solve the $\delta\mathcal{Q}[g]/\delta g = \delta\mathcal{Q}[C(\omega)]/\delta C(\omega) = 0$ as:

$$C(\omega) = \frac{1}{\kappa - i(\omega/T)}, \quad g_\lambda(k,\omega) = \frac{\lambda v_F}{T^2}\frac{1}{\kappa - i(\omega/T)}. \tag{4.23}$$

Take the Eq. [4.23] back into the Eq. [4.14], we shall get the ansatz in the presence of collision. Substitute the ansatz with collision considered to the current J defined in Eq. [4.9b], by performing similar calculations as Eq. [4.17] in Sec. [4.3.1], we obtain the conductivity in the presence of interactions:

$$\sigma(\omega) = \frac{\langle J\rangle}{E(\omega)} \approx \frac{2Q^2}{h}\frac{\hbar v_F}{-i\hbar\omega + \kappa k_B T}. \tag{4.24}$$

Note that we have restored $\hbar$ and k_B from dimensional analysis. Compared with the low frequency diverging result for the collisionless limit in Eq. [4.17], the conductivity with collisions has some broadening at finite temperature. The conductivity Eq. [4.24] shows that the zero momentum mode can be relaxed solely by the momentum conserved internal scattering process among excitaions, i.e., the FUS. This physical picture is further plotted in Fig. [4.2.(b-c)]. Take the inverse of Eq. [4.24], the resistivity in the DC limit shows the linear-T dependence, i.e., the Planckian dissipation:

$$\rho(\omega \to 0) \sim \frac{\pi\kappa k_B}{Q^2 v_F} T = AT, \tag{4.25}$$

with the coefficient $A = \pi\kappa k_B/Q^2 v_F$. A one-dimensional Dirac system whose linear dispersion survives the interaction can be captured by a single model-dependent parameter, the Fermi velocity v_F. Combined with the temperature T, the only time scale in the continuous limit is the Planckian time $\tau_p = \hbar/k_B T$. Such a time scale gives the scattering rate for particle-hole excitations in an impurity-free Dirac system, and sets up an upper bound for the resistivity at finite temperature $\rho = AT$. The coefficient is $A \propto \kappa \propto R_1/v_F^2 \propto |V(q)/v_F|^2$, which shows that the resistivity is also positively related to the interaction strength in the perturbative region, in accordance with the previous results in wrapping graphene sheet to large-diameter metallic carbon nanotubes [7].

4.4 Lattice model and DMRG simulations

We have shown that a 1D Dirac system with FUS supports linear T-dependent resistivity in Sec. [4.3]. Here, we propose a fermionic lattice model in Sec. [4.4.1], which possesses a low-energy Hamiltonian Eq. [4.4]. We use the Jordan-Wigner transformation to map the fermionic model to a spin model, and then use the density-matrix renormalization group (DMRG) to numerically confirm its gaplessness, at least to leading order in the interaction, and linear resistivity over a range of temperatures in Sec. [4.4.2]. Of course it is difficult to rule out the emergence of a tiny gap by numerical methods, but such a gap would not modify the linear-in-T resistivity except at temperatures comparable to the gap.

4.4.1 Lattice model

We start by considering the following fermionic model defined on the lattice:

$$\begin{aligned}
\tilde{H} &= \tilde{H}_0 + \tilde{H}_2 + \tilde{H}_3 \\
\tilde{H}_0 &= +t\sum_i [-i\xi a_i^\dagger b_i + i\xi b_i^\dagger a_i - ib_i^\dagger a_{i+1} + ia_{i+1}^\dagger b_i] \\
\tilde{H}_2 &= \frac{V_2}{4}\sum_i \left[(a_i^\dagger b_i - b_i^\dagger a_i)(a_{i+1}^\dagger b_{i+1} - b_{i+1}^\dagger a_{i+1}) + (b_i^\dagger a_{i+1} - a_{i+1}^\dagger b_i)(b_{i+1}^\dagger a_{i+2} - a_{i+2}^\dagger b_{i+1})\right] \\
\tilde{H}_3 &= \frac{V_3}{4}\sum_i \left[(a_i^\dagger a_i - b_i^\dagger b_i)(a_{i+1}^\dagger a_{i+1} - b_{i+1}^\dagger b_{i+1}) + (b_i^\dagger b_i - a_{i+1}^\dagger a_{i+1})(b_{i+1}^\dagger b_{i+1} - a_{i+2}^\dagger a_{i+2})\right].
\end{aligned} \tag{4.26}$$

Here, the $\tilde{H}_0$ stands for the free Hamiltonian and $\tilde{H}_2 + \tilde{H}_3$ is the interaction. The form of the interaction is obtained by seeking to construct a Hamiltonian which has FUS as its naive continuum limit, then symmetrizing the Hamiltonian, i.e., ensuring that it does not include a relevant, gap-opening dimerization at least at leading order. The $a_i^\dagger$ and $b_i^\dagger$ denote the creation operators for two distinct degrees of freedom at the same point in i-th unit-cell. When $\xi = 1$, the Bloch Hamiltonian for $\tilde{H}_0$ can be linearized around $k = 0$, and has the Dirac-like structure as given in Eq. [4.1]. The interaction can also be transformed into momentum space. When $V_2 = V_3$, to the leading order the interaction will only contain the FUS given in Eq. [4.5].

The model Eq. [4.26] can also be transformed into a spin model in a finite length lattice with open boundary condition. Upon using the Jordan-Wigner transformation [6]: $S_{i,a}^+ = a_i^\dagger e^{i\pi\sum_{k<i}(a_k^\dagger a_k + b_k^\dagger b_k)}$, $S_{i,b}^+ = b_i^\dagger e^{i\pi\sum_{k<i}(a_k^\dagger a_k + b_k^\dagger b_k) + a_i^\dagger a_i}$, $S_{i,a}^z = a_i^\dagger a_i - 1/2$ and $S_{i,b}^z = b_i^\dagger b_i - 1/2$, we arrive at the following transformation dictionary: $a_i^\dagger b_i - b_i^\dagger a_i = S_{i,a}^+ S_{i,b}^- - S_{i,a}^- S_{i,b}^+$, $b_i^\dagger a_{i+1} - a_{i+1}^\dagger b_i = S_{i,b}^+ S_{i+1,a}^- - S_{i,b}^- S_{i+1,a}^+$. Substituting the above into Eq. [4.26], we obtain the spin model:

$$H^S = H_0^S + H_2^S + H_3^S, \tag{4.27}$$

where each term is given by:

$$H_0^S = -\sum_{i=1}^{N}\left[it\xi\left(S_{i,a}^+S_{i,b}^- - S_{i,a}^-S_{i,b}^+\right) + it\left(S_{i,b}^+S_{i+1,a}^- - S_{i,b}^-S_{i+1,a}^+\right)\right] \tag{4.28a}$$

$$H_2^S = \frac{V_2}{4}\sum_i\Big[(S_{i,a}^+S_{i,b}^- - S_{i,a}^-S_{i,b}^+)(S_{i+1,a}^+S_{i+1,b}^- - S_{i+1,a}^-S_{i+1,b}^+) + (S_{i,b}^+S_{i+1,a}^- - S_{i,b}^-S_{i+1,a}^+)(S_{i+1,b}^+S_{i+2,a}^- - S_{i+1,b}^-S_{i+2,a}^+)\Big] \tag{4.28b}$$

$$H_3^S = \frac{V_3}{4}\sum_i\Big[(S_{i,a}^z - S_{i,b}^z)(S_{i+1,a}^z - S_{i+1,b}^z) + (S_{i+1,a}^z - S_{i,b}^z)(S_{i+2,a}^z - S_{i+1,b}^z)\Big]. \tag{4.28c}$$

We would like to evaluate the gap and see the relaxation of current for $V_2 = V_3 = V$, with $\xi = 1$. We further provide the charge current density operator:

$$j_{i+1} = (+tQ)[b_i^\dagger a_{i+1} + a_{i+1}^\dagger b_i] = (+tQ)[S_i^{+(b)}S_{i+1}^{-(a)} + S_i^{(-)b}S_{i+1}^{+(a)}], \tag{4.29}$$

which with density-density interactions satisfies the standard continuity equation for the local charge density for each unit cell $\rho_n = Q(a_n^\dagger a_n + b_n^\dagger b_n)$:

$$\frac{\partial\rho_i(t)}{\partial t} + (j_{i+1} - j_i) = 0. \tag{4.30}$$

Two aspects of this current operator may deserve a brief remark. The current operator will be slightly modified if we wish to have a local continuity equation for every site, rather than every unit cell, as might be appropriate if the a and b sites are in different spatial locations, but this does not significantly affect the long-wavelength currents relevant for transport, as we have verified numerically in test cases [1]. Second, with the symmetrized interaction we have chosen on the lattice, which is not a pure density-density interaction but rather only part of one, the total charge is clearly still conserved. However, the equation of continuity is modified by some terms beyond the leading order that we are interested in [2]. The DC charge conductivities may be found via the Kubo formula:

$$\sigma = \lim_{t_M\to\infty}\lim_{N\to\infty}\frac{1}{NT}\mathrm{Re}\int_0^{t_M} dt\langle J(t)J(0)\rangle, \tag{4.31}$$

where the total charge current for a system with N unit cells at time t is $J(t) = \sum_{i=1}^N j_i(t)$ [33, 141, 142, 175, 119].

[1] In fact, we can simply define a system with no-internal spatial structure of each unit cell, and view the $a_i^\dagger$ ($b_i^\dagger$) as pseudo spin $c_{\uparrow,i}^\dagger$ ($c_{\downarrow,i}^\dagger$) sits right on the center of i-th unit cell. In the latter case, we only have one site per unit cell, and the operator $\rho_n = Q(a_n^\dagger a_n + b_n^\dagger b_n) = Q(c_{\uparrow,n}^\dagger c_{\uparrow,n} + c_{\downarrow,n}^\dagger c_{\downarrow,n})$ precisely gives the $U(1)$ charge density on each site, as well as the corresponding unit cell.

[2] In the lattice, the full current density that satisfies the continuity equation with local charge density $\rho_j = a_j^\dagger a_j + b_j^\dagger b_j$ would be: $j_j = j_j^0 + j_j'$, with $j_j^0 = tQ(b_{j-1}^\dagger a_j + a_j^\dagger b_{j-1})$ is what we defined above, the higher order additional four-fermion terms $j_j' = (iV_2Q)(b_{j-2}^\dagger a_{j-1}b_{j-1}^\dagger a_j - a_{j-1}^\dagger b_{j-2}a_j^\dagger b_{j-1} - a_{j-1}^\dagger b_{j-2}b_{j-1}^\dagger a_j + b_{j-2}^\dagger a_{j-1}a_j^\dagger b_{j-1})/4 + (iV_2Q)(b_{j-1}^\dagger a_j b_j^\dagger a_{j+1} - a_j^\dagger b_{j-1}a_{j+1}^\dagger b_j + a_j^\dagger b_{j-1}b_j^\dagger a_{j+1} - b_{j-1}^\dagger a_j a_{j+1}^\dagger b_j)/4$ comes from the interaction V_2 which is not in the form of product of density.

4.4.2 t-DMRG results

At first, we confirm that the lattice model Eq. [4.5] is gapless using the density matrix renormalization group [281], which expresses the the wavefunction as a variational matrix-product state [218]. The Hamiltonian contains fairly complicated three-site interaction terms, making it more complicated than typical tight-binding chains. By employing a general technique to represent the Hamiltonian as a matrix-product operator (MPO) [106], we find that it can be achieved with an MPO size of 10×10. In the spin language, the model possesses a U(1) symmetry corresponding to the conservation of the total magnetization $M = \sum_i \langle S_i^z \rangle$ (equivalent to the particle number in the fermionic language), which is exploited in the DMRG algorithm.

The ground state is found in the $M = 0$ sector (or half filling). We can look at the neutral gap $\Delta_0 = E_1(M = 0) - E_0(M = 0)$, as well as at the gaps in various magnetization sectors: $\Delta_{M_0} = E_0(M = M_0) - E_0(M = 0)$ $(M_0 > 0)$, which corresponds to the flipping of M_0 spins (or to the removal of M_0 particles in the fermionic language). Using DMRG, we compute these gaps for system sizes up to $L = 400$. Fig. [4.3] shows a typical result for $V = V_2 = V_3 = 0.4$. We find that all gaps scale linearly with $1/L$, making an extrapolation for $L \to \infty$ very easy. The extrapolated values are very small (of the order of $10^{-4} - 10^{-3}$), consistent with the expectation that the system remains gapless for finite V.

We also calculate a full phase diagram in the $V_2 - V_3$ plane, shown in Fig. 4.4. This gives us an indication of how V_2 and V_3 may be chosen while keeping the system gapless.

To evaluate the conductivity, we proceed using standard techniques [62, 121, 15]: Finite temperatures are implemented by going from a pure state to the density operator. We enlarge the local Hilbert space to include an auxiliary part, which is traced out when performing expectation values. The state at $\beta = 1/T = 0$ is exactly initialized on a finite chain with $L = 96$ and then propagated to the desired β. After that, the state is perturbed by applying the current operator and propagated in real time up, which yields the current correlation function $\langle J(t)J \rangle / L$. We have chosen the system size large enough as not to allow the current to reach the finite system boundaries at the end of the simulation. Since the Hamiltonian contains more than nearest-neighbor interactions, we cannot use a standard time-evolving block decimation algorithm but instead employ the time-dependent variational principle (TDVP) [84]. We use a two-site TDVP algorithm and variationally compress the MPS at each time step.

During the time propagation, the entanglement entropy grows, and we dynamically increase the bond dimension χ of the MPS representation by keeping the truncation error fixed; we have varied this control parameter in order to ensure that our results are converged). The imaginary time evolution is stopped once $\chi = 800$, which allows us to reach temperatures of $1/T = 16$. In order to reach lower T, we continue the cooling using a constant χ, and we have verified that this second truncation parameter does not influence the results (while the truncation error is not fixed during the cooling beyond $1/T = 16$, this regime is not key to our message, and the results should only be viewed as providing additional support). The ensuing real time evolution is stopped once $\chi = 1600$ is reached, since any further propaga-

tion becomes prohibitively slow. We employ further standard optimizations that allow us to maximize the use of numerical resources [123]: (i) Counterpropagating the auxiliary space limits the growth of entanglement; (ii) Splitting up the propagation into a forward and a backward one increases the achievable $t_{\max}$. In the forward propagation, we can (iii) exploit the approximate translational invariance in the middle of the chain (reducing the perturbation to the local term Eq. [4.29]), as well as (iv) the spinflip symmetry of the current operator.

For small $V = V_2 = V_3$, the entanglement buildup is relatively small, but we are also very close to the integrable point $V = 0$, resulting in very long relaxation times; and vice versa for large V. Faced with these trade-offs, we find that we need to go to $V = 3$ to be able to evaluate the current correlations. The results are shown in Fig. 4.5. It turns out that we still cannot reach time scales which are long enough to quantitatively compute the integral in Eq. (4.31), we observe that below $T = 1/8 \sim 1/10$, the different curves essentially collapse onto one curve for the times we are able to access. Assuming that this collapse will continue to hold for the inaccessible times as well, this means that the integral over $\langle J(t)J\rangle/L$ becomes independent of T in this regime. Due to the prefactor of $1/T$ in Eq. (4.31), this points towards a resistivity which is indeed proportional to T in the low-temperature regime.

4.5 Discussion and outlook

While the possibility of metals with linear-in-T resistivity has been an actively discussed topic for many years, there are relatively few concrete models verified to possess this property, especially if one requires the interactions to be local and non-random. The main results here start from developing a low-energy model for a 1D Dirac fermionic system in which particle-hole Umklapp-like scattering is the dominant process. By using the standard bosonization theory, we showed that this interaction is irrelevant and will not modify the band structure to the leading order. We used kinetic equations to study the transport properties for a fermionic model with Dirac-like dispersion, which coincides with the well-known results for 1D two-channel ballistic transport. We further calculated the conductivity in the presence of the scattering, and show the broadening from collision of quasi-particles in finite temperature.

In the low frequency limit, the resistivity linearly depends on temperature, the feature known as Planckian dissipation. We further provided a lattice realization with the Dirac model as its low-energy limit. By using the Jordan-Wigner transformation, we transformed the lattice model to a spin model. We were able to solve it for system sizes up to $L = 400$ in the static case and up to $L = 96$ in the dynamic case with finite temperature, by using the density-matrix renormalization group (DMRG). The results of the simulations are consistent with the predictions of the field theory. The scaling regime in this Dirac-like 1D fermionic model could be relevant in single-walled carbon nanotubes or cold atomic systems [7, 292], providing a route if the interactions are strong to the experimental observation of Planckian dissipation in 1D systems. The FUS may also be viewed as a intrinsic current relaxation mechanism for the edge of a clean quantum spin Hall insulator [137].

Verifying transport similar to that proposed for the 2D Dirac liquid in a 1D model provides an alternative point of view on the origin of bad metallic behavior, distinct from scenarios involving quantum criticality. While one could view the Fermi gas as a point in the phase diagram, rather than a phase as in higher dimensions, observables generally evolve continuously into the Luttinger liquid, unlike moving from a quantum critical point into a neighboring phase. Observing the dominance of Umklapp-like scattering in this model complements other possibilities for transport theory in one dimension dominated by other irrelevant operators [206].

One direction for future work comes from isolating the relaxation time from other pieces of the conductivity to see whether there is a crossover with temperature in the source of the linear-in-temperature behavior. This would allow comparison to such a crossover in conductivity of doped Hubbard models observed in recent work using quantum Monte Carlo continued to real time.[101] This would also allow direct comparison of the current relaxation time at strong interactions to the Planckian scale $\hbar/k_BT$. Of course underlying physics in that study is almost certainly different, and our model is less directly relevant to the linear resistivity of high-T_c superconductors.

Although we have focused in this work on the case where the system remaining gapless after turning on the interaction, one can generalize our treatment for the collision-dominated regime to gapped phases so long as the Landau Fermi-liquid quasi-particle description is still valid. The seemingly complicated model Eq. [4.26] provides a route to realizing the conjectured Planckian upper bound to the resistivity for a class of interacting semimetals in 1D. More generally, the analytical and numerical methods available to explore transport in low spatial dimensions make it feasible to search for evidence of other physics originally proposed for higher dimensions, as we have done here for the Dirac fluid.

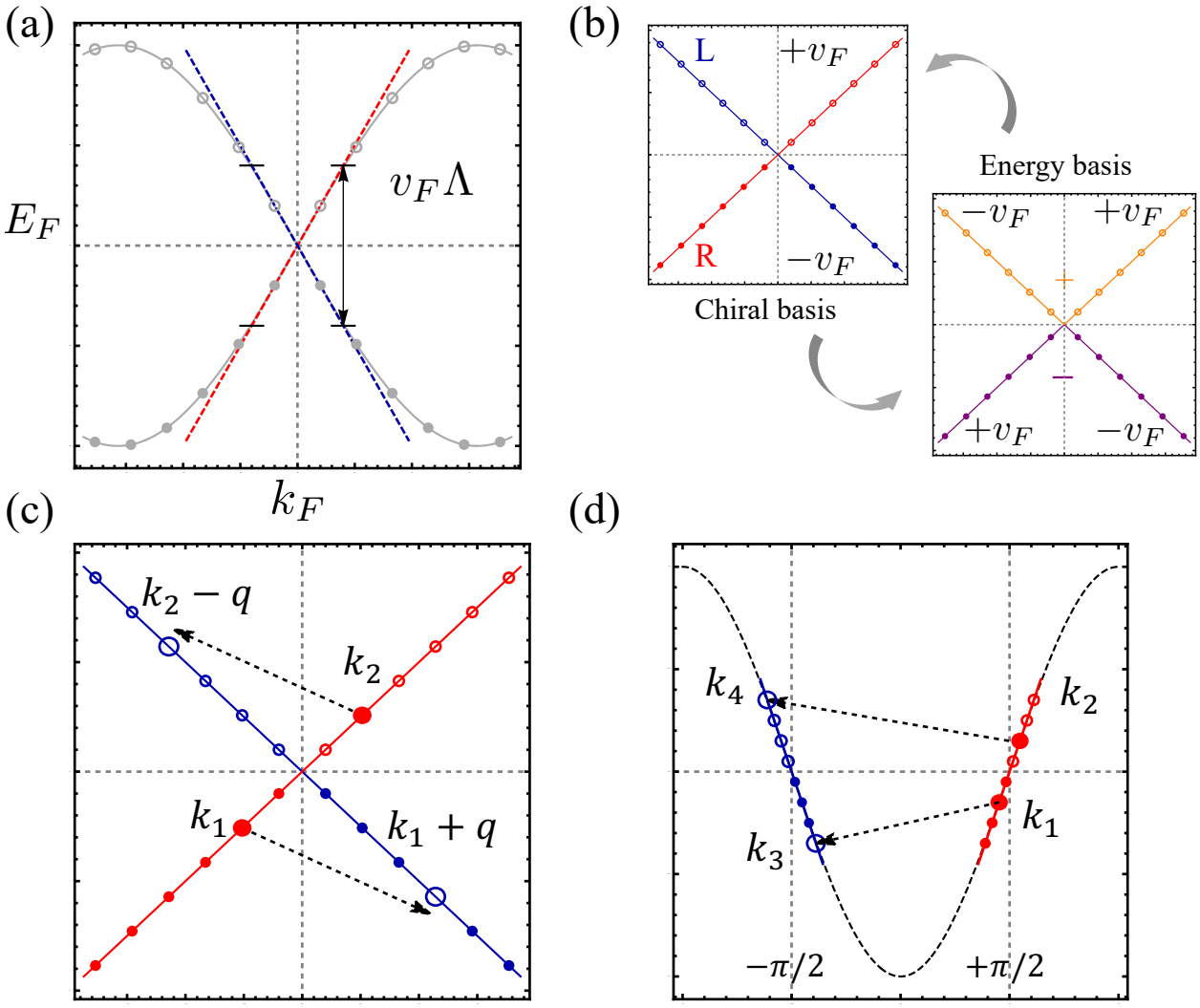

Figure 4.1: Fermionic spectrum linearization and scattering processes based on it. (a) A 1D non-interacting metallic band can be linearized close to the Fermi level E_F within the energy cutoff $v_F\Lambda$. (b) The linearized spectrum can be described by the chiral basis, with the red modes moving to the right with velocity $+v_F$ and blue modes moving to the left with velocity $-v_F$ in real space. The 1D-Dirac crossing can be viewed as the edge states of a quantum spin Hall insulator [137]. The linearized spectrum can also be written in the energy basis, where states are labeled by positive (orange) and negative (purple) energies. The velocities for different quasi-particles are also shown in the figure. (c) Illustration for particle-hole scattering or fast Umklapp-like scattering (FUS). Two right movers with momentum k_1 and k_2 are scattered to the left moving branch with momentum $k_1 + q$ and $k_2 - q$. Note that the total momentum is conserved in this process. (d) Conventional Umklapp scattering in 1D metal for two right movers (k_1, k_2) scattering into two left movers (k_3, k_4). Note that for conventional Umklapp scattering, the Fermi points for the right and left movers are different (say at $\pm\pi/2$.). The momentum is conserved only up to a reciprocal vector $G = 2\pi$, i.e., there is a large momentum transfer in the scattering process.

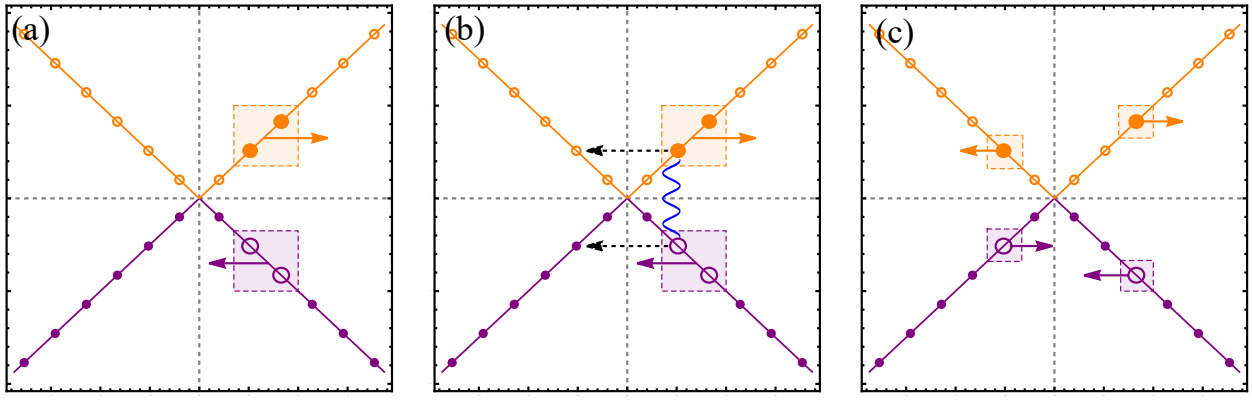

Figure 4.2: Generation and relaxation of charge current in a particle-hole symmetric system. Note that, the linear dispersion with an X-type Dirac crossing can be viewed as the edge states of a quantum spin Hall insulator [137]. (a) Generation of the zero momentum mode under external electric field. The net charge current for the states in the plot is $J = 4Qv_F$. (b) Collision between the particle and hole via the interaction (waved line) based on the initial state shown in (a). (c) Final state after scattering process in (b), which has zero momentum and zero charge current.

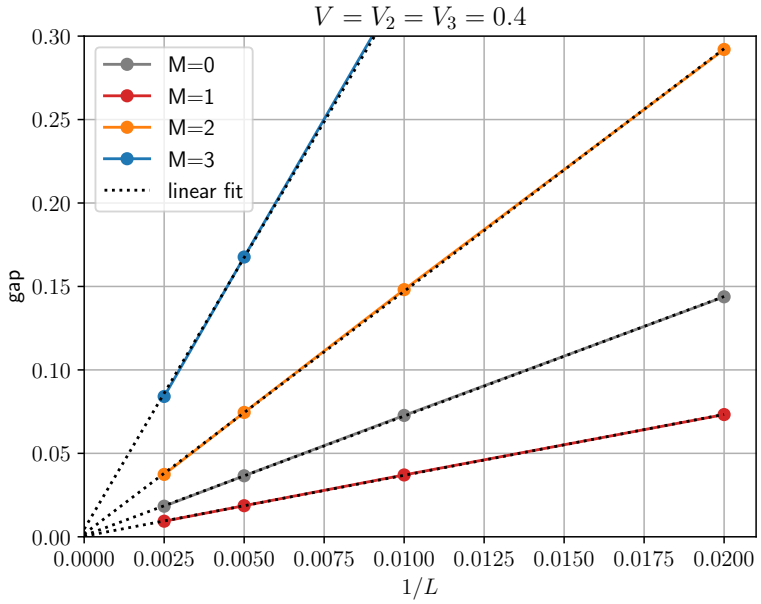

Figure 4.3: Excitation gaps in various sectors of the total magnetization M of model Eq. [4.5] for $V_2 = V_3 = 0.4$ as a function of the inverse chain length $1/L$, calculated using DMRG with open boundary conditions.

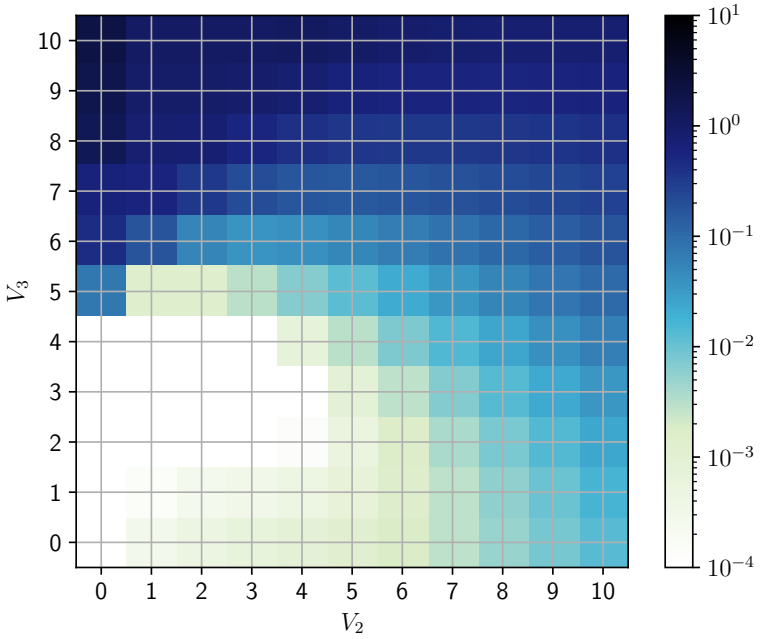

Figure 4.4: Phase diagram of the excitation gap of model Eq. [4.5] as a function of V_2 and V_3. For each point, the $M = 1$ gap is interpolated in the system size for $L = 100, 200, 400$.

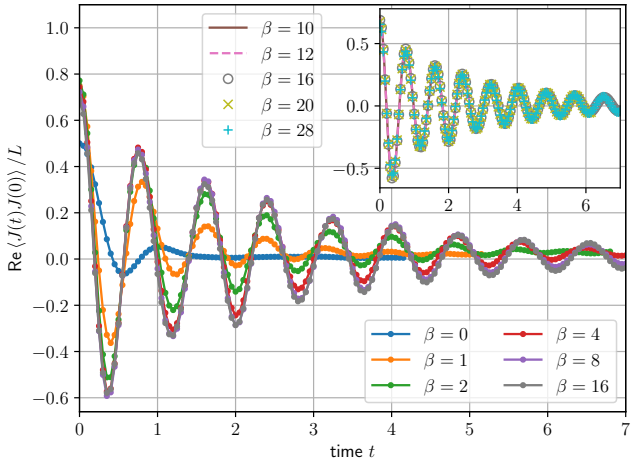

Figure 4.5: Time-dependent current-current correlation function at $V_2 = V_3 = 3$ calculated using DMRG.

Chapter 5

Edge networks induced by bulk topology

In this chapter, we introduce an effective edge network theory to characterize the boundary topology of coupled edge states generated from various types of topological insulators. Two examples studied are a two-dimensional second-order topological insulator and three-dimensional topological fullerenes, which involve multi-leg junctions. As a consequence of bulk-edge correspondence, these edge networks can faithfully predict properties such as the energy and fractional charge related to the bound states (edge solitons) in the aforementioned systems, including several aspects that were previously complicated or obscure.

5.1 Introduction

A central feature of topological insulators (TI) is the bulk-edge correspondence: a d-dimensional TI with given symmetries has a bulk energy gap but symmetry protected gapless $d-1$ dimensional boundary excitations [117, 68, 181, 67, 202, 90, 182]. Recent studies on higher-order TIs generalized this bulk-edge correspondence. An n-th order TI has protected gapless modes of co-dimension n [18, 17, 149, 60, 216, 234, 126, 124, 61, 230, 70, 254]. A two-dimensional (2d) second order topological insulator (2d SOTI), for instance, is an insulator with gapped edge but gapless corners [18, 17, 149, 60], i.e., there are localized in-gap states at corners under open boundary conditions. The higher order TIs can be derived from gapping out boundary Hamiltonian [149, 126, 124, 61]. More specifically, to obtain a 2d SOTI, one can gap out a single helical edge state [18, 17, 149], or alternately a pair of coupled counter-propagating helical edge states [149, 301, 289]. The point of this paper is to develop an effective theory to describe coupled edge states more generally and their dependence on the topology of the system boundary, which allows a description of the domain-wall states that remain at the intersection of edges for various types of edge junctions.

Meanwhile, one can think of the connected problem of higher order TIs. If we put an ordinary 2d TI on a closed surface of some 3d manifold, is it possible to have gapped

2d faces and 1d edges, but gapless 0d corner modes? Topological fullerenes [208] are an example of this kind of system. They are polyhedral surfaces wrapped by the Haldane honeycomb lattice model [85], leaving wedge disclination defects at the vertices [209, 208]. While these fullerenes do not currently exist in nature, very recent experiments indicate that twisted bilayer graphene at small twist angle supports a network of domain walls with threefold junctions ("Y-junctions") [102, 286, 240]. These domain walls [113] are not strictly topologically protected but conductance is expected to be high at the length scales of this network. If the planar system has non-vanishing Chern number, these topological fullerenes have gapped bulk and hinge states (here a "hinge state" is localized at the intersection of two 2d surfaces), but characteristic corner-localized in-gap states. These corner states can be related to the existence of nontrivial defect states bound to isolated wedge disclinations [247, 78, 19]. The connection between the fullerene problem and the 2d SOTI can be viewed as follows: the classification of 2d SOTI is derived from that of TIs in 1d, which is identical to the classification of co-dimension 2 topological defects [248, 49, 149, 231]. This implies that the topological fullerenes and certain classes of 2d SOTI should be describable in the same framework. The emergence of states bound to defects (such as disclination or dislocation) has previously been explained in several cases by edge soliton theory, i.e., the effective theory for a pair of coupled counter-propagating helical edge states [153, 200, 204, 209, 131]. Although this theory is able to predict the fractional charge bound to the (edge) soliton [237, 75, 111] in those examples, one needs to extend the approach in order to incorporate crystalline symmetries in more complicated systems and obtain faithful bound state energies. (Note that in a system of noninteracting fermions, fractional charge should be thought of as an offset or displacement of the charge density, rather than as a property of elementary excitations.)

In this article, we propose a generic edge network theory to capture the boundary topology of coupled edge states. As a consequence of the bulk-edge correspondence, the edge states carry the necessary information of their topological insulator parents. By assigning proper boundary conditions on edge states at their vertices, the edge networks correctly predict the existence of bound states (edge solitons) and other information. We further considered edge states living on the hinges of varies 3d manifolds, where the edge states are generated from topological insulators attached on corresponding surfaces. Such edge networks can faithfully predict the energy and fractional charge of bound states located at the vertices, going beyond previous edge soliton theories. These edge networks are shown here to capture the key properties of topological fullerenes as well as some 2d SOTIs, and it is hoped that they will be useful for other problems as well.

The rest of the chapter is organized as follows: In Sec. 5.2, we briefly review basic facts and notation for an edge network made from multiple pairs of coupled helical edge states. In Sec. 5.3, we discuss the minimal edge network constrained to lie on a closed 1d loop, and show the existence of bound state with fractional charge in the presence of certain symmetries. Based on this we further propose *a 2d SOTI* that can be easily realized with atoms in an optical lattice. In Sec. 5.4, we consider edge networks with a multi-leg vertex. We first derive the bound state energy and charge for a Y-junction via a scattering matrix approach in Sec. 5.4.1. Then, in Sec. 5.4.2, we apply the results in Sec. 5.4.1 to the

tetrahedral topological fullerene as an example. Starting from edge networks, we *connect* the tetrahedral topological fullerene to the 2d SOTI we proposed. We summarize the main results in Sec. 5.5 with an eye toward future developments and applications of this picture.

5.2 Description of edge network

We start with several pairs of coupled helical edge states, e.g., living on the hinges of the 3d manifold shown in Fig.[5.1.(a)]. The network is described by the effective Hamiltonian:

$$H_{\text{edge}} = \sum_i \int dx_i \Psi^\dagger(x_i)(-iv_i\partial_{x_i}\sigma_z + \mathcal{M}_i(\theta_i))\Psi(x_i). \tag{5.1}$$

Here, i labels the hinges, and x_i is the coordinate set along a specific hinge. The two component wave-function $\Psi(x_i) = (\psi_\alpha(x_i), \psi_\beta(x_i))^T$ denotes a pair of coupled counter-propagating helical edge states living on i-th hinge, and varies smoothly on the scale of the lattice constant. The magnitude of edge velocity v is set identical for all edge states, and their directions should be compatible with the positive direction of x_i. The mass term $\mathcal{M}_i(\theta_i) = m\cos\theta_i\sigma_x + m\sin\theta_i\sigma_y$ describes the coupling on hinge x_i, where $\sigma_{x,y,z}$ are Pauli matrixes. Without loss of generality, we assume that $m \geq 0$ and $0 \leq \theta_i \leq 2\pi$. If $m = 0$, the helical edge states are decoupled and their energy spectrum is gapless. A non-zero mass term can locally gap out a pair of edge states, which is the situation that we are interested in.

To the Hamiltonian we need to add proper boundary conditions for these edge states at vertices where two or more edges come together. The boundary condition describe the scattering process at the junction. By doing so we can solve Eq.[5.1] and predict the existence of localized edge solitons that lie in the (bulk and edge) gaps, as well as their properties.

Before discussing edge network on specific configuration, we point out that the Hamiltonian Eq.[5.1] may be generalized into the case of Helical Luttinger liquid [285, 288, 96, 71]:

$$\tilde{H}_{\text{edge}} = \sum_i (H_0^i + H_{\text{int}}^i). \tag{5.2}$$

The noninteracting Hamiltonian H_0^i on each hinge can be divided into two parts: the linearized free Dirac field $H_{0,1}^i$ and their coupling ($H_{0,2}^i$) with two real-valued classical scalar field $\lambda_{1,2}(x_i)$ [35]:

$$\begin{aligned} H_{0,1}^i &= -v\int dx_i(\psi_{\alpha,i}^\dagger i\partial_{x_i}\psi_{\alpha,i} - \psi_{\beta,i}^\dagger i\partial_{x_i}\psi_{\beta,i}), \\ H_{0,2}^i &= \int dx_i(\lambda_{1,i}\psi_{\alpha,i}^\dagger\psi_{\beta,i} + i\lambda_{2,i}\psi_{\beta,i}^\dagger\psi_{\alpha,i} + \text{H.c.}). \end{aligned} \tag{5.3}$$

Here $\psi_{\alpha(\beta),i}$ ($\lambda_{1(2),i}$) is short for $\psi_{\alpha(\beta)}(x_i)$ ($\lambda_{1,2}(x_i)$). Compared with $\mathcal{M}_i(\theta_i)$ in Hamiltonian Eq.[5.1], we find that $\lambda_{1,i} = m\cos\theta_i$ and $\lambda_{2,i} = m\sin\theta_i$. For helical Luttinger liquid, we only

need to consider the forward scattering $H^i_{\text{int},2}$ and chiral interaction $H^i_{\text{int},4}$ [285, 288, 96, 71]:

$$\begin{aligned} H^i_{\text{int},2} &= g_{2,i}\int dx_i(\psi^\dagger_{\alpha,i}\psi_{\alpha,i}\psi^\dagger_{\beta,i}\psi_{\beta,i}), \\ H^i_{\text{int},4} &= \frac{g_{4,i}}{2}\int dx_i(\psi^\dagger_{\alpha,i}\psi_{\alpha,i}\psi^\dagger_{\alpha,i}\psi_{\alpha,i}+\psi^\dagger_{\beta,i}\psi_{\beta,i}\psi^\dagger_{\beta,i}\psi_{\beta,i}), \end{aligned} \tag{5.4}$$

where $g_{2,i}$ and $g_{4,i}$ are interacting constants. One can conduct the standard bosonization procedure for Hamiltonian Eq.[5.2] by defining bosonic field $\partial_{x_i}\tilde{\varphi}_i = -\pi[\rho_\alpha(x_i)+\rho_\beta(x_i)]$ and $\partial_{x_i}\tilde{\theta}_i = \pi[\rho_\alpha(x_i)-\rho_\beta(x_i)]$, where $\rho_{\alpha(\beta)}(x_i)$ stands for the density for counter-propagating edge states, i.e. $\rho_{\alpha(\beta)}(x_i) = \psi^\dagger_{\alpha(\beta),i}\psi_{\alpha(\beta),i}$. The $\tilde{\theta}_i$ here should be distinguished from θ_i in effective mass $\mathcal{M}$. The Bosonized Hamiltonian for each hinge, $H^i_B = H^i_{B,0}+H^i_{B,1}$ reads:

$$\begin{aligned} H^i_{B,0} &= \frac{1}{2\pi}\int dx_i[uK(\partial_{x_i}\tilde{\theta}_i)^2+\frac{u}{K}(\partial_x\tilde{\varphi}_i)^2], \\ H^i_{B,1} &= \frac{1}{2\pi a}\int dx_i m\cos(\tilde{\varphi}_i-\theta_i). \end{aligned} \tag{5.5}$$

Here, $u \equiv v\sqrt{(1+g_4/2)^2-(g_2/2)^2}$ is the velocity, $K = \sqrt{(1+g_4/2-g_2/2)/(1+g_4/2+g_2/2)}$ is the Luttinger parameter, and a is the lattice constant whose inverse stands for the momentum cut off of vacuum [71, 35, 224]. The Hamiltonian H^i_B is also interacting, and the interaction $H^i_{B,1}$ can be minimized by set $\tilde{\varphi}(x_i) = \theta(x_i)+\pi$. Referring to the bonsonized conserved current $j^\mu_i = \epsilon^{\mu\nu}\partial_\nu\tilde{\varphi}(x_i)/2\pi \approx \epsilon^{\mu\nu}\partial_\nu\theta(x_i)/2\pi$, for the simplest two terminal junction with two legs $x_{1,2}$ (see in Fig.[5.1.(b)]), the topological charge $\hat{Q}$ is given by [35, 66]:

$$\hat{Q} \equiv \int dx j_\mu(x) \propto \frac{\epsilon^{01}}{2\pi}[\theta(x_2=+\infty)-\theta(x_1=-\infty)]. \tag{5.6}$$

A mass kink of $\mathcal{M}_i(\theta_i)$ implies nonzero topological charge $\hat{Q}$, see in Fig.[5.1.(b)]. This is in accordance with the soliton charge N_s derived from non-interacting Fermionic theory [237, 75, 111], see also Eq.[5.7] in later on Sec. 5.3. For simplicity, in the rest of our article we will focus on the non-interacting model Eq.[5.1]. It is reasonable to believe that the value of soliton charge remains unchanged when turning on interaction because it can be calculated from properties away from the junction. However, the response of bound state energy with respect to external flux may be modified by interaction, and may need a deeper description, e.g., by boundary conformal field theory [193, 97].

5.3 Edge states on closed 1d loop

We first consider the minimal example of an edge network, a pair of helical edge states living on the boundary of a closed 1d loop, as shown in Fig.[5.1.(c)]. The point is to determine how symmetries fix the free coefficients introduced in the previous discussion. The basis is

chosen as $\Psi(x_i) = (\psi_\alpha(x_i), \psi_\beta(x_i))^T$, where $\psi_\alpha(x_i)$ ($\psi_\beta(x_i)$) denotes the chiral edge states propagating in the clockwise (anti-clockwise) direction. We set four coordinates $x_{i=1,2,3,4} \geq 0$, and define $x_5 = x_1$. The coupling for edge states on each leg is given by an effective mass $\mathcal{M}_i(\theta_i)$, where we have set $v = m = 1$ for simplicity. We use a set of trial wave functions $\Phi(x_i)_{o(e)} = \frac{1}{\sqrt{N_{o(e)}}} \exp(-|(x_i - x_i^{o(e)}) \sin\varphi|)\chi(x_i)_{o(e)}$ to look for bound states localized the origin (o) and end (e) of i-th edge, with $\chi(x_i)_{o(e)} = (a_i^{o(e)}, b_i^{o(e)})^T$. Here $a_{o(e)}, b_{o(e)}$, φ and normalization constant $1/\sqrt{N_\pm}$ are coefficients to be determined.

Substituting the trial wave function $\Phi(x_i)_{o(e)}$ into Eq.[5.1] for each individual edge, we find modes localized at two ends of i-th edge. For the states at the origin of i-th edge, we have the wave function $\chi(x_i)_o = e^{i\delta_i^o}(e^{i(\varphi-\theta_i)}, 1)^T$ with energy $\epsilon_i^o = \cos\varphi$. For the states at the end, we have $\chi(x_i)_e = e^{i\delta_i^e}(e^{-i(\varphi+\theta_i)}, 1)^T$ with energy $\epsilon_i^e = \cos\varphi$. Here, $\delta_i^{o,e}$ are overall phase factors. The wave-function we solved previously should satisfy the boundary condition at the corner, i.e., $\Phi(x_{i+1} \to x_{i+1}^o)_o = \Phi(x_i \to x_i^e)_e$ and $\epsilon_{i+1}^o = \epsilon_i^e$. If $\theta_i = \theta_{i+1}$, the only allowed solution is $\varphi = 0$, which means that the localization length $\xi = 1/|\sin\varphi| \to \infty$ and no bound state exists. If $\theta_i \neq \theta_{i+1}$, we have a mass kink at the intersection of i-th and $i+1$-th edge. The solution corresponds to an un-paired edge soliton [153] localized at the intersection, with energy and fractional fermion number [237, 75, 111] given by:

$$\varphi = |\theta_{i+1} - \theta_i|/2,\ E = \mathrm{sgn}(\theta_{i+1} - \theta_i)\cos\varphi,\ N_s = -\frac{\varphi}{\pi}. \tag{5.7}$$

Since we measure the charge with respect to the vacuum, there is a minus sign for the soliton charge N_s. Eq.[5.7] predicts the existence of a domain wall state for any two adjoint edges. More specifically, the edge soliton derived from the aforementioned effective theory can be used to explain fractional charge in varies systems, such as the bound states induced by magnetic domain wall in the quantum spin hall effect [200], or the localized state bound to 2d disclination (dislocation) defect in topological insulators [209, 204].

The minimal edge network can explain the corner states in at least some kinds of 2d SOTI. The 2d SOTIs have gapped bulk and edges, but gapless corners. They can be derived from gapping out topological edge states. Heuristically, one potential way to get a 2d SOTI is by stacking 1d TIs, making the 0d boundaries of these 1d TIs form another set of 1d TIs in the perpendicular direction. This is one way to obtain the quadrupole insulator [18, 17]. Alternatively, one can couple a pair of (or more) counter-propagating helical edge states living on the boundary of 2d TI and gap them out. Here we will use the latter picture extensively. Crystalline symmetries [183, 226, 228, 227] with unitary symmetry operator U, such as reflection [149], inversion[124] and rotation symmetry [234, 61, 126], can constrain the distribution of effective mass term $\mathcal{M}_i(\theta_i)$ on the boundary. On the edges compatible with crystalline symmetry, $[\mathcal{M}_i(\theta_i), U] = 0$. If two adjoint edges are related by crystalline symmetry with operator U, then $U^\dagger \mathcal{M}_i(\theta_i) U = \mathcal{M}_{i+1}(\theta_{i+1})$. If $\mathcal{M}_i(\theta_i) \neq \mathcal{M}_{i+1}(\theta_{i+1})$, a domain wall state emerges at the intersection of two adjoining edges, as demonstrated before.

Distinct from corner-localized zero modes in a 2d second-order topological superconductor [149, 301], we find that, in the absence of particle-hole symmetry and chiral symmetry [149, 226, 150, 253], one can have corner states with non-zero energy. The system we

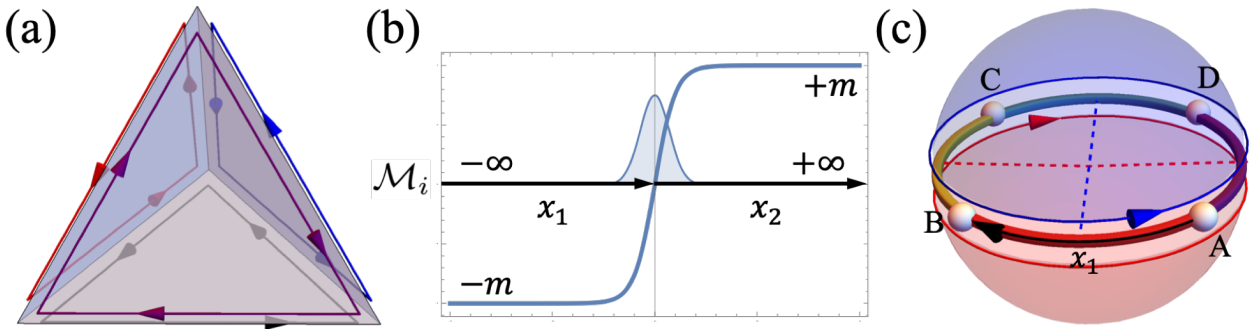

Figure 5.1: (a) An edge network living on the hinges of a tetrahedron. (b) A mass kink and corresponding soliton in two terminal junction. (c) The minimal edge network. A pair of coupled counter-propagating helical edge states are represented by the blue and red arrows, which can be generated from two Chern insulators with opposite Chern number (see the blue and red hemisphere). The four axes $x_{1,2,3,4}$ are set along the loop in anti clockwise direction, with origins at A, B, C, D, respectively. For simplicity we only plot x_1. The red and blue dashed lines stand for two reflection-symmetric axes.

consider has two reflection-symmetric axes, as shown in Fig.[5.1.(c)]. The reflection operator for the red axis is $U_b = \sigma_x$, while the reflection operator for the blue axis is $U_r = \sigma_y$. Edge $AB(x_1)$ and $CD(x_3)$ are reflection symmetric edges for U_b, thus the only symmetry-allowed mass term is $\pm\sigma_x$. Similarly edge $AD(x_4)$ and $BC(x_2)$ are reflection symmetric edges for U_r, thus the only symmetry-allowed mass term is $\pm\sigma_y$. In summary, the effective mass terms on four edges $x_{1,2,3,4}$ are:

$$\begin{aligned} \mathcal{M}_1(0) &= +\sigma_x, \quad \mathcal{M}_2(\frac{\pi}{2}) = +\sigma_y, \\ \mathcal{M}_3(\pi) &= -\sigma_x, \quad \mathcal{M}_4(\frac{3\pi}{2}) = -\sigma_y. \end{aligned} \tag{5.8}$$

Referring to Eq.[5.7], we find $\varphi = \pi/4$, $E = \cos\varphi = 1/\sqrt{2}$, and $N_s = -1/4$ for each corner, corresponding to four edge solitons on the loop.

SOTIs have been claimed to be appear in various systems [223, 194, 108], including bismuth [217]. Based on recent progress of two-dimensional spin-orbit coupling in cold atom system [161, 287], we provide a feasible experimental proposal of 2d SOTI with edge mass distribution as Eq.[5.8]. By stacking two Chern insulator layers with opposite Chern numbers (which can be easily realized in experiments by adding a magnetic field with gradient), the

2d tight-binding Hamiltonian for our model is:

$$\begin{aligned}H =&-\sum_{\langle\vec{i},\vec{j}\rangle_s} t_\alpha(\hat{c}^\dagger_{\vec{i}\uparrow s}\hat{c}_{\vec{j}\uparrow s}-\hat{c}^\dagger_{\vec{i}\downarrow s}\hat{c}_{\vec{j}\downarrow s})+\sum_{\langle\vec{i}\rangle_s} m_z^s(\hat{n}_{\vec{i}\uparrow s}-\hat{n}_{\vec{i}\downarrow s})\\&+\sum_{\langle\vec{i}\rangle}(+\lambda_1\hat{c}^\dagger_{\vec{i},\uparrow,+}\hat{c}_{\vec{i},\downarrow,-}+\lambda_1\hat{c}^\dagger_{\vec{i},\downarrow,+}c_{\vec{i},\uparrow,-}+\text{H.c.})+\sum_{\langle\vec{i}\rangle}(-\lambda_2\hat{c}^\dagger_{\vec{i},\uparrow,+}\hat{c}_{\vec{i},\downarrow,-}+\lambda_2\hat{c}^\dagger_{\vec{i},\downarrow,+}c_{\vec{i},\uparrow,-}+\text{H.c.})\\&+\big[\sum_{\langle j_x\rangle_s}\big(it_{\text{so}}(\hat{c}^\dagger_{j_x\uparrow}\hat{c}_{j_x+1\downarrow}-\hat{c}^\dagger_{j_x\uparrow}\hat{c}_{j_x-1\downarrow})+\text{H.c.}\big)\big]+\big[\sum_{\langle j_y\rangle_s} t_{\text{so}}(\hat{c}^\dagger_{j_y\uparrow}\hat{c}_{j_y+1\downarrow}-\hat{c}^\dagger_{j_y\uparrow}\hat{c}_{j_y-1\downarrow})+\text{H.c.}\big].\end{aligned}$$

Here, $s=\pm$ stands for layer index. The positive $t_{\alpha=x,y}$ and t_{so} denotes, respectively, the inner-layer spin conserved and spin-flip hopping. The m_z^s represents an effective Zeeman term, with $m_z^+=m_z$ and $m_z^-=-m_z$, which can be realized by a magnetic field with gradient. The spin-flip hopping t_{so} and $\lambda_{1,2}$ comes from the spin-orbit coupling induced by effective inner-layer and inter-layer Raman coupling, respectively. Transforming H into the momentum space yields $H=\sum_{\boldsymbol{k},\sigma,\sigma'}\hat{c}^\dagger_{\boldsymbol{k},\sigma}\mathcal{H}_{\sigma,\sigma'}(\boldsymbol{k})\hat{c}_{\boldsymbol{k},\sigma'}$, with

$$\begin{aligned}\mathcal{H}(\boldsymbol{k})=&2t_{so}\sin(k_x)\tau_1+2t_{so}\sin(k_y)\tau_2+(m_z-2t_x\cos k_x-2t_y\cos k_y)\tau_3\sigma_3+\lambda_1\tau_1\sigma_1+\lambda_2\tau_2\sigma_2,\end{aligned}\tag{5.9}$$

where $\boldsymbol{\tau}$ and $\boldsymbol{\sigma}$ are Pauli matrices in spin space and layer space, respectively. If $\lambda_1=\lambda_2=\lambda=0$, the Hamiltonian Eq.[5.9] has particle-hole symmetry $\mathcal{P}=\tau_1\sigma_3\mathcal{K}$, time-reversal symmetry $\mathcal{T}=\tau_2\sigma_2\mathcal{K}$, and chiral symmetry $\mathcal{S}=\tau_3\sigma_1$, where $\mathcal{K}$ stands for complex conjugate. With $|m_z|<2t_x+2t_y$, the system can be viewed as a robust index spin hall effect [299]. Aside from aforementioned non-spatial symmetries, one can also define the spatial symmetry operator $\hat{U}^{\eta_\mathcal{T}\eta_\mathcal{P}}$. Here $\eta_{\mathcal{T},\mathcal{P}}=+(-)$ denotes, respectively, that $\hat{U}$ commutes (anti-commutes) with time reversal or particle-hole symmetry operator. When $\lambda_1\neq 0$, but $\lambda_2=0$, Eq.[5.9] respects two reflection symmetries $\hat{U}_x^{++}=\tau_2\sigma_2$, $\hat{U}_y^{+-}=\tau_1\sigma_1$. The bulk can be viewed as a topological crystalline insulator in two copies of $\text{BDI}^{\hat{U}_x^{++}}$ class, each of them has a $\mathbb{Z}$ classification [183, 226, 49]. Locally breaking the reflection symmetry on reflection symmetric edge can gap out the helical edge states by a unique mass term, which is odd under reflection and leads to the presence of corner localized zero modes [70]. We further confirm the presence of zero modes both numerically and analytically in appendix. Thus when $\lambda_2=0$, Eq.[5.9] stands for a 2d SOTI with an extrinsic $\mathbb{Z}^2$ and intrinsic $\mathbb{Z}$ classification [70, 254]. In realistic cold atom experiments, the detection of the fractional charge at the corner can be conducted by conventional single site resolution. By turning on an s-wave onsite interaction for atoms [161], this model becomes a 2d second order topological superfluid.

A small but non-zero λ_2 breaks the chiral and particle hole symmetry, and gaps out the helical edge states from the original index spin hall effect. *In this case Eq.[5.9] is no-longer a well defined 2d SOTI.* For simplicity we assume that $\lambda_1=\lambda_2=\lambda$ in following text. By projecting the low energy Hamiltonian of Eq.[5.9] into the helical edge states derived from $\lambda=0$, one can get the effective edge Hamiltonian identical to Eq.[5.8], leading to the similar set of gapped edges and gapless corners.

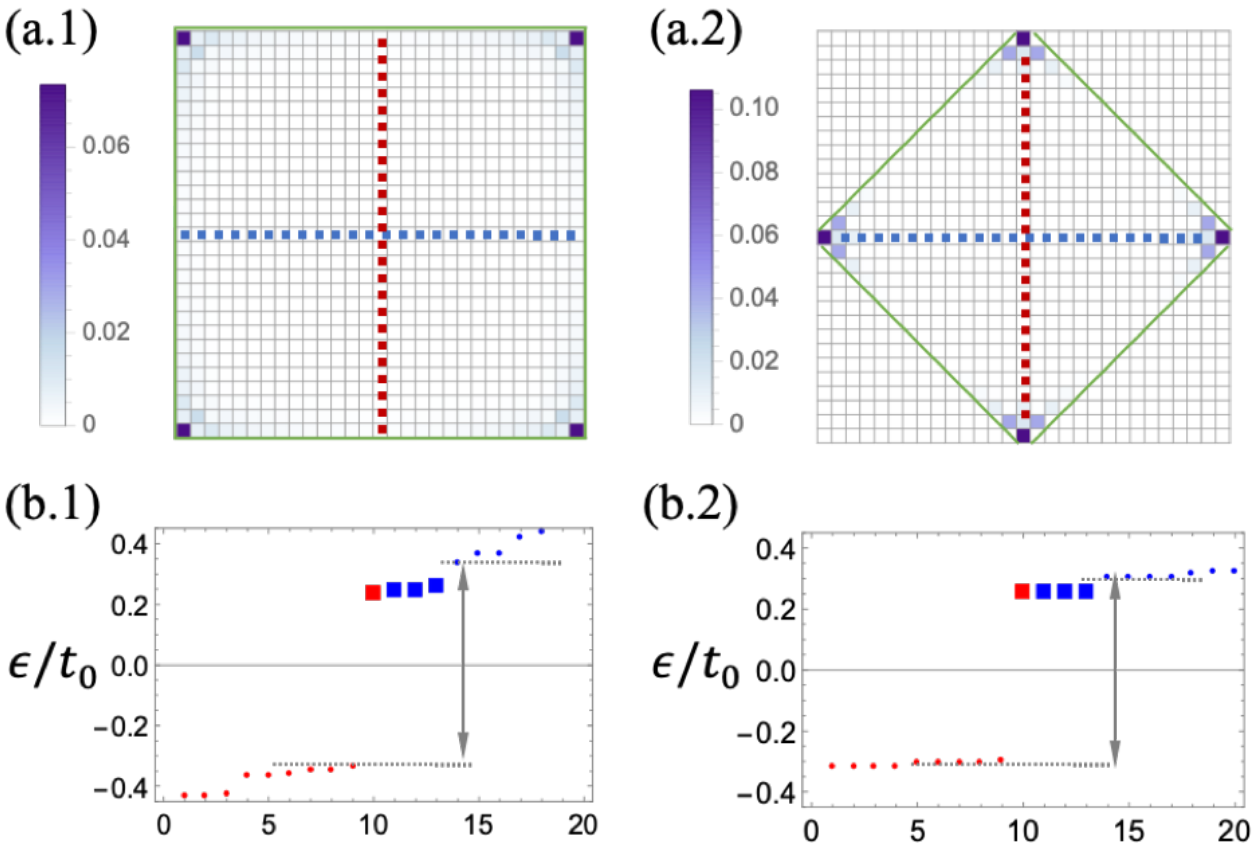

Figure 5.2: Numerical results from model Hamiltonian Eq.[5.9] with two different boundary conditions (marked by green solid lines). (a.1,2) are wave function density for the occupied in gap state, each square stands for one unit cell. The red and blue dashed lines stand for two reflection symmetric axes. (b.1,2) are the energy spectrum close to Fermi surface for the corresponding boundary condition in (a). The squares stand for the corner modes, and the red (blue) stands for the occupied (unoccupied) states at half-filling. The calculations are done with $t_x = t_y = t_0$, $t_{so} = 0.8t_0$, $M = 0.90t_0$ and $\lambda_{1,2} = 0.3t_0$ for 30×30 lattice.

We further confirm the analytic results by numerically diagonalizing the Hamiltonian Eq.[5.9] for two different boundary conditions, as shown in Fig.[5.2.(a)]. We find four corner modes with non-zero energy for both patterns. Fig.[5.2.(b)] shows the energy spectrum close to the Fermi surface. The inter-layer coupling λ opens a gap $E_{\text{gap}} \approx 2\lambda$ at the boundary, and we can see clearly four corner-localized in gap states. At half-filling, one out of four in-gap states is filled, which compensates the $-1/4$ defect charge at each corner.

5.4 Edge states in multi-leg junction

We now turn to study edge networks with multiple pairs of edge states coming together at a vertex (or equivalently a junction). Fig.[5.3.(a)] shows a Y-junction with six edge states living on three legs. For each semi-infinite axis $x_i (i = 1, 2, 3)$, we use the $\psi_\alpha(x_i)$ and $\psi_\beta(x_i)$ to denote the outgoing and incoming chiral edge states for the i-th leg, respectively. Instead of matching wave functions by hand as in the previous minimal 1D edge network, here, we introduce a more generic scattering matrix approach: injecting a mode along a specified leg will lead to reflection and transmission after scattering at the junction, and the poles of scattering matrix implies the existence of bound states. We make the following assumptions to capture the scattering process: (1) Away from the junction, each chiral edge state should be identical to that of an isolated Chern insulator layer, at most up to a global phase factor; (2) During the scattering process, the edge states from the same Chern insulator layer should maintain their amplitude, but could capture a phase shift. The value of the phase shift depends on the details of scattering, but will be constrained by symmetries in specific examples.

5.4.1 Scattering theory for Y-junction

For an isolated junction, the incoming and outgoing scattering modes can be described by combining incoming and outgoing chiral edge states. Different from localized state, for scattering state with momentum k, we denote $\eta = v/m$ and set $k\eta = \sinh\varphi > 0$. Then for $x_i > 0$, under the basis $\big(\psi_\alpha(x_i), \psi_\beta(x_i)\big)^T$, for each individual leg, from Eq.[5.1] we can derive normalized wave function of incoming and outgoing modes as: $\psi^T_{\text{in}}(x_i) = (e^{-\varphi - i\theta_i}, 1)^T/\sqrt{1+e^{-2\varphi}}$, $\psi^T_{\text{out}}(x_i) = (e^{\varphi - i\theta_i}, 1)^T/\sqrt{1+e^{+2\varphi}}$, with the corresponding energy $E/m = +\cosh\varphi$. If we inject a mode along negative x_1 direction, the wave function on leg x_1 is given by $\Psi_1(x_1) = e^{-ikx_1}\psi_{\text{in}}(x_1) + r_1 e^{ikx_1}\psi_{\text{out}}(x_1)$. Meanwhile, the wave function on leg x_2 is given by $\Psi_2(x_2) = t_{12}e^{ikx_2}\psi_{\text{out}}(x_2)$, and $\Psi_3(x_3) = t_{13}e^{ikx_3}\psi_{\text{out}}(x_3)$ for wave function on leg x_3. We have used r_1 for reflection coefficient on leg x_1, and t_{12} (t_{13}) for transmission coefficient for the scattering from x_1 to x_2 (x_3). With this we can expand the wave function around the intersection as:

$$\begin{cases} \Psi_1(0) = \big(\dfrac{e^{-\varphi-i\theta_1}}{\sqrt{1+e^{-2\varphi}}} + r_1\dfrac{e^{\varphi-i\theta_1}}{\sqrt{1+e^{2\varphi}}}\big)\psi_\alpha(x_1=0) + \big(\dfrac{1}{\sqrt{1+e^{-2\varphi}}} + \dfrac{r_1}{\sqrt{1+e^{2\varphi}}}\big)\psi_\beta(x_1=0), \\ \Psi_2(0) = t_{12}\dfrac{e^{\varphi-i\theta_2}}{\sqrt{1+e^{2\varphi}}}\psi_\alpha(x_2=0) + t_{12}\dfrac{1}{\sqrt{1+e^{2\varphi}}}\psi_\beta(x_2=0), \\ \Psi_3(0) = t_{13}\dfrac{e^{\varphi-i\theta_3}}{\sqrt{1+e^{2\varphi}}}\psi_\alpha(x_3=0) + t_{13}\dfrac{1}{\sqrt{1+e^{2\varphi}}}\psi_\beta(x_3=0). \end{cases} \tag{5.10}$$

In Fig.[5.3.(a)], the edge states in same color are from the same Chern insulator layer. Due to the continuity of edge state wave function for each individual layer, we have $\psi_\alpha(x_1 \to 0^+) = \psi_\beta(x_3 \to 0^+)$, $\psi_\beta(x_1 \to 0^+) = \psi_\alpha(x_2 \to 0^+)$, and $\psi_\beta(x_2 \to 0^+) = \psi_\alpha(x_3 \to 0^+)$.

During the scattering process they can capture an additional phase factor $e^{i\alpha_i}$, which depends on the details of the scattering process. This leads to:

$$\begin{cases} \dfrac{e^{-\varphi-i\theta_1}}{\sqrt{1+e^{-2\varphi}}} + r_1\dfrac{e^{\varphi-i\theta_1}}{\sqrt{1+e^{2\varphi}}} = t_{13}\dfrac{1}{\sqrt{1+e^{2\varphi}}}e^{i\alpha_1}, \\ t_{12}\dfrac{e^{\varphi-i\theta_2}}{\sqrt{1+e^{2\varphi}}} = \big(\dfrac{1}{\sqrt{1+e^{-2\varphi}}} + r_1\dfrac{1}{\sqrt{1+e^{2\varphi}}}\big)e^{i\alpha_2}, \\ t_{13}\dfrac{e^{\varphi-i\theta_3}}{\sqrt{1+e^{2\varphi}}} = t_{12}\dfrac{1}{\sqrt{1+e^{2\varphi}}}e^{i\alpha_3}. \end{cases} \tag{5.11}$$

With this we can solve r_1, t_{12} and t_{13} in the term of φ, α_i, and θ_i. By injecting modes along the negative directions of rest two legs (see in Appendix), we can derive whole coefficients for the scattering matrix S:

$$S = \frac{1}{e^{3\varphi}-e^{i\Lambda}}\begin{pmatrix} \tilde{r}_1 & \tilde{t}_{12} & \tilde{t}_{13} \\ \tilde{t}_{21} & \tilde{r}_2 & \tilde{t}_{23} \\ \tilde{t}_{31} & \tilde{t}_{32} & \tilde{r}_3 \end{pmatrix}, \quad \Lambda = \sum_i(\theta_i+\alpha_i). \tag{5.12}$$

For arbitrary scattering process, $\Psi_{\text{out}} = S\Psi_{\text{in}}$, where $\Psi^T_{\text{in(out)}} = \big(\psi(x_1),\ \psi(x_2),\ \psi(x_3)\big)_{\text{out(in)}}$. The pole of the scattering matrix, $e^{3\varphi}-e^{i\Lambda}=0$, implies the existence of bound state localized at the junction. Note that, in the presence of edge soliton, each of these semi-infinite legs contributes a fractional charge $-\theta_i/2\pi$. With these we find:

$$\frac{E}{m} = \cosh\varphi = \cos\left(\frac{\Lambda+2n\pi}{3}\right),\ n\in\mathbb{Z},\ N_s = -\frac{\sum_i\theta_i}{2\pi}. \tag{5.13}$$

As we mentioned before, $\Lambda = \sum_i(\theta_i+\alpha_i)$, which depends on the details of scattering. The energy-phase relation Eq.[5.13] for 3-leg Y-junction can be easily generalized to l-leg junction:

$$\frac{E}{m} = \cosh\varphi = \cos\left(\frac{\Lambda}{l}\right),\ N_s = -\frac{\sum_i\theta_i}{2\pi}, \tag{5.14}$$

where we have let $2n\pi$ be absorbed into Λ for latter convenience.

5.4.2 Application to topological fullerenes

The multi-leg edge junction can be used to describe the bound state in an isolated wedge disclination [209, 208, 247, 78, 19], which is the building block of topological fullerenes [209, 208]. More specifically, the Y-junction edge network mentioned above can be used to analyze one vertex of tetrahedral topological fullerenes (as shown in Fig.[5.1.(a)]), which is a wedge disclination defect with Frank index $f=3$ (or 180° Frank angle). The Frank index f here stands for the number of 60° Chern insulator layers taken away from the complete Haldane lattice. In order to build the edge network for such a disclination, let us first consider three

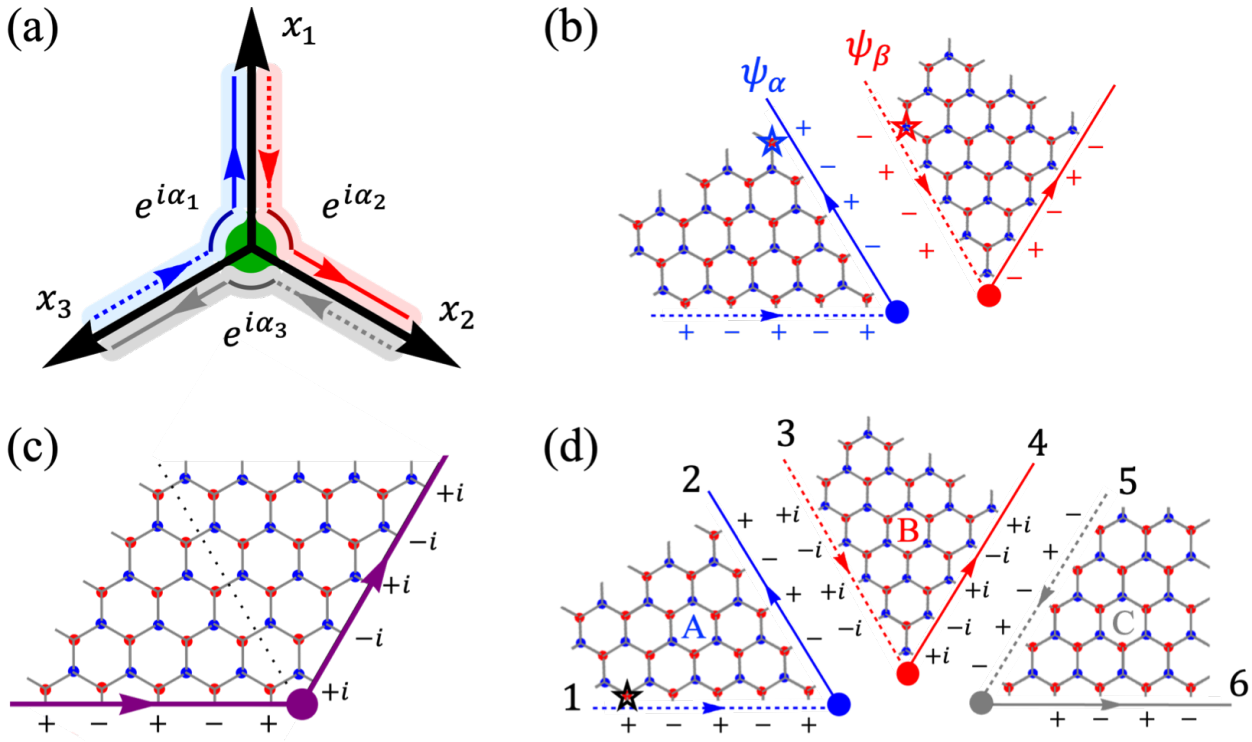

Figure 5.3: (a) Edge network for a vertex with three legs (Y-junction). The center of the junction is marked by the green disk. Three coordinates, $x_{1,2,3}$ start from the center and point outward. The solid and dashed arrows in blue, red and gray stands for three pairs of coupled helical edge states. Edge states in the same color are from the same Chern insulator layer. (b) Edge states for two isolated 60° Chern insulator slices. The blue (red) $\pm$ stands for the relevant phase factor of edge states measured from $\psi_{\alpha(\beta)}$, with two individual reference points (marked by stars). (c) Edge states for an individual 120° Chern insulator slice. (d) A vertex of the type appearing in tetrahedron topological fullerenes and relevant edge states. The $\pm$ stands for the relevant phase factor of edge states measured from edge states ψ_1 whose reference point is marked by black star.

60° semi-infinite triangular layers (A,B,C) of Haldane honeycomb lattice coming together, as shown in Fig.[5.3.(d)]. Each layer is coupled with its two neighbors across the seams. The tight-binding Hamiltonian for such a disclination is given by [85, 209, 208]:

$$\mathcal{H} = -t_0 \sum_{\langle i,j \rangle} (c_i^\dagger c_j + \text{H.c.}) - t_1 \sum_{\langle\langle i,j \rangle\rangle} (e^{-i\phi_{ij}} c_i^\dagger c_j + \text{H.c.}). \tag{5.15}$$

Here, $c_i^\dagger$ (c_i) is creation (annihilation) operator for spinless fermion on i-th site. The t_0 and t_1 denotes, respectively, the nearest-neighbor hopping and next-nearest-neighbor hopping amplitudes. The $e^{i\phi_{ij}}$ provides an additional phase factor for next-nearest-neighbor hopping. Within the topological region, each individual layer can provide chiral edge states surround-

ing the bulk. The local Chern vector[27] for each layer points outside the plane of the paper, which ensures six edge states propagating according to the pattern in the figure.

These six edge states are not independent. The blue (red, gray) edge states $1, 2$ $(3, 4;$ $5, 6)$ come from the same triangular layer, and they are connected by $\psi_{2j}(x_j \to 0^+) = \psi_{2j-1}(x_{j+2} \to 0^+)$. If an edge state is coupled with its time-reversal counterpart across the seam, we say this seam does not have phase mismatch. The total wave function on a lattice site across the seam is given by $\varphi_{\text{edge},\alpha}(x_i) = e^{ik_E a}\psi_\alpha(x_i)$ and $\varphi_{\text{edge},\beta}(x_i) = e^{-ik_E a}\psi_\beta(x_i)$, respectively, where k_E denotes the edge momentum and a stands for the lattice constant. The $\psi_{\alpha,\beta}(x_i)$ here should be understood as the edge states on corresponding sub lattice. The effective coupling between two states is $\int d\tau\lambda\varphi^*_{\text{edge},\alpha}(x_i)\varphi_{\text{edge},\beta}(x_i)$, with λ stands for the bond across the seam. The integral is done within a unit cell. For an isolated disclination, the total phase mismatch $\sum_i \theta_i$ for all legs (seams) is fixed in the absence of external flux. Due to the quantization of charge pumping, to the lowest order the function $\sum_i \alpha_i$ should be linear to $\sum_i \theta_i$, i.e. $\sum_i \alpha_i = A\sum_i \theta_i + B$. The coefficients A, B are related to the parameters from the tight-binding model, such as the effective radius ρ and the Haldane gap $m = 3\sqrt{3}t_1$[209]. By comparing with the results from exact diagonalizing the tight-binding Hamiltonian Eq.[5.15] (see in Appendix), we find that, for Haldane gap $m \approx t_0 = 1$,

$$\varphi = \frac{2\sum_i \theta_i - \pi/2}{3},\ E = \cos\varphi,\ N_s = -\frac{\sum_i \theta_i}{2\pi}. \tag{5.16}$$

Similarly, for the vertex of an octahedral topological fullerene, the number of legs is $l = 6 - 2 = 4$, and we further have $\varphi = 2\sum_i \theta_i/4$, $E = \cos\varphi$, and $N_s = -\sum_i \theta_i/2\pi$ (with $1 \le i \le 4$). For the vertex of an icosahedral topological fullerene, the number of legs is $l = 6-1 = 5$, and we further have $\varphi = (2\sum_i \theta_i + \pi/2)/5$, $E = \cos\varphi$, $N_s = -\sum_i \theta_i/2\pi$ (with $1 \le i \le 5$).

We now turn to determine the value of θ_i for each leg[209], especially for the cases with external flux. Let us first consider the process of combining two smaller 60°-layers in Fig.[5.3.(b)] to a larger 120°-layer in Fig.[5.3.(c)]. The two smaller layers are cut from the same Haldane honeycomb lattice model, and they are next to each other in the original lattice. With the open boundary condition, both of them can hold chiral edge states, which are denoted by red and blue arrows in Fig.[5.3.(b)]. We can set a simultaneous coordinate for both layers across the seam, thus the total wave function on a lattice site on the blue (red) edge is $\varphi_{\text{edge},\alpha}(\xi) = e^{-ik_E\xi}\psi_\alpha(\xi)$ $(\varphi_{\text{edge},\beta} = e^{ik_E\xi}\psi_\beta(\xi))$. In the presence of inversion symmetry, $k_E a = \pi$ for Haldane honeycomb lattice model [209]. Thus the base functions $e^{ik_E\xi}$ oscillates with a period of two sites. In order to glue two layers back to a larger layer without phase mismatch across the seam, the amplitudes should be in the pattern in Fig.[5.3.(b)]. However, as shown in Fig.[5.3.(c)], the edge states has an additional phase shift when bypassing the corner. This leads to $i\psi_\alpha = -\psi_\beta$ or $\psi_\alpha = i\psi_\beta$. Thus we have that the proper phase difference across the seam should be $\pm i$, which is the case for no phase mismatch. To avoid any ambiguity induced by the gauge chosen for wave functions, we define the effective mass term $\mathcal{M}_i(\theta_i)$ on each leg with respect to the scenario without phase mismatch. Thus if there is no phase mismatch on a certain leg, then $\mathcal{M}_i(\theta_i = 0) = m\sigma_x$.

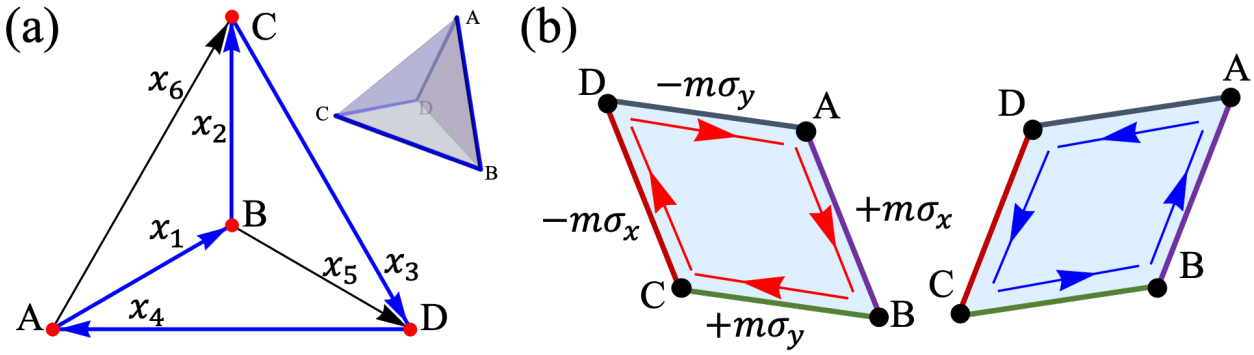

Figure 5.4: (a) Edge network and relevant coordinates for tetrahedral topological fullerene. The blue line shows the traversal along the hinges. (b) Mass distribution of edge network for tetrahedral topological fullerene. Cutting the Tetrahedron along the blue line in (a) leads to two parallelograms in (b), which helps to map the tetrahedral topological fullerenes to a 2d SOTI (Eq.[5.9]).

Note that, for a wedge disclination with Frank index $f = 3$ in Fig.[5.3.(d)], if we glue AB and BC across the seam as shown in Fig.[5.3.(b)], the system can be viewed as a Haldane honeycomb lattice on the half plane. The gluing process means that we have chosen to measure the relevant phase factor of edge states on all layers from ψ_1 with a fixed reference point. Thus the coupling across the seams AB and BC should not have a phase mismatch, thus $\mathcal{M}_1(0) = \mathcal{M}_2(0) = m\sigma_x$. However, the lower boundaries of A and C has phase mismatch and $\mathcal{M}_3(\pi/2) = m\sigma_y$ [209]. Finally, referring to Eq.[5.16], we have $\varphi = \pi/6$, $E = \cos\pi/6$ and $N_s = -1/4$ for the vertex of Tetrahedral topological fullerene. Eq.[5.16] also stands in the presence of external flux. Adding an external flux Φ opposite to local Chern vector at the center of junction is equivalent to change the coupling pattern with additional phase factor $e^{i\Phi}$ for the bond across the Dirac string [209, 208]. For simplicity we can put the Dirac string along x_3, thus $\theta_3 = \phi + \pi/2$ and Eq.[5.16] can be written as $\varphi = 2\Phi/3 + \pi/6$. More specifically, if $\Phi = \pi/2$, we have $\sum_i \theta_i = \pi$ and $\varphi = \pi/2$. Thus the external flux $\Phi = \pi/2$ moves the bound state energy to $E = \cos\varphi = 0$, as well as the fractional charge to $N_s = -\sum_i \theta_i/2 = -1/2$. This is consisted with the analysis from symmetry: an external flux with $\Phi = \pi/2$ can restore the particle hole symmetry of the system [208]. Thus the bound state energy should be 0 and the fractional charge should be $-1/2$. Similar results apply for vertices of octahedral and icosahedral topological fullerenes (see in Appendix), and are in accordance with numerical results [209, 208].

The corner states in topological fullerenes can be further explained by the edge networks with a group of multi-leg junctions. In Fig.[5.4.(a)] we plot the edge network for the tetrahedral topological fullerene, with $\mathcal{M}_1(0) = m\sigma_x$, $\mathcal{M}_2(\pi/2) = m\sigma_y$, $\mathcal{M}_3(\pi) = -m\sigma_y$, $\mathcal{M}_4(3\pi/2) = -m\sigma_x$, and $\mathcal{M}_5(0) = \mathcal{M}_6(0) = m\sigma_x$. However, Eq.[5.16] is derived for an isolated vertex with all coordinates point outward, which is slightly different from the settings in Fig.[5.4.(a)]. Note that, for a pair of helical edge states living on a i-th hinge with effective

mass $\mathcal{M}_i(\theta_i)$, changing the direction of coordinates is equivalent to changing the mass term to $\tilde{\mathcal{M}}_i\big((-\theta_i) \bmod 2\pi\big)$. Thus for each individual vertex, we can first flip the coordinates to the pattern in Fig.[5.3.(a)], by then using Eq.[5.16] we find four corner localized states with $E = \cos\pi/6$ and $N_s = -1/4$.

5.5 Disucssion and outlook

We have constructed a generic edge network theory and shown its ability to capture the boundary topology of coupled edge states with different geometric constraints. We first discussed the minimal edge network on a closed 1d loop, and demonstrated that crystalline symmetry can produce spatial-dependent mass term, leading to the domain wall states at the intersection of adjoint edges. After discussing a model 2d second-order TI, we constructed edge networks for multi-leg junctions, which can faithfully reflect the properties of bound states in disclination defects. The edge network can include polyhedral hinges, which allows determination of the corner states in topological fullerenes. These results can help to understand the origin of topologically generated localized states in a variety of situations.

We can view the similarities between the 2D second-order TI and the 3D topological fullerine as reflecting the fact that the classification of 2d SOTI is derived from that of TIs in 1d, which is the same as classification of co-dimension 2 topological defects [248, 49, 149], including point defects in surfaces. In this sense, the 2d SOTI we proposed is in the same topological class as a corresponding system with wedge disclination defects. Based on effective edge theory, we can map the topological fullerenes to the 2d SOTI Eq.[5.9] derived from gapping out helical edge states in Sec. 5.3. For any polyhedron, one can traverse all the vertices along hinges without repeats. The traversal forms a closed 1d loop (see the blue thick arrows in Fig.[5.4.(a)]). We can cut the polyhedron into two congruent Chern insulator layers along the traversal, as shown in Fig.[5.4.(b)]. The two Chern insulator layers can be viewed as a "twisted" index spin hall effect. The edges on the closed 1d loop are gapped out by the gluing process, and the effective mass changes after bypassing each corner due to crystalline symmetries, leading to an edge soliton with fractional charge located at the corner. This is identical to the generation of fractional charge in our 2d SOTI model. Similarly, we can also map the octahedral and icosahedral topological fullerenes to (less natural) 2d SOTIs. However, it is still an open questions that whether we can connect all topological phases that exhibit quantized corner charge to certain higher order topological phases [70].

More generally, the networks of edges discussed here could be generalized to incorporate proximity-induced superconductivity or Luttinger liquid corrections, or conceivably to include additional localized degrees of freedom such as boundary Majorana states or spins as in previous studies of the Kondo effect in Y-junctions [193]. In the cases discussed here, there are enough symmetries or other physical constraints to determine the key properties of the localized states in an edge network quite directly, while in other situations the properties such as fractional offset charges might be actively tuned by symmetry-breaking perturba-

tions. Planar networks of helical edges and three-leg junctions have recently been discovered in bilayer graphene at small twist angles, which suggests that the study of edge networks is likely to become increasingly relevant to experiment.

5.6 Appendix

5.6.1 Edge network for two-terminal junction

In this section, we look into the scattering theory of the simplest two-terminal junction. In order to keep in accordance with the scattering theory in Sec. 5.4.1, we set the positive direction of the two legs being opposite to each other and pointing outside the junction. This switches the θ_1 to $-\theta_1$ compared with the notation in Sec. 5.3.

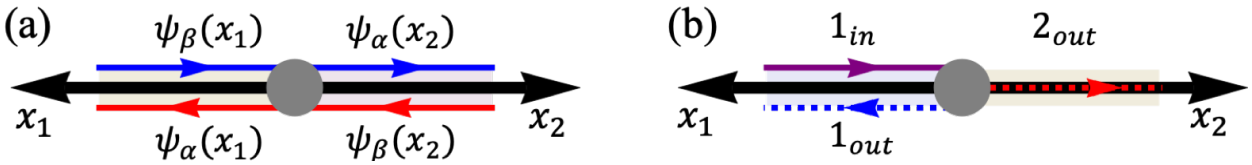

Figure 5.5: 1D Scattering process. (a) Edge network for two terminal junction. (b) The scattering process for two terminal junction with a wave inject along negative x_1 direction.

We construct the conventional scattering theory as following: suppose we have a wave injected along the negative x_1 direction. The wave function on leg x_1 is given by $\Psi_1 = e^{-ikx_1}\psi_{1,\text{in}} + re^{ikx_1}\psi_{1,\text{out}}$. Meanwhile, the wave function on leg x_2 is given by $\Psi_2 = te^{ikx_2}\psi_{2,\text{out}}$. Here r and t stand for the reflection and transmission coefficients, respectively. Different from a localized state, for a scattering state with momentum k, we denote $\eta = v/m$ and set $k\eta = \sinh\varphi > 0$. Then for $x_i > 0$, using the basis $\big(\psi_\alpha(x_i), \psi_\beta(x_i)\big)^T$, for each individual leg, from Eq.[5.1] we can derive a normalized wave function of incoming and outgoing modes as: $\psi^T_{\text{in}}(x_i) = (e^{-\varphi - i\theta_i}, 1)^T/\sqrt{1+e^{-2\varphi}}$, $\psi^T_{\text{out}}(x_i) = (e^{\varphi - i\theta_i}, 1)^T/\sqrt{1+e^{+2\varphi}}$, with corresponding energy $E/m = +\cosh\varphi$. We can expand the wave function around the junction by the combination of incoming and outgoing edge states:

$$\begin{cases} \Psi_1(0) = \left(\dfrac{e^{-\varphi - i\theta_1}}{\sqrt{1+e^{-2\varphi}}} + r\dfrac{e^{\varphi - i\theta_1}}{\sqrt{1+e^{2\varphi}}}\right)\psi_\alpha(x_1 = 0) + \left(\dfrac{1}{\sqrt{1+e^{-2\varphi}}} + \dfrac{r}{\sqrt{1+e^{2\varphi}}}\right)\psi_\beta(x_1 = 0), \\ \Psi_2(0) = t\dfrac{e^{\varphi - i\theta_2}}{\sqrt{1+e^{2\varphi}}}\psi_\alpha(x_2 = 0) + t\dfrac{1}{\sqrt{1+e^{2\varphi}}}\psi_\beta(x_2 = 0). \end{cases} \tag{5.17}$$

As shown in Fig.[5.5], $\psi_\alpha(x_1) = \psi_\beta(x_2)$ and $\psi_\beta(x_1) = \psi_\alpha(x_2)$ since they are from the same Chern insulator. For the SOTI Eq.[5.9], the wave function should be continuous at the

junction:

$$\begin{cases} \dfrac{e^{-\varphi-i\theta_1}}{\sqrt{1+e^{-2\varphi}}}+r\dfrac{e^{\varphi-i\theta_1}}{\sqrt{1+e^{2\varphi}}}=t\dfrac{1}{\sqrt{1+e^{2\varphi}}}, \\ \dfrac{1}{\sqrt{1+e^{-2\varphi}}}+r\dfrac{1}{\sqrt{1+e^{2\varphi}}}=t\dfrac{e^{\varphi-i\theta_2}}{\sqrt{1+e^{2\varphi}}}. \end{cases} \tag{5.18}$$

By solving this we derive:

$$\begin{cases} r=r'=e^{\varphi}\dfrac{e^{i(\theta_1+\theta_2)}-1}{e^{2\varphi}-e^{i(\theta_1+\theta_2)}}, \\ t=e^{i\theta_2}\dfrac{e^{2\varphi}-1}{e^{2\varphi}-e^{i(\theta_1+\theta_2)}}, \\ t'=e^{i\theta_1}\dfrac{e^{2\varphi}-1}{e^{2\varphi}-e^{i(\theta_1+\theta_2)}}. \end{cases} \tag{5.19}$$

The reflection and transmission coefficients r and t satisfy conservation of probability current:

$$|r|^2+|t|^2=\frac{e^{2\varphi}(2-2\cos(\theta_1+\theta_2))+e^{4\varphi}+1-2e^{2\varphi}}{e^{4\varphi}+1-2e^{2\varphi}\cos(\theta_1+\theta_2)}=1. \tag{5.20}$$

Finally we have the scattering matrix for two terminal junction as:

$$S=\begin{pmatrix} t & r \\ r' & t' \end{pmatrix}=\frac{1}{e^{2\varphi}-e^{i(\theta_1+\theta_2)}}\begin{pmatrix} \tilde{t} & \tilde{r} \\ \tilde{r}' & \tilde{t}' \end{pmatrix}. \tag{5.21}$$

One can easily check that the scattering matrix is unitary $S^\dagger S=\mathbf{1}$. The coefficients of scattering matrix, see in Eq.[5.19] has simultaneous poles:

$$e^{i\theta_1+i\theta_2}-e^{2\varphi}=0,\ 2\varphi=i(\theta_1+\theta_2+2n\pi),\ n\in\mathbb{Z}, \tag{5.22}$$

which stands for bound states localized at the junction with energy and fractional charge as:

$$E=\cosh\varphi=\cos\left(\frac{\varphi}{2}\right),\ N_s=-\frac{|\theta_2+\theta_1|}{2\pi}. \tag{5.23}$$

Remember that θ_1 here is equal to $-\theta_1$ in Sec. 5.3 due to the flipping of x_1-leg's direction, the above results is in accordance with Eq.[5.7]. We further define η as:

$$\eta=\frac{r}{t}=\frac{(e^{i\theta_1}-e^{-i\theta_2})}{(e^{\varphi}-e^{-\varphi})}. \tag{5.24}$$

The argument and the absolute value of η are:

$$\arg(\eta)=\arctan\left(\frac{\sin\theta_1+\sin\theta_2}{\cos\theta_1-\cos\theta_2}\right)=\frac{\pi}{2}-\frac{\theta_1-\theta_2}{2}, \tag{5.25}$$

$$|\eta|^2=\frac{2-2\cos\theta_1\cos\theta_2+2\sin\theta_1\sin\theta_2}{e^{2\varphi}+e^{-2\varphi}-2}=\frac{\sin^2(\frac{\theta_1+\theta_2}{2})}{\sinh^2\varphi}. \tag{5.26}$$

Thus the bound state energy can also be parametrized by reflection and transmission coefficents as:

$$E^2=\cosh^2\varphi=\frac{|t|^2}{|r|^2}\sin^2(\frac{\theta_1+\theta_2}{2})+1. \tag{5.27}$$

5.6.2 Edge networks for a Y-junction

In this section, we provide more details about the edge network description of a three-leg junction ("Y-junction").

5.6.2.1 Bound states from matching wave function

Different from the scattering matrix approach in Sec. 5.4.1, here we get the same results by matching the trial wave function and validate that the poles of scattering states do correspond to localized states. We can derive the trial wave function by using the similar method in Sec. 5.3. Substitute the trial wave function $\chi(x_i)$ in to Eq.[5.1] for each leg independently, we find the modes localized at two ends of i-th edge, with $\chi(x_i) = e^{i\delta_i}(e^{i(\varphi-\theta_i)}, 1)^T$ for energy $\epsilon_i^o = \cos\varphi$. This gives the relation between a_i and b_i on the same leg. More specifically: for the leg 1, we have $\chi(x_1) = e^{i\delta_1}(e^{i(\varphi-\theta_1)}, 1)^T$, with the basis $\Psi(x_1) = (\psi_2(x_1), \psi_3(x_1))^T$; for the leg 2, we have $\chi(x_2) = e^{i\delta_2}(e^{i(\varphi-\theta_2)}, 1)^T$, with the basis $\Psi(x_2) = (\psi_4(x_2), \psi_5(x_2))^T$; for the leg 3, we have $\chi(x_3) = e^{i\delta_3}(e^{i(\varphi-\theta_3)}, 1)^T$, with the basis $\Psi(x_3) = (\psi_6(x_3), \psi_1(x_3))^T$.

Due to the continuity of the bound state wave function, the boundary conditions are:

$$\begin{cases} e^{i\delta_3}e^{i\alpha_1}\psi_1(x_3 \to 0^+) = e^{i\delta_1}e^{i(\varphi-\theta_1)}\psi_2(x_1 \to 0^+), \\ e^{i\delta_1}e^{i\alpha_2}\psi_3(x_1 \to 0^+) = e^{i\delta_2}e^{i(\varphi-\theta_2)}\psi_4(x_2 \to 0^+), , \\ e^{i\delta_2}e^{i\alpha_3}\psi_5(x_2 \to 0^+) = e^{i\delta_3}e^{i(\varphi-\theta_3)}\psi_6(x_3 \to 0^+), \end{cases} \tag{5.28}$$

where $\alpha_{i=1,2,3}$ are phase factors acquired across the junction as mentioned in main text. We also have $\psi_1(x_3 \to 0^+) = \psi_2(x_1 \to 0^+)$, $\psi_3(x_1 \to 0^+) = \psi_4(x_2 \to 0^+)$, $\psi_5(x_2 \to 0^+) = \psi_6(x_3 \to 0^+)$ since they are the edge states from the same Chern insulator layer. With these we have:

$$e^{i(\alpha_1+\alpha_2+\alpha_3)} = e^{i(3\varphi-\theta_1-\theta_2-\theta_3)}, \tag{5.29}$$

which is equivalent to

$$\begin{aligned} &3\varphi = \sum_i(\theta_i + \alpha_i) + 2n\pi,\ n \in \mathbb{Z}, \\ &\frac{E}{m} = \cos\varphi,\ N_s = -\frac{\sum_i \theta_i}{2\pi}. \end{aligned} \tag{5.30}$$

This is in accordance with Eq.[5.13] in main text. Thus the poles of the scattering matrix do correspond to the localized states at the junction. Similar results also apply for a vertex of octahedral or icosahedral topological fullerenes, as shown in Sec. 5.4.1.

5.6.2.2 Y-junction scattering matrix

In this section we provide more details about how to derive the full scattering matrix Eq.[5.12] in Sec. 5.4.1. Similarly to the two terminal junction, for the scattering states of Y-junction, we denote $\eta = v/m$. We set $k\eta = \sinh\varphi > 0$. Then for $x_i > 0$, under the basis $\big(\psi_\alpha(x_i), \psi_\beta(x_i)\big)^T$, for each individual leg, from Eq.[5.1] we can derive normalized wave

function of incoming and outgoing modes as: $\psi_{\text{in}}^T(x_i) = (e^{-\varphi - i\theta_i}, 1)^T/\sqrt{1+e^{-2\varphi}}$, $\psi_{\text{out}}^T(x_i) = (e^{\varphi - i\theta_i}, 1)^T/\sqrt{1+e^{+2\varphi}}$, with corresponding energy $E/m = +\cosh\varphi$. As mentioned in main text, we first inject the mode along negative x_1 direction. The wave function on leg x_1 is given by $\Psi_1 = e^{-ikx_1}\psi_{1,\text{in}} + re^{ikx_1}\psi_{1,\text{out}}$. Meanwhile, the wave function on leg x_2 is given by $\Psi_2 = t_{12}e^{ikx_2}\psi_{2,\text{out}}$, and the wave function on leg x_3 is given by $\Psi_3 = t_{13}e^{ikx_3}\psi_{3,\text{out}}$. We can expand the wave function around the intersection as:

$$\begin{cases} \Psi_1(0) = \left(\dfrac{e^{-\varphi - i\theta_1}}{\sqrt{1+e^{-2\varphi}}} + r\dfrac{e^{\varphi - i\theta_1}}{\sqrt{1+e^{2\varphi}}}\right)\psi_\alpha(x_1=0) + \left(\dfrac{1}{\sqrt{1+e^{-2\varphi}}} + \dfrac{r}{\sqrt{1+e^{2\varphi}}}\right)\psi_\beta(x_1=0), \\ \Psi_2(0) = t_{12}\dfrac{e^{\varphi - i\theta_2}}{\sqrt{1+e^{2\varphi}}}\psi_\alpha(x_2=0) + t_{12}\dfrac{1}{\sqrt{1+e^{2\varphi}}}\psi_\beta(x_2=0), \\ \Psi_3(0) = t_{13}\dfrac{e^{\varphi - i\theta_3}}{\sqrt{1+e^{2\varphi}}}\psi_\alpha(x_3=0) + t_{13}\dfrac{1}{\sqrt{1+e^{2\varphi}}}\psi_\beta(x_3=0). \end{cases} \tag{5.31}$$

Note that due to the continuity of edge state wave function for each individual layer, we have $\psi_\alpha(x_1 \to 0^+) = \psi_\beta(x_3 \to 0^+)$, $\psi_\beta(x_1 \to 0^+) = \psi_\alpha(x_2 \to 0^+)$, and $\psi_\beta(x_2 \to 0^+) = \psi_\alpha(x_3 \to 0^+)$. Following the assumption we made in Sec. 5.4, during the scattering process, the amplitude of the chiral edge states from same triangular Chern insulator is conserved, but they may acquire an additional phase factor α_i when by passing the junction. By matching the coeffients of $\psi_{\alpha(\beta),i}$ we have:

$$\begin{cases} \dfrac{e^{-\varphi - i\theta_1}}{\sqrt{1+e^{-2\varphi}}} + r\dfrac{e^{\varphi - i\theta_1}}{\sqrt{1+e^{2\varphi}}} = t_{13}\dfrac{1}{\sqrt{1+e^{2\varphi}}}e^{i\alpha_1}, \\ t_{12}\dfrac{e^{\varphi - i\theta_2}}{\sqrt{1+e^{2\varphi}}} = \left(\dfrac{1}{\sqrt{1+e^{-2\varphi}}} + r\dfrac{1}{\sqrt{1+e^{2\varphi}}}\right)e^{i\alpha_2}, \\ t_{13}\dfrac{e^{\varphi - i\theta_3}}{\sqrt{1+e^{2\varphi}}} = t_{12}\dfrac{1}{\sqrt{1+e^{2\varphi}}}e^{i\alpha_3}. \end{cases} \tag{5.32}$$

From the above equation we derive that:

$$\begin{cases} r_1 = \dfrac{e^{\varphi}\left(e^{i\sum_i(\theta_i+\alpha_i)} - e^{\varphi}\right)}{e^{3\varphi} - e^{i\sum_i(\alpha_i+\theta_i)}}, \\ t_{12} = \dfrac{e^{i(\alpha_2+\theta_2)}e^{\varphi}(e^{2\varphi}-1)}{e^{3\varphi} - e^{i\sum_i(\alpha_i+\theta_i)}}, \\ t_{13} = \dfrac{e^{i(\alpha_2+\theta_2+\alpha_3+\theta_3)}(e^{2\varphi}-1)}{e^{3\varphi} - e^{i\sum_i(\alpha_i+\theta_i)}}. \end{cases} \tag{5.33}$$

One can check that the scattering is unitary:

$$|r|^2 + |t_{12}|^2 + |t_{13}|^2 = 1. \tag{5.34}$$

To derive the full scattering matrix, we can further inject the mode along negative x_2 (x_3) direction. By following the similar procedure for injecting along negative x_1 direction,

we have:

$$\begin{cases} r_2 = \dfrac{e^{\varphi}(e^{i\sum_i(\theta_i+\alpha_i)} - e^{\varphi})}{e^{3\varphi} - e^{i\sum_i(\alpha_i+\theta_i)}}, \\ t_{23} = \dfrac{e^{i(\alpha_3+\theta_3)}e^{\varphi}(e^{2\varphi}-1)}{e^{3\varphi} - e^{i\sum_i(\alpha_i+\theta_i)}}, \\ t_{21} = \dfrac{e^{i(\alpha_1+\theta_1+\alpha_3+\theta_3)}(e^{2\varphi}-1)}{e^{3\varphi} - e^{i\sum_i(\alpha_i+\theta_i)}}. \end{cases} \tag{5.35}$$

$$\begin{cases} r_3 = \dfrac{e^{\varphi}(e^{i\sum_i(\theta_i+\alpha_i)} - e^{\varphi})}{e^{3\varphi} - e^{i\sum_i(\alpha_i+\theta_i)}}, \\ t_{31} = \dfrac{e^{i(\alpha_1+\theta_1)}e^{\varphi}(e^{2\varphi}-1)}{e^{3\varphi} - e^{i\sum_i(\alpha_i+\theta_i)}}, \\ t_{32} = \dfrac{e^{i(\alpha_1+\theta_1+\alpha_2+\theta_2)}(e^{2\varphi}-1)}{e^{3\varphi} - e^{i\sum_i(\alpha_i+\theta_i)}}. \end{cases} \tag{5.36}$$

Finally, we derive scattering matrix as:

$$S = \begin{pmatrix} r_1 & t_{12} & t_{13} \\ t_{21} & r_2 & t_{23} \\ t_{31} & t_{32} & r_3 \end{pmatrix} = \frac{1}{e^{3\varphi} - e^{i\Lambda}} \begin{pmatrix} \tilde{r}_1 & \tilde{t}_{12} & \tilde{t}_{13} \\ \tilde{t}_{21} & \tilde{r}_2 & \tilde{t}_{23} \\ \tilde{t}_{31} & \tilde{t}_{32} & \tilde{r}_3 \end{pmatrix}, \tag{5.37}$$

where $kv/m = \sinh\varphi,\ \Lambda = \sum_i(\theta_i + \alpha_i)$. The poles of S denotes the existence of bound state with energy:

$$\frac{E}{m} = \cosh\varphi = \cos\left(\frac{\Lambda + 2n\pi}{3}\right),\ n \in \mathbb{Z}, \tag{5.38}$$

which is the Eq.[5.13] in main text. It is easy to check that the Scattering matrix here is unitary, i.e., $S^{\dagger}S = \mathbf{1}$. Eq.[5.13] can be generalized to l-leg junction: $E/m = \cosh\varphi = \cos[(\Lambda + 2n\pi)/l],\ n \in \mathbb{Z},\ N_s = -\sum_i \theta_i/2\pi$. For latter convenience we let $2n\pi$ be absorbed into $\sum_i \alpha_i$.

5.6.2.3 Comparison with numerical results from exact diagonalization of tight-binding Hamiltonian

The bound-state energy Eq.[5.14] is depending on $\Lambda = \sum_i(\theta_i + \alpha_i)$. As we showed in main text, $\sum_i \alpha_i = A\sum_i \theta_i + B$, substitute these into Eq.[5.14] we have:

$$\frac{E}{m} = \cos\left[\frac{(1+A)\sum_i \theta_i + B}{6-f}\right], \tag{5.39}$$

where $l = f - 6$ is the number of legs for a disclination with Frank index f. In order to figure out the value of A, B and derive the full response function as Eq.[5.16], in principle we need two data points (the bound state energy at two different flux value Φ) from the exact diagonalizing tight-binding Hamiltonian Eq.[5.9]. In fact, we do take two data points

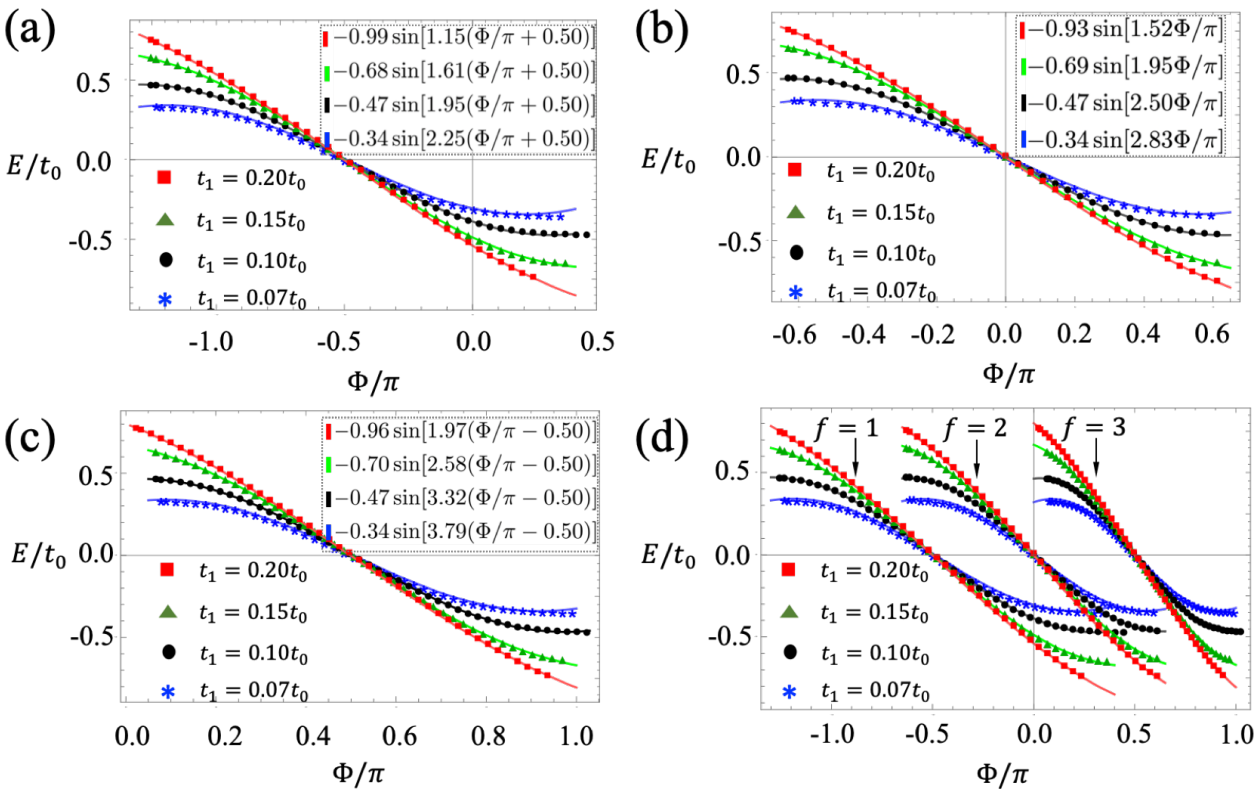

Figure 5.6: Bound state energy with external flux. The dots are from exactly diagonalizing the Haldane model Eq.[5.15]. The solid lines are fittings from exact diagonalization, which take the form of energy-phase (flux) relation Eq.[5.40]. (a) Disclination with Frank index $f = 1$. (b) Disclination with Frank index $f = 2$. (c) Disclination with Frank index $f = 3$. We also plot (a-c) in the same frame, as shown in (d). In (a-d), the red, green, black, and blue lines or dots denote, respectively, $t_1 = 0.2t_0$ ($m = 1.04t_0$), $t_1 = 0.15t_0$ ($m = 0.78t_0$), $t_1 = 0.10t_0$ ($m = 0.52t_0$), and $t_1 = 0.07t_0$ ($m = 0.36t_0$). Here, t_0 stands for nearest neighbor hopping, t_1 stands for next-nearest neighbor hopping with $\phi_{ij} = \pi/2.$, and $m = 3\sqrt{3}t_1$ stands for Haldane mass, as shown in the main text. The equations on the left bottom side are the fitting of the numerical results from exact diagonalization. The calculation is done for 800 unit cells within each 60° slice.

directly for $m \approx t_0$ and get Eq.[5.16] in the main text. However, note that for Frank index $f = 3$ ($f = 1$), although the response of bound state energy with respect to external flux for different m are different, adding an external flux $\Phi = -\pi/2$ ($\Phi = +\pi/2$) can restore the particle hole symmetry, and move the bound state energy to zero. Thus we can define $\Phi_0 = |B/(1 + A)| = (\sum_i \theta_i) \bmod \pi$, which is fixed for given f. Note that $\sum_i \theta_i$ is the total phase mismatch at the junction. With these Eq.[5.39] can be reduced to:

$$\frac{E}{m} = \sin\left[\frac{(1 + A)\pi(\Phi/\pi \pm \Phi_0/\pi)}{6 - f}\right]. \tag{5.40}$$

The plus or minus sign here depends on whether the local Chern vector is align with or opposite to the direction of external flux. Now we only need one date point (for example, the energy of bound state in the absence of external flux) from exact diagonalization to get the value A in Eq.[5.40] and reproduce Eq.[5.16] directly. For $m = 3\sqrt{3}t_1 \approx t_0 = 1$, we derive A first and Eq.[5.40] is then simplified as:

$$\begin{cases} E_{\text{Tetrahedron}}(\Phi) = \cos\left(\dfrac{2\Phi}{3} + \dfrac{\pi}{6}\right), \\ E_{\text{Octahedron}}(\Phi) = \cos\left(\dfrac{2\Phi}{4} + \dfrac{\pi}{2}\right), \\ E_{\text{Icosahedron}}(\Phi) = \cos\left(\dfrac{2\Phi}{5} + \dfrac{7\pi}{10}\right), \end{cases} \tag{5.41}$$

which is Eq.[5.16] in the presence of external flux Φ.

We further compare the results from Eq.[5.16] with full numerical results derived from exactly diagonalizing the tight-binding Hamiltonian Eq.[5.15], as shown in Fig.[5.6]. We plot the bound state energy with external flux (Φ) under different Haldane mass $m = 3\sqrt{3}t_1$ and different Frank index f. The direct fittings of numerical results do take the form of Eq.[5.40], as shown in the left-bottom of each sub-figure.

5.6.2.4 Comparison to numerical results from continuous model

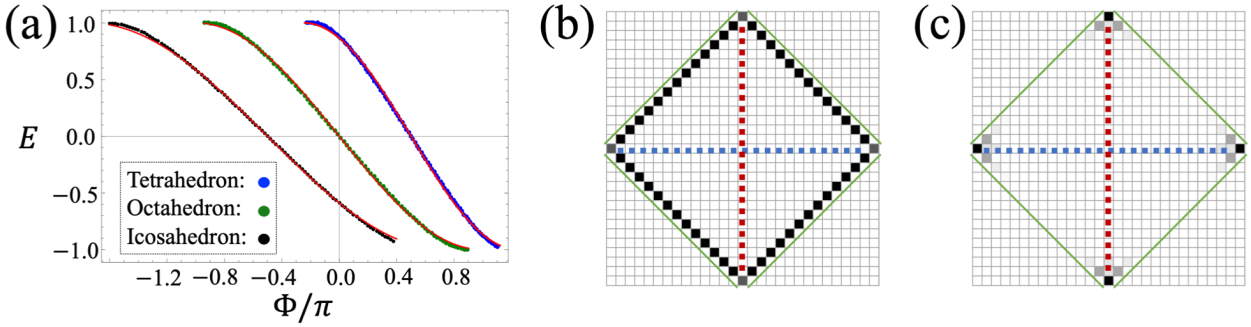

Figure 5.7: (a) Bound state energy with external flux. The dots are numerical results for solving Eq.[5.42]. The blue dots are for one vertex of tetrahedral topological fullerenes (disclination with Frank index $f = 3$). The green dots are for one vertex of octahedral topological fullerenes (disclination with Frank index $f = 2$). The black dots are for one vertex of icosahedral topological fullerenes (disclination with Frank index $f = 1$). The red lines are relevant results from Eq.[5.30]. (b-c) The wave function density for mid gap state in (b) Quadrupole insulator, and (c) 2d SOTI from Eq.[5.9] proposed in main text. The red and blue dashed lines stand for the reflection symmetric axes for $x-$ and $y-$ directions, respectively. The green solid lines stand for the boundary.

The bound state energy with respect to external flux from continuous model for conical singularities [209] is given by:

$$\sqrt{\frac{m-E}{m+E}} = \frac{K_{\nu-1/2}(\kappa\rho)}{K_{\nu+1/2}(\kappa\rho)} \tag{5.42}$$

where

$$\kappa = \sqrt{m^2 - E^2},\ \nu = \frac{j - \frac{\Phi}{2\pi} + \frac{f}{4}}{1 - \frac{f}{6}}. \tag{5.43}$$

Here m is the Haldane mass, ρ stands for the radius of the hole in disclination, E is the bound state energy, j is half integer, f is Frank index and stands for the number of $\pi/3$ wedges removed, Φ denotes the external flux, and $K(\kappa\rho)$ is modified Bessel functions of the second kind. We have set the positive direction of external flux opposite to local Chern vector. In practice, in order to derive full energy-flux relation for given m, one may need (at least) one data point (bound state energy at given Φ) from exact diagonalizing Eq.[5.9] to get the value of effective radius ρ. After that we can derive the bound state energy with external flux from (numerically) solving Eq.[5.42].

We have shown that our analytic results in Eq.[5.40] fit quite well with the numerical results from diagonalizing tight-binding model in previous subsection. Our method also give the proper results from solving Eq.[5.42] directly, as shown in Fig.[5.7.(a)]. From here we know that, the phase shift $\sum_i \alpha_i$ should be a function of Haldane mass m and effective radius ρ.

5.6.3 Boundary Hamiltonian for arbitrary edge

In this section we derive the effective edge Hamiltonian for an arbitrary edge. Note that the in gap state wave function distribution for our Tetrahedral type TI (Eq.[5.9]) is different from that of Quadrupole insulator, see in Fig.[5.7.(b,c)]. We further show that our Tetrahedral type 2d SOTI can hold fractional charge at the corner of rectangular boundaries, regardless of the orientation of the rectangle.

The Bloch Hamiltonian for our Tetrahedral type TI is Eq.[5.9], as shown in main text. In the absence of inter-layer coupling, i.e. $\lambda = 0$, the system can be viewed as index spin hall effect:

$$\begin{aligned}\mathcal{H}(\vec{k})_{\text{QSH}} =& 2t_{\text{so}}\sin(k_x)\tau_1 + 2t_{\text{so}}\sin(k_y)\tau_2 \\ &+(m_z - 2t_x\cos k_x - 2t_y\cos k_y)\tau_3\sigma_3,\end{aligned} \tag{5.44}$$

which also respects C_4 symmetry with $U_4 = e^{i\pi/4\tau_z}$. Around $(k_x = 0, k_y = 0)$, the low energy version for Hamiltonian Eq.[5.44] is given by:

$$h(\vec{k}) = 2t_{\text{so}}k_x\tau_1 + 2t_{\text{so}}k_y\tau_2 + (\tilde{m}_z + t_x k_x^2 + t_y k_y^2)\tau_3\sigma_3, \tag{5.45}$$

where $\tilde{m}_z = m_z - 2t_x - 2t_y$. For simplicity we assume $t_x = t_y = t_0$.

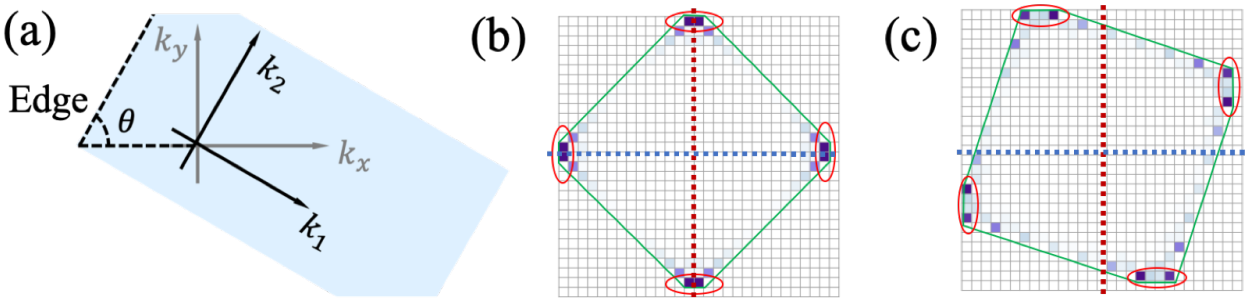

Figure 5.8: (a) Edge along $\hat{e}_2 = \cos\theta\hat{e}_x + \sin\theta\hat{e}_y$ direction (marked by dashed line). (b,c) Corner charge (in gap state wave function density) in the presence of different boundary conditions. The dashed blue and red lines stand for two reflection symmetric axes, the green solid line denotes the boundary of tetrahedral type TI. The corner localized charge is marked by red circles. (b) Boundary configuration respects original reflection symmetry. (c) Boundary configuration does not respect original reflection symmetry.

In order to figure out the edge states at the cut along $\vec{e}_2 = \cos\theta\hat{e}_x + \sin\theta\hat{e}_y$ direction (see in Fig.[5.8].(a)), we define a new set of basis in both spatial and momentum spaces:

$$\begin{cases} x = x_1\sin\theta + x_2\cos\theta, \\ y = -x_1\cos\theta + x_2\sin\theta, \end{cases} \quad \begin{cases} k_x = k_1\sin\theta + k_2\cos\theta, \\ k_y = -k_1\cos\theta + k_2\sin\theta. \end{cases} \tag{5.46}$$

Substituting Eq.[5.46] into Eq.[5.45], the Low energy Hamiltonian can be written in the form of $k_{1,2}$:

$$\begin{aligned} h(\vec{k}) =& 2t_{\rm so}(k_1\sin\theta + k_2\cos\theta)\tau_1 + (\tilde{m}_z + t_0k_1^2 + t_0k_2^2)\tau_3\sigma_3 \\ &+2t_{\rm so}(-k_1\cos\theta + k_2\sin\theta)\tau_2. \end{aligned} \tag{5.47}$$

Consider the model Hamiltonian Eq.[5.47] defined on the half-space $x_1 > 0$ in the $x_1 - x_2$ plane. We replace $k_1 \to -i\partial_{x_1}, k_2 \to 0$, and neglect the higher order terms in Eq.[5.47]:

$$\tilde{h}(x_1) = (-i\partial_{x_1}2t_{\rm so}\sin\theta)\sigma_1 + (i\partial_{x_1}2t_{\rm so}\cos\theta)\sigma_2 + \tilde{m}_z\sigma_3\tau_3. \tag{5.48}$$

By using the ansatz $\psi_0 = e^{\eta x_1}\phi$, we can find a pair of counter-propagating edge states:

$$\begin{cases} \Psi_\uparrow = \dfrac{e^{-2t_{\rm so}x_1/\tilde{m}_z}}{\sqrt{N_\uparrow}}(e^{-i\theta/2}, e^{i\theta/2}, 0, 0)^T, \\ \Psi_\downarrow = \dfrac{e^{-2t_{\rm so}x_1/\tilde{m}_z}}{\sqrt{N_\downarrow}}(0, 0, -e^{-i\theta/2}, e^{i\theta/2})^T, \end{cases} \tag{5.49}$$

where $N_{\uparrow(\downarrow)}$ is the normalization constant. This procedure [202] leads to a 2×2 effective Hamiltonian defined by $H^{\alpha,\beta}_{\rm edge}(k_2) = \langle\Psi_\alpha|\, h(\vec{k})\,|\Psi_\beta\rangle$, to the leading order in k_2, we arrive at the effective Hamiltonian for helical edge states:

$$h^0_{\rm edge} = 2t_{so}k_2\sigma_z. \tag{5.50}$$

Similarly, the inter-layer coupling $\lambda_1\tau_1\sigma_1$ (or $\lambda_2\tau_2\sigma_2$), under the basis $\Psi_{\alpha,\beta}$, gives birth to an additional term $-\lambda_1 \sin\theta\sigma_y$ (or $-\lambda_2 \cos\theta\sigma_x$). In summary, under the basis $\Psi_{\alpha,\beta}$, the total effective edge Hamiltonian is given by:

$$h_{\text{edge}} = 2t_{so}k_2\sigma_z - \lambda_2 \cos\theta\sigma_x - \lambda_1 \sin\theta\sigma_y. \tag{5.51}$$

By following the method introduced in [301], one can verify that Eq.[5.51] is capable to describe not only an individual edge but also the closed loop formed by edges. As we have mentioned in main text, if $\lambda_2 = 0$ but $\lambda_1 \neq 0$, the Eq.[5.9] describes a 2D SOTI in BDI class. The effective edge Hamiltonian Eq.[5.51] is reduced to:

$$h_{\text{edge}} = 2t_{so}k_2\sigma_z - \lambda_1 \sin\theta\sigma_y. \tag{5.52}$$

For each edge, one can assign a set of coordinates whose edge points along $\hat{e}_2$ direction as in Fig.[5.8.(a)]. The coordinates for the left-upper edge ($\theta_1 = +\pi/2$) and right-upper edge ($\theta_2 = -\pi/2$) are shown in Fig.[5.9.(a)]. The effective mass term changes from $\mathcal{M}(\theta_1) = -\lambda_1$ to $\mathcal{M}(\theta_1) = +\lambda_1$, leading to a zero mode (Fig.[5.9.(a)]) localized at the intersection (Fig.[5.9.(b)]).

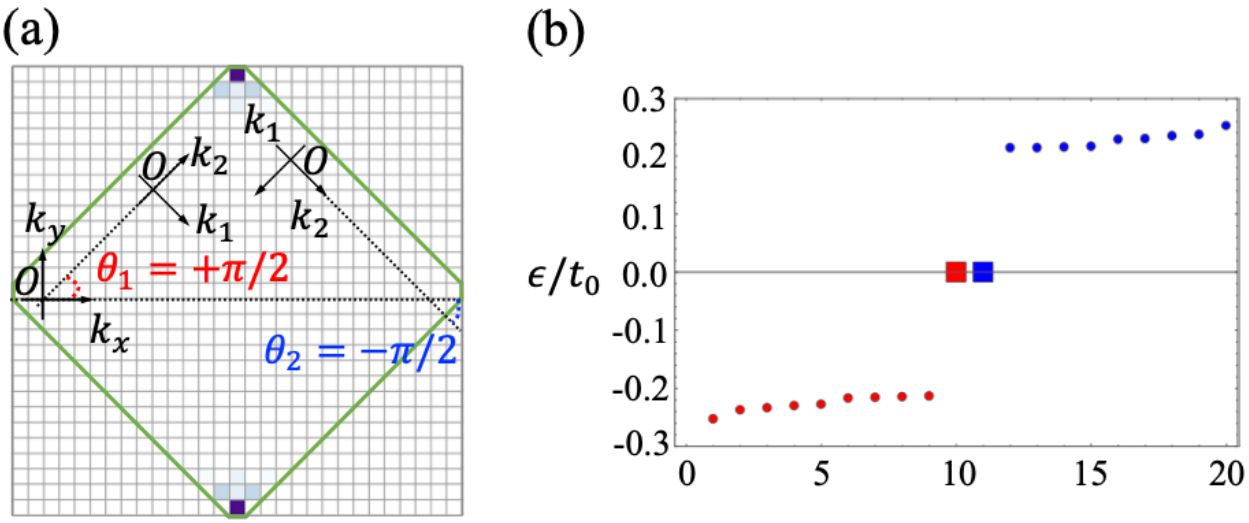

Figure 5.9: Numerical results from model Hamiltonian Eq.[5.9] which is in 2D SOTI region. (a) Wave function density for the occupied in gap state, each square stands for one unit cell. (b) The energy spectrum close to Fermi surface for the corresponding boundary condition in (a). The calculations are done with $t_x = t_y = t_0$, $t_{so} = 0.8t_0$, $M = 0.90t_0$, and $\lambda_1 = 0.3t_0$, $\lambda_2 = 0$ for 30×30 lattice.

If $\lambda_1 = \lambda_2 = \lambda$, the above low energy Hamiltonian Eq.[5.51] is reduced to:

$$h_{\text{edge}} = 2t_{so}k_2\sigma_z - \lambda \cos\theta\sigma_x - \lambda \sin\theta\sigma_y, \tag{5.53}$$

and we can define the effective mass term as:

$$\begin{aligned}\mathcal{M}_i &= -\lambda(\cos\theta_i\sigma_x + \sin\theta_i\sigma_y) \\ &= -\lambda(\cos\theta_i\hat{e}_x + \sin\theta_i\hat{e}_y)\cdot(\sigma_x\hat{e}_x + \sigma_y\hat{e}_y + \sigma_z\hat{e}_z) \\ &= -\lambda\vec{e}_i\cdot\vec{\sigma}.\end{aligned} \tag{5.54}$$

This related the effective mass term of i-th edge to its orientation $\hat{e}_i = \cos\theta_i\vec{e}_x + \sin\theta_i\vec{e}_y$. According to our previous results, the kink of effective mass term at the corner can give birth to corner localized charge. The value of the charge (edge soliton) N_s is:

$$N_s = -\frac{\theta_2 - \theta_1}{2} = -\frac{\delta\theta}{2}. \tag{5.55}$$

For any rectangular boundary, $\delta\theta = \pi/2$ since two adjoint edges are perpendicular to each other. Thus the corner localized fractional charge should be $-1/4e$, regardless the orientation of rectangle. We have confirmed this by exact diagonalizing the tight-binding Hamiltonian, as shown in Fig.[5.8.(b,c)]. This result can be generalized to the corner state with arbitrary fractional charge by tuning the angle θ between two adjoint edges.

5.6.4 2d SOTI and zero mode

As we have mentioned in main text, if $\lambda_2 = 0$ but $\lambda_1 \neq 0$, the Eq.[5.9] describes a 2D SOTI in BDI class with two additional symmetries U_x^{++} and U_y^{+-}. The low energy Hamiltonian Eq.[5.45] can be written as: $h_{\text{low}} = k_x\gamma_1 + k_y\gamma_2 + m\gamma_0$, where $\gamma_1 = \tau_1\sigma_0$, $\gamma_2 = \tau_2\sigma_0$, $m = \tilde{m}_z$ and $\gamma_0 = \tau_3\sigma_3$. For BDI class we can build the real Clifford algebras [183, 184]: $Cl_{3,3} = \{i\gamma_1, i\gamma_2, i\mathcal{TP}, \mathcal{P}, i\mathcal{P}, \gamma_0\}$ whose generators are anti-commuting with each other. Similar to previous works [183], one can define an additional symmetry operator $M_x = i\gamma_x U_x^{++}$, where $M_x^2 = +1$ and M_x anticommutes with all operators in the bracket. The extension problem of Clifford algebras, $Cl_{3,3} = \{i\gamma_1, i\gamma_2, i\mathcal{TP}, \mathcal{P}, i\mathcal{P}, \gamma_0\} \to Cl_{3,4} = \{i\gamma_1, i\gamma_2, i\mathcal{TP}, \mathcal{P}, i\mathcal{P}, \gamma_0, M_x\}$, whose classifying space is R_0, gives a classification $\pi_0(R_0) = \mathbb{Z}$. One can further add an additional symmetry operator $M_y = i\mathcal{TP}\gamma_y U_y^{+-}$, where $M_y^2 = 1$ and M_y commutes with every generator in $Cl_{3,4}$. Thus M_y can block diagonalize the bulk into two copies of BDI + U_x^{++}, each of which has a $\mathbb{Z}$ classification. On the other hand, one reflection symmetric edge automatically breaks the other reflection symmetry since the edge is a 1d system. For example, the $x-$ reflection symmetric edge automatically breaks the $y-$ reflection symmetry, which reduce the classification to one copy of BDI + U_x^{++} ($\mathbb{Z}$). This leads to gapless edge states on U_x symmetric edges. By further locally breaking U_x for x-reflection symmetric edge, the edge states is gapped out by a unique mass term which is odd under U_x and guarantees the presence of zero mode. Thus the corresponding 2d SOTI has an intrinsic $\mathbb{Z}$ classification.

5.6.5 Fractional charge for edge soliton

In the absence of particle hole symmetry, the domain wall state for a SSH chain can hold bound state with non-zero energy and fractional charge aside from $-1/2e$ [111, 75]. In this

section, we summarized and slightly modified their previous works [111] and derive the similar results for edge solitons. This is in accordance with the results Eq.[5.6] from bosonization in Sec. 5.2.

Suppose we have a one-dimensional Dirac Hamiltonian in the external field φ:

$$\hat{H}(\varphi) = -i\partial_x\sigma_z + \epsilon\sigma_x + \varphi(x)\sigma_y. \tag{5.56}$$

For simplicity we assume that $\epsilon > 0$. Up to a global normalization constant and a unitary transformation this Hamiltonian can be connected to Hamiltonian Eq.[5.53]. In the absence of $\epsilon\sigma_x$, the Hamiltonian respects the charge conjugation symmetry and can hold zero mode when $\varphi(x)$ has a kink. The presence of $\epsilon\sigma_x$ breaks the charge conjugation symmetry of the system. We will see later on that this Hamiltonian can hold bound state with nonzero energy and fractional charge.

In the vacuum where the system does not hold a soliton, $\varphi = \varphi_0 = \text{const}$. We denote $\varphi_0 = \mu$ for simplicity. In the presence of a soliton, $\varphi(x) = \varphi_s(x)$, and in principle the $\varphi_s(x)$ should have a kink. In order to compute the charge, we need to derive the eigenstates of this two situation. The Schrodinger equation for these two scenarios can be written as:

$$\hat{H}(\varphi_0)\psi_E^0 = E^0\psi_E^0,\ \hat{H}(\varphi_s)\psi_E^s = E^s\psi_E^s, \tag{5.57}$$

where ψ_E^0 stands for the normal state without solitons, ψ_E^s stand for the situation in the presence of soliton.

The charge density at level E is $\rho_E(x) = \psi_E^\dagger(x) \times \psi_E(x)$, and the physical charge density is got by integrating ρ_E over all negative E, since the negative energy levels are filled in the half-filling:

$$\rho(x) = \int_{-\infty}^{0} dE\rho_E(x). \tag{5.58}$$

Finally the soliton charge is obtained by integrating the charge density in the soliton field over all x, but to avoid an infinity, we must subtract a similar integral of the charge density when no soliton is present:

$$Q = \int dx(\rho_s(x) - \rho_0(x)). \tag{5.59}$$

We can calculate the exact value of Q even if we do not know the exact form of $\varphi(x)$. All we need to know about φ_s is that it interpolates between opposite "vacuum" values as x passes from $-\infty$ to $+\infty$:

$$\varphi_s(+\infty) = |\varphi_0| = \mu,\ \varphi_s(-\infty) = -|\varphi_0| = -\mu. \tag{5.60}$$

We now study the eigenstates of Eq.[5.57]. The vacuum problem is trivial: the wave functions are plane waves $\propto e^{ikx}$ and the spectrum is continuous $E^0 = \pm(k^2 + \mu^2 + \epsilon^2)^{1/2}$.

In the presence of soliton, we first assume that the wave-function of the eigenstate is $(u, v)^T$. Thus we have:

$$\begin{pmatrix} -i\partial_x & -i\varphi(x) + \epsilon \\ i\varphi(x) + \epsilon & i\partial_x \end{pmatrix} \begin{pmatrix} u \\ v \end{pmatrix} = E \begin{pmatrix} u \\ v \end{pmatrix}, \tag{5.61}$$

which can be simplified as:

$$\begin{cases} -i\partial_x u + (-i\varphi(x) + \epsilon)v = Eu, \\ (i\varphi(x) + \epsilon)u + i\partial_x v = Ev. \end{cases} \tag{5.62}$$

In order to solve these two equations, we first add up two equations:

$$-i\partial_x(u - v) + i\varphi(x)(u - v) + \epsilon(u + v) = E(u + v), \tag{5.63}$$

and then subtract the second equation from the first one, such that we have:

$$-i\partial_x(u + v) - i\varphi(x)(u + v) - \epsilon(u - v) = E(u - v). \tag{5.64}$$

We define the new parameters:

$$U = \frac{u + v}{\sqrt{2}}, \quad V = \frac{u - v}{\sqrt{2}}, \tag{5.65}$$

then we can rewrite the result as:

$$\begin{cases} (-i\partial_x + i\varphi(x))V = (E - \epsilon)U, \\ (-i\partial_x - i\varphi(x))U = (E + \epsilon)V. \end{cases} \tag{5.66}$$

From the second line of Eq.[5.66] we know that

$$V = \frac{-i(\partial_x + \varphi(x))}{E + \epsilon}U. \tag{5.67}$$

Substitute this into the first line of Eq.[5.66], we have:

$$-(\partial_x^2 - \varphi^2(x) + \partial_x\varphi(x))U = (E^2 - \epsilon^2)U. \tag{5.68}$$

From Eq.[5.66] and Eq.[5.68] we can figure out a possible solution:

$$U = \exp[-\int^x dx'\varphi_x(x')], \quad V = 0, \tag{5.69}$$

corresponds to the energy $E = \epsilon$. Note that the U is localized at the kink $x = 0$ due to the form of $\varphi_s(x)$.

To calculate the particle density, we still need to know the eigenstate for all negative energy solutions. We assume that $U \propto e^{ikx}$ and $\varphi \approx \pm\mu$ at large x limit, thus we have the normalized factor:

$$1 = |u_k|^2 + |v_k|^2 = |U_k|^2 + |V_k|^2 = U^2\frac{2E}{E + \epsilon}, \tag{5.70}$$

from which we can figure out the normalized wave function for the negative energy:

$$U = \sqrt{\frac{E + \epsilon}{2E}}U_k, \quad V = -\frac{i}{\sqrt{2E(E + \epsilon)}}(\partial_x + \varphi(x))U_k. \tag{5.71}$$

This gives the wave function in originally basis:

$$\psi_k = \begin{pmatrix} u_k \\ v_k \end{pmatrix}, \tag{5.72}$$

where

$$\begin{cases} u_k = \dfrac{1}{\sqrt{2}}\left(\sqrt{\dfrac{E+\epsilon}{2E}} - \dfrac{i}{\sqrt{2E(E+\epsilon)}}(\partial_x + \varphi(x))\right)U_k, \\ v_k = \dfrac{1}{\sqrt{2}}\left(\sqrt{\dfrac{E+\epsilon}{2E}} + \dfrac{i}{\sqrt{2E(E+\epsilon)}}(\partial_x + \varphi(x))\right)U_k. \end{cases} \tag{5.73}$$

The wave function ψ_k satisfies:

$$\hat{H}(\varphi)\psi_k = E\psi_k, \quad E = -\sqrt{k^2+\mu^2+\epsilon^2}. \tag{5.74}$$

The Charge-density at negative E is given by:

$$\begin{aligned} \rho_k(x) &= |u_k|^2 + |v_k|^2 \\ &= [(E+\epsilon/2E)]|U_k|^2 + [2E(E+\epsilon)]^{-1}|(\partial_x+\varphi)U_k(x)|^2 \\ &= |U_k(x)|^2 + [4E(E+\epsilon)]^{-1}\partial_x^2|U_k(x)|^2 \\ &\quad + [2E(E+\epsilon)]^{-1}\partial_x[|U_k(x)|^2\varphi(x)] \end{aligned} \tag{5.75}$$

where the validity of second line comes from Eq.[5.68].

The soliton charge is the integral over all x and k above evaluated with $\varphi = \varphi_s$, minus a similar integral in the vacuum; but in the vacuum, $|U_k|^2 \equiv \varphi(x) = \mu$, such that the last two term in Eq.[5.75] vanished. Thus we have the soliton charge:

$$N_s = \int dx \int_{-\infty}^{+\infty} \frac{dk}{2\pi}[|U_k^s(x)|^2 - |U_k^0(x)|^2] + \int_{-\infty}^{\infty} \frac{dk}{2\pi}\frac{1}{4E(E+\epsilon)}[\partial_x|U_k^s(x)|^2 + 2|U_k^s(x)|^2\varphi_s(x)]|_{x=-\infty}^{x=+\infty}. \tag{5.76}$$

The double integral can be evaluated by completeness: The U_k^0 represent all the Schrodinger modes in the vacuum, while the U_k^s are one short of being complete in the soliton sector, since the normalized bound state is not among them. Hence the first term contributes -1 to Q. To evaluate the second term in Eq.[5.76], let us consider the wave function in the presence of a soliton when $x = \pm\infty$. These may be given in terms of transmission (T) and reflection coefficients (R):

$$U_k^s(+\infty) = Te^{ikx}, \quad U_k^s(-\infty) = e^{ikx} + Re^{-ikx}. \tag{5.77}$$

Thus, upon dropping oscillatory terms, we are left with the soliton charge:

$$N_s = -1 + \int_{-\infty}^{+\infty} \frac{dk}{2\pi}\frac{\mu}{2E(E+\epsilon)}[|T|^2 + (|R|^2+1)], \tag{5.78}$$

where the plus sign between the contributions at $x = +\infty$ and at $x = -\infty$ arises because of sign reversal in $\varphi_s(x)$. Unitarity, $|T|^2 + |R|^2 = 1$, permits a final evaluation:

$$N_s = -\frac{1}{\pi} \arctan\left(\frac{\mu}{\epsilon}\right). \tag{5.79}$$

Note that, if we denote $\epsilon = m\cos\theta$ and $\varphi_s(\pm\infty) = \pm\mu = m\sin(\mp\theta)$, Eq.[5.79] is reduced to:

$$N_s = -\frac{1}{\pi} \arctan(\tan\theta) = -\frac{\theta - (-\theta)}{2\pi}, \tag{5.80}$$

which is in accordance with Eq.[5.6] derived from bosonization of the helical Luttinger liquid.

Bibliography

[1] David Aasen, Parsa Bonderson, and Christina Knapp. "Torsorial actions on G-crossed braided tensor categories". In: *arXiv preprint arXiv:2107.10270* (2021).

[2] David Aasen, Zhenghan Wang, and Matthew B. Hastings. "Adiabatic paths of Hamiltonians, symmetries of topological order, and automorphism codes". In: *Phys. Rev. B* 106.8 (2022), p. 085122. DOI: 10.1103/PhysRevB.106.085122.

[3] Alexander G. Abanov. "Hopf term induced by fermions". In: *Physics Letters B* 492.3 (2000), pp. 321–323. DOI: https://doi.org/10.1016/S0370-2693(00)01118-7.

[4] Peter Arnold, Guy David Moore, and Laurence G Yaffe. "Transport coefficients in high temperature gauge theories (I): leading-log results". In: *Journal of High Energy Physics* 2000.11 (2000), pp. 001–001. DOI: 10.1088/1126-6708/2000/11/001.

[5] Joseph E. Avron, Daniel Osadchy, and Ruedi Seiler. "A Topological Look at the Quantum Hall Effect". In: *Physics Today* 56.8 (2003), pp. 38–42. DOI: 10.1063/1.1611351.

[6] Murod S Bahovadinov, Oğuz Gülseren, and Jürgen Schnack. "Local entanglement and string order parameter in dimerized models". In: *J. Phys.: Condens. Matter* 31.50 (2019), p. 505602. DOI: 10.1088/1361-648x/ab41b5.

[7] Leon Balents and Matthew P. A. Fisher. "Correlation effects in carbon nanotubes". In: *Phys. Rev. B* 55.18 (1997), R11973–R11976. DOI: 10.1103/PhysRevB.55.R11973.

[8] Ajit C. Balram et al. "Fractionally charged skyrmions in fractional quantum Hall effect". In: *Nature Communications* 6.1 (2015), p. 8981. DOI: 10.1038/ncomms9981.

[9] Maissam Barkeshli. "Transitions between chiral spin liquids and Z_2 spin liquids". In: *arXiv preprint arXiv:1307.8194* (2013).

[10] Maissam Barkeshli, Chao-Ming Jian, and Xiao-Liang Qi. "Theory of defects in Abelian topological states". In: *Phys. Rev. B* 88.23 (2013), p. 235103. DOI: 10.1103/PhysRevB.88.235103.

[11] Maissam Barkeshli, Chao-Ming Jian, and Xiao-Liang Qi. "Twist defects and projective non-Abelian braiding statistics". In: *Phys. Rev. B* 87.4 (2013), p. 045130. DOI: 10.1103/PhysRevB.87.045130.

[12] Maissam Barkeshli and Xiao-Liang Qi. "Synthetic Topological Qubits in Conventional Bilayer Quantum Hall Systems". In: *Phys. Rev. X* 4.4 (2014), p. 041035. DOI: 10.1103/PhysRevX.4.041035.

[13] Maissam Barkeshli and Xiao-Liang Qi. "Topological Nematic States and Non-Abelian Lattice Dislocations". In: *Phys. Rev. X* 2.3 (2012), p. 031013. DOI: 10.1103/PhysRevX.2.031013.

[14] Maissam Barkeshli et al. "Symmetry fractionalization, defects, and gauging of topological phases". In: *Phys. Rev. B* 100.11 (2019), p. 115147. DOI: 10.1103/PhysRevB.100.115147.

[15] Thomas Barthel. "Matrix product purifications for canonical ensembles and quantum number distributions". In: *Phys. Rev. B* 94.11 (2016), p. 115157. DOI: 10.1103/PhysRevB.94.115157.

[16] B. Bauer et al. "Chiral spin liquid and emergent anyons in a Kagome lattice Mott insulator". In: *Nature Communications* 5.1 (2014), p. 5137. DOI: 10.1038/ncomms6137.

[17] Wladimir A. Benalcazar, B. Andrei Bernevig, and Taylor L. Hughes. "Electric multipole moments, topological multipole moment pumping, and chiral hinge states in crystalline insulators". In: *Phys. Rev. B* 96.24 (2017), p. 245115. DOI: 10.1103/PhysRevB.96.245115.

[18] Wladimir A. Benalcazar, B. Andrei Bernevig, and Taylor L. Hughes. "Quantized electric multipole insulators". In: *Science* 357.6346 (2017), pp. 61–66. DOI: 10.1126/science.aah6442.

[19] Wladimir A. Benalcazar, Jeffrey C. Y. Teo, and Taylor L. Hughes. "Classification of two-dimensional topological crystalline superconductors and Majorana bound states at disclinations". In: *Phys. Rev. B* 89.22 (2014), p. 224503. DOI: 10.1103/PhysRevB.89.224503.

[20] VL Berezinskii. "Destruction of long-range order in one dimensional and two dimensional systems having a continuous symmetry group I. Classical systems". In: *Sov. Phys. JETP* 32.3 (1971), pp. 493–500.

[21] VL Berezinskii. "Destruction of long-range order in one dimensional and two dimensional systems possessing a continuous symmetry group. II. Quantum systems". In: *Sov. Phys. JETP* 34.3 (1972), pp. 610–616.

[22] B. Andrei Bernevig, Taylor L. Hughes, and Shou-Cheng Zhang. "Quantum Spin Hall Effect and Topological Phase Transition in HgTe Quantum Wells". In: *Science* 314.5806 (2006), pp. 1757–1761. DOI: 10.1126/science.1133734.

[23] B. Andrei Bernevig and Shou-Cheng Zhang. "Quantum Spin Hall Effect". In: *Phys. Rev. Lett.* 96.10 (2006), p. 106802. DOI: 10.1103/PhysRevLett.96.106802.

[24] B.A. Bernevig and T.L. Hughes. *Topological Insulators and Topological Superconductors*. Princeton University Press, 2013.

[25] Jean-Sébastien Bernier, K. Sengupta, and Yong Baek Kim. "Biaxial spin-nematic phase of two-dimensional disordered rotor models and $S = 1$ bosons in optical lattices". In: *Phys. Rev. B* 74.15 (2006), p. 155124. DOI: 10.1103/PhysRevB.74.155124.

[26] B. Bertini et al. "Finite-temperature transport in one-dimensional quantum lattice models". In: *Rev. Mod. Phys.* 93.2 (2021), p. 025003. DOI: 10.1103/RevModPhys.93.025003.

[27] Raffaello Bianco and Raffaele Resta. "Mapping topological order in coordinate space". In: *Phys. Rev. B* 84.24 (2011), p. 241106. DOI: 10.1103/PhysRevB.84.241106.

[28] Samuel Bieri et al. "Gapless chiral spin liquid in a kagome Heisenberg model". In: *Phys. Rev. B* 92.6 (2015), p. 060407. DOI: 10.1103/PhysRevB.92.060407.

[29] Marcel Bischoff et al. "Spontaneous symmetry breaking from anyon condensation". In: *Journal of High Energy Physics* 2019.2 (2019), p. 62.

[30] Jacob C. Bridgeman and Daniel Barter. "Computing data for Levin-Wen with defects". In: *Quantum* 4 (2020), p. 277. DOI: 10.22331/q-2020-06-04-277.

[31] M. E. Brooks-Bartlett et al. "Magnetic-Moment Fragmentation and Monopole Crystallization". In: *Phys. Rev. X* 4.1 (2014), p. 011007. DOI: 10.1103/PhysRevX.4.011007.

[32] J. A. N. Bruin et al. "Similarity of Scattering Rates in Metals Showing T-Linear Resistivity". In: *Science* 339.6121 (2013), pp. 804–807. DOI: 10.1126/science.1227612.

[33] Vir B. Bulchandani, Christoph Karrasch, and Joel E. Moore. "Superdiffusive transport of energy in one-dimensional metals". In: *Proc. Nat. Acad. Sci.* 117.23 (2020), pp. 12713–12718. DOI: 10.1073/pnas.1916213117.

[34] C. G. Callan and J. A. Harvey. "Anomalies and fermion zero modes on strings and domain walls". In: *Nuclear Physics B* 250.1 (1985), pp. 427–436. DOI: https://doi.org/10.1016/0550-3213(85)90489-4.

[35] Claudio Chamon et al. *Topological aspects of condensed matter physics: lecture notes of the les houches summer school*. Vol. 103. Oxford University Press, 2017. DOI: 10.1093/acprof:oso/9780198785781.001.0001.

[36] Shailesh Chandrasekharan. "Anomaly cancellation in 2+1 dimensions in the presence of a domain wall mass". In: *Phys. Rev. D* 49.4 (1994), pp. 1980–1987. DOI: 10.1103/PhysRevD.49.1980.

[37] Ming-Che Chang. *Online lecture notes for "Topology in condensed matter systems"*. eprint: https://phy.ntnu.edu.tw/~changmc/Teach/Topo/Topo.html.

[38] Bin-Bin Chen et al. "Quantum spin liquid with emergent chiral order in the triangular-lattice Hubbard model". In: *Phys. Rev. B* 106.9 (2022), p. 094420. DOI: 10.1103/PhysRevB.106.094420.

[39] Xie Chen, Zheng-Cheng Gu, and Xiao-Gang Wen. "Classification of gapped symmetric phases in one-dimensional spin systems". In: *Phys. Rev. B* 83.3 (2011), p. 035107. DOI: 10.1103/PhysRevB.83.035107.

[40] Xie Chen, Zheng-Cheng Gu, and Xiao-Gang Wen. "Complete classification of one-dimensional gapped quantum phases in interacting spin systems". In: *Phys. Rev. B* 84.23 (2011), p. 235128. DOI: 10.1103/PhysRevB.84.235128.

[41] Xie Chen, Zheng-Cheng Gu, and Xiao-Gang Wen. "Local unitary transformation, long-range quantum entanglement, wave function renormalization, and topological order". In: *Phys. Rev. B* 82.15 (2010), p. 155138. DOI: 10.1103/PhysRevB.82.155138.

[42] Xie Chen, Zheng-Xin Liu, and Xiao-Gang Wen. "Two-dimensional symmetry-protected topological orders and their protected gapless edge excitations". In: *Phys. Rev. B* 84.23 (2011), p. 235141. DOI: 10.1103/PhysRevB.84.235141.

[43] Xie Chen, Yuan-Ming Lu, and Ashvin Vishwanath. "Symmetry-protected topological phases from decorated domain walls". In: *Nature Communications* 5.1 (2014), p. 3507.

[44] Xie Chen et al. "Symmetry protected topological orders and the group cohomology of their symmetry group". In: *Phys. Rev. B* 87.15 (2013), p. 155114. DOI: 10.1103/PhysRevB.87.155114.

[45] Xie Chen et al. "Symmetry-Protected Topological Orders in Interacting Bosonic Systems". In: *Science* 338.6114 (2012), pp. 1604–1606. DOI: 10.1126/science.1227224.

[46] Ji-Yao Chen et al. "$SU(3)_1$ Chiral Spin Liquid on the Square Lattice: A View from Symmetric Projected Entangled Pair States". In: *Phys. Rev. Lett.* 125.1 (2020), p. 017201. DOI: 10.1103/PhysRevLett.125.017201.

[47] Meng Cheng and Dominic J. Williamson. "Relative anomaly in (1 + 1)d rational conformal field theory". In: *Phys. Rev. Research* 2.4 (2020), p. 043044. DOI: 10.1103/PhysRevResearch.2.043044.

[48] Meng Cheng et al. "Translational Symmetry and Microscopic Constraints on Symmetry-Enriched Topological Phases: A View from the Surface". In: *Phys. Rev. X* 6.4 (2016), p. 041068. DOI: 10.1103/PhysRevX.6.041068.

[49] Ching-Kai Chiu et al. "Classification of topological quantum matter with symmetries". In: *Rev. Mod. Phys.* 88.3 (2016), p. 035005. DOI: 10.1103/RevModPhys.88.035005.

[50] Tessa Cookmeyer, Johannes Motruk, and Joel E. Moore. "Four-Spin Terms and the Origin of the Chiral Spin Liquid in Mott Insulators on the Triangular Lattice". In: *Phys. Rev. Lett.* 127.8 (2021), p. 087201. DOI: 10.1103/PhysRevLett.127.087201.

[51] V. Crépel et al. "Microscopic study of the Halperin–Laughlin interface through matrix product states". In: *Nature Communications* 10.1 (2019), p. 1860. DOI: 10.1038/s41467-019-09169-y.

[52] V. Crépel et al. "Model states for a class of chiral topological order interfaces". In: *Nature Communications* 10.1 (2019), p. 1861. DOI: 10.1038/s41467-019-09168-z.

[53] Jesse Crossno et al. "Observation of the Dirac fluid and the breakdown of the Wiedemann Franz law in graphene". In: *Science* 351.6277 (2016), pp. 1058–1061. DOI: 10.1126/science.aad0343.

[54] Kedar Damle and Subir Sachdev. "Nonzero-temperature transport near quantum critical points". In: *Phys. Rev. B* 56.14 (1997), pp. 8714–8733. DOI: 10.1103/PhysRevB.56.8714.

[55] Roberto B. Diener and Tin-Lun Ho. "^{52}Cr Spinor Condensate: A Biaxial or Uniaxial Spin Nematic". In: *Phys. Rev. Lett.* 96.19 (2006), p. 190405. DOI: 10.1103/PhysRevLett.96.190405.

[56] T. Dombre and N. Read. "Nonlinear σ models for triangular quantum antiferromagnets". In: *Phys. Rev. B* 39.10 (1989), pp. 6797–6801. DOI: 10.1103/PhysRevB.39.6797.

[57] Maxime Dupont and Joel E. Moore. "Universal spin dynamics in infinite-temperature one-dimensional quantum magnets". In: *Phys. Rev. B* 101.12 (2020), p. 121106. DOI: 10.1103/PhysRevB.101.121106.

[58] Dominic V. Else and T. Senthil. "Strange Metals as Ersatz Fermi Liquids". In: *Phys. Rev. Lett.* 127.8 (2021), p. 086601. DOI: 10.1103/PhysRevLett.127.086601.

[59] Andrew M. Essin and Michael Hermele. "Classifying fractionalization: Symmetry classification of gapped $\mathbb{Z}_2$ spin liquids in two dimensions". In: *Phys. Rev. B* 87.10 (2013), p. 104406. DOI: 10.1103/PhysRevB.87.104406.

[60] Motohiko Ezawa. "Higher-Order Topological Insulators and Semimetals on the Breathing Kagome and Pyrochlore Lattices". In: *Phys. Rev. Lett.* 120.2 (2018), p. 026801. DOI: 10.1103/PhysRevLett.120.026801.

[61] Chen Fang and Liang Fu. "Rotation Anomaly and Topological Crystalline Insulators". In: *arXiv:1709.01929* (2017).

[62] Adrian E. Feiguin and Steven R. White. "Finite-temperature density matrix renormalization using an enlarged Hilbert space". In: *Phys. Rev. B* 72.22 (2005), p. 220401. DOI: 10.1103/PhysRevB.72.220401.

[63] Benjamin E. Feldman et al. "Observation of a nematic quantum Hall liquid on the surface of bismuth". In: *Science* 354.6310 (2016), pp. 316–321. DOI: 10.1126/science.aag1715.

[64] E. Fradkin. *Field Theories of Condensed Matter Physics, 2nd ed.* Cambridge University Press, Cambridge, England, 2013.

[65] Lars Fritz et al. "Quantum critical transport in clean graphene". In: *Phys. Rev. B* 78.8 (2008), p. 085416. DOI: 10.1103/PhysRevB.78.085416.

[66] Jürg Fröhlich and Pieralberto Marchetti. "Bosonization, topological solitons and fractional charges in two-dimensional quantum field theory". In: *Communications in Mathematical Physics* 116.1 (1988), pp. 127–173. DOI: 10.1007/BF01239028.

[67] Liang Fu and C. L. Kane. "Topological insulators with inversion symmetry". In: *Phys. Rev. B* 76.4 (2007), p. 045302. DOI: 10.1103/PhysRevB.76.045302.

[68] Liang Fu, C. L. Kane, and E. J. Mele. "Topological Insulators in Three Dimensions". In: *Phys. Rev. Lett.* 98.10 (2007), p. 106803. DOI: 10.1103/PhysRevLett.98.106803.

[69] Patrick Gallagher et al. "Quantum-critical conductivity of the Dirac fluid in graphene". In: *Science* 364.6436 (2019), pp. 158–162. DOI: 10.1126/science.aat8687.

[70] Max Geier et al. "Second-order topological insulators and superconductors with an order-two crystalline symmetry". In: *Phys. Rev. B* 97.20 (2018), p. 205135. DOI: 10.1103/PhysRevB.97.205135.

[71] T. Giamarchi. *Quantum Physics in One Dimension*. Clarendon Press, 2003. DOI: 10.1093/acprof:oso/9780198525004.001.0001.

[72] Vitaly L Ginzburg and Lev D Landau. "On the theory of superconductivity". In: *On superconductivity and superfluidity*. Springer, 2009, pp. 113–137.

[73] Ivan Glasser et al. "Exact parent Hamiltonians of bosonic and fermionic Moore–Read states on lattices and local models". In: *New Journal of Physics* 17.8 (2015), p. 082001. DOI: 10.1088/1367-2630/17/8/082001.

[74] J. Goldstone. "Field theories with Superconductor solutions". In: *Il Nuovo Cimento (1955-1965)* 19.1 (1961), pp. 154–164. DOI: 10.1007/BF02812722.

[75] Jeffrey Goldstone and Frank Wilczek. "Fractional Quantum Numbers on Solitons". In: *Phys. Rev. Lett.* 47.14 (1981), pp. 986–989. DOI: 10.1103/PhysRevLett.47.986.

[76] Shou-Shu Gong, Wei Zhu, and D. N. Sheng. "Emergent Chiral Spin Liquid: Fractional Quantum Hall Effect in a Kagome Heisenberg Model". In: *Scientific Reports* 4.1 (2014), p. 6317. DOI: 10.1038/srep06317.

[77] Shou-Shu Gong et al. "Global phase diagram of competing ordered and quantum spin-liquid phases on the kagome lattice". In: *Phys. Rev. B* 91.7 (2015), p. 075112. DOI: 10.1103/PhysRevB.91.075112.

[78] Sarang Gopalakrishnan, Jeffrey C. Y. Teo, and Taylor L. Hughes. "Disclination Classes, Fractional Excitations, and the Melting of Quantum Liquid Crystals". In: *Phys. Rev. Lett.* 111.2 (2013), p. 025304. DOI: 10.1103/PhysRevLett.111.025304.

[79] Martin Greiter, Darrell F. Schroeter, and Ronny Thomale. "Parent Hamiltonian for the non-Abelian chiral spin liquid". In: *Phys. Rev. B* 89.16 (2014), p. 165125. DOI: 10.1103/PhysRevB.89.165125.

[80] Tarun Grover and T. Senthil. "Topological Spin Hall States, Charged Skyrmions, and Superconductivity in Two Dimensions". In: *Phys. Rev. Lett.* 100.15 (2008), p. 156804. DOI: 10.1103/PhysRevLett.100.156804.

[81] Adolfo G. Grushin. *Online lecture notes for "Introduction to topological matter"*. eprint: https://grushingroup.cnrs.fr/topointro2021/.

[82] Zheng-Cheng Gu and Michael Levin. "Effect of interactions on two-dimensional fermionic symmetry-protected topological phases with Z_2 symmetry". In: *Phys. Rev. B* 89.20 (2014), p. 201113. DOI: 10.1103/PhysRevB.89.201113.

[83] Zheng-Cheng Gu and Xiao-Gang Wen. "Tensor-entanglement-filtering renormalization approach and symmetry-protected topological order". In: *Phys. Rev. B* 80.15 (2009), p. 155131. DOI: 10.1103/PhysRevB.80.155131.

[84] Jutho Haegeman et al. "Unifying time evolution and optimization with matrix product states". In: *Phys. Rev. B* 94.16 (2016), p. 165116. DOI: 10.1103/PhysRevB.94.165116.

[85] F. D. M. Haldane. "O(3) Nonlinear σ Model and the Topological Distinction between Integer- and Half-Integer-Spin Antiferromagnets in Two Dimensions". In: *Phys. Rev. Lett.* 61.8 (1988), pp. 1029–1032. DOI: 10.1103/PhysRevLett.61.1029.

[86] B. I. Halperin. "Statistics of Quasiparticles and the Hierarchy of Fractional Quantized Hall States". In: *Phys. Rev. Lett.* 52.18 (1984), pp. 1583–1586. DOI: 10.1103/PhysRevLett.52.1583.

[87] Bo Han, Huajia Wang, and Peng Ye. "Generalized Wen-Zee terms". In: *Phys. Rev. B* 99.20 (2019), p. 205120. DOI: 10.1103/PhysRevB.99.205120.

[88] Jung Hoon Han. *Skyrmions in condensed matter*. Vol. 278. Springer, 2017.

[89] Sean A. Hartnoll et al. "Theory of the Nernst effect near quantum phase transitions in condensed matter and in dyonic black holes". In: *Phys. Rev. B* 76.14 (2007), p. 144502. DOI: 10.1103/PhysRevB.76.144502.

[90] M. Z. Hasan and C. L. Kane. "Colloquium: Topological insulators". In: *Rev. Mod. Phys.* 82.4 (2010), pp. 3045–3067. DOI: 10.1103/RevModPhys.82.3045.

[91] Allen Hatcher. *Algebraic Topology*. Cambridge University Press, 2002.

[92] Yin-Chen He and Yan Chen. "Distinct Spin Liquids and Their Transitions in Spin-1/2 XXZ Kagome Antiferromagnets". In: *Phys. Rev. Lett.* 114.3 (2015), p. 037201. DOI: 10.1103/PhysRevLett.114.037201.

[93] Yin-Chen He, D. N. Sheng, and Yan Chen. "Chiral Spin Liquid in a Frustrated Anisotropic Kagome Heisenberg Model". In: *Phys. Rev. Lett.* 112.13 (2014), p. 137202. DOI: 10.1103/PhysRevLett.112.137202.

[94] Michael Hermele and Victor Gurarie. "Topological liquids and valence cluster states in two-dimensional SU(N) magnets". In: *Phys. Rev. B* 84.17 (2011), p. 174441. DOI: 10.1103/PhysRevB.84.174441.

[95] Sebastian Hild et al. "Far-from-Equilibrium Spin Transport in Heisenberg Quantum Magnets". In: *Phys. Rev. Lett.* 113.14 (2014), p. 147205. DOI: 10.1103/PhysRevLett.113.147205.

[96] Chang-Yu Hou, Eun-Ah Kim, and Claudio Chamon. "Corner Junction as a Probe of Helical Edge States". In: *Phys. Rev. Lett.* 102.7 (2009), p. 076602. DOI: 10.1103/PhysRevLett.102.076602.

[97] Chang-Yu Hou et al. "Junctions of multiple quantum wires with different Luttinger parameters". In: *Phys. Rev. B* 86.7 (2012), p. 075451. DOI: 10.1103/PhysRevB.86.075451.

[98] Wen-Jun Hu, Shou-Shu Gong, and D. N. Sheng. "Variational Monte Carlo study of chiral spin liquid in quantum antiferromagnet on the triangular lattice". In: *Phys. Rev. B* 94.7 (2016), p. 075131. DOI: 10.1103/PhysRevB.94.075131.

[99] Wen-Jun Hu et al. "Variational Monte Carlo study of a chiral spin liquid in the extended Heisenberg model on the kagome lattice". In: *Phys. Rev. B* 91.4 (2015), p. 041124. DOI: 10.1103/PhysRevB.91.041124.

[100] Yuting Hu, Yidun Wan, and Yong-Shi Wu. "Boundary Hamiltonian Theory for Gapped Topological Orders". In: *Chinese Physics Letters* 34.7, 077103 (2017), p. 077103. DOI: 10.1088/0256-307X/34/7/077103.

[101] Edwin W. Huang et al. "Strange metallicity in the doped Hubbard model". In: *Science* 366.6468 (2019), pp. 987–990. DOI: 10.1126/science.aau7063.

[102] Shengqiang Huang et al. "Topologically Protected Helical States in Minimally Twisted Bilayer Graphene". In: *Phys. Rev. Lett.* 121.3 (2018), p. 037702. DOI: 10.1103/PhysRevLett.121.037702.

[103] Yen-Ta Huang and Dung-Hai Lee. "Non-abelian bosonization in two and three spatial dimensions and applications". In: *Nuclear Physics B* 972 (2021), p. 115565. DOI: https://doi.org/10.1016/j.nuclphysb.2021.115565.

[104] Yichen Huang, C. Karrasch, and J. E. Moore. "Scaling of electrical and thermal conductivities in an almost integrable chain". In: *Phys. Rev. B* 88.11 (2013), p. 115126. DOI: 10.1103/PhysRevB.88.115126.

[105] Sebastian Huber. *Online lecture notes for "Topological quantum numbers in condensed matter systems"*. eprint: https://cmt-qo.phys.ethz.ch/education/spring-semester-2013--topological-quantum-numbers-in-condensed-m.html.

[106] C. Hubig, I. P. McCulloch, and U. Schollwöck. "Generic construction of efficient matrix product operators". In: *Phys. Rev. B* 95.3 (2017), p. 035129. DOI: 10.1103/PhysRevB.95.035129.

[107] Ling-Yan Hung and Yidun Wan. "Generalized ADE classification of topological boundaries and anyon condensation". In: *Journal of High Energy Physics* 2015.7 (2015), p. 120.

[108] Stefan Imhof et al. "Topolectrical-circuit realization of topological corner modes". In: *Nature Physics* 14.9 (2018), pp. 925–929. DOI: 10.1038/s41567-018-0246-1.

[109] D. A. Ivanov. "Non-Abelian Statistics of Half-Quantum Vortices in p-Wave Superconductors". In: *Phys. Rev. Lett.* 86.2 (2001), pp. 268–271. DOI: 10.1103/PhysRevLett.86.268.

[110] R. Jackiw and C. Rebbi. "Solitons with fermion number $\frac{1}{2}$". In: *Phys. Rev. D* 13.12 (1976), pp. 3398–3409. DOI: 10.1103/PhysRevD.13.3398.

[111] R. Jackiw and G. Semenoff. "Continuum Quantum Field Theory for a Linearly Conjugated Diatomic Polymer with Fermion Fractionization". In: *Phys. Rev. Lett.* 50.6 (1983), pp. 439–442. DOI: 10.1103/PhysRevLett.50.439.

[112] Yanyu Jia et al. "Evidence for a monolayer excitonic insulator". In: *Nature Physics* 18.1 (2022), pp. 87–93. DOI: 10.1038/s41567-021-01422-w.

[113] Long Ju et al. "Topological valley transport at bilayer graphene domain walls". In: *Nature* 520.7549 (2015), pp. 650–655. DOI: 10.1038/nature14364.

[114] Leo P Kadanoff and Paul C Martin. "Hydrodynamic equations and correlation functions". In: *Annals of Physics* 24 (1963), pp. 419–469. DOI: https://doi.org/10.1016/0003-4916(63)90078-2.

[115] V. Kalmeyer and R. B. Laughlin. "Equivalence of the resonating-valence-bond and fractional quantum Hall states". In: *Phys. Rev. Lett.* 59.18 (1987), pp. 2095–2098. DOI: 10.1103/PhysRevLett.59.2095.

[116] Vadim Kalmeyer and R. B. Laughlin. "Theory of the spin liquid state of the Heisenberg antiferromagnet". In: *Phys. Rev. B* 39.16 (1989), pp. 11879–11899. DOI: 10.1103/PhysRevB.39.11879.

[117] C. L. Kane and E. J. Mele. "Quantum Spin Hall Effect in Graphene". In: *Phys. Rev. Lett.* 95.22 (2005), p. 226801. DOI: 10.1103/PhysRevLett.95.226801.

[118] Y.-C. Kao and D.-H. Lee. "Bulk versus edge in the quantum Hall effect". In: *Phys. Rev. B* 54.23 (1996), pp. 16903–16906. DOI: 10.1103/PhysRevB.54.16903.

[119] Anton Kapustin and Lev Spodyneiko. "Absence of Energy Currents in an Equilibrium State and Chiral Anomalies". In: *Phys. Rev. Lett.* 123.6 (2019), p. 060601. DOI: 10.1103/PhysRevLett.123.060601.

[120] Anton Kapustin and Lev Spodyneiko. "Higher-dimensional generalizations of Berry curvature". In: *Phys. Rev. B* 101.23 (2020), p. 235130. DOI: 10.1103/PhysRevB.101.235130.

[121] C Karrasch, J H Bardarson, and J E Moore. "Reducing the numerical effort of finite-temperature density matrix renormalization group calculations". In: *New Journal of Physics* 15.8 (2013), p. 083031. DOI: 10.1088/1367-2630/15/8/083031.

[122] Hikaru Kawamura and Seiji Miyashita. "Phase Transition of the Two-Dimensional Heisenberg Antiferromagnet on the Triangular Lattice". In: *Journal of the Physical Society of Japan* 53.12 (1984), pp. 4138–4154. DOI: 10.1143/JPSJ.53.4138.

[123] D.M. Kennes and C. Karrasch. "Extending the range of real time density matrix renormalization group simulations". In: *Computer Physics Communications* 200 (2016), pp. 37–43. DOI: https://doi.org/10.1016/j.cpc.2015.10.019.

[124] Eslam Khalaf. "Higher-order topological insulators and superconductors protected by inversion symmetry". In: *Phys. Rev. B* 97.20 (2018), p. 205136. DOI: 10.1103/PhysRevB.97.205136.

[125] Eslam Khalaf et al. "Charged skyrmions and topological origin of superconductivity in magic-angle graphene". In: *Science Advances* 7.19 (2021), eabf5299. DOI: 10.1126/sciadv.abf5299.

[126] Eslam Khalaf et al. "Symmetry Indicators and Anomalous Surface States of Topological Crystalline Insulators". In: *Phys. Rev. X* 8.3 (2018), p. 031070. DOI: 10.1103/PhysRevX.8.031070.

[127] Alexei Kitaev. "Anyons in an exactly solved model and beyond". In: *Annals of Physics* 321.1 (2006), pp. 2–111. DOI: https://doi.org/10.1016/j.aop.2005.10.005.

[128] Alexei Kitaev. "Periodic table for topological insulators and superconductors". In: *AIP Conference Proceedings* 1134.1 (2009), pp. 22–30. DOI: 10.1063/1.3149495.

[129] Alexei Kitaev and Liang Kong. "Models for Gapped Boundaries and Domain Walls". In: *Communications in Mathematical Physics* 313.2 (2012), pp. 351–373.

[130] Maurice Kleman and Oleg D Lavrentovich. *Soft matter physics: an introduction*. Springer, 2003.

[131] Jelena Klinovaja and Daniel Loss. "Fractional charge and spin states in topological insulator constrictions". In: *Phys. Rev. B* 92.12 (2015), p. 121410. DOI: 10.1103/PhysRevB.92.121410.

[132] K. v. Klitzing, G. Dorda, and M. Pepper. "New Method for High-Accuracy Determination of the Fine-Structure Constant Based on Quantized Hall Resistance". In: *Phys. Rev. Lett.* 45.6 (1980), pp. 494–497. DOI: 10.1103/PhysRevLett.45.494.

[133] Shingo Kobayashi et al. "Abe homotopy classification of topological excitations under the topological influence of vortices". In: *Nuclear Physics B* 856.2 (2012), pp. 577–606. DOI: https://doi.org/10.1016/j.nuclphysb.2011.11.003.

[134] Liang Kong. "Anyon condensation and tensor categories". In: *Nuclear Physics B* 886 (2014), pp. 436–482. DOI: https://doi.org/10.1016/j.nuclphysb.2014.07.003.

[135] Liang Kong and Hao Zheng. "A mathematical theory of gapless edges of 2d topological orders. Part II". In: *Nuclear Physics B* 966 (2021), p. 115384. DOI: https://doi.org/10.1016/j.nuclphysb.2021.115384.

[136] Liang Kong and Hao Zheng. "Gapless edges of 2d topological orders and enriched monoidal categories". In: *Nuclear Physics B* 927 (2018), pp. 140–165. DOI: https://doi.org/10.1016/j.nuclphysb.2017.12.007.

[137] Markus König et al. "Quantum Spin Hall Insulator State in HgTe Quantum Wells". In: *Science* 318.5851 (2007), pp. 766–770. DOI: 10.1126/science.1148047.

[138] J M Kosterlitz and D J Thouless. "Ordering, metastability and phase transitions in two-dimensional systems". In: 6.7 (1973), p. 1181. DOI: 10.1088/0022-3719/6/7/010.

[139] Stefanos Kourtis and Maria Daghofer. "Combined Topological and Landau Order from Strong Correlations in Chern Bands". In: *Phys. Rev. Lett.* 113.21 (2014), p. 216404. DOI: 10.1103/PhysRevLett.113.216404.

[140] Mark J. H. Ku et al. "Imaging viscous flow of the Dirac fluid in graphene". In: *Nature* 583.7817 (2020), pp. 537–541. DOI: 10.1038/s41586-020-2507-2.

[141] Ryogo Kubo. "Statistical-Mechanical Theory of Irreversible Processes. I. General Theory and Simple Applications to Magnetic and Conduction Problems". In: *J. Phys. Soc. Jpn.* 12.6 (1957), pp. 570–586. DOI: 10.1143/JPSJ.12.570.

[142] Ryogo Kubo, Mario Yokota, and Sadao Nakajima. "Statistical-Mechanical Theory of Irreversible Processes. II. Response to Thermal Disturbance". In: *J. Phys. Soc. Jpn.* 12.11 (1957), pp. 1203–1211. DOI: 10.1143/JPSJ.12.1203.

[143] Hsin-Hua Lai. "Possible uniform-flux chiral spin liquid states in the SU(3) ring-exchange model on the triangular lattice". In: *Phys. Rev. B* 87.20 (2013), p. 205111. DOI: 10.1103/PhysRevB.87.205111.

[144] Tian Lan, Juven C. Wang, and Xiao-Gang Wen. "Gapped Domain Walls, Gapped Boundaries, and Topological Degeneracy". In: *Phys. Rev. Lett.* 114.7 (2015), p. 076402. DOI: 10.1103/PhysRevLett.114.076402.

[145] Tian Lan et al. "Gapped domain walls between 2+1D topologically ordered states". In: *Phys. Rev. Research* 2.2 (2020), p. 023331. DOI: 10.1103/PhysRevResearch.2.023331.

[146] L.D. Landau and E.M. Lifshitz. *Fluid Mechanics: Landau and Lifshitz: Course of Theoretical Physics, Volume 6*. Elsevier Science, 2013.

[147] L.D. Landau and E.M. Lifshitz. *Statistical Physics: Landau and Lifshitz: Course of Theoretical Physics, Volume 5*. Elsevier Science, 2013.

[148] Lev Davidovich Landau. "On the theory of phase transitions. I." In: *Zh. Eksp. Teor. Fiz.* 11 (1937), p. 19.

[149] Josias Langbehn et al. "Reflection-Symmetric Second-Order Topological Insulators and Superconductors". In: *Phys. Rev. Lett.* 119.24 (2017), p. 246401. DOI: 10.1103/PhysRevLett.119.246401.

[150] Alexander Lau, Jeroen van den Brink, and Carmine Ortix. "Topological mirror insulators in one dimension". In: *Phys. Rev. B* 94.16 (2016), p. 165164. DOI: 10.1103/PhysRevB.94.165164.

[151] R. B. Laughlin. "Anomalous Quantum Hall Effect: An Incompressible Quantum Fluid with Fractionally Charged Excitations". In: *Phys. Rev. Lett.* 50.18 (1983), pp. 1395–1398. DOI: 10.1103/PhysRevLett.50.1395.

[152] Dung-Hai Lee and Xiao-Gang Wen. "Edge excitations in the fractional-quantum-Hall liquids". In: *Phys. Rev. Lett.* 66.13 (1991), pp. 1765–1768. DOI: 10.1103/PhysRevLett.66.1765.

[153] Dung-Hai Lee, Guang-Ming Zhang, and Tao Xiang. "Edge Solitons of Topological Insulators and Fractionalized Quasiparticles in Two Dimensions". In: *Phys. Rev. Lett.* 99.19 (2007), p. 196805. DOI: 10.1103/PhysRevLett.99.196805.

[154] Michael Levin and Zheng-Cheng Gu. "Braiding statistics approach to symmetry-protected topological phases". In: *Phys. Rev. B* 86.11 (2012), p. 115109. DOI: 10.1103/PhysRevB.86.115109.

[155] Michael Levin and T. Senthil. "Deconfined quantum criticality and Néel order via dimer disorder". In: *Phys. Rev. B* 70.22 (2004), p. 220403. DOI: 10.1103/PhysRevB.70.220403.

[156] Maciej Lewenstein, Anna Sanpera, and Veronica Ahufinger. *Ultracold Atoms in Optical Lattices: Simulating quantum many-body systems*. OUP Oxford, 2012.

[157] Linhao Li, Masaki Oshikawa, and Yunqin Zheng. "Symmetry protected topological criticality: Decorated defect construction, signatures and stability". In: *arXiv preprint arXiv:2204.03131* (2022).

[158] Elliott H. Lieb. "Flux Phase of the Half-Filled Band". In: *Phys. Rev. Lett.* 73.16 (1994), pp. 2158–2161. DOI: 10.1103/PhysRevLett.73.2158.

[159] Elliott H. Lieb and Werner Liniger. "Exact Analysis of an Interacting Bose Gas. I. The General Solution and the Ground State". In: *Phys. Rev.* 130.4 (1963), pp. 1605–1616. DOI: 10.1103/PhysRev.130.1605.

[160] DB Litvin. "Tables of crystallographic properties of magnetic space groups". In: *Acta Crystallographica Section A: Foundations of Crystallography* 64.3 (2008), pp. 419–424.

[161] Xiong-Jun Liu, K. T. Law, and T. K. Ng. "Realization of 2D Spin-Orbit Interaction and Exotic Topological Orders in Cold Atoms". In: *Phys. Rev. Lett.* 112.8 (2014), p. 086401. DOI: 10.1103/PhysRevLett.112.086401.

[162] Yuhai Liu et al. "Superconductivity from the condensation of topological defects in a quantum spin-Hall insulator". In: *Nature Communications* 10.1 (2019), p. 2658. DOI: 10.1038/s41467-019-10372-0.

[163] Ana Lopez and Eduardo Fradkin. "Effective field theory for the bulk and edge states of quantum Hall states in unpolarized single layer and bilayer systems". In: *Phys. Rev. B* 63.8 (2001), p. 085306. DOI: 10.1103/PhysRevB.63.085306.

[164] Ana Lopez and Eduardo Fradkin. "Universal structure of the edge states of the fractional quantum Hall states". In: *Phys. Rev. B* 59.23 (1999), pp. 15323–15331. DOI: 10.1103/PhysRevB.59.15323.

[165] Da-Chuan Lu. "Nonlinear sigma model description of deconfined quantum criticality in arbitrary dimensions". In: *arXiv preprint arXiv:2209.00670* (2022).

[166] Yuan-Ming Lu. "Lieb-schultz-mattis theorems for symmetry protected topological phases". In: *arXiv preprint arXiv:1705.04691* (2017).

[167] Yuan-Ming Lu and Dung-Hai Lee. "Spin quantum Hall effects in a spin-1 topological paramagnet". In: *arXiv preprint arXiv:1212.0863* (2012).

[168] Yuan-Ming Lu, Ying Ran, and Masaki Oshikawa. "Filling-enforced constraint on the quantized Hall conductivity on a periodic lattice". In: *Annals of Physics* 413 (2020), p. 168060. DOI: https://doi.org/10.1016/j.aop.2019.168060.

[169] Yuan-Ming Lu and Ashvin Vishwanath. "Classification and properties of symmetry-enriched topological phases: Chern-Simons approach with applications to Z_2 spin liquids". In: *Phys. Rev. B* 93.15 (2016), p. 155121. DOI: 10.1103/PhysRevB.93.155121.

[170] Yuan-Ming Lu and Ashvin Vishwanath. "Theory and classification of interacting integer topological phases in two dimensions: A Chern-Simons approach". In: *Phys. Rev. B* 86.12 (2012), p. 125119. DOI: 10.1103/PhysRevB.86.125119.

[171] Andrew Lucas. "Sound waves and resonances in electron-hole plasma". In: *Phys. Rev. B* 93.24 (2016), p. 245153. DOI: 10.1103/PhysRevB.93.245153.

[172] Andrew Lucas and Kin Chung Fong. "Hydrodynamics of electrons in graphene". In: *Journal of Physics: Condensed Matter* 30.5 (2018), p. 053001. DOI: 10.1088/1361-648x/aaa274.

[173] Andrew Lucas et al. "Transport in inhomogeneous quantum critical fluids and in the Dirac fluid in graphene". In: *Phys. Rev. B* 93.7 (2016), p. 075426. DOI: 10.1103/PhysRevB.93.075426.

[174] Andreas W W Ludwig. "Topological phases: classification of topological insulators and superconductors of non-interacting fermions, and beyond". In: 2016.T168 (2016), p. 014001. DOI: 10.1088/0031-8949/2015/T168/014001.

[175] J. M. Luttinger. "Theory of Thermal Transport Coefficients". In: *Phys. Rev.* 135 (6A 1964), A1505–A1514. DOI: 10.1103/PhysRev.135.A1505.

[176] Nobuki Maeda. "Chiral anomaly and effective field theory for the quantum Hall liquid with edges". In: *Physics Letters B* 376.1 (1996), pp. 142–147. DOI: https://doi.org/10.1016/0370-2693(96)00274-2.

[177] K. A. Matveev and A. Furusaki. "Decay of Fermionic Quasiparticles in One-Dimensional Quantum Liquids". In: *Phys. Rev. Lett.* 111.25 (2013), p. 256401. DOI: 10.1103/PhysRevLett.111.256401.

[178] N. D. Mermin. "The topological theory of defects in ordered media". In: *Rev. Mod. Phys.* 51.3 (1979), pp. 591–648. DOI: 10.1103/RevModPhys.51.591.

[179] Andrej Mesaros and Ying Ran. "Classification of symmetry enriched topological phases with exactly solvable models". In: *Phys. Rev. B* 87.15 (2013), p. 155115. DOI: 10.1103/PhysRevB.87.155115.

[180] Max A. Metlitski and Ryan Thorngren. "Intrinsic and emergent anomalies at deconfined critical points". In: *Phys. Rev. B* 98.8 (2018), p. 085140. DOI: 10.1103/PhysRevB.98.085140.

[181] J. E. Moore and L. Balents. "Topological invariants of time-reversal-invariant band structures". In: *Phys. Rev. B* 75.12 (2007), p. 121306. DOI: 10.1103/PhysRevB.75.121306.

[182] Joel E. Moore. "The birth of topological insulators". In: *Nature* 464 (2010), pp. 194–. DOI: 10.1038/nature08916.

[183] Takahiro Morimoto and Akira Furusaki. "Topological classification with additional symmetries from Clifford algebras". In: *Phys. Rev. B* 88.12 (2013), p. 125129. DOI: 10.1103/PhysRevB.88.125129.

[184] Takahiro Morimoto, Akira Furusaki, and Christopher Mudry. "Anderson localization and the topology of classifying spaces". In: *Phys. Rev. B* 91.23 (2015), p. 235111. DOI: 10.1103/PhysRevB.91.235111.

[185] Markus Müller, Lars Fritz, and Subir Sachdev. "Quantum-critical relativistic magnetotransport in graphene". In: *Phys. Rev. B* 78.11 (2008), p. 115406. DOI: 10.1103/PhysRevB.78.115406.

[186] Markus Müller and Subir Sachdev. "Collective cyclotron motion of the relativistic plasma in graphene". In: *Phys. Rev. B* 78.11 (2008), p. 115419. DOI: 10.1103/PhysRevB.78.115419.

[187] Youngwoo Nam et al. "Electron–hole collision limited transport in charge-neutral bilayer graphene". In: *Nature Physics* 13.12 (2017), pp. 1207–1214. DOI: 10.1038/nphys4218.

[188] Yoichiro Nambu. "Quasi-Particles and Gauge Invariance in the Theory of Superconductivity". In: *Phys. Rev.* 117.3 (1960), pp. 648–663. DOI: 10.1103/PhysRev.117.648.

[189] Pierre Nataf et al. "Chiral Spin Liquids in Triangular-Lattice SU(N) Fermionic Mott Insulators with Artificial Gauge Fields". In: *Phys. Rev. Lett.* 117.16 (2016), p. 167202. DOI: 10.1103/PhysRevLett.117.167202.

[190] Titus Neupert et al. "Fractional (Chern and topological) insulators". In: *Physica Scripta* T164 (2015), p. 014005. DOI: 10.1088/0031-8949/2015/t164/014005.

[191] Anne E. B. Nielsen, Germán Sierra, and J. Ignacio Cirac. "Local models of fractional quantum Hall states in lattices and physical implementation". In: *Nature Communications* 4.1 (2013), p. 2864. DOI: 10.1038/ncomms3864.

[192] Joseph Orenstein et al. "Frequency- and temperature-dependent conductivity in $YBa_2Cu_3O_{6+x}$ crystals". In: *Phys. Rev. B* 42.10 (1990), pp. 6342–6362. DOI: 10.1103/PhysRevB.42.6342.

[193] Masaki Oshikawa, Claudio Chamon, and Ian Affleck. "Junctions of three quantum wires". In: *Journal of Statistical Mechanics: Theory and Experiment* 2006.02 (2006), P02008.

[194] Christopher W. Peterson et al. "A quantized microwave quadrupole insulator with topologically protected corner states". In: *Nature* 555 (2018), pp. 346–. DOI: 10.1038/nature25777.

[195] S. Petit et al. "Observation of magnetic fragmentation in spin ice". In: *Nature Physics* 12.8 (2016), pp. 746–750. DOI: 10.1038/nphys3710.

[196] Trung V Phan, Justin CW Song, and Leonid S Levitov. "Ballistic heat transfer and energy waves in an electron system". In: *arXiv preprint arXiv:1306.4972* (2013).

[197] Frank Pollmann et al. "Symmetry protection of topological phases in one-dimensional quantum spin systems". In: *Phys. Rev. B* 85.7 (2012), p. 075125. DOI: 10.1103/PhysRevB.85.075125.

[198] Mark de Wild Propitius. "Topological interactions in broken gauge theories". In: *arXiv preprint hep-th/9511195* (1995).

[199] Xiao-Liang Qi. "A new class of (2+1)-dimensional topological superconductors with Z_8 topological classification". In: *New Journal of Physics* 15.6 (2013), p. 065002. DOI: 10.1088/1367-2630/15/6/065002.

[200] Xiao-Liang Qi, Taylor L. Hughes, and Shou-Cheng Zhang. "Fractional charge and quantized current in the quantum spin Hall state". In: *Nature Physics* 4 (2008), p. 273. DOI: 10.1038/nphys913.

[201] Xiao-Liang Qi, Yong-Shi Wu, and Shou-Cheng Zhang. "Topological quantization of the spin Hall effect in two-dimensional paramagnetic semiconductors". In: *Phys. Rev. B* 74.8 (2006), p. 085308. DOI: 10.1103/PhysRevB.74.085308.

[202] Xiao-Liang Qi and Shou-Cheng Zhang. "Topological insulators and superconductors". In: *Rev. Mod. Phys.* 83.4 (2011), pp. 1057–1110. DOI: 10.1103/RevModPhys.83.1057.

[203] Pierre Ramond. *Field theory: a modern primer*. Routledge, 2020.

[204] Ying Ran, Yi Zhang, and Ashvin Vishwanath. "One-dimensional topologically protected modes in topological insulators with lattice dislocations". In: *Nature Physics* 5.4 (2009), pp. 298–303.

[205] N. Read and Dmitry Green. "Paired states of fermions in two dimensions with breaking of parity and time-reversal symmetries and the fractional quantum Hall effect". In: *Phys. Rev. B* 61.15 (2000), pp. 10267–10297. DOI: 10.1103/PhysRevB.61.10267.

[206] T. Maurice Rice, Neil J. Robinson, and Alexei M. Tsvelik. "Umklapp scattering as the origin of T-linear resistivity in the normal state of high-T_c cuprate superconductors". In: *Phys. Rev. B* 96.22 (2017), p. 220502. DOI: 10.1103/PhysRevB.96.220502.

[207] Joseph J Rotman and Joseph Jonah Rotman. *An introduction to homological algebra*. Vol. 2. Springer, 2009.

[208] Andreas Rüegg, Sinisa Coh, and Joel E. Moore. "Corner states of topological fullerenes". In: *Phys. Rev. B* 88.15 (2013), p. 155127. DOI: 10.1103/PhysRevB.88.155127.

[209] Andreas Rüegg and Chungwei Lin. "Bound States of Conical Singularities in Graphene-Based Topological Insulators". In: *Phys. Rev. Lett.* 110.4 (2013), p. 046401. DOI: 10.1103/PhysRevLett.110.046401.

[210] Subir Sachdev. "Nonzero-temperature transport near fractional quantum Hall critical points". In: *Phys. Rev. B* 57.12 (1998), pp. 7157–7173. DOI: 10.1103/PhysRevB.57.7157.

[211] Subir Sachdev. "Theory of finite-temperature crossovers near quantum critical points close to,or above, their upper-critical dimension". In: *Phys. Rev. B* 55.1 (1997), pp. 142–163. DOI: 10.1103/PhysRevB.55.142.

[212] Subir Sachdev and Jinwu Ye. "Gapless spin-fluid ground state in a random quantum Heisenberg magnet". In: *Phys. Rev. Lett.* 70.21 (1993), pp. 3339–3342. DOI: 10.1103/PhysRevLett.70.3339.

[213] K V Samokhin. "Lifetime of excitations in a clean Luttinger liquid". In: *Journal of Physics: Condensed Matter* 10.31 (1998), pp. L533–L538. DOI: 10.1088/0953-8984/10/31/002.

[214] Lucile Savary and Leon Balents. "Coulombic Quantum Liquids in Spin-1/2 Pyrochlores". In: *Phys. Rev. Lett.* 108.3 (2012), p. 037202. DOI: 10.1103/PhysRevLett.108.037202.

[215] Thomas Scaffidi, Daniel E. Parker, and Romain Vasseur. "Gapless Symmetry-Protected Topological Order". In: *Phys. Rev. X* 7.4 (2017), p. 041048. DOI: 10.1103/PhysRevX.7.041048.

[216] Frank Schindler et al. "Higher-order topological insulators". In: *Science Advances* 4.6 (2018). DOI: 10.1126/sciadv.aat0346.

[217] Frank Schindler et al. "Higher-order topology in bismuth". In: *Nature Physics* 14.9 (2018), pp. 918–924. DOI: 10.1038/s41567-018-0224-7.

[218] Ulrich Schollwöck. "The density-matrix renormalization group in the age of matrix product states". In: *Annals of Physics* 326.1 (2011), pp. 96–192. DOI: https://doi.org/10.1016/j.aop.2010.09.012.

[219] Darrell F. Schroeter et al. "Spin Hamiltonian for which the Chiral Spin Liquid is the Exact Ground State". In: *Phys. Rev. Lett.* 99.9 (2007), p. 097202. DOI: 10.1103/PhysRevLett.99.097202.

[220] T. Senthil and Matthew P. A. Fisher. "Competing orders, nonlinear sigma models, and topological terms in quantum magnets". In: *Phys. Rev. B* 74.6 (2006), p. 064405. DOI: 10.1103/PhysRevB.74.064405.

[221] T. Senthil et al. "Deconfined Quantum Critical Points". In: *Science* 303.5663 (2004), pp. 1490–1494. DOI: 10.1126/science.1091806.

[222] T. Senthil et al. "Quantum criticality beyond the Landau-Ginzburg-Wilson paradigm". In: *Phys. Rev. B* 70.14 (2004), p. 144407. DOI: 10.1103/PhysRevB.70.144407.

[223] Marc Serra-Garcia et al. "Observation of a phononic quadrupole topological insulator". In: *Nature* 555 (2018), pp. 342–. DOI: 10.1038/nature25156.

[224] Ramamurti Shankar. *Bosonization I: The Fermion Boson Dictionary*. Cambridge University Press, 2017, pp. 319–333. DOI: 10.1017/9781139044349.018.

[225] Gal Shavit and Yuval Oreg. "Domain Formation Driven by the Entropy of Topological Edge Modes". In: *Phys. Rev. Lett.* 128.15 (2022), p. 156801. DOI: 10.1103/PhysRevLett.128.156801.

[226] Ken Shiozaki and Masatoshi Sato. "Topology of crystalline insulators and superconductors". In: *Phys. Rev. B* 90.16 (2014), p. 165114. DOI: 10.1103/PhysRevB.90.165114.

[227] Ken Shiozaki, Masatoshi Sato, and Kiyonori Gomi. "Topological crystalline materials: General formulation, module structure, and wallpaper groups". In: *Phys. Rev. B* 95.23 (2017), p. 235425. DOI: 10.1103/PhysRevB.95.235425.

[228] Ken Shiozaki, Masatoshi Sato, and Kiyonori Gomi. "Topology of nonsymmorphic crystalline insulators and superconductors". In: *Phys. Rev. B* 93.19 (2016), p. 195413. DOI: 10.1103/PhysRevB.93.195413.

[229] J. Sirker, R. G. Pereira, and I. Affleck. "Diffusion and Ballistic Transport in One-Dimensional Quantum Systems". In: *Phys. Rev. Lett.* 103.21 (2009), p. 216602. DOI: 10.1103/PhysRevLett.103.216602.

[230] Robert-Jan Slager et al. "Impurity-bound states and Green's function zeros as local signatures of topology". In: *Phys. Rev. B* 92.8 (2015), p. 085126. DOI: 10.1103/PhysRevB.92.085126.

[231] Robert-Jan Slager et al. "The space group classification of topological band-insulators". In: *Nature Physics* 9 (2013), pp. 98–102. DOI: 10.1038/nphys2513.

[232] S. L. Sondhi et al. "Skyrmions and the crossover from the integer to fractional quantum Hall effect at small Zeeman energies". In: *Phys. Rev. B* 47.24 (1993), pp. 16419–16426. DOI: 10.1103/PhysRevB.47.16419.

[233] Jun Liang Song, Gordon W. Semenoff, and Fei Zhou. "Uniaxial and Biaxial Spin Nematic Phases Induced by Quantum Fluctuations". In: *Phys. Rev. Lett.* 98.16 (2007), p. 160408. DOI: 10.1103/PhysRevLett.98.160408.

[234] Zhida Song, Zhong Fang, and Chen Fang. "$(d-2)$-Dimensional Edge States of Rotation Symmetry Protected Topological States". In: *Phys. Rev. Lett.* 119.24 (2017), p. 246402. DOI: 10.1103/PhysRevLett.119.246402.

[235] Dan M. Stamper-Kurn and Masahito Ueda. "Spinor Bose gases: Symmetries, magnetism, and quantum dynamics". In: *Rev. Mod. Phys.* 85.3 (2013), pp. 1191–1244. DOI: 10.1103/RevModPhys.85.1191.

[236] G. R. Stewart. "Non-Fermi-liquid behavior in d- and f-electron metals". In: *Rev. Mod. Phys.* 73.4 (2001), pp. 797–855. DOI: 10.1103/RevModPhys.73.797.

[237] W. P. Su, J. R. Schrieffer, and A. J. Heeger. "Soliton excitations in polyacetylene". In: *Phys. Rev. B* 22.4 (1980), pp. 2099–2111. DOI: 10.1103/PhysRevB.22.2099.

[238] Zhiyuan Sun, D. N. Basov, and M. M. Fogler. "Adiabatic Amplification of Plasmons and Demons in 2D Systems". In: *Phys. Rev. Lett.* 117.7 (2016), p. 076805. DOI: 10.1103/PhysRevLett.117.076805.

[239] Zhiyuan Sun, Dmitry N. Basov, and Michael M. Fogler. "Universal linear and nonlinear electrodynamics of a Dirac fluid". In: *Proc. Nat. Acad. Sci.* 115.13 (2018), pp. 3285–3289. DOI: 10.1073/pnas.1717010115.

[240] S S Sunku et al. "Photonic crystals for nano-light in moiré graphene superlattices". In: *Science* 362.6419 (2018), pp. 1153–1156. DOI: 10.1126/science.aau5144.

[241] Aaron Szasz et al. "Chiral Spin Liquid Phase of the Triangular Lattice Hubbard Model: A Density Matrix Renormalization Group Study". In: *Phys. Rev. X* 10.2 (2020), p. 021042. DOI: 10.1103/PhysRevX.10.021042.

[242] H. Takagi et al. "Systematic evolution of temperature-dependent resistivity in $La_{2-x}Sr_xCuO_4$". In: *Phys. Rev. Lett.* 69.20 (1992), pp. 2975–2978. DOI: 10.1103/PhysRevLett.69.2975.

[243] Akihiro Tanaka and Xiao Hu. "Many-Body Spin Berry Phases Emerging from the π-Flux State: Competition between Antiferromagnetism and the Valence-Bond-Solid State". In: *Phys. Rev. Lett.* 95.3 (2005), p. 036402. DOI: 10.1103/PhysRevLett.95.036402.

[244] Yijun Tang et al. "Thermalization near Integrability in a Dipolar Quantum Newton's Cradle". In: *Phys. Rev. X* 8.2 (2018), p. 021030. DOI: 10.1103/PhysRevX.8.021030.

[245] Nicolas Tarantino, Netanel H. Lindner, and Lukasz Fidkowski. "Symmetry fractionalization and twist defects". In: *New Journal of Physics* 18.3 (2016), p. 035006. DOI: 10.1088/1367-2630/18/3/035006.

[246] Jeffrey C Y Teo. "Globally symmetric topological phase: from anyonic symmetry to twist defect". In: *Journal of Physics: Condensed Matter* 28.14 (2016), p. 143001. DOI: 10.1088/0953-8984/28/14/143001.

[247] Jeffrey C. Y. Teo and Taylor L. Hughes. "Existence of Majorana-Fermion Bound States on Disclinations and the Classification of Topological Crystalline Superconductors in Two Dimensions". In: *Phys. Rev. Lett.* 111.4 (2013), p. 047006. DOI: 10.1103/PhysRevLett.111.047006.

[248] Jeffrey C. Y. Teo and C. L. Kane. "Topological defects and gapless modes in insulators and superconductors". In: *Phys. Rev. B* 82.11 (2010), p. 115120. DOI: 10.1103/PhysRevB.82.115120.

[249] Jeffrey C. Y. Teo, Abhishek Roy, and Xiao Chen. "Unconventional fusion and braiding of topological defects in a lattice model". In: *Phys. Rev. B* 90.11 (2014), p. 115118. DOI: 10.1103/PhysRevB.90.115118.

[250] Ronny Thomale et al. "Parent Hamiltonian for the chiral spin liquid". In: *Phys. Rev. B* 80.10 (2009), p. 104406. DOI: 10.1103/PhysRevB.80.104406.

[251] Alex Thomson and Jason Alicea. "Recovery of massless Dirac fermions at charge neutrality in strongly interacting twisted bilayer graphene with disorder". In: *Phys. Rev. B* 103.12 (2021), p. 125138. DOI: 10.1103/PhysRevB.103.125138.

[252] Ryan Thorngren, Ashvin Vishwanath, and Ruben Verresen. "Intrinsically gapless topological phases". In: *Phys. Rev. B* 104.7 (2021), p. 075132. DOI: 10.1103/PhysRevB.104.075132.

[253] Luka Trifunovic and Piet Brouwer. "Bott periodicity for the topological classification of gapped states of matter with reflection symmetry". In: *Phys. Rev. B* 96.19 (2017), p. 195109. DOI: 10.1103/PhysRevB.96.195109.

[254] Luka Trifunovic and Piet W. Brouwer. "Higher-Order Bulk-Boundary Correspondence for Topological Crystalline Phases". In: *Phys. Rev. X* 9.1 (2019), p. 011012. DOI: 10.1103/PhysRevX.9.011012.

[255] D. C. Tsui, H. L. Stormer, and A. C. Gossard. "Two-Dimensional Magnetotransport in the Extreme Quantum Limit". In: *Phys. Rev. Lett.* 48.22 (1982), pp. 1559–1562. DOI: 10.1103/PhysRevLett.48.1559.

[256] Farzan Vafa. "Defect dynamics in active polar fluids vs. active nematics". In: *Soft Matter* 18.42 (2022), pp. 8087–8097.

[257] Oskar Vafek. *Quasiparticles and vortices in the high temperature cuprate superconductors*. The Johns Hopkins University, 2004.

[258] Chandra M. Varma. "Colloquium: Linear in temperature resistivity and associated mysteries including high temperature superconductivity". In: *Rev. Mod. Phys.* 92.3 (2020), p. 031001. DOI: 10.1103/RevModPhys.92.031001.

[259] G. Vidal. "Classical Simulation of Infinite-Size Quantum Lattice Systems in One Spatial Dimension". In: *Phys. Rev. Lett.* 98.7 (2007), p. 070201. DOI: 10.1103/PhysRevLett.98.070201.

[260] Guifré Vidal. "Efficient Classical Simulation of Slightly Entangled Quantum Computations". In: *Phys. Rev. Lett.* 91.14 (2003), p. 147902. DOI: 10.1103/PhysRevLett.91.147902.

[261] G. E. Volovik. "Fermion zero modes on vortices in chiral superconductors". In: *Journal of Experimental and Theoretical Physics Letters* 70.9 (1999), pp. 609–614. DOI: 10.1134/1.568223.

[262] Chong Wang et al. "Deconfined Quantum Critical Points: Symmetries and Dualities". In: *Phys. Rev. X* 7.3 (2017), p. 031051. DOI: 10.1103/PhysRevX.7.031051.

[263] Qing-Rui Wang, Shang-Qiang Ning, and Meng Cheng. "Domain Wall Decorations, Anomalies and Spectral Sequences in Bosonic Topological Phases". In: *arXiv preprint arXiv:2104.13233* (2021).

[264] Yan-Qi Wang, Chunxiao Liu, and Yuan-Ming Lu. "Theory of topological defects and textures in two-dimensional quantum orders with spontaneous symmetry breaking". In: *arXiv preprint arXiv:2211.13207* (2022).

[265] Yan-Qi Wang, Chunxiao. Liu, and Joel E. Moore. In: *arXiv:2208.14056* (2022).

[266] Yan-Qi Wang and Joel E. Moore. "Boundary edge networks induced by bulk topology". In: *Phys. Rev. B* 99.15 (2019), p. 155102. DOI: 10.1103/PhysRevB.99.155102.

[267] Yan-Qi Wang et al. "Minimal one-dimensional model of bad metal behavior from fast particle-hole scattering". In: *Phys. Rev. B* 107.10 (2023), p. L100301. DOI: 10.1103/PhysRevB.107.L100301.

[268] X. G. Wen. "Gapless boundary excitations in the quantum Hall states and in the chiral spin states". In: *Phys. Rev. B* 43.13 (1991), pp. 11025–11036. DOI: 10.1103/PhysRevB.43.11025.

[269] X. G. Wen. "Mean-field theory of spin-liquid states with finite energy gap and topological orders". In: *Phys. Rev. B* 44.6 (1991), pp. 2664–2672. DOI: 10.1103/PhysRevB.44.2664.

[270] X. G. Wen. "Topological orders in rigid states". In: *International Journal of Modern Physics B* 04.02 (1990), pp. 239–271. DOI: 10.1142/S0217979290000139.

[271] X. G. Wen, Frank Wilczek, and A. Zee. "Chiral spin states and superconductivity". In: *Phys. Rev. B* 39.16 (1989), pp. 11413–11423. DOI: 10.1103/PhysRevB.39.11413.

[272] X. G. Wen and A. Zee. "Shift and spin vector: New topological quantum numbers for the Hall fluids". In: *Phys. Rev. Lett.* 69.6 (1992), pp. 953–956. DOI: 10.1103/PhysRevLett.69.953.

[273] X.-G. Wen. *Quantum Field Theory of Many-Body Systems*. Oxford University Press, New York, 2004.

[274] Xiao-Gang Wen. "Classifying gauge anomalies through symmetry-protected trivial orders and classifying gravitational anomalies through topological orders". In: *Phys. Rev. D* 88.4 (2013), p. 045013. DOI: 10.1103/PhysRevD.88.045013.

[275] Xiao-Gang Wen. "Colloquium: Zoo of quantum-topological phases of matter". In: *Rev. Mod. Phys.* 89.4 (2017), p. 041004. DOI: 10.1103/RevModPhys.89.041004.

[276] Xiao-Gang Wen. "Quantum orders and symmetric spin liquids". In: *Phys. Rev. B* 65.16 (2002), p. 165113. DOI: 10.1103/PhysRevB.65.165113.

[277] Xiao-Gang Wen. "Symmetry-protected topological invariants of symmetry-protected topological phases of interacting bosons and fermions". In: *Phys. Rev. B* 89.3 (2014), p. 035147. DOI: 10.1103/PhysRevB.89.035147.

[278] Xiao-Gang Wen. "Topological orders and edge excitations in fractional quantum Hall states". In: *Advances in Physics* 44.5 (1995), pp. 405–473. DOI: 10.1080/00018739500101566.

[279] Xueda Wen et al. "Flow of (higher) Berry curvature and bulk-boundary correspondence in parametrized quantum systems". In: *arXiv e-prints*, arXiv:2112.07748 (2021).

[280] J. Wess and B. Zumino. "Supergauge transformations in four dimensions". In: *Nuclear Physics B* 70.1 (1974), pp. 39–50. DOI: https://doi.org/10.1016/0550-3213(74)90355-1.

[281] Steven R. White. "Density matrix formulation for quantum renormalization groups". In: *Phys. Rev. Lett.* 69.19 (1992), pp. 2863–2866. DOI: 10.1103/PhysRevLett.69.2863.

[282] Alexander Wietek, Antoine Sterdyniak, and Andreas M. Läuchli. "Nature of chiral spin liquids on the kagome lattice". In: *Phys. Rev. B* 92.12 (2015), p. 125122. DOI: 10.1103/PhysRevB.92.125122.

[283] Frank Wilczek and A. Zee. "Linking Numbers, Spin, and Statistics of Solitons". In: *Phys. Rev. Lett.* 51.25 (1983), pp. 2250–2252. DOI: 10.1103/PhysRevLett.51.2250.

[284] Edward Witten. "Global aspects of current algebra". In: *Nuclear Physics B* 223.2 (1983), pp. 422–432. DOI: https://doi.org/10.1016/0550-3213(83)90063-9.

[285] Congjun Wu, B. Andrei Bernevig, and Shou-Cheng Zhang. "Helical Liquid and the Edge of Quantum Spin Hall Systems". In: *Phys. Rev. Lett.* 96.10 (2006), p. 106401. DOI: 10.1103/PhysRevLett.96.106401.

[286] Xiao-Chuan Wu, Chap-Ming Jian, and Cenke Xu. "Coupled Wire description of the Correlated Physics in Twisted Bilayer Graphene". In: *arXiv:1811.08442* (2018).

[287] Zhan Wu et al. "Realization of two-dimensional spin-orbit coupling for Bose-Einstein condensates". In: *Science* 354.6308 (2016), pp. 83–88. DOI: 10.1126/science.aaf6689. eprint: http://science.sciencemag.org/content/354/6308/83.full.pdf.

[288] Cenke Xu and J. E. Moore. "Stability of the quantum spin Hall effect: Effects of interactions, disorder, and $\mathbb{Z}_2$ topology". In: *Phys. Rev. B* 73.4 (2006), p. 045322. DOI: 10.1103/PhysRevB.73.045322.

[289] Zhongbo Yan, Fei Song, and Zhong Wang. "Majorana Corner Modes in a High-Temperature Platform". In: *Phys. Rev. Lett.* 121.9 (2018), p. 096803. DOI: 10.1103/PhysRevLett.121.096803.

[290] Xu Yang et al. "Dyonic Lieb-Schultz-Mattis theorem and symmetry protected topological phases in decorated dimer models". In: *Phys. Rev. B* 98.12 (2018), p. 125120. DOI: 10.1103/PhysRevB.98.125120.

[291] Weicheng Ye et al. "Topological characterization of Lieb-Schultz-Mattis constraints and applications to symmetry-enriched quantum criticality". In: *SciPost Phys.* 13 (2022), p. 066. DOI: 10.21468/SciPostPhys.13.3.066.

[292] Hideo Yoshioka and Arkadi A. Odintsov. "Electronic Properties of Armchair Carbon Nanotubes: Bosonization Approach". In: *Phys. Rev. Lett.* 82.2 (1999), pp. 374–377. DOI: 10.1103/PhysRevLett.82.374.

[293] Jan Zaanen. "Planckian dissipation, minimal viscosity and the transport in cuprate strange metals". In: *SciPost Phys.* 6.5 (2019), p. 61. DOI: 10.21468/SciPostPhys.6.5.061.

[294] Jan Zaanen. "Why the temperature is high". In: *Nature* 430.6999 (2004), pp. 512–513. DOI: 10.1038/430512a.

[295] Michael P. Zaletel, Roger S. K. Mong, and Frank Pollmann. "Topological Characterization of Fractional Quantum Hall Ground States from Microscopic Hamiltonians". In: *Phys. Rev. Lett.* 110.23 (2013), p. 236801. DOI: 10.1103/PhysRevLett.110.236801.

[296] Qiu Zhang and Tao Li. "Bosonic resonating valence bond theory of the possible chiral spin-liquid state in the triangular-lattice Hubbard model". In: *Phys. Rev. B* 104.7 (2021), p. 075103. DOI: 10.1103/PhysRevB.104.075103.

[297] Wanzhou Zhang, Ruoxi Yin, and Yancheng Wang. "Pair supersolid with atom-pair hopping on the state-dependent triangular lattice". In: *Phys. Rev. B* 88.17 (2013), p. 174515. DOI: 10.1103/PhysRevB.88.174515.

[298] Yi Zhang, Ying Ran, and Ashvin Vishwanath. "Topological insulators in three dimensions from spontaneous symmetry breaking". In: *Phys. Rev. B* 79.24 (2009), p. 245331. DOI: 10.1103/PhysRevB.79.245331.

[299] Bin Zhou et al. "Finite Size Effects on Helical Edge States in a Quantum Spin-Hall System". In: *Phys. Rev. Lett.* 101.24 (2008), p. 246807. DOI: 10.1103/PhysRevLett.101.246807.

[300] W. Zhu, D. N. Sheng, and Kun Yang. "Topological Interface between Pfaffian and Anti-Pfaffian Order in $\nu = 5/2$ Quantum Hall Effect". In: *Phys. Rev. Lett.* 125.14 (2020), p. 146802. DOI: 10.1103/PhysRevLett.125.146802.

[301] Xiaoyu Zhu. "Tunable Majorana corner states in a two-dimensional second-order topological superconductor induced by magnetic fields". In: *Phys. Rev. B* 97.20 (2018), p. 205134. DOI: 10.1103/PhysRevB.97.205134.

[302] Zheng Zhu, D. N. Sheng, and Ashvin Vishwanath. "Doped Mott insulators in the triangular-lattice Hubbard model". In: *Phys. Rev. B* 105.20 (2022), p. 205110. DOI: 10.1103/PhysRevB.105.205110.